

**^{18}F LABELED BILE ACID ANALOGUES AS
MOLECULAR IMAGING TOOLS TO MONITOR
HEPATOBIILIARY TRANSPORT IN DRUG-INDUCED
CHOLESTASIS AND LIVER DISEASE**

STEF DE LOMBAERDE

Thesis submitted to obtain the degree of Doctor in Pharmaceutical Sciences

Promotors:

Prof. Dr. Apr. Filip De Vos

Prof. Dr. Ir. Christian Vanhove

Members of the Examination Committee

Prof. Dr. Pieter Annaert

Faculty of Pharmaceutical Sciences, KULeuven

Dr. Filipe Elvas

Department of Nuclear Medicine, Antwerp University Hospital

Prof. Dr. Bieke Lambert

Faculty of Medicine, Ghent University

Prof. Dr. Katrien Remaut

Faculty of Pharmaceutical Sciences, Ghent University

Prof. Dr. Christophe Stove

Faculty of Pharmaceutical Sciences, Ghent University

Prof. Dr. Hans Van Vlierberghe

Faculty of Medicine, Ghent University

The author and promotors give the authorization to consult and to copy parts of this thesis for personal use only. Any other use is limited by the Laws of Copyright, especially concerning the obligation to refer to the source whenever results are cited from this thesis.

De auteur en promotoren geven de toestemming dit proefschrift voor raadpleging ter beschikking te stellen en delen ervan te kopiëren voor persoonlijk gebruik. Elk ander gebruik valt onder de beperking van het auteursrecht, in het bijzonder tot de verplichting de bron te vermelden bij het aanhalen van resultaten uit dit proefschrift.

Gent, Augustus 2018

Stef De Lombaerde

Dankwoord

Nu ik begonnen ben met schrijven van dit dankwoord, besef ik maar al te goed dat er een einde gekomen is aan een lange weg. Een weg die ik met behoorlijk wat mensen samen heb afgelegd en waarbij iedereen op zijn of haar unieke manier bijgedragen heeft tot het eindresultaat dat jullie nu kunnen lezen.

Zonder promotor zou er van een doctoraat helemaal geen sprake zijn. Vandaar dat ik eerst en vooral prof. De Vos wil bedanken voor de kans die hij mij gegeven heeft om te doctoreren in het labo voor radiofarmacie. Filip, bedankt om via je vakken mijn interesse te wekken in de fascinerende wereld van nucleaire geneeskunde. Je voorzag het doctoraat van voldoende uitdagingen en gaf mij de vrijheid om deze zelfstandig te mogen aanpakken. Bedankt ook voor het nalezen van de publicaties en de kansen om mijn werk internationaal voor te stellen.

Mijn copromotor, prof. Christian Vanhove, zou ik ook graag willen bedanken. Chris, je staat altijd paraat om iedereen te helpen met raad en daad, wat ik ten zeerste apprecieerde de afgelopen jaren! Bedankt voor je welgemeende interesse in het onderzoek en voor alle praktische tips die daarmee gepaard gaan! Bedankt ook voor het nalezen van de vele doorgestuurde artikels en hoofdstukken van dit doctoraat: het zal ongetwijfeld behoorlijk wat tijd in beslag genomen!

I would certainly also like to thank the reading committee of my doctoral dissertation. Thank you for sharing your insights from other points of view, and providing me with valuable feedback. I appreciate all the effort you put in reading this dissertation and discussing it with me on a Friday evening!

Prof. Hans Van Vlierberghe, Lindsey Devisscher en het hepatologie team van het UZ Gent wens ik ook graag te bedanken voor de fijne, constructieve samenwerking! Dankzij jullie werd mijn oorspronkelijk enkel (radio)chemische kennis, meer opengetrokken naar de klinische aspecten van leveronderzoek. De hulp bij het uitkiezen, uitvoeren en evalueren van de verschillende muismodellen voor leverschade kon ik ook zeer zeker appreciëren. Vooral dan de meer praktische tips: bvb. hoe moet ik dat dier nu precies vastnemen zonder dat het voor beide partijen een traumatische ervaring moet zijn...

De mannen van medicinale chemie o.l.v. prof. Van Calenbergh wil ik ook graag bedanken om te tonen hoe organische synthese écht moet! Izet, bedankt voor het opnemen van de vele massaspectra en NMR's!

Nog een essentiële component om het doctoraat tot een goed einde te brengen (of zelfs nog maar te beginnen) was de cyclotronafdeling van het UZ Gent. Zonder ^{18}F zou er immers niet al te veel te vertellen vallen in dit boek... Jan, John, Cedric, Sam, Eline, Lieselotte: bedankt voor de ontelbare korte bestralingen en spoelingen van de targets! Meestal kwam ik al van 's morgens aan jullie oren zagen om wat fluor, veelal tussen drukke patiëntenproducties door: sorry daarvoor :)! Ken, een speciaal woordje van dank voor jou! Je was mijn begeleider tijdens de masterproefperiode en werd sindsdien een soort van wetenschappelijke mentor! Bedankt om vanaf toen te geloven in mijn kunnen en mij warm te maken om de uitdaging van wetenschappelijk onderzoek aan te gaan! Gedurende de eerste paar maanden van het doctoraat (gevuld met héél veel fails), was jouw positivisme en (radiochemische)

ondersteuning zeker welkom! Bovendien heb je de andere doctoraatsstudenten en mij ook heel wat andere dingen bijgebracht die niet gerelateerd zijn aan radiochemie, maar die zullen we wijselijk maar voor onszelf houden...

Als er dan wat fluor samengesprokkeld was en de radiosynthese gebeurd, moest er natuurlijk ook heel wat afgescand worden op het Infinity lab! Béné, bedankt voor alle praktische ondersteuning en de fijne babbels (+ flauwe mopjes) tussendoor! Collega-doctoraatsstudenten Kim, Valerie, Julie, Emma en Sam: merci om van tijd tot tijd voor de vrolijke noot te zorgen tijdens scandagen (en vooral op congres)!

Dan belanden we bij de mensen waar ik de afgelopen jaren het meest lief en leed mee gedeeld heb: de collega's van het labo radiofarmacie! Eerst en vooral "radfarsquad": Jeroen, Nick, Glenn en Tristan! Samen hebben we heel wat gezeverd, gelachen en ons vooral veel afgevraagd wie er nu het diepst in de miserie zat met zijn proeven! Ik houd vooral veel goede herinneringen over aan de leadership foundation course, moeten we zeker eens overdoen! Jeroen, merci om gedurende 4 jaar de rust en kalmte in ons bureau te garanderen (Gregoriaans gezang helpt altijd)! Ook bedankt om goed zorg te dragen voor mij: ik denk hierbij dan vooral aan het corrigeren van mijn navigatiefouten en 's morgens vroeg in Londen medicamenten voor mij te gaan zoeken :)! Best wel grappig dat we het doctoraat samen afsluiten hoe het begonnen is: brakken in het practicum van biomedische. Nick, ik heb ongelofelijk veel bijgeleerd van je wetenschappelijke verbloemingstechnieken, je hebt hier een echt talent voor! Door jouw filmpjes heb ik ook een hele nieuwe appreciatie gekregen voor metal! Glenn, dankzij uw quotes ga ik het fantastisch vinden om ooit een accident te hebben op de Antwerpse ring! Ik laat zeker weten hoe de ervaring was! Tristan, na onze eerste ontmoeting een drietal jaar geleden vroeg ik mij af wat ze hier in godsnaam hadden binnen gegooid. Drie jaar later vraag ik mij nog steeds hetzelfde af. Maar nu serieus: ik bewonder jouw rechttoe rechtaan aanpak van problemen, daar kan ik af en toe nog wel iets van leren!

Sara, bedankt voor het warme welkom in de "galzuurfamilie", de fijne tijd samen in het labo en natuurlijk de vele tips & tricks i.v.m. celletjes, proefdieren, scannen, ... Zonder jou zou ik zeker niet zo'n vlotte start gehad hebben! Ik kon mij bovendien geen betere meter voorstellen :)! Tessa, zo lang was je niet bij ons, maar we hebben je onder andere in San Sebastian alleszins snel en goed leren kennen als een zotte flapuit! Veel succes nog aan het VIB ;)! Sarah, veel geluk moet ik je niet meer wensen met het doctoraat, een succesproject als PSMA verkoopt zichzelf he!

Een labo met enkel maar doctoraatsstudenten, dat komt ook niet goed! Ghilaine, Valerie, Nico, Wim, Caroline en team Melle: Joeri en Lieve: het was aangenaam om samen te werken met jullie in het labo! Op de vele uitstapjes, etentjes en sportdagen konden we het ook altijd goed vinden met elkaar! Ghilaine, zonder jouw administratieve ondersteuning zou het labo nog meer in het honderd lopen: bedankt om iedereen altijd tijdig te voorzien van de gewenste producten en documenten! Valerie, 'ndankt è voor de hilarische middagpauzes en om de frustraties tijdens eindeloze practicumdagen wat te delen! Nico, "bedankt" om mij te voorzien van de meest loze liedjes, die dan ook nog eens dagen vast in mijn hoofd zaten...

Mijn thesisstudenten Martijn, Karen en Esther verdienen ook zeker een vermelding voor alle hulp en de enthousiaste wijze waarop zij meegegaan zijn in mijn galzuurverhaal: merci!

Eens goed kunnen ventileren bij vrienden maakt een doctoraat wat draaglijker! Bedankt aan alle vrienden of kennissen die ooit eens gevraagd hebben: “wel, hoe is dat nu met uw doctoraat?”, waarna ze waarschijnlijk af en toe wel eens een veel te lange en saaie klaagzaag hebben moeten aanhoren... Speciale dank gaat uit naar Kristof, Julie, Peter, Jolien, Stany, Marieke en Geert voor de vele ontspannende avonden die we samen doorgebracht hebben, de zalige feestjes (we zouden ze nu niet zo goed meer verteren), cinemabezoekjes en zoveel meer! Als alle doctoraten eindelijk achter de rug zijn, gaat er nog eens een serieus feestje gegeven moeten worden :)!!

Uiteraard wil ik ook graag mijn familie, en in de eerste plaats mijn ouders en zus bedanken voor hun jarenlange steun en het warme nest om naar terug te keren na een lange les-, practicum-, of werkdag! Jullie hebben altijd achter mij gestaan en mij steeds alle kansen gegeven om mijn passie voor wetenschap te volgen! Ma, bedankt voor alle “mental support” momentjes, de fruit-uurtjes en om mij de “voor de vooruit- mentaliteit” (-soms proberen-) bij te brengen! Pa, geen moeite is je ooit teveel geweest om ervoor te zorgen dat ik veilig en op tijd (en natuurlijk ook voorzien van voldoende eten) een examen kon starten! Emily, merci om het ook niet altijd serieus te moeten houden door je relativiseringsvermogen en Cheetie-verhalen!

Mijn schoonfamilie: Marc, Hilde, Sophie, Thomas en Domien stonden ook altijd klaar om mij te steunen met raad en daad! “Hoe is het met de muizekes?” was alleszins een frequent voorkomende vraag aan tafel :)!

Ook aan alle neven, nichten, tantes, nonkels, grootouders ... van mijn (schoon)familie: bedankt voor jullie interesse en steun!!

En saving the best for last ... Liefste Lisa, woorden schieten te kort om uit te drukken hoeveel jij betekent voor mij! Na een lastige dag slaagde je er altijd opnieuw in om een lach op mijn gezicht te toveren! De laatste paar weken was ik misschien wel niet altijd even aanspreekbaar, en dat is natuurlijk niet zo gemakkelijk geweest voor een sociale, vlotte vrouw zoals jij :)! Bedankt voor je begrip en geduld, ik zorg ervoor dat er vanaf nu opnieuw wat meer quality time is :)!

Bedankt allemaal!

Stef

Table of contents

Dankwoord

Table of contents

List of abbreviations

Outline

Chapter 1: General Introduction	1
PART 1: THE LIVER	1
1.1 Macroscopic anatomy and physiology of the liver.....	2
1.2 Microscopic architecture of the liver	3
1.3 Bile: constituents and functions	6
1.4 Bile acids	8
1.4.1 Structure and chemical properties.....	8
1.4.2 Biosynthesis.....	11
1.4.3 Transport of bile acids in the enterohepatic circulation.....	14
PART 2: MOLECULAR IMAGING	24
1.1 What is molecular imaging and why do we need it?	24
1.1.1 General overview	24
1.1.2 Multi-modality imaging.....	27
1.1.3 Small animal imaging.....	28
1.2 Computed Tomography (CT)	29
1.3 Single Photon Emission Computed Tomography (SPECT)	31
1.4 Positron Emission Tomography (PET).....	34
1.4.1 Physical principles and detection system	34
1.4.2 2-[¹⁸ F]Fluoro-2-deoxy-D-glucose ([¹⁸ F]FDG), the workhorse of PET	38
1.4.3 PET versus SPECT.....	39

1.4.4	Production of PET radionuclides with a cyclotron	40
1.4.5	Fluoro-18 PET-radiochemistry.....	41
	Part 1 and 2 References	45
Chapter 2: Molecular Imaging In Liver Disease		55
2.1	Background of focused liver diseases.....	56
2.1.1	Drug-induced liver injury (DILI)	56
2.1.2	Cirrhosis.....	61
2.1.3	Hepatocellular carcinoma (HCC)	63
2.2	Molecular imaging of hepatobiliary function	64
2.2.1	MRI contrast agents	65
2.2.2	SPECT tracers.....	67
2.2.3	PET tracers.....	70
	References.....	77
Chapter 3: Scope And Aims		84
Chapter 4: Development Of Fluorinated Bile Acids For PET Imaging		90
4.1	Introduction.....	91
4.2	Materials and methods.....	95
4.2.1	Synthesis of lead compound 3β-[¹⁸ F]fluorocholeic acid	95
4.2.2	Synthesis of other ¹⁸ F labeled bile acid analogues.....	100
4.3	Results.....	106
4.3.1	Synthesis of lead compound 3β-[¹⁸ F]fluorocholeic acid	106
4.3.2	Synthesis of other ¹⁸ F labeled bile acid analogues.....	108
4.4	Discussion	110
4.5	Conclusion	112
4.6	Experimental section: precursor and reference compound synthesis	113
4.7	References	124

Chapter 5: <i>In Vitro</i> Evaluation Of Fluorinated Bile Acids	128
5.1 Introduction	129
5.2 Materials and methods.....	131
5.2.1 Radiosynthesis of ¹⁸ F labeled bile acids	131
5.2.2 LogD(7.4) determination	131
5.2.3 <i>In vitro</i> investigation of stability.....	131
5.2.4 <i>In vitro</i> uptake assay.....	132
5.2.5 <i>In vitro</i> efflux assay.....	133
5.3 Results.....	135
5.3.1 LogD(7.4) determination	135
5.3.2 <i>In vitro</i> investigation of stability.....	135
5.3.3 <i>In vitro</i> uptake assay.....	135
5.3.4 <i>In vitro</i> efflux assay.....	138
5.4 Discussion	141
5.5 Conclusion	143
5.6 References	144
Chapter 6: <i>In Vivo</i> Evaluation Of ¹⁸F Labeled Bile Acids In Wild-Type Mice	146
6.1 Introduction	147
6.2 Materials and methods.....	149
6.2.1 Radiosynthesis.....	149
6.2.2 PET imaging protocol and animal experiments	149
6.3 Results.....	152
6.3.1 Evaluation of lead compound 3β-[¹⁸ F]FCA.....	152
6.3.2 Comparison of the different ¹⁸ F labeled bile acids	159
6.4 Discussion	162
6.5 Conclusion	165

6.6	References	166
Chapter 7: Valorization Of 3β-[¹⁸F]FCA In Liver Disease Models		170
7.1	Introduction	171
7.2	Materials and methods.....	173
7.2.1	Animal models.....	173
7.2.2	RNA extraction and RT-qPCR.....	175
7.2.3	PET imaging protocol.....	176
7.3	Results.....	178
7.3.1	Drug-induced cholestasis by cyclosporin administration	178
7.3.2	Acute liver injury by APAP overdose	180
7.3.3	Cholangiopathy by DDC diet	181
7.3.4	NASH by MCD diet.....	183
7.3.5	HCC by DEN administration.....	186
7.3.6	Alcoholic cirrhosis by CCl ₄ administration.....	189
7.4	Discussion	191
7.5	Conclusion	195
7.6	References	196
Chapter 8: General Conclusions		199
Chapter 9: Broader International Context, Relevance And Future Perspectives		205
9.1	Development of radiolabeled bile acids for molecular imaging of the liver.....	206
9.2	(Future) application areas	210
9.2.1	Preclinical drug development	210
9.2.2	Clinical research	212
9.3	References	215
Chapter 10: Summary – Samenvatting – Curriculum Vitae		218

List of abbreviations

[¹⁸ F]FDG	2-[¹⁸ F]fluoro-2-deoxy-D-glucose
^{99m} Tc-GSA	^{99m} Tc galactosyl serum albumin
AB	Arterial blood
ABC	ATP-Binding Cassette transporter
Ac ₂ O	Acetic anhydride
AcCl	Acetyl chloride
AcN	Acetonitrile
ALT	Alanine transaminase
APAP	Acetaminophen
ASBT	Apical Sodium-dependent Bile acid Transporter (<i>SLC10A2</i> gene)
AST	Aspartate transaminase
ATP	Adenosine triphosphate
AUC	Area under the curve
BC	Biliary clearance
BCLC	Barcelona Clinic Liver Cancer
BCRP	Breast Cancer Resistance Protein (<i>ABCG2</i> gene)
BGO	Bismuth germanate
BOLD-MRI	Blood oxygen level dependent MRI
BSEP	Bile Salt Export Pump (<i>ABCB11</i> gene)
CA	Cholic acid
CA-lys-TFA	Cholic acid trifluoroacetyl lysine
CAME	Cholic acid methyl ester
CA-sar-TFMA	cholylsarcosine trifluoro-N-methyl-acetamide
CDCA	Chenodeoxycholic acid
cDNA	Complementary deoxyribonucleic acid
CH ₂ Cl ₂	Dichloromethane
CHO	Chinese Hamster Ovary
CoA	Co-enzyme A
CPT	Child-Pugh-Turcotte

CT	Computed Tomography
CV	Coefficient of variation
DAST	Diethylaminosulfur trifluoride
DCE-MRI	Dynamic contrast enhanced MRI
DDC	3,5-diethoxycarbonyl- 1,4-dihydrocollidine
DIAD	Diisopropyl azodicarboxylate
DIC	Drug-induced cholestasis
DILI	Drug-induced liver injury
DMAP	Dimethylaminopyridine
DMEM	Dulbecco's modified Eagle's medium
DMF	N, N-dimethylformamide
DMSO	Dimethyl sulfoxide
EbG	Estradiol-17 β -glucuronide
EC	Electron capture
EEDQ	N-Ethoxycarbonyl-2-ethoxy-1,2-dihydroquinoline
E_{kin}	Kinetic energy
Et ₃ N	Triethylamine
EtOAc	Ethyl acetate
EtOH	Ethanol
eV	electronVolt
FCA	Fluorochoholic acid
FCDCA	Fluorochenodeoxycholic acid
FGCA	Fluoroglycocholic acid
FLR	Future liver remnant
FOV	Field of view
FXR	Farnesoid X receptor
GBCAs	Gadolinium-based contrast agents
GBI	Gallbladder and intestines
Gd-BOPTA	Gadobenate dimeglumine
Gd-EOB-DTPA	Gadoxetic acid
GMP	Good Manufacturing Practice

GOS	Gadolinium oxysulphide
GSH	Glutathione
HBSS	Hanks' Balanced Salt Solution
HC	Hepatic clearance
HCC	Hepatocellular carcinoma
HEK	Human Embryonic Kidney
HEPES	(4-(2-hydroxyethyl)-1-piperazineethanesulfonic acid
HPLC	High performance liquid chromatography
ID	Injected dose (i.e. injected tracer activity)
IMPD	Investigational medicinal product dossier
INR	International normalized ratio
LFTs	Liver function tests
LG	Leaving group
LOR	Line of response
LSO	Lutetium oxyorthosilicate
LYSO	Lutetium-yttrium oxyorthosilicate
MATE1	Multi-drug And Toxin Extrusion transporter 1 (<i>SLC47A1</i> gene)
MCD	Methionine choline deficient
MeOH	Methanol
MIPs	Maximum intensity projections
MRI	Magnetic Resonance Imaging
mRNA	Messenger ribonucleic acid
MRP	Multidrug Resistance-associated Protein (<i>ABCC</i> gene)
MsCl	Mesyl chloride
n.d.c. RY	Non-decay corrected radiochemical yield
NAFLD	Non-alcoholic fatty liver disease
NAPQI	N-acetyl-p-benzoquinone imine
NASH	Non-alcoholic steatohepatitis
NBS	N-bromosuccinimide
NMR	Nuclear magnetic resonance

NTCP	Sodium-dependent Taurocholate Cotransporting Polypeptide (<i>SLC10A1</i> gene)
OATP	Organic Anion Transporting Polypeptide (<i>SLCO</i> gene)
OI	Optical imaging
OST α/β	Organic Solute Transporter (<i>SLC51A/B</i> gene)
PBS	Phosphate buffered saline
PCR	Polymerase chain reaction
PET	Positron Emission Tomography
PFIC	Progressive familial intrahepatic cholestasis
P-gp	P-glycoprotein (<i>ABCB1</i> gene)
PMT	Photon multiplier tubes
PPh ₃	Triphenyl phosphine
PXR	Pregnane X Receptor
QSAR	Quantitative Structure-Activity Relationship
RNA	Ribonucleic acid
ROI	Region of interest
RP	Radiochemical purity
RT	Room temperature
RT-qPCR	Real-time quantitative polymerase chain reaction
SD	Standard deviation
SPECT	Single Photon Emission Computed Tomography
TAC	Time-activity curve
TBR	Tumor-to-background ratio
TC	Taurocholate
Tf ₂ O	Triflic anhydride
THF	Tetrahydrofuran
TLC	Thin layer chromatography
TOF	Time of flight
TsCl	Tosyl chloride
US	Ultrasound
VDR	Vitamin D Receptor

Outline

The liver plays a vital role in maintaining homeostasis in the body through essential physiological functions. One of these is the production of bile, a complex fluid containing organic and inorganic solutes. The bulk of the organic constituents is comprised of bile acids, amphiphilic steroid derivatives that are synthesized in the liver and excreted in the small intestine where they help to emulsify fat and solubilize fat-soluble vitamins. Bile acids undergo an efficient enterohepatic cycle, meaning they are reabsorbed in the intestines and are taken back to the liver through the portal circulation. Bile acid transport proteins warrant the efficient hepatobiliary transport of bile acids and their subsequent enterohepatic circulation.

However, disturbances in hepatobiliary transport of bile acids can occur and lead to a toxic accumulation of bile acids in the liver, termed cholestasis. Cholestasis can present itself if drugs interfere with the bile acid transporters, or in certain liver diseases. It is therefore both important to detect this toxicity early on in drug development of new candidate drugs, and to have a representative view on liver function with regards to bile acid transport in liver disease patients.

The first part of the dissertation will provide the reader with the necessary background on the liver, molecular imaging and liver disease. **Chapter 1** gives a general introduction on liver physiology, bile acid structure and physicochemical properties, biosynthesis and transport. Furthermore, an introduction to molecular imaging is given, with a special focus on Positron Emission Tomography (PET) and ^{18}F radiochemistry. **Chapter 2** covers the topic of molecular imaging in liver disease. First, a concise background on the different liver diseases that are covered in this dissertation, is presented. Then, an overview is given of the recent advances in molecular imaging of the liver. Finally, **Chapter 3** covers the research questions that will be investigated in the experimental chapters that follow.

CHAPTER 1:

GENERAL INTRODUCTION

PART 1: THE LIVER

PART 2: MOLECULAR IMAGING

PART 1: THE LIVER

1.1 Macroscopic anatomy and physiology of the liver

The liver is a visceral organ that is situated in the upper-right and part of the upper-left quadrant of the abdominal cavity. This red-brown colored organ is divided into two large lobes (left and right) and two smaller central lobes (quadrate and caudate lobes) (Cotoi & Quaglia 2016). It is the largest internal organ and gland of the human body, accounting for roughly 1500 grams or 2.5 % of the adult body weight (Juza & Pauli 2014).

The liver plays a vital part in maintaining physiological homeostasis; its functions can be categorized in three major parts. Firstly, it is the organ where a plethora of endogenous substances are synthesized: coagulation factors, hormones, carbohydrates, amino acids, cholesterol, bile acids etc. Secondly, the liver is also a storage for vitamins (A, D, K, B12), minerals and glycogen. Finally, it is responsible for metabolizing (and detoxifying) endogenous and exogenous substances (Bennink et al. 2012; Geisel et al. 2015).

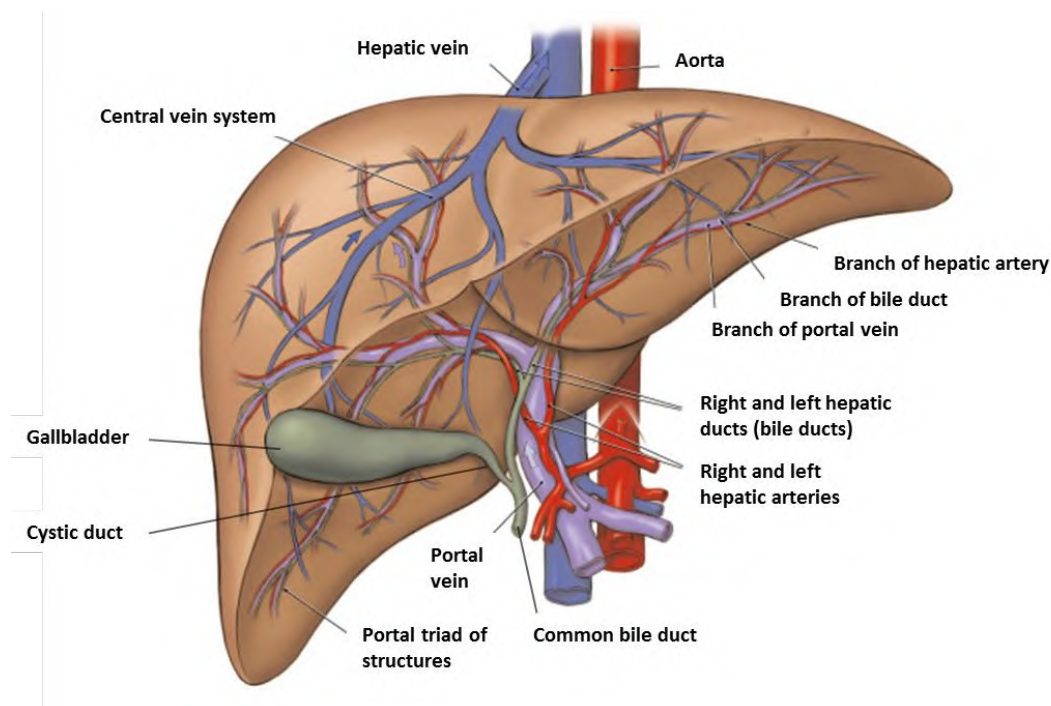


Figure 1.1: Vasculature and anatomy of the liver, gallbladder and major bile ducts
(permission obtained and adapted from MediVisuals Inc ©, 2007).

To fulfill its physiological functions, the liver is highly vascularized and receives up to 25 % of the total cardiac output at rest. The vasculature of the liver is unique in the human body, in the sense that it is the only organ that has a dual blood supply (Figure 1.1). The liver receives oxygenated blood from the hepatic artery and nutrient-rich, partly deoxygenated blood from the portal vein (that originates from the gastro-intestinal tract). The former provides 25-30 %, while the latter accounts for 70–75 % of the hepatic blood supply. Branches of the hepatic artery and portal vein are dispersed throughout the liver and end in liver sinusoids, where arterial and portal venous blood are mixed. After uptake and processing of oxygen, nutrients, hormones etc. by the hepatocytes, venous blood is collected in central veins that eventually drain in the vena cava inferior (Abdel-Misih & Bloomston 2010).

Situated beneath the liver is the gallbladder (Figure 1.1). This muscular sac stores bile fluid that is important for lipid digestion in the intestines (cfr. *Infra*). Bile is produced by the liver and flows through an elaborate biliary tree network before it drains in the hepatic bile duct. The cystic duct, stemming from the gallbladder, joins the hepatic bile duct to form the common bile duct that finally ends in the ampulla of Vater. Both bile and pancreatic digestive juices enter the duodenum here under control of the sphincter of Oddi. In a fasted state, the majority of bile is stored in the gallbladder. However, when a meal is taken, the hormone cholecystokinin is released by the small intestine that induces gallbladder contractions and relaxes the sphincter of Oddi (Hofmann 2009; Keplinger & Bloomston 2014).

1.2 Microscopic architecture of the liver

The cell type that accounts for the majority of liver volume (78 %) is the hepatocyte. Hepatocytes are polarized epithelial cells that are responsible for the synthesis, metabolic, endocrine and exocrine function of the liver (Si-Tayeb et al. 2010; Juza & Pauli 2014). In the smallest functional units of the liver, the lobules, hepatocytes are arranged radially around a central hepatic vein in the middle of a hexagonal lobule (Figure 1.2). At each of the six corners, a portal triad can be found, which consists of a hepatic artery, a portal vein and a bile duct. Branches from the hepatic artery and portal vein flow through a system of sinusoids before exiting the lobule through the central hepatic vein (Si-Tayeb et al. 2010).

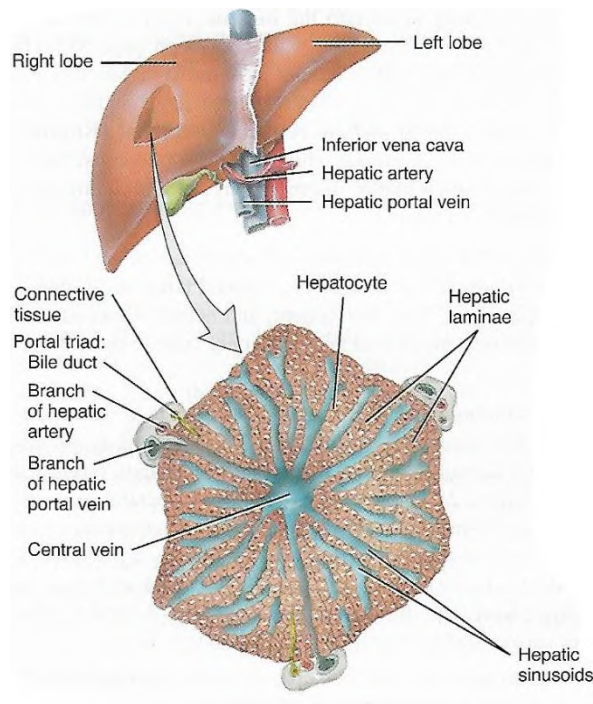


Figure 1.2: Representation of a liver lobule and its constituents (from Tortora, 2009).

The sinusoidal endothelial cells are faced by the basolateral membranes of the hepatocytes, separated by the space of Disse (Gissen & Arias 2015) (Figure 1.3). Uptake of blood components by the liver parenchyma is facilitated by the plate-like arrangement of single- or double cell thick hepatocytes and furthermore by the sinusoids' unique endothelial cell-lining (Treyer & Müsch 2013). The endothelial cells contain fenestrae: small openings arranged in groups that form sieve plates. This greatly improves the permeability of the endothelial cells, allowing efficient exchange of micro- and macromolecules in sinusoidal blood with the hepatocytes (Wisse et al. 1996; Brunt et al. 2014).

At the apical (canalicular) sides of adjacent hepatocytes, narrow channels are found that serve as a site of bile excretion: the bile canaliculi. These canaliculi are sealed to the hepatocytes by tight junctions and form an elaborate interconnected network. Bile produced by the hepatocytes (primary bile) is transported through the canaliculi to the bile ducts of the portal triad. Bile ducts are composed of cholangiocytes that regulate the pH and osmotic water flow to the bile ducts by absorbing bile salts, glucose and amino acids from primary bile, and excreting HCO_3^- and Cl^- . This results in "ductal" bile, which the network of bile ducts transports into larger ducts and finally enters the common bile duct (Gissen & Arias 2015; Treyer & Müsch 2013; Masyuk et al. 2008).

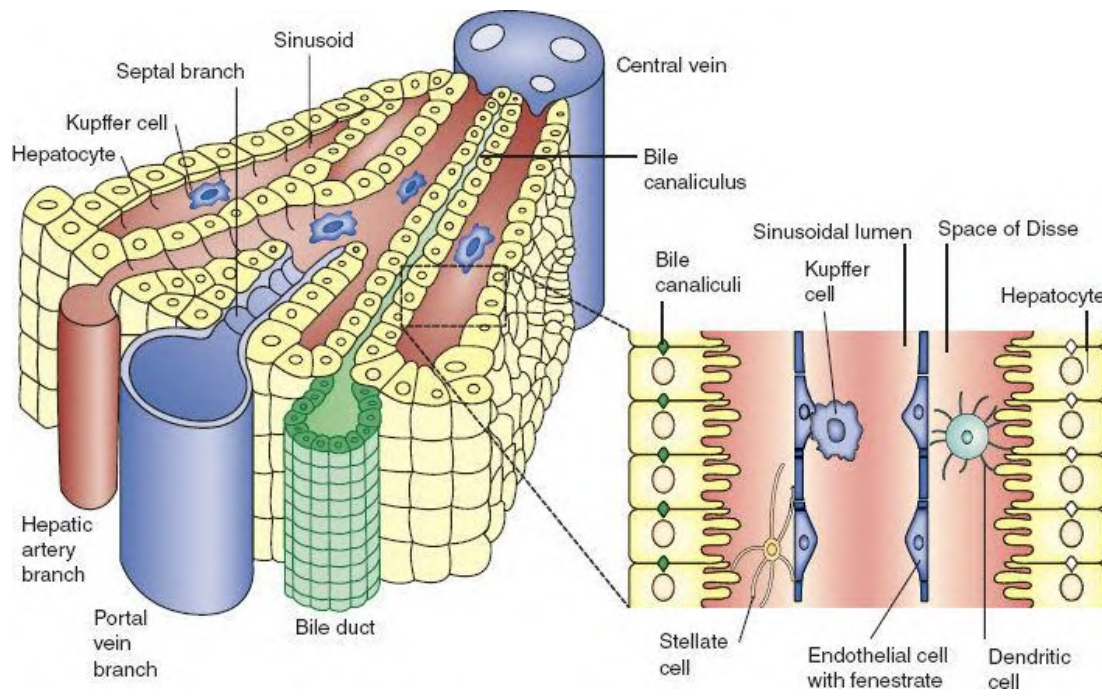


Figure 1.3: Microscopic architecture of a liver lobule (from: www.aneskey.com).

Another important constituent of the microscopic liver architecture is the Kupffer cell. Kupffer cells are the resident macrophages of the liver that are, among other immune cells, localized in the sinusoids. As a major part of the mononuclear phagocytic system of the human body, they neutralize immunogens and particulates originating from the gastrointestinal tract and are thus indispensable for the immune system's first line of defense (Dixon et al. 2013; Krishna 2013).

In the space of Disse lie hepatic stellate cells: highly specialized mesenchymal cells that are responsible for maintaining the extracellular matrix of the hepatic micro-environment. Stellate cells remain dormant in healthy tissue and contain the largest vitamin A reservoir of the body. When hepatocyte injury occurs, the stellate cells will differentiate into activated myofibroblast-like cells that create a provisional scar at the injury site. Furthermore, growth factors and cytokines are released that aid in hepatic regeneration. Prolonged and recurrent activation of stellate cells however will result in liver fibrosis, which is characterized by extensive scar tissue formation. This disruption of the complex hepatic architecture can eventually result in a decreased liver function (Yin & Evason 2013; Wake 2006).

1.3 Bile: constituents and functions

Bile is a complex fluid that is made up of inorganic and organic solutes in approximately 95 % water. Its composition can vary depending on the place where it is found: primary bile produced by the hepatocytes does not have the same contents as ductal bile, as a result of cholangiocyte activity in the bile ducts and gallbladder. The bulk of the organic constituents of bile is made up of bile acids (60-70 %), followed by phospholipids (20-30 %), cholesterol (4-10 %), proteins (such as plasma proteins, albumin and hepatic enzymes; 1-4 %) and bile pigments (primarily bilirubin glucuronide, 0.5 %). Ions such as Na^+ , K^+ , Cl^- , and HCO_3^- represent the major part of the inorganic bile components. Heavy metals (Cu, Mn, Fe, Zn) can also be found, but to a lesser extent (Frisch & Hofmann 2012; Boyer 2013).

As a digestive fluid, bile helps to emulsify ingested dietary fat in the small intestine. Bile acids contain a hydrophobic and hydrophilic part in their molecular structure (cfr. infra) and thus can act as tensioactive agents. They form microscopic fat droplets, on which the pancreatic lipases and esterases have easier access to perform their function in digesting fat. The released lipids (fatty acids, mono/diglycerides, cholesterol) and bile acids can then assemble in so-called mixed micelles (Figure 1.4). These spheroidal structures are about 2-10 nm in size and contain a hydrophilic exterior and a hydrophobic interior (Tortora & Derrickson 2009). Micelles aid in solubilizing and absorption of lipids and hydrophobic substances such as cholesterol and vitamins (K, A, D, E) from the intestine (Hofmann 1999; Hofmann & Hagey 2014).

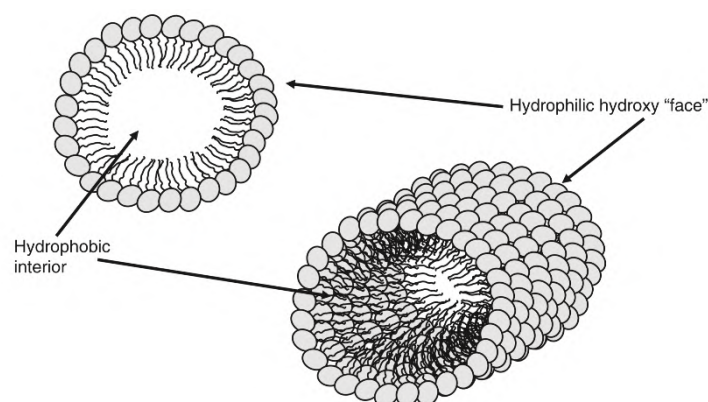


Figure 1.4: Schematic representation of a micelle. On the left is a classical spheroidal micelle; on the right is a cylindrical micelle (from: Stamp & Jenkins 2008).

Besides its digestive purpose, bile also has an important excretory function. Various endogenous (e.g. bilirubin conjugates) and exogenous compounds (drugs and their metabolites) are excreted in bile after their hepatic uptake (Giacomini & Tweedie 2010). When bile is released in the intestines, these molecules can be eliminated from the body through the faeces, or they can be reabsorbed. This cycle is called the enterohepatic circulation and can result in variable plasma drug levels or greatly influence the length of a drug's biological effect (Hosey et al. 2014). Estimation of the extent of biliary excretion of a drug is therefore of great importance. Quantitative Structure-Activity Relationship (QSAR) studies have suggested that molecules with an anionic moiety and a molecular weight >475 Da have a higher chance to display biliary excretion, while Log D or Log P values are not correlated to a higher degree of biliary elimination (Yang et al. 2009).

Bile acid molecules also have several other functions:

They are the main osmotic driving force for bile excretion. Active transport of bile acids from the hepatocyte into bile (cfr. infra) creates a large concentration gradient: bile acid concentration in the hepatocyte is 1-2 μM , whereas it is > 1000 μM in canalicular bile. As a result of the osmotic effect, water and filterable ions will flow into the canaliculi (Trauner & Boyer 2003; Hofmann 1999).

As bile acids are exclusively synthesized from cholesterol, they represent a means to eliminate excess cholesterol from the body. Furthermore, mixed micelles that bile acids help formulate, can also ultimately remove cholesterol by the faeces (Li & Chiang 2009).

Bile acids help protect the intestines from bacterial overgrowth. This can be observed in cirrhotic patients or after bile duct obstruction in lab animals (Slocum et al. 1992; Gunnarsdottir et al. 2003; Pande et al. 2009). The exact mechanism is yet to be elucidated, but probably is a combination of the direct cytotoxic effect of bile acids on the bacteria and the induction of Farnesoid X receptor (FXR) signaling, which leads to antibacterial actions of the intestinal mucosa (Maillette de Buy Wenniger & Beuers 2010).

There is increasing evidence that bile acids also function as signaling compounds in the liver, bile ducts and intestine. They have the capability to stimulate nuclear receptors such as FXR, Pregnane X Receptor (PXR) and Vitamin D Receptor (VDR) that consequently trigger transcription of genes (Hylemon et al. 2009; Staudinger et al. 2001; Makishima et al. 2002). It

was found that bile acids can influence their own synthesis, transport and metabolism in this manner. Additionally, they have an impact on triglyceride and lipoprotein metabolism (Lefebvre et al. 2009).

1.4 Bile acids

1.4.1 Structure and chemical properties

Bile acids are steroid derivatives that are characterized by their amphiphilic nature: they contain both a hydrophobic and a hydrophilic side in their molecular structure and are as such able to perform their function in digestion of lipids (cfr. 1.3). The precursor molecule for their biosynthesis is cholesterol, a 27 carbon counting steroid (27 C). After several biotransformations (cfr. 1.4.2), a bile acid (24 C) is obtained. The carbon atoms of the steroid structure are numbered following the convention that was established in the 1930's (Figure 1.5) (Hofmann & Hagey 2014).

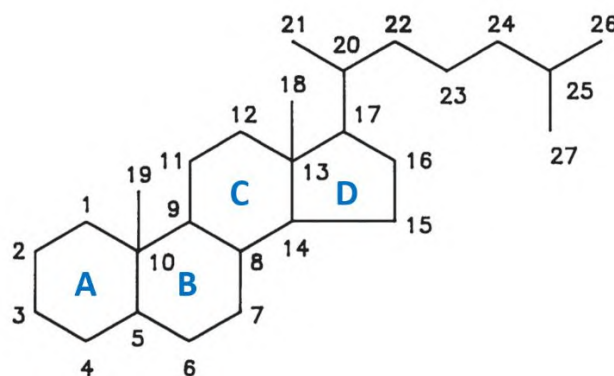


Figure 1.5: Steroid structure with carbon and ring nomenclature
(adapted from Hofmann & Hagey 2014).

The main differences between the structure of cholesterol and a generic bile acid are as follows (Figure 1.6). Firstly, the cholesterol side chain is shortened by three carbons and the terminal carbon is oxidized to a carboxyl group. Secondly, the 3β -hydroxy group of cholesterol is epimerized to a 3α -hydroxy group. Additional hydroxylation reactions can take place, mostly on the 7C or 12C in humans. Finally, the A and B ring junction of the steroid nucleus of cholesterol is flipped by reduction of the double bond at C5. The A and B ring junction is generally oriented “cis” in bile acids, which is denoted by the solid line connecting the C5 stereocenter to the C5 hydrogen atom (a 5β bile acid). The result of abovementioned

changes is a wedge-shaped structure with a non-polar hydrophobic steroid side and a polar, hydrophilic side (hydroxyl and carboxyl functional groups) (Figure 1.7) (Hofmann & Hagey 2014; Vaz & Ferdinandusse 2017; Stamp & Jenkins 2008).

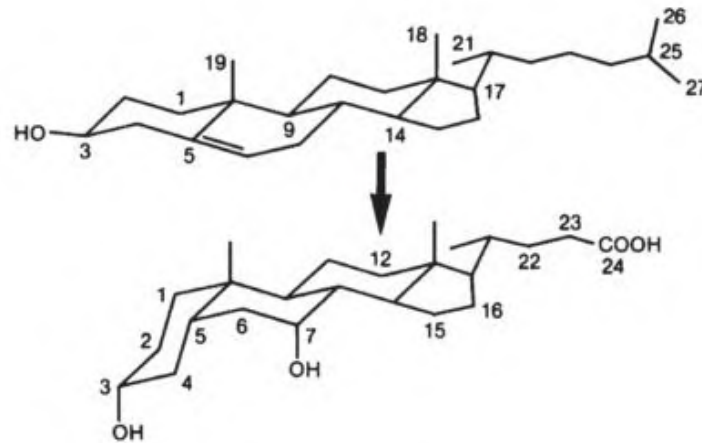


Figure 1.6: Chair conformations of cholesterol (top) and chenodeoxycholic acid (bottom) (from Hofmann & Hagey 2014).

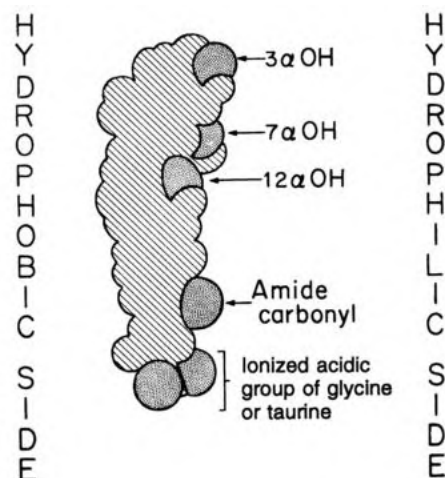


Figure 1.7: Space filling model of a (conjugated) cholic acid molecule (adapted from Hofmann & Hagey 2008).

The carboxylic acid functional group of unconjugated bile acids has a $pK_a \approx 5$. This group can be conjugated with amino acids in the hepatocytes, predominantly glycine and taurine in humans (Figure 1.8). Conjugated bile acids are termed bile salts. The introduction of an electron-withdrawing amide bond has a profound effect on the pK_a of the carboxylic acid group, which is translated to altered physicochemical properties of the resulting

conjugated bile acid. Glycine conjugated bile acids have a $pK_a \approx 4$, whereas taurine conjugation drops the pK_a to ≈ 2 or less (Fini & Roda 1987). Conjugated bile acids are therefore more ionized at physiological pH. As a result, their aqueous solubility increases, the passive permeability through cell membranes decreases and their emulsifying properties are strengthened (Maillette de Buy Wenniger & Beuers 2010; Hofmann & Mysels 1992).

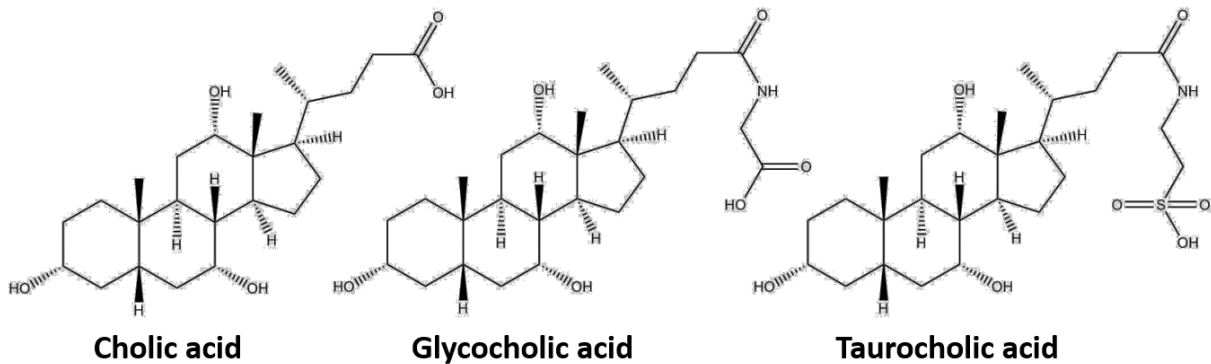


Figure 1.8: Structures of cholic acid, its glycine (glycocholic acid) and taurine conjugate (taurocholic acid).

The spectrum of bile acids that the hepatocytes produce, can vary and is species-dependent. In man, the most common bile acids are cholic acid ($3\alpha, 7\alpha, 12\alpha$ hydroxylated; $\approx 34\%$), chenodeoxycholic acid ($3\alpha, 7\alpha$ hydroxylated; $\approx 39\%$) and deoxycholic acid ($3\alpha, 12\alpha$ hydroxylated; $\approx 24\%$). Ursodeoxycholic acid ($3\alpha, 7\beta$ hydroxylated) and lithocholic acid (3α hydroxylated) are found to a lesser extent (Figure 1.9) (Park et al. 2006). They are most often found conjugated with glycine or taurine in a ratio of 3 to 1 (Chiang 2013). The bile acid profile of mice on the other hand, consists predominantly of cholic acid ($\approx 44\%$) and α/β -muricholic acid ($3\alpha, 6\beta, 7\alpha/\beta$ hydroxylated; $\approx 45\%$), a rodent specific bile acid. Virtually all bile acids in mice are conjugated with taurine ($>97\%$), because the murine enzyme responsible for conjugation (cfr. *infra*) is specific to taurine rather than glycine (Alnouti et al. 2008).

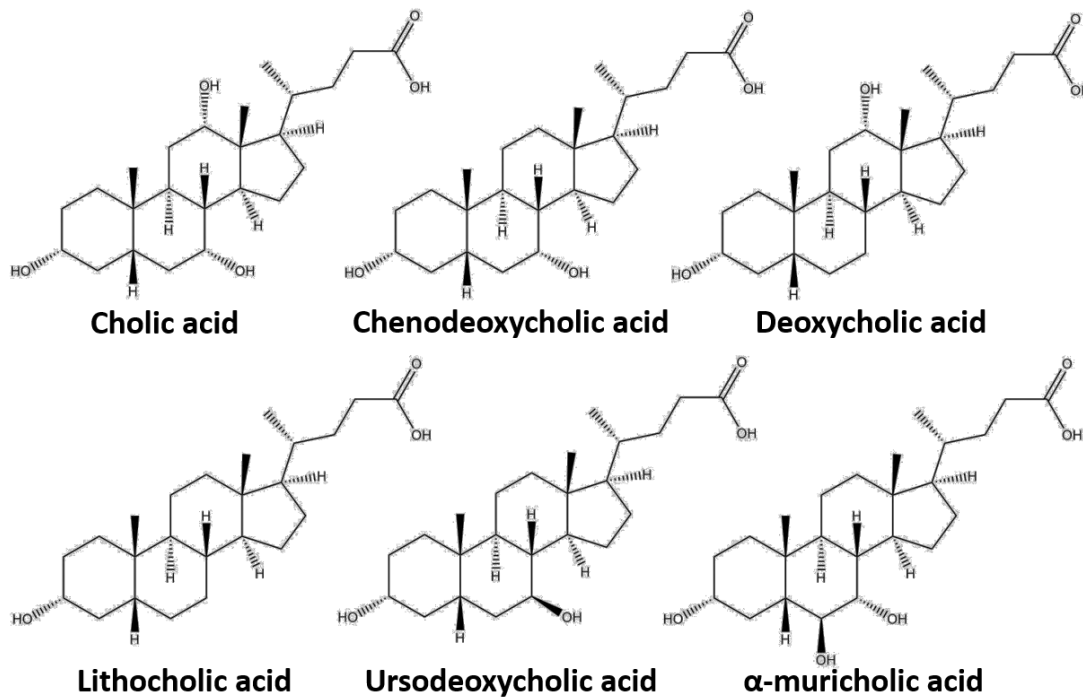


Figure 1.9: Structures of the most common bile acids in man and mouse.

1.4.2 Biosynthesis

The biosynthesis of bile acids in the hepatocytes from cholesterol is an intricate, multistep process that involves at least 17 specialized enzymes and accounts for 90 % of cholesterol breakdown (Russell 2009). The end-products of the *de novo* synthesis are termed primary bile acids. In man, these are cholic and chenodeoxycholic acid (Chiang 2013). They are, together with secondary bile acids (cfr. infra), part of a bile acid pool that is 2-4 g in total weight. Only a minority of this amount (≈ 5 %) is lost daily in the faeces due to their efficient recycling in the enterohepatic cycle (Vaz & Ferdinandusse 2017). Up to 10-12 cycles per day can be observed (Heubi et al. 2007). The loss of bile acids in faeces is compensated by the *de novo* synthesis so bile acid homeostasis is preserved.

To date, four different biosynthesis pathways have been elucidated. The classical (or neutral) pathway is by far the most important one, accounting for approx. 90 % of total bile acid synthesis (Smith et al. 2009). The alternative (or acidic) pathway, the Yamasaki pathway and the 25-hydroxylation pathway are also distinguished (Figure 1.10). What makes the biosynthesis complex, is that some intermediates are interchangeable between pathways. The order in which the substrates undergo their transformations is not fixed (Vaz &

Ferdinandusse 2017). An in-depth coverage of bile acid biosynthesis can be found in the publication of Vaz & Ferdinandusse 2017.

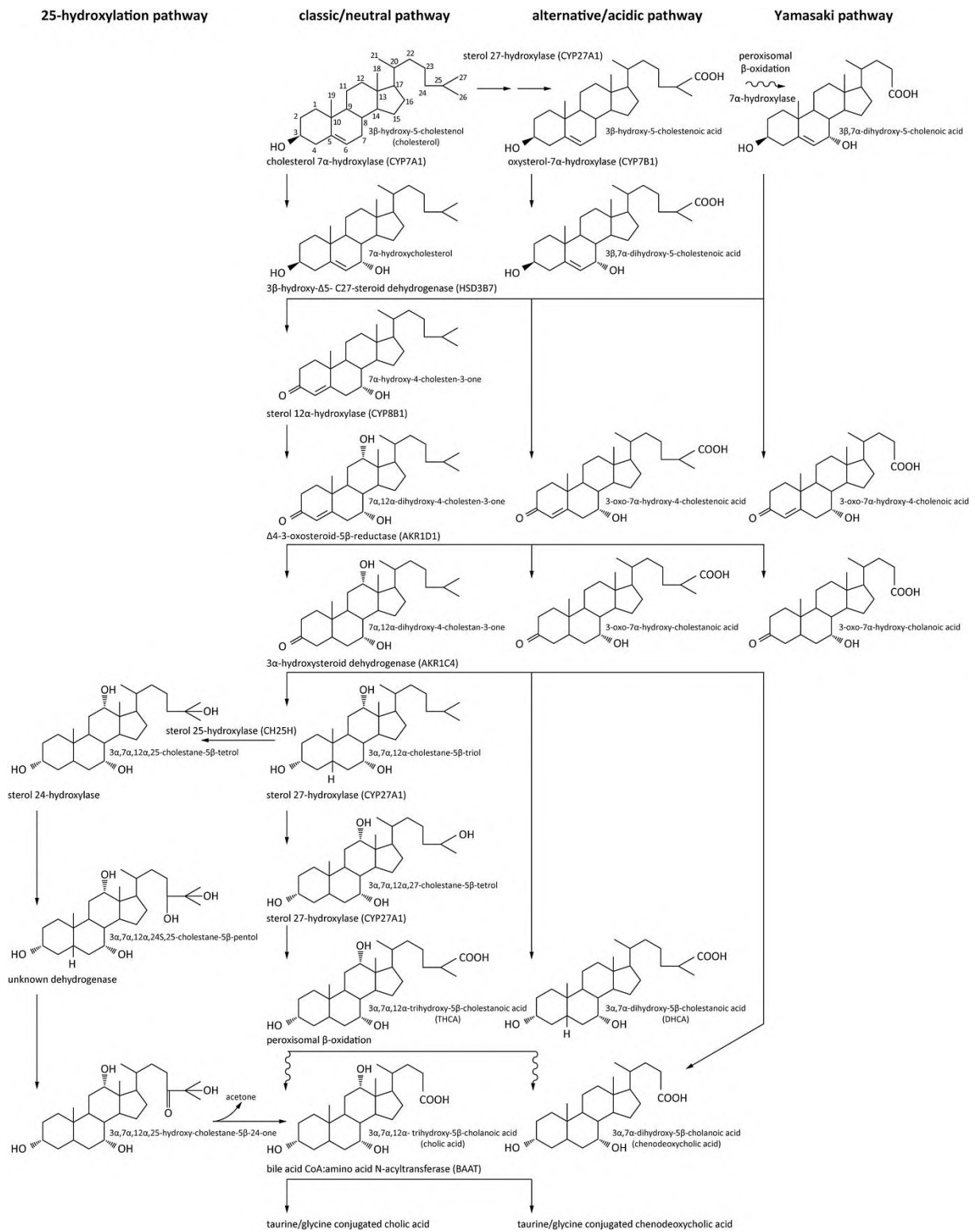


Figure 1.10: The different bile acid biosynthesis pathways (adapted from Vaz & Ferdinandusse 2017).

The classical pathway starts with the hydroxylation of cholesterol to 7 α -hydroxycholesterol by the enzyme sterol 7 α -hydroxylase (CYP7A1). This enzyme is located on the endoplasmatic reticulum and is expressed exclusively in the liver. It represents the rate-limiting step of bile acid synthesis (Russell 2003). Intermediate 7 α -hydroxycholesterol is then oxidized at C3 and the 5 Δ double bond is isomerized to form 7 α -hydroxy-4-cholesten-3-one. A pivotal change to the steroid structure is made by 5 β -reductase, which reduces the double bond to form a 5 β -bile acid precursor. Generating this “kinked” structure is essential for a bile acid’s functionality. The 3-oxo group is consequently reduced to a 3 α -hydroxyl. The enzyme sterol 12-hydroxylase (CYP8B1) can introduce a 12 α -hydroxyl functional group on the intermediate. If this happens, the eventual end product of the biosynthesis will be cholic acid, if not, it will be chenodeoxycholic acid. In a final step, the carboxyl functional group is created at C27 of the side chain by sterol 27-hydroxylase (CYP27A1). The side chain is then shortened by peroxisomal β -oxidation to form a 24C cholic- or chenodeoxycholic acid molecule (Vaz & Ferdinandusse 2017; Russell 2009).

In the alternative (or acidic) pathway, cholesterol is first converted into a C27 carboxylic acid intermediate (hence the “acidic”), followed by steroid modifications and peroxisomal β -oxidation. This pathway has a preference for the production of chenodeoxycholic acid and plays a larger role in young infants than in adults (Russell 2003; Setchell et al. 1988). The Yamasaki and 27-hydroxylation pathways are depicted in Figure 1.10. Their exact contributions to the bile acid pool is not yet fully understood (Vaz & Ferdinandusse 2017).

Another important aspect of bile acid biosynthesis is their conjugation with an amino acid. First, a bile acid is activated to a Co-enzyme A (CoA) ester at the C24 carboxylic acid function. The CoA ester is, together with glycine or taurine, a good substrate for the subsequent conjugation reaction that is highly efficiently catalyzed by the bile acid CoA amino acid N-acyltransferase enzyme. Approximately 98 % of all bile acids that are excreted in bile from the liver are conjugated with an amino acid (Russell 2003).

A bile acid can not only be conjugated with glycine or taurine. Sulfation by bile acid sulfotransferase introduces a sulfonate group on the 3C-hydroxyl functional group. Of all human bile acids, only the highly hydrophobic lithocholic acid is mostly present in its sulfated

form to help reduce its toxic effect (Palmer & Bolt 1971; Hofmann 2004). Glucuronidation by UDP-glucuronosyltransferase 1A3 at the C24 carboxyl or C3-hydroxyl functional groups is also possible, but is insignificant under physiological conditions (Hofmann 2007).

Abovementioned biosynthesis reactions alone do not account for the entire spectrum of bile acids that can be found in the body. During their enterohepatic cycling, bile acids come into contact with micro-organisms present in the gut. They can be metabolized by bacterial enzymes that are present in the distal intestine. Conjugated bile acids go through deconjugation and bacterial dehydratases can remove the 7 α -hydroxyl to form a 7-deoxy bile acid. Cholic acid can in this way be modified to deoxycholic acid; chenodeoxycholic acid to lithocholic acid (Figure 1.9). These “damaged” primary bile acids are called secondary bile acids and are also reabsorbed from the intestines. Once back in the hepatocyte, secondary bile acids can be reconstituted with an amino acid or sulfated (in the case of lithocholic acid) and continue their enterohepatic cycle (Hofmann 2014; Hylemon et al. 2009).

1.4.3 Transport of bile acids in the enterohepatic circulation

As described earlier, the enterohepatic cycle of bile acids is remarkably efficient: only 5 % of the bile acid pool is lost in the faeces on a daily basis (Figure 1.11). This is however not that straightforward, given the fact that the overwhelming majority of bile acids is present in their conjugated form at physiological pH and these ionized molecules have to cross multiple plasma membranes. Their effective uptake from the intestines by the enterocytes, transport towards the blood stream, reuptake in the liver by hepatocytes and excretion in bile canaliculi are however all warranted by a number of specialized, active bile acid transport proteins that will be discussed in the following section (see Figure 1.12 and Table 1.1 for complete overview).

Nomenclature of these bile acid transport proteins dictates that human variants are written in capital letters, whereas rodent variants are not. E.g.: human NTCP; rat ntcp.

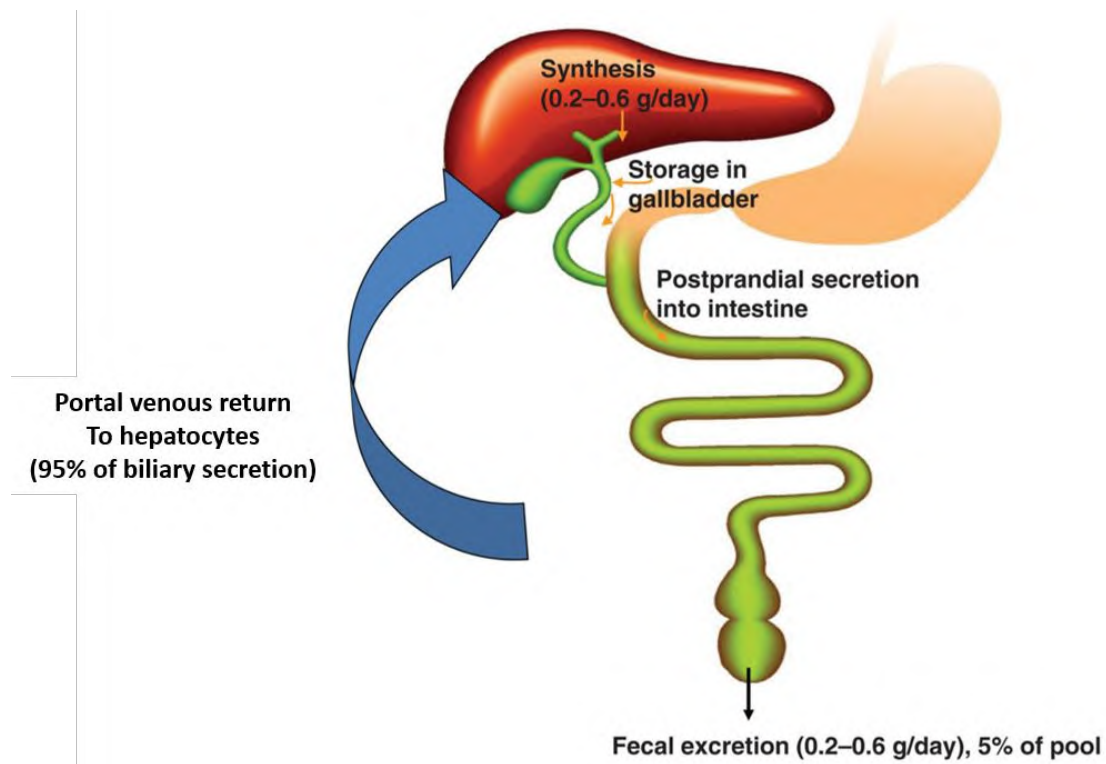


Figure 1.11: Schematic representation of the enterohepatic cycle of bile acids (adapted from Chiang, 2013).

1.4.3.1 Basolateral bile acid transport in the hepatocyte

Bile acids present in arterial or (predominantly) in portal venous blood can actively be taken up by bile acid transporters present on the basolateral (or sinusoidal) side of the hepatocytes, i.e. the side of the cells facing the sinusoids. Uptake is mediated mainly by the Sodium-dependent Taurocholate Cotransporting Polypeptide (NTCP) and the Organic Anion Transporting Polypeptide (OATP) family of transporters. The Multidrug Resistance-associated Protein family (MRP) can also be found at the basolateral plasma membrane and is capable of transporting bile acids back into the bloodstream (MRP3 and MRP4). The importance of MRP is negligible under physiological conditions, yet gains in significance when cholestasis, a pathological bile acid overload in the liver, occurs (Dawson et al. 2009).

Table 1.1: Overview of human bile acid transport proteins, their gene and location
(adapted from J.G. Marin et al. 2016).

Gene	Transport protein	Present on	Membrane
<i>ABCB11</i>	BSEP	Hepatocytes	Apical
<i>ABCC2</i>	MRP2	Hepatocytes Renal epithelium	Apical
<i>ABCC3</i>	MRP3	Hepatocytes Cholangiocytes Renal epithelium Enterocytes	Basal
<i>ABCC4</i>	MRP4	Hepatocytes Renal epithelium	Basal
<i>SLC10A1</i>	NTCP	Hepatocytes	Basal
<i>SLC10A2</i>	ASBT	Enterocytes Cholangiocytes Renal epithelium	Apical
<i>SLCO1B1</i>	OATP1B1	Hepatocytes	Basal
<i>SLCO1B3</i>	OATP1B3	Hepatocytes	Basal
<i>SLC51A</i>	OST α	Enterocytes Cholangiocytes Renal epithelium	Basal
<i>SLC51B</i>	OST β	Enterocytes Cholangiocytes Renal epithelium	Basal

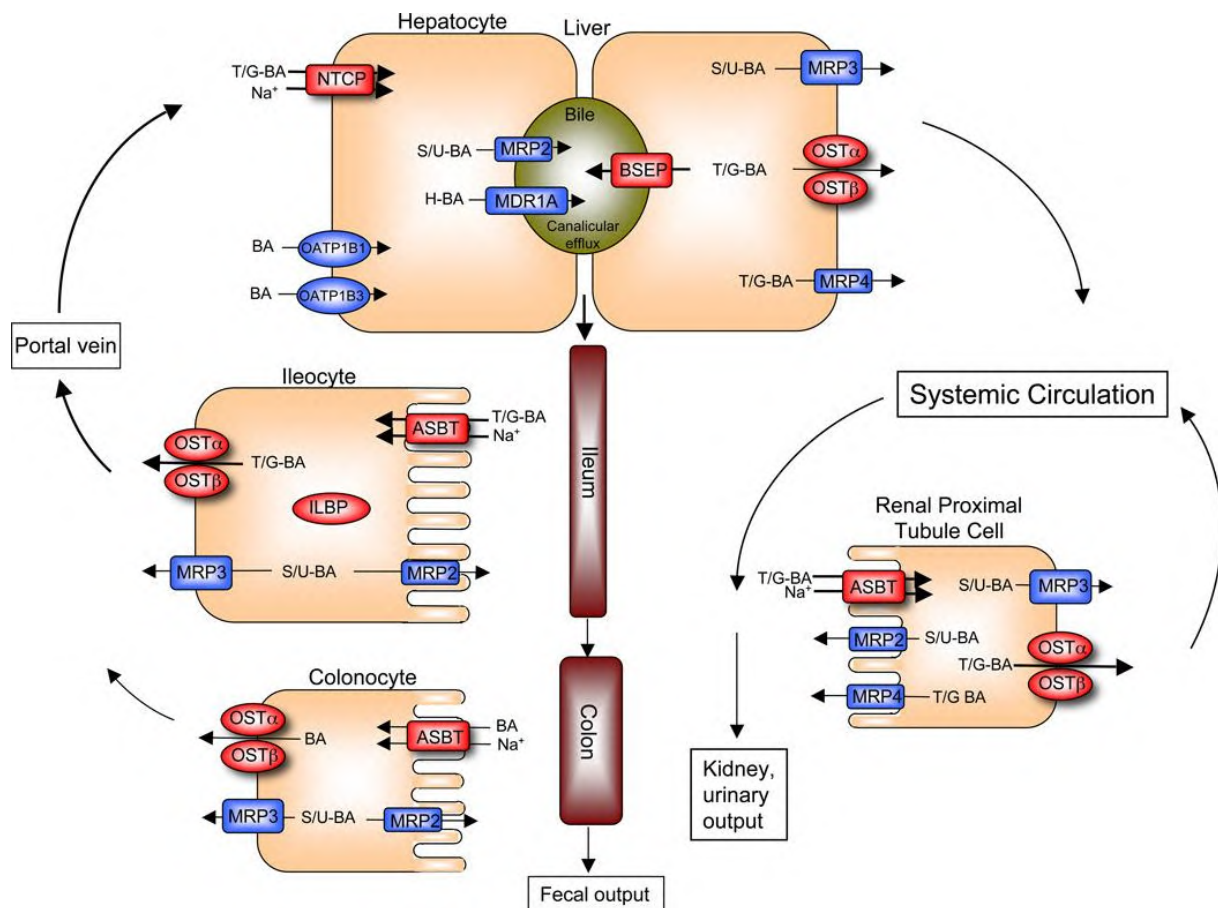


Figure 1.12: Schematic representation of the enterohepatic cycle, maintained by active bile acid transport proteins in the hepatocyte, enterocytes (ileum and colon) and renal cells (from: Dawson, 2011).

NTCP

NTCP is a member of the Solute Carrier 10 type transporters (*SLC10A1*) and found exclusively at the basolateral membrane of hepatocytes (J.G. Marin et al. 2016; Kullak-Ublick et al. 1997). It is the dominant transporter (approx. 90 % of bile acid uptake) responsible for basolateral uptake of both bile acids and bile salts, but with a higher affinity for the latter (Halilbasic et al. 2013). Human NTCP shares 77 % of the amino acids of rat ntcp and their functional capacity is highly similar, although NTCP has a higher affinity for taurocholate than its rodent counterpart (Trauner & Boyer 2003). Although its substrate specificity is mostly limited to bile acids, NTCP can also transport other substances such as estrone-3-sulphate, bromosulphophthalein and the drugs rosuvastatin and micafungin (Ho et al. 2006; Yanni et al. 2010; Stieger 2011).

NTCP transports one bile acid molecule and two sodium ions into the hepatocyte in one concerted process. In effect, NTCP makes use of the sodium gradient over the cell membrane that is maintained by the Na^+/K^+ -ATPase and can therefore be considered a secondary active cotransporter. This way, even though the concentration gradient of bile acids is steep between sinusoidal blood and the hepatocyte, efficient uptake is still guaranteed (Boyer 2013; Stieger 2011)

OATP

OATP's belong to the large Solute Carrier O (*SLCO*) group and can be divided in multiple families (OATP1 until OATP6) that share more than 40 % amino acid composition. These can on their turn be subdivided in subfamilies of isoforms that share more than 60 % amino acid composition (e.g. OATP1A, OATP1B and OATP1C). More than 10 human and 15 rodent isoforms can be distinguished (Figure 1.13) (Hagenbuch & Meier 2004; Klaassen & Aleksunes 2014).

OATPs are found in multiple tissues in the body: brain, kidneys, liver, placenta etc (Klaassen & Aleksunes 2014). The isoforms OATP1B1 (*SLCO1B1*) and OATP1B3 (*SLCO1B3*) are of particular interest as the primary human isoforms in the liver. They play a critical role in the sodium-independent uptake of a broad variety of anionic substances. As OATP1B1 and OATP1B3 are active secondary antiporters, uptake of an anionic substrate has to be compensated by efflux of a HCO_3^- -anion (Martinez-Becerra et al. 2011; Leuthold et al. 2008). Their mostly overlapping substrate spectrum encompasses bilirubin and its conjugates, prostaglandins, thyroxine, triiodothyronine, steroid hormones and drugs such as statins, digoxin, paclitaxel, antibiotics, etc (Boyer 2013). As anionic molecules, bile acids and salts can also use OATP1B1 and OATP1B3, but this transport is quantitatively less important compared to uptake by NTCP (Trauner & Boyer 2003). The primary isoform of oatp on rodent basolateral hepatocyte membrane is *oatp1b2*, which shares most of the substrate specificity of its human OATP1B1 and OATP1B3 counterparts. Also present are *oatp1a1* and *oatp1a4* (König 2011; Klaassen & Aleksunes 2014).

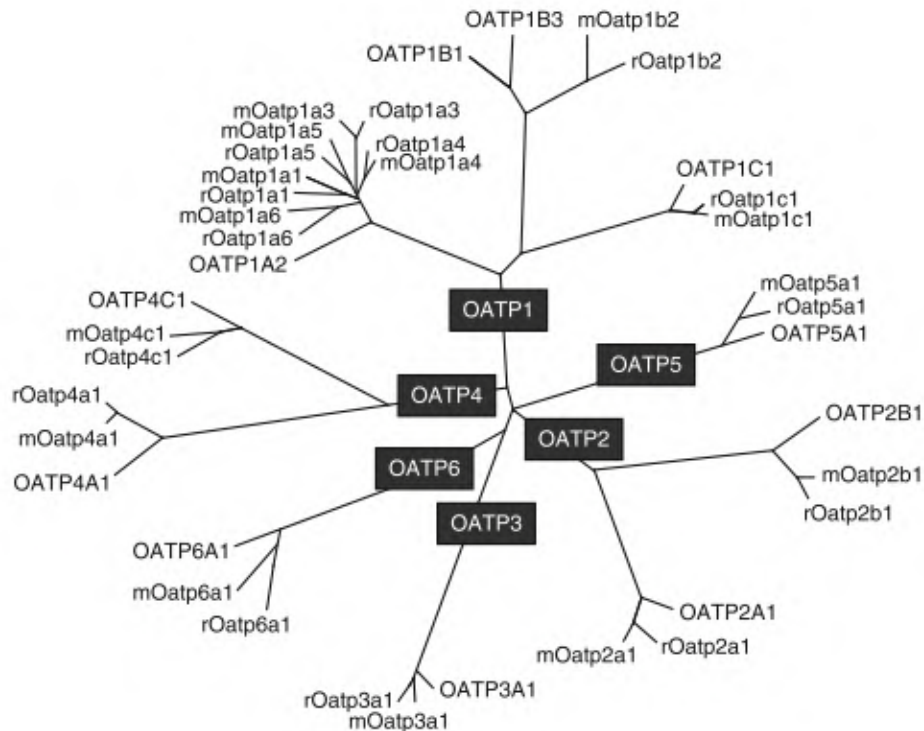


Figure 1.13: Overview of the different OATP families and subfamilies; m stands for murine and r for rat (from: König 2011).

MRP

Basolateral efflux of bile acids towards extrahepatic circulation is mediated by MRP3 and MRP4. They are both members of the ATP-Binding Cassette transporter (ABC) family (*ABCC3* & *ABCC4* respectively) and thus depend on ATP-hydrolysis for their active transport. MRP3 is localized at the basolateral membrane of human and rodent hepatocytes (Stieger 2011). Furthermore, the protein can be found basolaterally on kidney distal tubules, cholangiocytes and enterocytes of the ileum and colon (Rost et al. 2001; Scheffer et al. 2002). A large range of conjugated anions are substrate of MRP3: leukotriene C₄, estradiol-17 β -glucuronide, bilirubin conjugates, etc. Only a select few bile acids (e.g. glycocholate) are low affinity substrates for human MRP3, whereas rat *mrp3* shows a broader bile acid specificity and has higher affinity (Keppler 2011).

MRP4 can be found at the basolateral membrane of human and rodent hepatocytes and at the apical membrane of kidney proximal tubule epithelial cells (van Aubel et al. 2002; Rius et al. 2003). MRP4 substrates are monoanionic bile acids (that are solely co-transported with reduced glutathione), prostaglandins, leukotrienes, folate and steroids (Rius et al. 2006; Keppler 2011).

1.4.3.2 Apical (canalicular) bile acid transport in the hepatocyte

Once synthesized or taken up again in the hepatocyte, bile acids have to be transported into the bile canaliculi against a steep concentration gradient. Consequently, active canalicular transport of bile acids is needed and mainly tasked to the Bile Salt Export Pump (BSEP) and to a lesser extent the Multidrug Resistance-associated Protein 2.

BSEP

Just as MRP, BSEP is a member of the ABC transporter family (*ABCB11*), which means it requires ATP-hydrolysis for its active transport. BSEP is the primary transporter for excretion of bile acids in the bile canaliculi. It represents the rate-limiting step of bile acid transport into bile and is tightly regulated to keep intrahepatic bile acid levels low enough to not cause toxicity. The protein is expressed almost exclusively in liver tissue (Langmann et al. 2003). Regarding its transport properties, BSEP is considered an almost exclusive bile salt transporter; bile acids are poorer substrates. Only the drugs pravastatin and micafungin were proven to be non-bile acid related substrates for BSEP so far (Hirano et al. 2005; Yanni et al. 2010; Stieger 2011; Thakkar et al. 2017).

A rare genetic disorder called Progressive Familial Intrahepatic Cholestasis 2 (PFIC-2) can present itself in patients that have a dysfunctional BSEP-gene. As bile acids are not efficiently removed from the hepatocytes, they accumulate, halt bile flow and cause cell damage due to their detergent-like function. Patients suffer from jaundice, pruritus and liver failure (Jacquemin 2012).

MRP2

MRP2 is a member of the ABC transporter family (*ABCC2*) and thus depends on ATP-hydrolysis for its active transport. Expression of MRP2 is ample in liver tissue and moderate in proximal tubules of the kidney (J.G. Marin et al. 2016). Its presence has also been established in the small intestine and colon (Fromm et al. 2000; Sandusky et al. 2002).

MRP2 can transport bile acids into the bile canaliculi, and more specifically, divalent (double anion) glucuronide- or sulfate conjugated bile salts. Given the relative presence of these molecules (cfr. supra), MRP2 cannot be considered the dominant bile acid efflux pump on the hepatocyte. It is however critically important for the biliary excretion of a plethora of anionic substances such as leukotrienes, estradiol-17 β -glucuronide, the waste product

bilirubin mono/diglucuronide and drugs such as paracetamol-glucuronide and methotrexate (Thakkar et al. 2017; Keppler 2011).

A mutation in the MRP2 gene results in the Dubin-Johnson syndrome, which does not cause fulminant liver toxicity but mild conjugated hyperbilirubinemia, unless competitive drug substrates for MRP2 are co-administered. The elevation of conjugated bilirubin in serum can be attributed to the compensatory role of MRP3: it transports bilirubin conjugates out of the hepatocytes into the extrahepatic circulation (Pauli-Magnus & Meier 2006; Stieger 2011).

1.4.3.3 Apical bile acid transport in the enterocyte

Uptake of bile acids and salts in the enterocytes of the small intestines happens by a combination of both passive and active processes. Passive diffusion of primary and secondary bile acids can take place along the entire small intestines and colon, as opposed to active transport that is largely limited to the ileum. The transporter responsible for recuperating the majority of bile acids and salts out of the ileal lumen is the Apical Sodium-dependent Bile acid Transporter (ASBT) (Dawson 2011; Xiao & Pan 2017). It is part of the SLC 10 family of transporters (*SLC10A2*) and besides its location on the apical membrane of enterocytes, ASBT also shows expression on apical membranes of renal proximal tubule cells and cholangiocytes (J.G. Marin et al. 2016; Dawson 2011).

Closely related in form, mechanism and function with the previously mentioned Ntcp, its substrate range is also rather limited to bile acids and salts, with a preference for the latter. ASBT is also an active secondary cotransporter: influx of a bile acid is accompanied by two Na⁺-ions and depends on the inwardly directed Na⁺-flux as its driving force (Xiao & Pan 2017).

1.4.3.4 Basolateral bile acid transport in the enterocyte

The protein tasked with transporting bile acids across the basolateral membrane of enterocytes towards the portal blood circulation is the heteromeric Organic Solute Transporter α - β (OST α - β). It is a member of the SLC 5 family and consists of 2 subunits: OST α (*SLC51A*) and OST β (*SLC51B*). Expression is found in most tissues, but is more abundant in ileal enterocytes, cholangiocytes and renal tubular cells (Ballatori et al. 2013). Besides transport of bile acids and salts, several other steroids are substrates of OST α - β . The

mechanism is believed to be facilitated diffusion: depending on the substrate's gradient over the cell, OST α - β mediates in-or efflux (Dawson 2011; Ballatori et al. 2013).

MRP3 is a minor contributor to basolateral enterocyte uptake of native bile acids, yet gains in importance for transport of sulfated or glucuronidated bile acids (Dawson 2011).

1.4.3.5 Cholehepatic shunt

A fraction of bile acids is subjected to reuptake from bile ducts into the cholangiocytes by ASBT on the apical side. OST α - β and MRP3 at the basolateral side then transports them back to bloodstream and the liver (Figure 1.14). This peculiar pathway is called the cholehepatic shunt (Anwer & Stieger 2013; de Lima Toccafondo Vieira & Tagliati 2014). Its role is not yet fully elucidated, but it can be important to reabsorb bile acids from the biliary tree if an obstruction causes a toxic accumulation of bile acids (Boyer 2013).

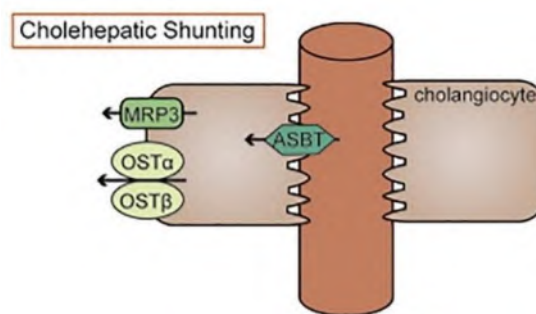


Figure 1.14: Cholehepatic shunt (adapted from Li et al. 2017).

1.4.3.6 Renal bile acid transport

Bile acids that are able to escape hepatic extraction, end up the systemic circulation and can be subjected to glomerular filtration in the kidneys. The kidneys can act as backup clearance organs if efficient hepatobiliary transport of bile acids is compromised due to liver failure (Rodrigues et al. 2014). Although glomerular filtration of bile acids is low due to their binding on serum albumin (protein binding up to 95 % for chenodeoxycholic acid derivatives; 60-80 % for cholic acid derivatives; Frisch & Hofmann 2012), small amounts can still end up in urine: approximately 0.5 mg is lost every day (Chiang 2013). If not for ASBT, present on the apical membrane of proximal tubule epithelial cells, this number could be much higher. Bile acids are taken up by ASBT from urine and subsequently transported back to the systemic circulation by OST α - β . Efflux pumps MRP2, MRP3 and MRP4 are also present on the epithelial cells, but expression levels are moderate in health (J.G. Marin et al. 2016).

PART 2: MOLECULAR IMAGING

1.1 What is molecular imaging and why do we need it?

1.1.1 General overview

Molecular imaging can be defined as *“the visual representation, characterization and quantification of biological processes at the cellular and subcellular levels within intact living organisms”* (quote from: Massoud et al. 2003). It is a multi-disciplinary field that comprises chemistry, nuclear medicine, radiology, pharmacology, cell biology, physics, mathematics and engineering (Kircher et al. 2012). The past two decades, it has become a valuable tool to comprehend certain biological phenomena, identify regions of pathology and explore the molecular origins and progression of a disease. Its application range is vast: oncology, neuroscience, cardiology, drug development, gene therapy and cell tracking are only a few of all the application areas of molecular imaging (James & Gambhir 2012).

Molecular imaging offers several advantages over conventional, structural (anatomical) imaging (Tian 2012; James & Gambhir 2012).

- Even though modern-day anatomical imaging techniques can map the body in great detail, a structural abnormality is often not detected in the early stage of a disease. This is because anatomical imaging modalities are not sensitive enough to detect abnormalities on a molecular level. The time between generation of a pathological molecular mechanism and the detection of a gross anatomical change is therefore lost by conventional anatomical imaging. Molecular imaging on the other hand, can detect a dysfunctional physiological pathway earlier.
- Molecular imaging studies are non-invasive and can therefore be repeated in the same patient or lab animal. In preclinical research, it is possible to acquire longitudinal data on biochemical pathways in the same animal, reducing the number of lab animals needed. This consequently lowers the cost and is in favor of the 3R principle.
- Pharmacokinetics and pharmacodynamics of a (new candidate) drug can be assessed more efficiently, hence potentially saving valuable resources and time.

Advantages of molecular imaging over conventional *in vitro* tests are the following:

- It offers the possibility to monitor and track cells in the body, without disturbing their natural environment. Traditional *in vitro* methods remove cells from their environment and therefore not always provide accurate information of the actual *in vivo* situation.
- Investigation of molecular processes and signaling can be done in real-time and is dynamic, whereas *in vitro* assays only provide a static picture.

A number of principal imaging modalities can be distinguished in the molecular imaging field. Computed Tomography (CT) is primarily used for its excellent anatomical image quality, but can also be considered a molecular imaging modality by using CT contrast agents (Chen et al. 2014; Ashton et al. 2015). CT utilizes differential attenuation of X-rays by tissues to generate an image. Magnetic Resonance Imaging (MRI) is an especially versatile modality that relies on the use of a powerful magnet and radiofrequency pulses to visualize protons in the body. It can generate both detailed anatomical information and physiological, functional information by using specialized MRI sequences such as dynamic contrast enhanced MRI (DCE-MRI) and blood oxygen level dependent MRI (BOLD-MRI) (James & Gambhir 2012). Optical imaging (OI) is an emerging technology in which light photons are generated *in vivo* and detected. The most widely used optical imaging variants are bioluminescence imaging and fluorescence imaging (Dufort et al. 2010; Chen et al. 2014). Ultrasound (US) exploits high-frequency sound waves and their reflections by biological tissues (James & Gambhir 2012). Lastly, the two functional imaging modalities Positron Emission Tomography (PET) and Single Photon Emission Computed Tomography (SPECT) use radiopharmaceuticals or so-called (radio)tracers and are termed nuclear imaging techniques.

A complete discussion of all abovementioned molecular imaging modalities is beyond the scope of this work and more detailed information can be found in publications by Weissleder et al. 2010; James & Gambhir 2012. However, the key characteristics of each modality are displayed in Table 1.2. Only the relevant technologies for this dissertation, namely, CT, SPECT and PET will be discussed in more detail further on in this chapter.

Table 1.2: Molecular imaging modality characteristics. Spatial resolution: the minimum distance that the imaging modality can differentiate two independently measured objects. Temporal resolution: time needed to acquire enough events to form an image of a dynamic process. Sensitivity: ability to distinguish a molecular probe from the background (unit: mol/l). Adapted from James & Gambhir 2012; Lu & Yuan 2015.

	Physical principle	Penetration depth	Probe quantity	Spatial resolution	Sensitivity	Temporal resolution	Cost
CT	X-rays	Limitless	Not applicable	50 -200 μm	10^{-6} mol/l	Minutes	€€
PET	Positron decay	Limitless	Nanograms	1-2 mm (preclinical) 5-7 mm (clinical)	10^{-11} - 10^{-12} mol/l	Seconds- minutes	€€€
SPECT	Low energy γ -rays	Limitless	Nanograms	1-2 mm (preclinical) 8-10 mm (clinical)	10^{-10} - 10^{-11} mol/l	Minutes	€€
MRI	Radio waves and magnetic spin of atoms	Limitless	Micrograms- milligrams	25 -100 μm	10^{-9} - 10^{-6} mol/l	Minutes-hours	€€€
Fluorescence imaging	Visible or near-infrared light	< 1 cm	Micrograms- milligrams	2-3 mm	10^{-9} - 10^{-12} mol/l	Seconds- minutes	€
Bioluminescence imaging		1-2 cm	Micrograms- milligrams	3-5 mm	10^{-15} - 10^{-17} mol/l	Seconds- minutes	€
US	High frequency soundwaves	Millimeters- centimeters	Micrograms- milligrams	50-500 μm	10^{-12} mol/l (with microbubbles)	Seconds- minutes	€

1.1.2 Multi-modality imaging

From Table 1.2 we can observe that each molecular imaging modality is characterized by specific strengths and weaknesses with regards to sensitivity, resolution, cost etc. As no single modality is perfect in itself, different imaging technologies can be combined to improve diagnostic accuracy. For example, the nuclear imaging techniques SPECT and PET have a very high sensitivity and can visualize functional processes in the body but are lacking in spatial resolution and less suited to visualize anatomy. These functional imaging techniques can be combined into one imaging device with a high resolution anatomical imaging modality such as CT and MRI. The resulting combined image allows researchers to accurately link functional data to anatomical regions, which improves the accuracy and confidence of the scan interpretation (Weissleder et al. 2010).

The first combined multi-modality molecular imaging systems were SPECT/CT and later PET/CT. Developed in the 1990's, they revolutionized disease diagnosis, characterization and treatment organization and follow-up (Weissleder et al. 2010). A possible disadvantage of acquiring these combined images, is the ionizing radiation burden for patients from both the injected radionuclide, required for SPECT and PET imaging, and the X-rays used to generate a CT-image. However, because CT does not provide enough soft tissue contrast for some applications (Figure 1.15), combined PET/MRI systems have been developed (2010-present). They provide excellent anatomical resolution without the use of ionizing radiation of CT. However, combined PET/MRI is technically a lot more challenging than PET/CT and the systems' high cost limit widespread use (Rausch et al. 2017).

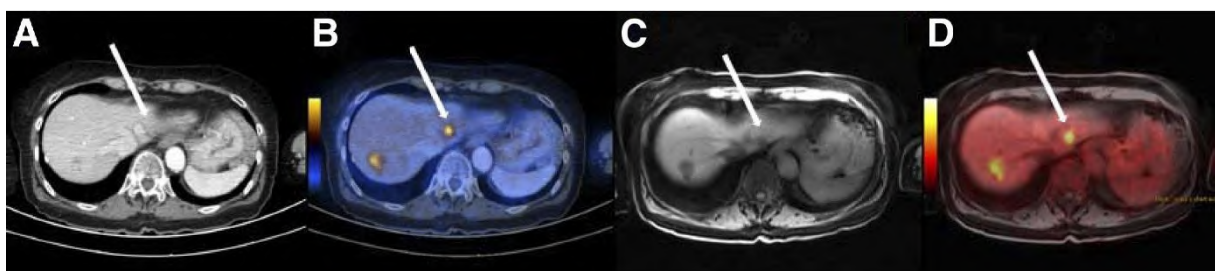


Figure 1.15: Multi-modality imaging example of a patient with liver metastases.

A is a contrast-enhanced CT. B is a fused image of A and a [^{18}F]FDG PET scan: hot spots show tumor tissue. C is an MRI scan of the same patient, while D is the fused PET/MRI scan.

The white arrow shows a liver metastasis that is nearly invisible on CT, yet can be detected by MRI (from Von Schulthess et al. 2013)

1.1.3 Small animal imaging

The use of lab animals has always been essential in the drug development process. They bridge the gap between evaluating a certain new compound *in vitro* and clinical applications in patients. Furthermore, using animal disease models was and is of pivotal use to gain understanding of disease processes and how to possibly alter them. The advent of molecular imaging provides unique opportunities to study diseases non-invasively and on a molecular level *in vivo*. By combining advanced animal models of disease with molecular imaging tools, project length can be shortened, more confidence in the obtained results is gained and the cost effectiveness of biomedical research is boosted (Cunha et al. 2014).

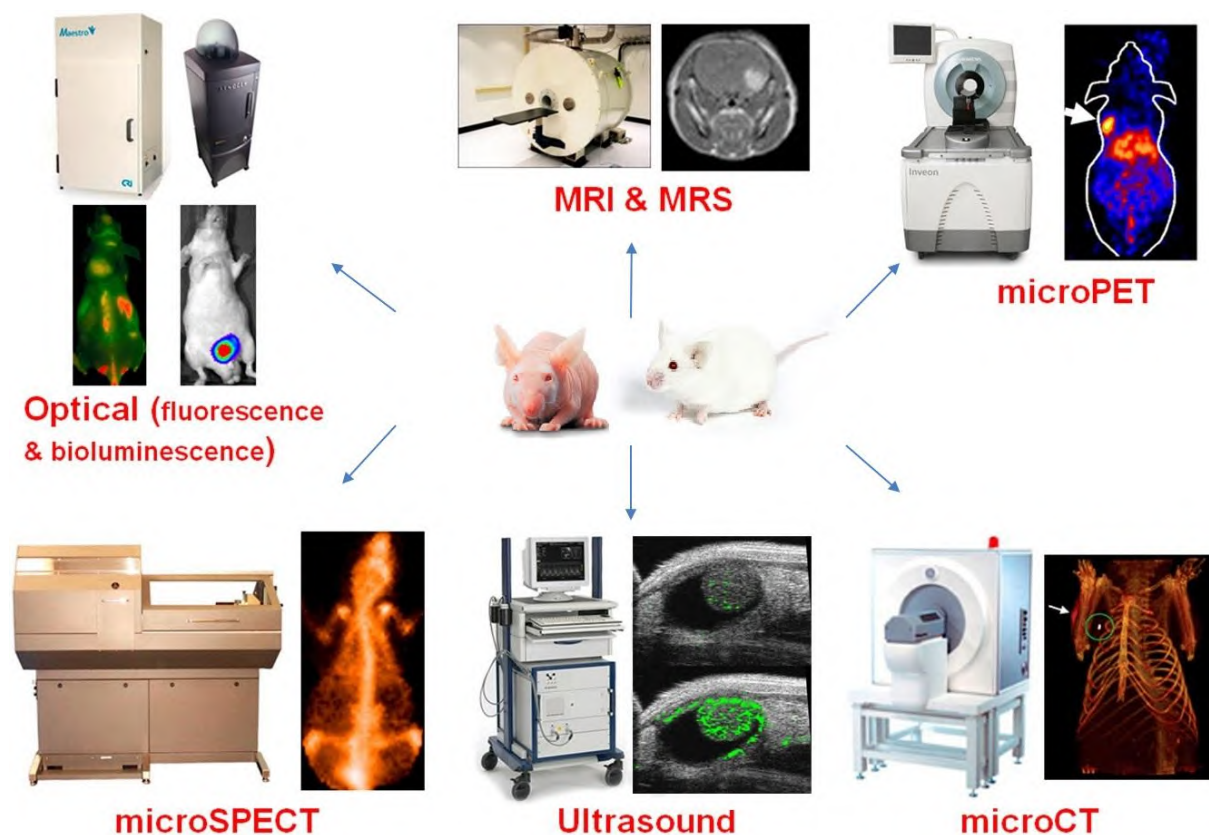


Figure 1.16: Overview of the different molecular imaging modalities in preclinical studies (adapted from CAI research group, University of Wisconsin, www.mi.wisc.edu)

Early molecular imaging experiments with small animals were performed with clinical (human) imaging equipment, but because of the large volume and mass difference between a human and a mouse or rat (average weight: 20 g and 250 g resp.), these experiments lacked the appropriate resolution and sensitivity. Development of dedicated small animal molecular imaging technology was needed. Over the past two decades, improvements in

both molecular imaging software and hardware have provided researchers with the preclinical small animal equivalents of clinical molecular imaging modalities, the so-called microPET, microCT, etc (Figure 1.16) (Cunha et al. 2014). Specific examples of these improvements will be given in the individual paragraphs on CT, SPECT and PET.

1.2 Computed Tomography (CT)

Computed tomography (CT) is a widely used and powerful imaging technique to generate high resolution three-dimensional (3D) anatomic images of a subject. It is important for the diagnosis of a wide spectrum of diseases: CT is the imaging modality of choice to study tissues with high relative contrast such as bones (contrast between calcified bones and soft tissue) and lungs (contrast between air and lung soft tissue). Although less suited for soft tissues, contrast agents can broaden CT's scope. CT is also often combined with SPECT or PET to provide anatomical correlation and attenuation correction (Weissleder et al. 2010).

CT has its roots in classical planar RX technology and basically consists of a X-ray source and X-ray detector that rotate around the subject and generate hundreds of two-dimensional (2D) X-ray images. These are subsequently reconstructed to a 3D-image by a computer algorithm (Figure 1.17).

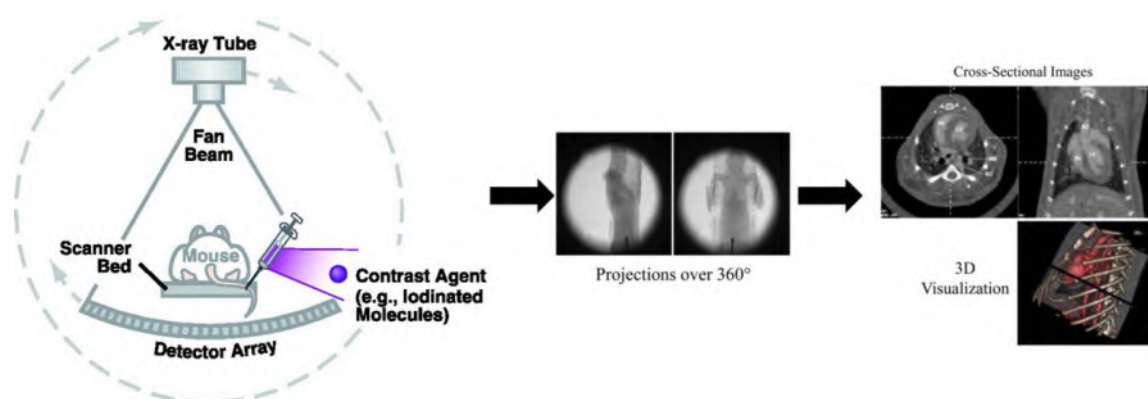


Figure 1.17: The CT image acquisition process

(adapted from James & Gambhir 2012; Ashton et al. 2015).

X-rays are produced in an X-ray tube that consists of an external high voltage supply, a filament, electron optics and an anode, all present in a glass enveloped vacuum (Figure 1.18). The filament is heated by an electric current to produce electrons that are accelerated

towards the anode by the applied voltage (typically 20-150 kilovolt). Electron optics then focus these accelerated electrons on a focal spot on the anode. The focal spot size is much smaller in a microCT X-ray tube than its clinical counterpart, which improves the image resolution. The anode (typically tungsten) decelerates the electrons and transforms their kinetic energy in heat and X-rays. Usually less than 1% of the kinetic energy is turned into X-rays. The formed X-rays exit the tube through a beryllium window and finally pass an aluminum filter. This filter is important to remove lower-energy X-rays that cannot fully penetrate the body and hence only mean an additional radiation burden (Weissleder et al. 2010; Ashton et al. 2015).

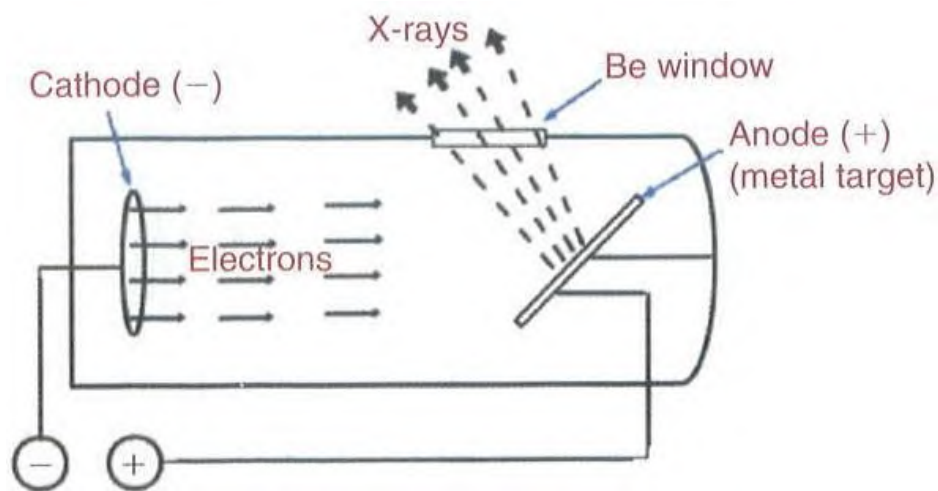


Figure 1.18: Schematic function of a X-ray tube (from Weissleder et al. 2010).

When traveling through the body of a patient or animal, X-rays can be attenuated (i.e.: absorbed) by tissue. Attenuation by a tissue is dependent of the thickness and its attenuation coefficient. X-ray attenuation in the body is determined by two mechanisms: the photoelectric effect and Compton scatter. The latter occurs when an X-ray photon collides with an electron. A part of the X-ray energy is transferred to the electron, thereby knocking it out of its atomic orbit. The resulting X-ray, that is now lower in energy, is deflected and can cause detector noise. Compton scatter decreases slightly with increasing X-ray energy, whereas it increases in materials with a higher mass density (electron density increases with mass density). The photoelectric effect occurs when all of the X-ray's energy is transferred to an electron. This effect is dependent on the energy of the incoming X-ray and the atomic weight of the material on which it hits. Higher atomic weight materials show a more pronounced photoelectric effect (Ashton et al. 2015).

More Compton scatter and photoelectric effect, mean a higher attenuation of X-rays (and lower incidence on the X-ray detector). These effects are more pronounced in high density tissues such as bone, which explains the use of CT as an excellent hard tissue anatomical imaging modality. Contrast agents bearing heavier atoms such as iodine or barium in their structure can be employed to enhance soft-tissue contrast (Ashton et al. 2015).

X-rays that are not attenuated by the body, reach the X-ray detector. The most commonly used detector consists of a Gadolinium oxysulphide (GOS) or thallium-doped cesium iodide (CsI:TI) phosphor screen that produces light as X-rays lose their energy on the screen. The produced light is then converted into electrical signals by a charge-coupled device (CCD) (Weissleder et al. 2010). Finally, these signals lead to the generation of hundreds of 2D-images, each taken at a different angle as the X-ray tube and detector spin around the subject. The 2D-images are then reconstructed into a 3D image with a computer algorithm.

1.3 Single Photon Emission Computed Tomography (SPECT)

SPECT is a 3D nuclear imaging modality that relies on the administration of low-energy gamma rays (90-300 keV) stemming from isomeric transition or electron capture (EC) decay of radionuclides (Table 1.3). The radionuclides are linked to a molecular probe (the radiotracer), which determines the biochemical pathway and organs that can be visualized in the body. SPECT can be useful to determine functional activity of the heart, kidneys, liver, lung, bone tissue, etc. It is the most regularly used nuclear imaging technique in a clinical setting (James & Gambhir 2012; Kagadis et al. 2010).

Table 1.3: The most commonly used SPECT radionuclides and their characteristics (adapted from Cunha et al. 2014).

Radionuclide	Decay mode	Half-life	Photon energies in keV and abundances (%)
^{99m}Tc	Isomeric transition	6.02 hours	140 (89)
^{67}Ga	Electron capture	3.26 days	93 (36); 184 (20); 296 (16)
^{123}I	Electron capture	13.2 hours	159 (83)
^{131}I	Beta minus	8.02 days	284 (6); 364 (81); 637 (7)
^{111}In	Electron capture	2.80 days	173 (90); 245 (94)
^{201}Tl	Electron capture	3.04 days	69 (27); 71 (46); 80 (20)

The gamma camera, generally based on the Anger principle, is the most important part of a SPECT system and consists of a collimator, a scintillation crystal, a light guide, photon multiplier tubes (PMTs) and positioning electronics (Figure 1.19). A SPECT system may consist of one or more gamma cameras.

Gamma rays originating from the subject are dispersed in every direction and hence make it difficult to locate the exact origin of the radioactive source. For this reason, a collimator is placed in front of the camera. This is a lead or tungsten honeycomb-like structure that absorbs all gamma rays that are not oriented perpendicular to the camera surface. A variety of collimators is available such as the most commonly used parallel hole collimator, fan-beam, cone-beam, (multi)pinhole and slit collimators. Each has its effect on sensitivity of the detector and magnification of the final image. Multi-pinhole collimators have become the standard for most preclinical microSPECT scanners (Weissleder et al. 2010; Cunha et al. 2014).

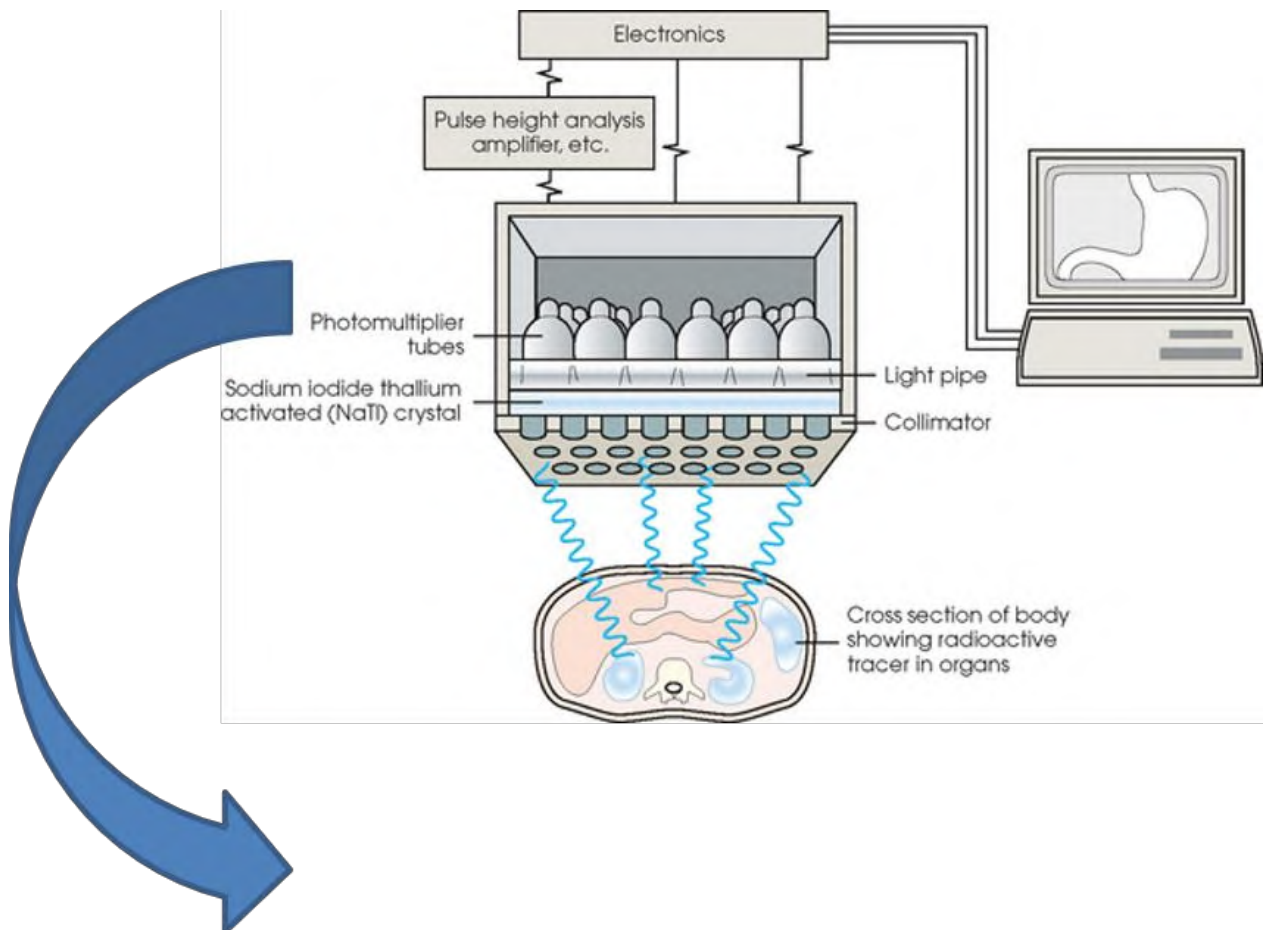


Figure 1.19: Schematic representation of the SPECT acquisition process. The gamma camera and its components are displayed. This camera rotates around the subject to generate multiple 2D projections that are finally reconstructed to a 3D image.

Figure adapted from radiologykey.com.

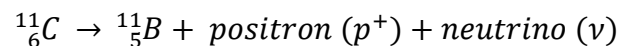
Collimator filtered gamma rays then reach the scintillation crystal, which is usually sodium iodide (NaI) doped with thallium. The crystal converts the gamma photon's energy (90-300 keV) into light photons (energies of a few eV). The amount of light that is generated is proportional to the photon's energy. Light photons are subsequently guided to PMT's where they strike the photocathode and are converted in photo-electrons. PMT's ensure amplification of these electrons to obtain an electrical signal. Positioning electronics pinpoint the location and energy of the gamma ray that reached the detector, resulting in a planar 2D image. Similar to CT, several planar 2D projections are acquired around the patient that are used to generate a 3D SPECT image using a reconstruction algorithm (Kagadis et al. 2010; Weissleder et al. 2010).

1.4 Positron Emission Tomography (PET)

1.4.1 Physical principles and detection system

PET is a nuclear imaging modality that relies on administration of radiotracers that show positron decay. Just as SPECT, PET has a broad application range to measure functionality of different tissues, depending on the radiolabeled molecular probe: oncology, cardiology, immunology, neurology etc (James & Gambhir 2012).

Positron emitting radionuclides can be produced with a cyclotron (paragraph 1.4.4) and are inherently unstable due to a proton excess in their atomic nuclei. To achieve a more stabilized nucleus, radioactive β^+ -decay occurs: the proton in excess will be converted to a neutron, a positron and a neutrino. An example of ^{11}C β^+ -decay is given below:



A positron is an anti-matter electron with a positive charge and is ejected from the nucleus with a certain kinetic energy (E_{kin}). The E_{kin} has a mean and maximum value and is specific to a certain β^+ -decay-radionuclide. Table 1.4 gives an overview of the most common PET radionuclides, their half-life and E_{kin} . Energy released from β^+ -decay that is not transferred to the E_{kin} of the positron, is given to the neutrino. This neutral particle carries no energy if the positron E_{kin} is maximal. The positron travels a certain distance based on its E_{kin} , losing energy every time it collides with neighboring electrons. After complete loss of its energy, the positron will combine with an electron, resulting in a short-lived positronium complex. Finally, the positronium will annihilate and all of its mass will be converted into two gamma photons of 511 keV that are emitted in opposite directions (Figure 1.20). The simultaneous detection of these two gamma photons that are emitted at an approximately 180° angle towards each other, form the basic principle of the PET detection system (Shukla & Kumar 2006; Kitson et al. 2009).

Table 1.4: Commonly used PET radionuclides with their half-life, average positron E_{kin} and average positron range (from Cal-González et al. 2013; Jødal et al. 2014).

Radionuclide	Half-life	Average positron E_{kin} (keV)	Average positron range in water (mm)
^{11}C	20.4 min	385.6	1.02
^{13}N	10.0 min	491.8	1.40
^{15}O	2.0 min	735.3	2.34
^{18}F	109.8 min	249.8	0.57
^{68}Ga	67.7 min	352.6 / 836.0	2.69
^{89}Zr	78.4 hours	402.7	1.27
^{124}I	4.176 days	825.9	3.4

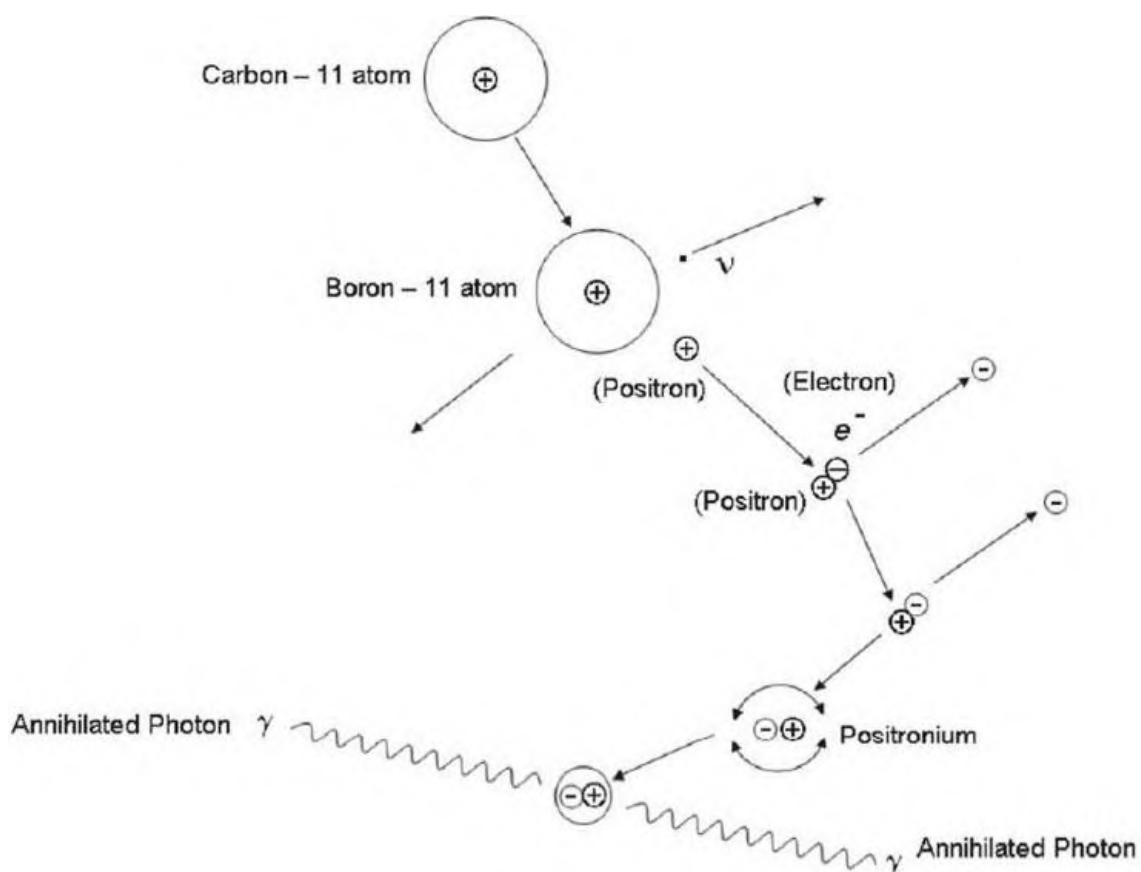


Figure 1.20: Schematic representation of positron decay and annihilation to form two 511 keV gamma photons (from Shukla & Kumar 2006).

A PET system is composed of multiple rings of scintillation detectors in which the patient is positioned. On their turn, these rings consist of multiple detector blocks (approx. 50 per ring (Hutchins et al. 2008)). Small scintillation crystals are arranged on a detector block to convert incident gamma photons to an electrical signal using 4 PMTs (Figure 1.21) (cfr. gamma detector; SPECT). When smaller scintillation crystals are used, the spatial resolution of the PET system can be improved. Scintillators for PET can be NaI, Bismuth germanate (BGO), lutetium oxyorthosilicate (LSO), gadolinium oxyorthosilicate (GSO) or lutetium-yttrium oxyorthosilicate (LYSO). LYSO and LSO are most commonly used because they are fast, dense and bright scintillators. Positioning electronics then determine the location on the detector that is stimulated (Lewellen 2008; Weissleder et al. 2010; Kagadis et al. 2010)..

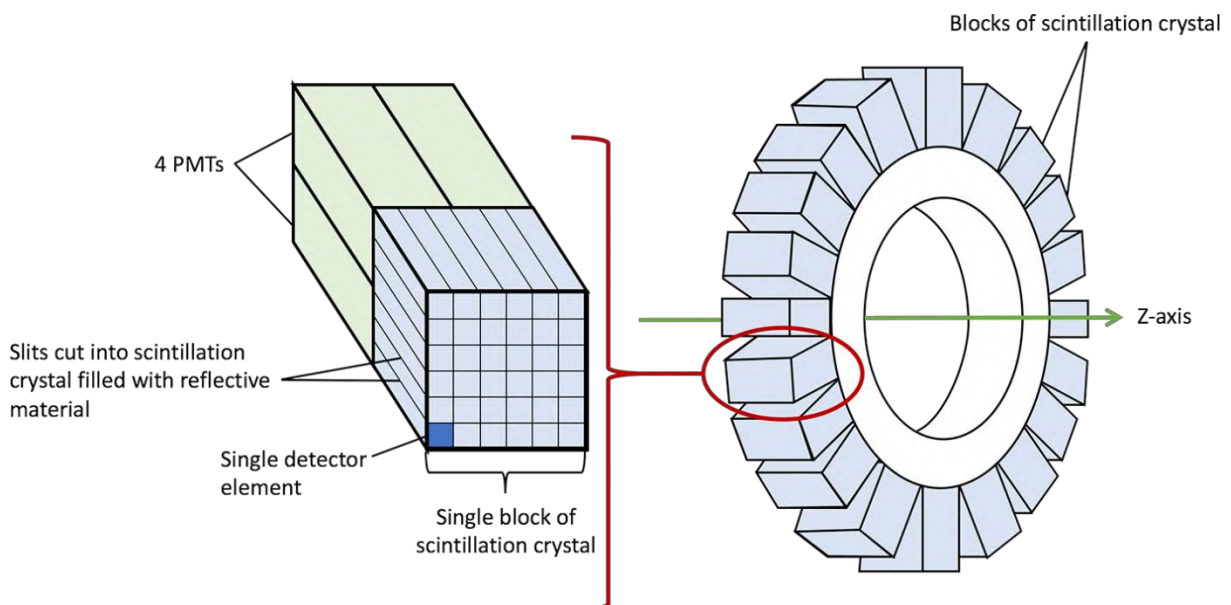


Figure 1.21: PET detector ring and detector block composition (from radiologycafe.com).

When β^+ -decay occurs in the body of the patient, the positron travels a certain distance in the tissue until its particular E_{kin} is depleted (Table 1.4). This positron range in tissue partly determines PET's spatial resolution. Annihilation of the positron results in two gamma rays that are emitted 180° from each other. If two opposite detector blocks receive a signal within a few nanoseconds of each other, a so-called coincidence event is detected (Figure 1.22). A line of response (LOR) can then be drawn from one detector element to another and marks the line on which the annihilation event took place. The LORs from thousands of coincidence events are stored in a sinogram and can be reconstructed to a 3D PET image (Fahey 2002; Weissleder et al. 2010)

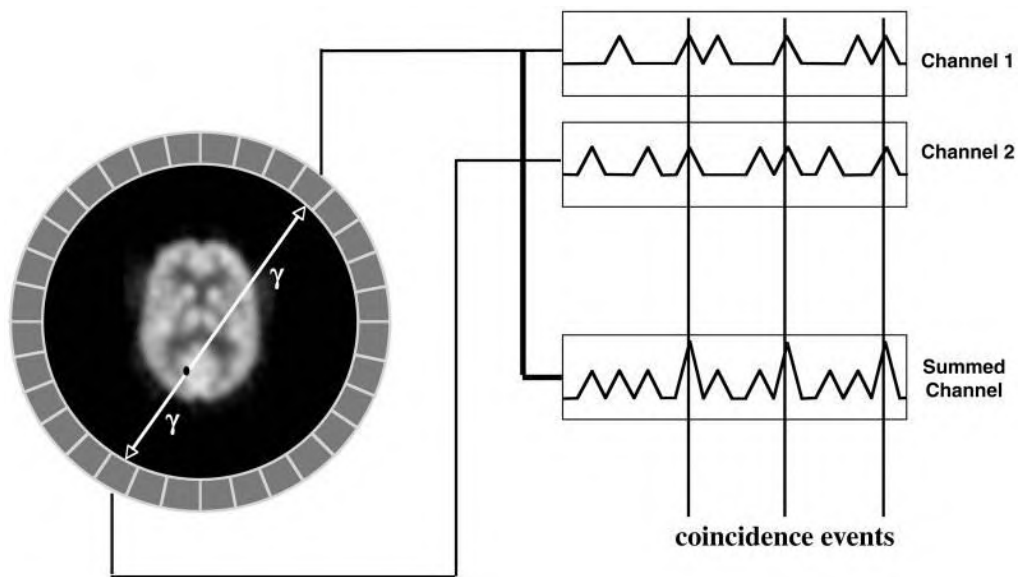


Figure 1.22: A representation of coincidence detection in PET. As an annihilation event occurs in the detector ring, two gamma photons stimulate opposing detector elements. A line of response can be drawn between these detector elements on which the annihilation event took place (from Lewellen 2008).

One of the recent PET novelties is time-of-flight (TOF) PET. It is based on the fact that each of the two 511 keV photons reaches opposing detectors at a slightly different time. By measuring the difference in photon arrival times, the probability of the annihilation origin can be confined to a subsection of the LOR (Figure 1.23). TOF-PET creates a better signal-to-noise ratio and hereby provides more accurate quantitative information (Kitson et al. 2009). To measure small time differences in photon arrivals, there is a need for fast electronics and scintillators, which are continuously improving (Rahmim & Zaidi 2008).

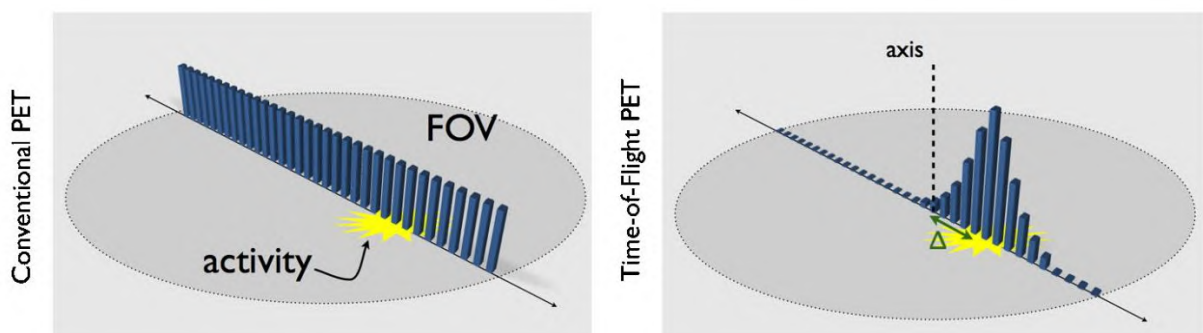


Figure 1.23: Schematic representation of the difference between conventional PET and time-of-flight PET (TOF-PET). A probability distribution of a recorded annihilation event within field of view (FOV) can be constructed in TOF-PET (adapted from Lonsdale & Beyer 2010).

Small animal PET imaging (microPET) shares the same image formation principles as human PET imaging, but faces unique challenges due to the much smaller subjects that need to be imaged. Therefore, the spatial resolution and sensitivity, i.e. the ability to detect photon emission events, has to be improved. Spatial resolution is mostly improved by reducing the size of the scintillation crystals from 4-6 mm (clinical PET) to 1-2mm (small animal PET). This will result in PET systems with a spatial resolution of 1-2 mm, whereas clinical PET systems have a spatial resolution of 5-7mm (Kagadis et al. 2010; James & Gambhir 2012). Recent improvements in preclinical hardware can even provide sub-millimeter spatial resolution. To increase detection efficiency the diameter of the detector ring is reduced from approx. 80 cm (clinical PET) to approx. 15 cm (small animal PET).

1.4.2 2-[¹⁸F]Fluoro-2-deoxy-D-glucose ([¹⁸F]FDG), the workhorse of PET

It is impossible not to mention 2-[¹⁸F]fluoro-2-deoxy-D-glucose ([¹⁸F]FDG) in a PET chapter, as this tracer is the most widely used PET radiopharmaceutical (approx. 90 % of all scans) and helped establish the clinical use of PET/CT. [¹⁸F]FDG is a glucose analogue, of which the hydroxy functional group on the 2 position is replaced with a positron emitting fluorine-18 (Figure 1.24). Once it is transported in the cell, it is phosphorylated by hexokinase to [¹⁸F]FDG-6-phosphate. Because of the 2-fluoro atom in its structure, [¹⁸F]FDG-6-phosphate is not metabolized any further like regular glucose: [¹⁸F]FDG-6-phosphate remains trapped inside the cell. [¹⁸F]FDG PET is therefore capable of visualizing tissue with a high glucose consumption, such as brain, heart and muscles but also tumor malignancies (Miller et al. 2008; Coenen et al. 2010).

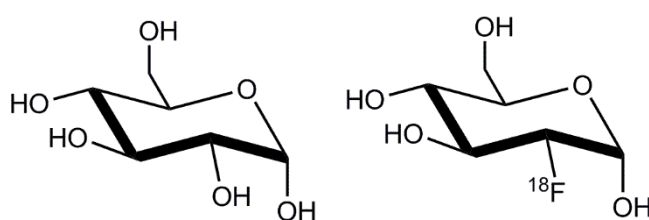


Figure 1.24: Chair structures of glucose (left) and 2-[¹⁸F]fluoro-2-deoxy-D-glucose (right).

[¹⁸F]FDG PET has become a valuable tool to spot malignancies, assess tumor growth and estimate tumor stage, measure therapeutic response and check for tumor recurrence (Weissleder et al. 2010).

1.4.3 PET versus SPECT

The nuclear imaging modalities PET and SPECT each have its merits and drawbacks, which will be discussed in this section.

Positron emitting radionuclides have short half-lives, relatively high gamma photon energies of 511 keV and are artificially generated with the help of a costly cyclotron. SPECT radionuclides however, have a relatively longer half-life and lower gamma photon energy. A nearby cyclotron is not required, which means that significant less infrastructure is needed to produce SPECT tracers and they can be used in more remote locations (Weissleder et al. 2010).

PET and SPECT are both tracer techniques, which means that they only introduce a very small amount of radiolabeled pharmaceutical in the body. Administering a large amount of contrast agent (in other molecular imaging techniques such as MRI or CT) could alter the homeostasis of the body function that the tracers try to visualize. Regarding design of a radiotracer, PET has significant advantages over SPECT. Most PET radionuclides are low in atomic mass and some are also found in biomolecules. When they are incorporated in a certain endogenous small molecule, this often does not alter the molecular structure significantly. Consequently, there is a higher probability that the resulting PET tracer visualizes the same biochemical pathway as the endogenous molecule. SPECT tracers on the other hand, rely on incorporating larger atoms, usually with the help of bulky complexation structures that have to be added to the endogenous molecule of interest (Miller et al. 2008; Rahmim & Zaidi 2008). However, some PET tracers also contain these larger complexation structures.

The sensitivity, i.e. the ability to indicate photon emission events, is much higher in PET (approx. 2-3 orders of magnitude bigger). Collimator use causes an inherent loss of sensitivity in SPECT, making PET the nuclear imaging modality of choice for quantification purposes (Rahmim & Zaidi 2008; Weissleder et al. 2010; Cunha et al. 2014).

Spatial resolution of the nuclear imaging modalities has improved over the years. Improvements in spatial resolution for both techniques are in essence limited by technology (design of collimators, detectors, ...), whereas PET is also limited by physics (e.g. positron range, cfr. supra). Preclinical spatial resolution for PET and SPECT is almost equal: 1-2 mm.

Recent advances in preclinical PET and SPECT hardware can even provide sub millimeter spatial resolution. Clinically, PET scores better: 5-7 mm (PET) vs 8-10 mm (SPECT) (Rahmim & Zaidi 2008; James & Gambhir 2012).

Temporal resolution is a measure of how well a process of interest can be imaged in function of time, i.e. how well it is suited for dynamic molecular imaging. SPECT has a worse temporal resolution, because data procurement relies on one or multiple rotating gamma cameras that only do acquisitions at fixed projection angles. Furthermore, SPECT's sensitivity is much lower. PET on the other hand, acquires data from all projection angles simultaneously because of its fixed detector ring that surrounds the examined subject (Rahmim & Zaidi 2008; Weissleder et al. 2010).

A major advantage of SPECT over PET is the ability to perform dual-tracer imaging. It is possible to simultaneously image two SPECT-tracers with different gamma energies. Two functions can be monitored in one single SPECT acquisition. Dual-tracer imaging reduces acquisition time and hence patient discomfort. Furthermore, the final images from the two different tracers are registered perfectly in space and time (Rahmim & Zaidi 2008).

1.4.4 Production of PET radionuclides with a cyclotron

A cyclotron is needed to provide positron emitting radionuclides that can then be incorporated in PET tracer molecules. It accelerates charged particles in high vacuum to enormous speed and energy as to allow a nuclear reaction in the target material. The result of this nuclear reaction is an artificial radionuclide that shows positron decay.

In essence, a cyclotron consists of an electromagnet that provides a magnetic field and two hollow electrodes between the electromagnet's poles (Figure 1.25). These hollow electrodes resemble the letter D and are therefore termed "dees". Both dees are hooked up to an alternating current. Charged particles can be introduced at the center of the space between the two dees, such as a proton (H^+) or hydride (H^-). These particles can then be accelerated by the electric field in the gap between the dees. After it enters the dee, only the magnetic field has an effect on the particle, which then describes a circular motion due to the Lorentz force. The polarity of the dees is inversed when the particle exits the dee, thereby accelerating it again. As this action continues over and over, the particle's velocity and orbit radius increase until it spirals to the edge of the cyclotron with enough energy

(MeV order of magnitude) to pass the Coulomb barrier and cause a nuclear reaction in a target nucleus. The beam is then extracted from the cyclotron by an electrostatic deflector (in the case of a positively charged proton) or passed through a stripping foil to remove the electrons from the hydride ion (Strijckmans 2001).

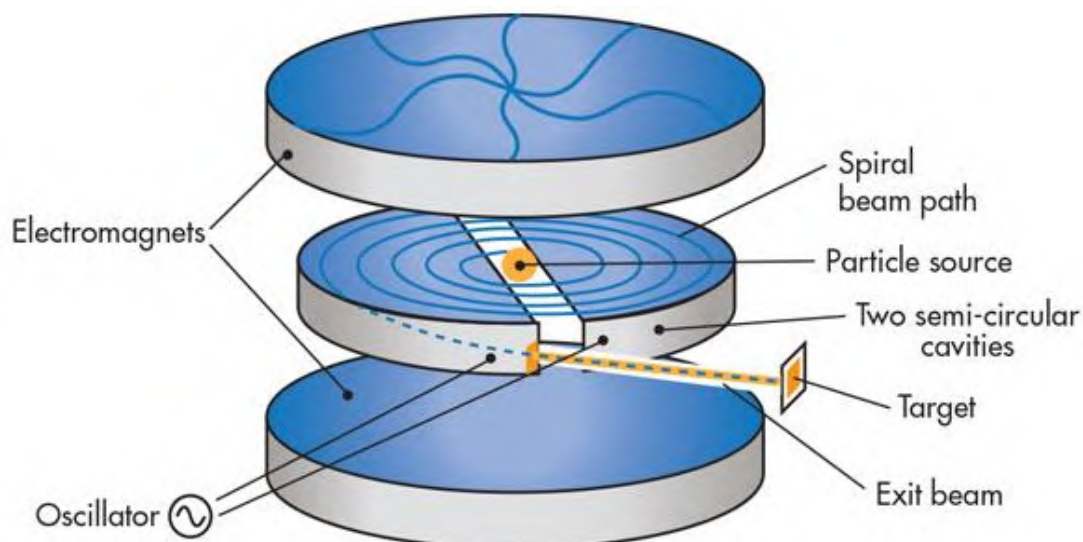


Figure 1.25: Principle of a cyclotron (from machinedesign.com).

The high energy particle is now guided towards the target material: a precursor for the production of positron emitting radionuclides. The production of ^{11}C for example, is primarily achieved by proton irradiation of a ^{14}N atom (in the form of nitrogen gas in the target), which then emits an alpha particle. This nuclear reaction can be noted as $^{14}\text{N} (p, \alpha) ^{11}\text{C}$. The ^{11}C radionuclide is generated in the chemical form of $[^{11}\text{C}]\text{CO}_2$ or $[^{11}\text{C}]\text{CH}_4$ if limited amounts of resp. oxygen and hydrogen are also present in the target. The ^{18}F isotope (anion) on the other hand, is produced by proton irradiation of ^{18}O enriched water ($[^{18}\text{O}]\text{H}_2\text{O}$). The nuclear reaction that follows, encompasses the introduction of a proton in the ^{18}O nucleus, while a neutron is expelled: the reaction is noted as $^{18}\text{O} (p, n) ^{18}\text{F}$ (Miller et al. 2008). The resulting $[^{18}\text{F}]\text{fluoride}$ ion ($[^{18}\text{F}]\text{F}^-$) can be introduced into a chemical structure to form a PET radiotracer. These strategies will be discussed below.

1.4.5 Fluoro-18 PET-radiochemistry

The ^{18}F radionuclide is arguably the most favorable PET radionuclide because of its manageable half-life (109.8 min) that still allows time to incorporate it in a chemical structure and its low positron energy. In fact, the ^{18}F positron has the lowest energy of all

PET radionuclides and will only travel a small distance in tissue (See also Table 1.4). Using a ^{18}F PET tracer is therefore beneficial to the resolution of acquired PET images (Miller et al. 2008).

In the field of medicinal chemistry, the peculiar physical properties of fluorine are often utilized. Fluorine has the highest electronegativity of all elements and can form a polarized covalent bond with carbon atoms: the F-C bond is the strongest single bond that can be made (O'Hagan 2008). Because of its small van der Waals radius, fluorine is often used as a bioisosteric substitution for hydrogen atoms and hydroxyl functions (fluorine: 1.47 Å ; hydrogen: 1.20 Å; oxygen: 1.52 Å) (Liang et al. 2013; Jacobson et al. 2014). This substitution is however not that straightforward. Introducing a fluorine atom in a molecule can have a dramatic effect on its lipophilicity (Svadberg 2012). Furthermore, a fluorine atom is a less avid hydrogen bond acceptor than hydroxyl functional groups. Introducing a fluorine atom in a molecule may therefore cause profoundly changed biological activity of the parent molecule, which can be of interest in drug development or other disciplines (Miller et al. 2008; O'Hagan 2008).

Strategies for ^{18}F radiolabeling can be divided into two categories: the direct or indirect labeling methods (Figure 1.26). Indirect labeling methods use a ^{18}F prosthetic group, a small radiolabeled alkyl or aryl subunit with reactive groups. The prosthetic group can then react with a more complex (bio)molecule. The indirect strategy is usually the best if the (bio)molecule to be labeled is not stable enough to endure direct ^{18}F radiolabeling. It does however require multi-step synthesis and the addition of the prosthetic group may alter the biochemical characteristics of the resulting PET tracer (Miller et al. 2008).

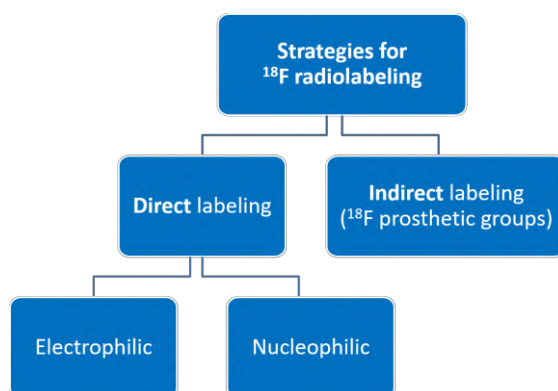


Figure 1.26 : Overview of ^{18}F radiolabeling strategies.

Direct radiolabeling reactions with ^{18}F can be categorized in an electrophilic or nucleophilic approach.

Electrophilic fluorination reactions require the presence of a F^+ -atom, which is commonly provided by $[^{18}\text{F}]\text{F}_2$ -gas. The production of $[^{18}\text{F}]\text{F}_2$ -gas requires proton irradiation of $[^{18}\text{O}]\text{O}_2$ gas (^{18}O (p, n) ^{18}F nuclear reaction) or deuteron irradiation of ^{20}Ne targets (^{20}Ne (d, α) ^{18}F nuclear reaction). Furthermore, the target has to be supplemented with $[^{19}\text{F}]\text{F}_2$ carrier gas. Electrophilic fluorination with $[^{18}\text{F}]\text{F}_2$ allows labeling of electron rich structures, such as alkenes or aromatic rings. Its specificity is however not that high, meaning that sometimes a mixture of ^{18}F labeled compounds can arise. Furthermore, radiopharmaceuticals that are produced with electrophilic fluorination have a lower specific activity. This radiopharmaceutical concept describes the amount of radioactivity per mass unit (or mole) of the radiopharmaceutical (both radiolabeled and cold, non-radiolabeled product). By adding fluorine carrier gas to the target, there is a larger chance that a ^{19}F instead of a ^{18}F isotope is introduced in the precursor molecule. Low specific activities may lead to receptor saturation, reduction of PET signal from specific binding and pharmacological effects (Miller et al. 2008; Jacobson et al. 2014).

Nucleophilic reactions with $[^{18}\text{F}]\text{fluoride}$ are the most common direct synthetic approach to produce a ^{18}F labeled compound. The anion can replace a suitable leaving group (mesylate, tosylate, triflate, nitro, ...) on a precursor molecule by a nucleophilic aromatic substitution or by an $\text{S}_{\text{N}}2$ mechanism on aliphatic positions. Functional groups of the precursor that can interfere with these reactions, have to first be protected. Polar aprotic solvents such as acetonitrile, N, N-dimethylformamide (DMF) and dimethyl sulfoxide (DMSO) favor reactions with $[^{18}\text{F}]\text{fluoride}$. Recently, successes have been reported with the polar protic solvents t-butanol and t-amylalcohol (Jacobson et al. 2014).

$[^{18}\text{F}]\text{fluoride}$ can be produced in high specific activities (in the range of 100 GBq/ μmol versus 100-600 MBq/ μmol for $[^{18}\text{F}]\text{F}_2$) by proton irradiation of $[^{18}\text{O}]\text{H}_2\text{O}$. However this aqueous environment blocks the nucleophilic capabilities of $[^{18}\text{F}]\text{fluoride}$ because the anion is shielded by water molecules. It is key that $[^{18}\text{F}]\text{fluoride}$ is dehydrated as good as possible, while keeping its solubility high in a polar aprotic solvent for the fluorination reaction. The $[^{18}\text{O}]\text{H}_2\text{O}$ - $[^{18}\text{F}]\text{fluoride}$ solution is therefore first passed through an anion exchange resin

column to trap the negatively charged [^{18}F]fluoride and recover the [^{18}O]H $_2$ O for repurification. The anion is consequently eluted from the column by an acetonitrile-water azeotropic mixture, containing a counterion (K $_2$ CO $_3$ or KHCO $_3$) and a phase transfer reagent (e.g. cryptand-222; a.k.a. Kryptofix or tetrabutyl ammonium). The azeotrope is evaporated and additional drying steps with acetonitrile can follow. The phase transfer reagent is critical for guaranteeing [^{18}F]fluoride's nucleophilicity in a polar aprotic solvent: cryptand-222 forms a soluble complex with a potassium cation, which leaves the [^{18}F]fluoride open for nucleophilic attack on the leaving group of a precursor for radiosynthesis (Figure 1.27) (Miller et al. 2008; Svadberg 2012).

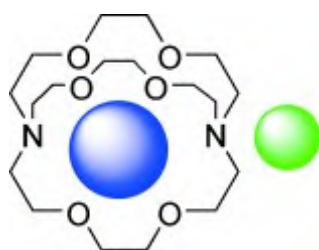


Figure 1.27: Molecular structure of cryptand-222 that forms a complex with a potassium (blue) and fluoride (green) ion (from Miller et al. 2008).

Part 1 and 2 References

- Abdel-Misih, S.R.Z. & Bloomston, M., 2010. Liver Anatomy. *Surgical Clinics of North America*, 90, pp.643–653.
- Alnouti, Y., Csanaky, I. & Klaassen, C., 2008. Quantitative profiling of bile acids and their conjugates in mouse liver, bile, plasma and urine using LC-MS/MS. *J Chromatogr B Analyt*, 873(2), pp.209–217.
- Anwer, M.S. & Stieger, B., 2013. Sodium-dependent bile salt transporters of the SLC10A transporter family: more than solute transporters. *Pflügers Archiv - European Journal of Physiology*, 466(1), pp.77–89.
- Ashton, J.R., West, J.L. & Badea, C.T., 2015. In vivo small animal micro-CT using nanoparticle contrast agents. *Frontiers in Pharmacology*, 6(NOV), pp.1–22.
- van Aubel, R. a M.H. et al., 2002. The MRP4/ABCC4 gene encodes a novel apical organic anion transporter in human kidney proximal tubules: putative efflux pump for urinary cAMP and cGMP. *Journal of the American Society of Nephrology : JASN*, 13(3), pp.595–603.
- Ballatori, N. et al., 2013. The heteromeric organic solute transporter, OST α -OST β /SLC51: A transporter for steroid-derived molecules. *Molecular Aspects of Medicine*, 34, pp.1–15.
- Bennink, R.J. et al., 2012. Liver function testing with nuclear medicine techniques is coming of age. *Seminars in Nuclear Medicine*, 42(2), pp.124–137.
- Boyer, J., 2013. Bile Formation and Secretion. *Compr Physiol.*, 3(3), pp.1035–1078.
- Brunt, E.M. et al., 2014. Pathology of the liver sinusoids. *Histopathology*, 64(7), pp.907–920.
- Cal-González, J. et al., 2013. Positron range estimations with PeneloPET. *Physics in Medicine and Biology*, 58, pp.5127–5152.
- Chen, Z.Y. et al., 2014. Advance of molecular imaging technology and targeted imaging agent in imaging and therapy. *BioMed Research International*, pp.1–12.
- Chiang, J., 2013. Bile Acid Metabolism and Signalling. *Compr Physiol*, 3(3), pp.1191–1212.

- Coenen, H.H. et al., 2010. Fluorine-18 radiopharmaceuticals beyond [18F]FDG for use in oncology and neurosciences. *Nuclear Medicine and Biology*, 37(7), pp.727–740.
- Cotoi, C.G. & Quaglia, A., 2016. Normal liver anatomy and introduction to liver histology. *Textbook of pediatric gastroenterology, hepatology and nutrition*, pp.609–612.
- Cunha, L. et al., 2014. Preclinical imaging: An essential ally in modern biosciences. *Molecular Diagnosis and Therapy*, 18(2), pp.153–173.
- Dawson, P.A., 2011. *Handbook of Experimental Pharmacology vol 201: Role of intestinal bile acid transporters in bile acid and drug disposition*,
- Dawson, P.A., Lan, T. & Rao, A., 2009. Bile acid transporters. *Journal of Lipid Research*, 50(12), pp.2340–2357.
- Dixon, L. et al., 2013. Kupffer Cells in the Liver. *Comprehensive Physiology*, 3(2), pp.785–797.
- Dufort, S. et al., 2010. Optical small animal imaging in the drug discovery process. *Biochimica et Biophysica Acta - Biomembranes*, 1798(12), pp.2266–2273.
- Fahey, F.H., 2002. Data Acquisition in PET Imaging. *journal of nuclear medicine technology*, 30, pp.39–49.
- Fini, A. & Roda, A., 1987. Chemical properties of bile acids. IV. Acidity constants of glycine-conjugated bile acids. *J Lipid Res*, 28(7), pp.755–759.
- Frisch, K. & Hofmann, A., 2012. Biliary secretion. *Functional Molecular Imaging in Hepatology*, pp.49–75.
- Fromm, M.F. et al., 2000. The effect of rifampin treatment on intestinal expression of human MRP transporters. *American Journal of Pathology*, 157(5), pp.1575–1580.
- Geisel, D. et al., 2015. Imaging-Based Liver Function Tests – Past , Present and Future. *Fortschr. Röntgenstr.*, pp.863–871.
- Giacomini, K.M. & Tweedie, D., 2010. Membrane transporters in drug development. *Nature reviews. Drug discovery*, 9(March), pp.215–236.

- Gissen, P. & Arias, I.M., 2015. Structural and functional hepatocyte polarity and liver disease. *Journal of Hepatology*, 63(4), pp.1023–1037.
- Gunnarsdottir, S. et al., 2003. Small intestinal motility disturbances and bacterial overgrowth in patients with liver cirrhosis and portal hypertension. *The American Journal of Gastroenterology*, 98(6), pp.1362–1370.
- Hagenbuch, B. & Meier, P.J., 2004. Organic anion transporting polypeptides of the OATP/SLC21 family: Phylogenetic classification as OATP/SLCO super-family, new nomenclature and molecular/functional properties. *Pflugers Archiv European Journal of Physiology*, 447(5), pp.653–665.
- Halilbasic, E., Claudel, T. & Trauner, M., 2013. Bile acid transporters and regulatory nuclear receptors in the liver and beyond. *Journal of Hepatology*, 58, pp.155–168
- Heubi, J.E. et al., 2007. Inborn errors of bile acid metabolism. *Semin Liver Dis*, 27(3), pp.282–294.
- Hirano, M. et al., 2005. Bile Salt Export Pump (BSEP / ABCB11) Can Transport a Nonbile Acid Substrate , Pravastatin. *Pharmacology*, 314(2), pp.876–882.
- Ho, R.H. et al., 2006. Drug and Bile Acid Transporters in Rosuvastatin Hepatic Uptake: Function, Expression, and Pharmacogenetics. *Gastroenterology*, 130(6), pp.1793–1806.
- Hofmann, a. F. & Hagey, L.R., 2008. Bile Acids: Chemistry, Pathochemistry, Biology, Pathobiology, and Therapeutics. *Cellular and Molecular Life Sciences*, 65(16), pp.2461–2483.
- Hofmann, a F., 2014. The continuing importance of bile acids in liver and intestinal disease. *Archives of internal medicine*, 159(22), pp.2647–58.
- Hofmann, a F. & Mysels, K.J., 1992. Bile acid solubility and precipitation in vitro and in vivo: the role of conjugation, pH, and Ca²⁺ ions. *Journal of lipid research*, 33(5), pp.617–26.
- Hofmann, A., 2004. Detoxification of Lithocholic Acid, A Toxic Bile Acid: Relevance to Drug Hepatotoxicity. *Drug Metabolism Reviews*, 36, pp.703–722.

- Hofmann, A., 2007. Why bile acid glucuronidation is a minor pathway for conjugation of endogenous bile acids in man. *Hepatology*, 45(4), pp.1083–1084.
- Hofmann, A.F., 1999. Bile Acids: The Good, the Bad, and the Ugly. *News in physiological sciences: an international journal of physiology produced jointly by the International Union of Physiological Sciences and the American Physiological Society*, 14, pp.24–29.
- Hofmann, A.F., 2009. The enterohepatic circulation of bile acids in mammals: form and functions. *Frontiers in bioscience: a journal and virtual library*, 14(September), pp.2584–2598.
- Hofmann, A.F. & Hagey, L.R., 2014. Key discoveries in bile acid chemistry and biology and their clinical applications: history of the last eight decades. *Journal of lipid research*, 55(8), pp.1553–1595.
- Hosey, C.M., Broccatelli, F. & Benet, L.Z., 2014. Predicting when Biliary Excretion of Parent Drug is a Major Route of Elimination in Humans. *The AAPS Journal*, 16(5), pp.1085–1096.
- Hutchins, G.D. et al., 2008. Small Animal PET Imaging. *ILAR journal*, 49(1), pp.54–65.
- Hylemon, P.B. et al., 2009. Bile acids as regulatory molecules. *Journal of Lipid Research*, 50(8), pp.1509–1520.
- J.G. Marin, J. et al., 2016. Bile Acids in Physiology, Pathology and Pharmacology. *Current Drug Metabolism*, 17(1), pp.4–29.
- Jacobson, O., Kiesewetter, D.O. & Chen, X., 2014. Fluorine-18 Radiochemistry, Labeling Strategies and Synthetic Routes. *Bioconjugate chemistry*, 26(1), pp.1–18.
- Jacquemin, E., 2012. Progressive familial intrahepatic cholestasis. *Clinics and Research in Hepatology and Gastroenterology*, 36(SUPPL.1), pp.S26–S35.
- James, M.L. & Gambhir, S.S., 2012. A Molecular Imaging Primer: Modalities, Imaging Agents, and Applications. *Physiological Reviews*, 92(2), pp.897–965.
- Jødal, L., Le Loirec, C. & Champion, C., 2014. Positron range in PET imaging: Non-conventional isotopes. *Physics in Medicine and Biology*, 59, pp.7419–7434.

- Juza, R.M. & Pauli, E.M., 2014. Clinical and surgical anatomy of the liver: A review for clinicians. *Clinical Anatomy*, 27(5), pp.764–769.
- Kagadis, G.C. et al., 2010. In vivo small animal imaging: current status and future prospects. *Medical physics*, 37(12), pp.6421–6442.
- Keplinger, K.M. & Bloomston, M., 2014. Anatomy and embryology of the biliary tract. *Surgical Clinics of North America*, 94(2), pp.203–217.
- Keppler, D., 2011. *Handbook of Experimental Pharmacology vol 201: Multidrug Resistance Proteins (MRPs, ABCs): Importance for Pathophysiology and Drug Therapy*,
- Kircher, M.F., Hricak, H. & Larson, S.M., 2012. Molecular imaging for personalized cancer care. *Molecular Oncology*, 6(2), pp.182–195.
- Kitson, S.L. et al., 2009. Clinical Applications of Positron Emission Tomography (PET) Imaging in Medicine: Oncology , Brain Diseases and Cardiology. *Current Radiopharmaceuticals*, 2, pp.224–253.
- Klaassen, C.D. & Aleksunes, L.M., 2014. Xenobiotic , Bile Acid , and Cholesterol Transporters: Function and Regulation. *Pharmacological Reviews*, 62(1), pp.1–96.
- König, J., 2011. *Handbook of Experimental Pharmacology vol 201: Uptake Transporters of the Human OATP Family*,
- Krishna, M., 2013. Microscopic anatomy of the liver. *Clinical Liver Disease*, 2, pp.4–7.
- Kullak-Ublick, G.A. et al., 1997. Chlorambucil-taurocholate is transported by bile acid carriers expressed in human hepatocellular carcinomas. *Gastroenterology*, 113(4), pp.1295–1305.
- Langmann, T. et al., 2003. Real-time reverse transcription-PCR expression profiling of the complete human ATP-binding cassette transporter superfamily in various tissues. *Clinical Chemistry*, 49(2), pp.230–238.
- Lefebvre, P., Cariou, B. & Lien, F., 2009. Role of bile acids and bile acid receptors in metabolic regulation. *Physiol Rev*, 89, pp.147–191.

- Leuthold, S. et al., 2008. Mechanisms of pH-gradient driven transport mediated by organic anion polypeptide transporters. *AJP: Cell Physiology*, 296(3), pp.C570–C582
- Lewellen, T.K., 2008. Recent developments in PET detector technology. *phys Med Biol.*, 53(17), pp.287–317.
- Li, T. & Chiang, J.Y.L., 2009. Regulation of bile acid and cholesterol metabolism by PPARs. *PPAR research*, pp.1–15.
- Li, Y. et al., 2017. Bile acids and intestinal microbiota in autoimmune cholestatic liver diseases. *Autoimmunity Reviews*, 16, pp.885–896.
- Liang, T., Neumann, C.N. & Ritter, T., 2013. Introduction of Fluorine and Fluorine-Containing Functional Groups. *Angew Chem Int Edit*, 52(32), pp.8214–8264.
- de Lima Toccafondo Vieira, M. & Tagliati, C.A., 2014. Hepatobiliary transporters in drug-induced cholestasis: a perspective on the current identifying tools. *Expert opinion on drug metabolism & toxicology*, 10(4), pp.581–97.
- Lonsdale, M.N. & Beyer, T., 2010. Dual-modality PET/CT instrumentation-Today and tomorrow. *European Journal of Radiology*, 73(3), pp.452–460.
- Lu, F. & Yuan, Z., 2015. PET / SPECT molecular imaging in clinical neuroscience : recent advances in the investigation of CNS diseases. *Quantitative Imaging in Medicine and Surgery*, 5(3), pp.433–447.
- Maillette de Buy Wenniger, L. & Beuers, U., 2010. Bile salts and cholestasis. *Digestive and liver disease : official journal of the Italian Society of Gastroenterology and the Italian Association for the Study of the Liver*, 42(6), pp.409–18.
- Makishima, M. et al., 2002. Vitamin D receptor as an intestinal bile acid sensor. *Science*, 296(5571), pp.1313–1316.
- Martinez-Becerra, P. et al., 2011. Further characterization of the electrogenicity and pH sensitivity of the human organic anion-transporting polypeptides OATP1B1 and OATP1B3. *Molecular pharmacology*, 79(3), pp.596–607.

- Massoud, T.F. et al., 2003. Molecular imaging in living subjects: seeing fundamental biological processes in a new light. *Genes & Development*, 17, pp.545–580.
- Masyuk, A.I., Masyuk, T. V. & LaRusso, N.F., 2008. Cholangiocyte primary cilia in liver health and disease. *Developmental Dynamics*, 237(8), pp.2007–2012.
- Miller, P.W. et al., 2008. Synthesis of ^{11}C , ^{18}F , ^{15}O , and ^{13}N Radiolabels for Positron Emission Tomography. *Angew. Chem*, 47, pp.8998–9033.
- O’Hagan, D., 2008. Understanding organofluorine chemistry. An introduction to the C–F bond. *Chem. Soc. Rev.*, 37, pp.308–319.
- Palmer, R.H. & Bolt, M.G., 1971. Bile acid sulfates. I. Synthesis of lithocholic acid sulfates and their identification in human bile. *Journal Of Lipid Research*, 12(6), pp.671–9.
- Pande, C., Kumar, A. & Sarin, S.K., 2009. Small-intestinal bacterial overgrowth in cirrhosis is related to the severity of liver disease. *Alimentary Pharmacology and Therapeutics*, 29(12), pp.1273–1281.
- Park, J.Y. et al., 2006. Bile acid analysis in biliary tract cancer. *Yonsei Medical Journal*, 47(6), pp.817–825.
- Pauli-Magnus, C. & Meier, P.J., 2006. Hepatobiliary transporters and drug-induced cholestasis. *Hepatology (Baltimore, Md.)*, 44, pp.778–87.
- Rahmim, A. & Zaidi, H., 2008. PET versus SPECT: strengths, limitations and challenges. *Nuclear medicine communications*, 29(3), pp.193–207.
- Rausch, I. et al., 2017. Technical and instrumental foundations of PET/MRI. *European Journal of Radiology*, 94(March), pp.A3–A13.
- Rius, M. et al., 2003. Cotransport of reduced glutathione with bile salts by MRP4 (ABCC4) localized to the basolateral hepatocyte membrane. *Hepatology*, 38(2), pp.374–384.
- Rius, M. et al., 2006. Substrate specificity of human ABCC4 (MRP4) -mediated cotransport of bile acids and reduced glutathione. *American Journal of Physiology - Gastrointestinal and Liver Physiology*, 290, pp.640–647.

- Rodrigues, A.D. et al., 2014. Drug-induced perturbations of the bile acid pool, cholestasis, and hepatotoxicity: Mechanistic considerations beyond the direct inhibition of the bile salt export pump. *Drug Metabolism and Disposition*, 42(4), pp.566–574.
- Rost, D. et al., 2001. Expression and localization of the multidrug resistance proteins MRP2 and MRP3 in human gallbladder epithelia. *Gastroenterology*, 121(5), pp.1203–1208.
- Russell, D.W., 2009. Fifty years of advances in bile acid synthesis and metabolism. *Journal of Lipid Research*, 50(Supplement), pp.S120–S125.
- Russell, D.W., 2003. The Enzymes, Regulation, and Genetics of Bile Acid Synthesis. *Annual Review of Biochemistry*, 72(1), pp.137–174.
- Sandusky, G.E. et al., 2002. Expression of multidrug resistance-associated protein 2 (MRP2) in normal human tissues and carcinomas using tissue microarrays. *Histopathology*, 41(1), pp.65–74.
- Scheffer, G.L. et al., 2002. Tissue distribution and induction of human multidrug resistant protein 3. *Laboratory investigation; a journal of technical methods and pathology*, 82(2), pp.193–201.
- Von Schulthess, G.K. et al., 2013. Clinical positron emission tomography/magnetic resonance imaging applications. *Seminars in Nuclear Medicine*, 43(1), pp.3–10.
- Setchell, K.D. et al., 1988. Hepatic bile acid metabolism during early development revealed from the analysis of human fetal gallbladder bile. *J. Biol. Chem.*, 263(32), pp.16637–16644.
- Shukla, A. & Kumar, U., 2006. Positron emission tomography: an overview. *journal of medical physics*, 31(1), pp.13–21.
- Si-Tayeb, K., Lemaigre, F.P. & Duncan, S.A., 2010. Organogenesis and Development of the Liver. *Developmental Cell*, 18(2), pp.175–189.
- Slocum, M. et al., 1992. Absence of intestinal bile promotes bacterial translocation. *The American Surgeon*, 58(3), pp.305–310.

- Smith, L.P. et al., 2009. The bile acid synthesis pathway is present and functional in the human ovary. *PLoS ONE*, 4(10), pp.1–6.
- Stamp, D. & Jenkins, G., 2008. An Overview of Bile-Acid Synthesis, Chemistry and Function. *Bile Acids*, (Issues in Toxicology: Bile acids: toxicology and bioactivity), pp.1–13.
- Staudinger, J.L. et al., 2001. The nuclear receptor PXR is a lithocholic acid sensor that protects against liver toxicity. *Proceedings of the National Academy of Sciences*, 98(6), pp.3369–3374.
- Stieger, B., 2011. *Handbook of Experimental Pharmacology vol 201: The Role of the Sodium-Taurocholate Cotransporting Polypeptide (NTCP) and of the Bile Salt Export Pump (BSEP) in Physiology and Pathophysiology of Bile Formation*
- Strijkmans, K., 2001. The isochronous cyclotron: Principles and recent developments. *Computerized Medical Imaging and Graphics*, 25(2), pp.69–78.
- Svadberg, A., 2012. *Nucleophilic Substitution Reactions for Positron Emission Tomography ; Factors Influencing the Reactivity of [18F] Fluoride*.
- Thakkar, N., Slizgi, J.R. & Brouwer, K.L.R., 2017. Effect of Liver Disease on Hepatic Transporter Expression and Function. *Journal of Pharmaceutical Sciences*, 106(9), pp.2282–2294.
- Tian, J., 2012. *Molecular Imaging: Fundamentals and Applications*, Springer.
- Tortora, G. & Derrickson, B., 2009. *Principles of anatomy and physiology: vol.2: Maintenance and continuity of the human body*, John Wiley & Sons.
- Trauner, M. & Boyer, J.L., 2003a. Bile Salt Transporters: Molecular Characterization , Function , and Regulation. *Physiol Rev*, 83, pp.633–671.
- Trauner, M. & Boyer, J.L., 2003b. Bile Salt Transporters: Molecular Characterization , Function , and Regulation TRANSPORT. , pp.633–671.
- Treyer, A. & Müsch, A., 2013. Hepatocyte Polarity. *Comprehensive Physiology*, (3), pp.243–287.

- Vaz, F.M. & Ferdinandusse, S., 2017. Bile acid analysis in human disorders of bile acid biosynthesis. *Molecular Aspects of Medicine*, 56, pp.10–24.
- Wake, K., 2006. Hepatic stellate cells: Three-dimensional structure, localization, heterogeneity and development. *Proceedings of the Japan Academy. Series B, Physical and biological sciences*, 82(4), pp.155–64.
- Weissleder, R. et al., 2010. *Molecular Imaging: Principles and Practice*, People's Medical Publishing House-USA.
- Wisse, E. et al., 1996. Structure and function of sinusoidal cells in the liver. *Toxicologic pathology*, 24(1), pp.100–111.
- Xiao, L. & Pan, G., 2017. An important intestinal transporter that regulates the enterohepatic circulation of bile acids and cholesterol homeostasis: The apical sodium-dependent bile acid transporter (SLC10A2/ASBT). *Clinics and Research in Hepatology and Gastroenterology*, 41(5), pp.509–515.
- Yang, X. et al., 2009. Prediction of Biliary Excretion in Rats and Humans Using Molecular Weight and Quantitative Structure–Pharmacokinetic Relationships. *The AAPS Journal*, 11(3), pp.511–525.
- Yanni, S.B. et al., 2010. In Vitro Investigation of the Hepatobiliary Disposition Mechanisms of the Antifungal Agent Micafungin in Humans and Rats. *Drug Metabolism and Disposition* 38 (10): 1848–56.
- Yin, C. & Evason, K., 2013. Hepatic stellate cells in liver development, regeneration, and cancer. *The Journal of Clinical Investigation*, 123(5), pp.1902–1910.

CHAPTER 2:

MOLECULAR IMAGING IN LIVER DISEASE

2.1 Background of focused liver diseases

2.1.1 Drug-induced liver injury (DILI)

2.1.1.1 *General overview of DILI*

As already stated in Chapter 1, the liver is a vital organ for the detoxification of endogenous and exogenous substances. Because of this specific role, the liver can unfortunately also be prone to injury. Drug-induced liver injury (DILI) is a major issue for the pharmaceutical industry and healthcare. It accounts for the majority of acute liver failure, is a prime cause of attrition for new candidate drugs in the drug development process and responsible for drug withdrawal from the market (Ostapowicz et al. 2002; Bernal & Wendon 2013). About 32 % of all drug withdrawals in the period 1975-2007 were due to hepatotoxicity (Stevens & Baker 2009) (Regev 2014).

DILI has a relatively low annual incidence: between 1 in 10 000 and 1 in 100 000 (Licata et al. 2017). Its diagnosis is therefore often missed, and usually relies on exclusion of other more common causes of liver injury. Clinical symptoms of DILI are not specific and may mimic liver diseases such as hepatitis, hepatic steatosis, acute cholangitis and primary biliary cirrhosis. The most common clinical image is acute hepatitis however. The severity degree of DILI symptoms can stretch from moderate elevation of liver function tests (LFTs) to malaise, jaundice, hyperbilirubinemia, pruritus or fulminant liver failure. Treatment of DILI consists primarily of stopping the administration of the causative drug. Irreversible liver damage may be prevented if this is done early and prognosis is good in most cases (Bleibel et al. 2007). Nonetheless, 10 % of DILI patients develop acute liver failure with coagulopathy and encephalopathy, with a need for transplantation in 40 % of the cases or death of the patient (Licata et al. 2017). Chronic liver diseases such as chronic hepatitis and cirrhosis can also develop (Bleibel et al. 2007).

The mechanisms behind DILI are often not fully understood. Most drugs that cause hepatotoxicity, do so idiosyncratically, meaning it is difficult to pinpoint an exact cause or mechanism (Corsini & Bortolini 2013). Prediction of these reactions is therefore not straightforward. It is thought that both genetic (polymorphisms in metabolizing enzymes, drug transporters etc.) and nongenetic factors (disease states, age, pregnancy, other drugs that are taken) could have an influence on idiosyncratic DILI (Roth & Lee 2017).

Contrary to these idiosyncratic adverse reactions, some drugs have a distinct hepatotoxic mechanism that has been elucidated. The most well-known example is probably the analgetic acetaminophen (or paracetamol) that is the most common cause of liver failure in the United States and United Kingdom (Figure 2.1) (Bernal & Wendon 2013). The largest amount of an administered acetaminophen dose (> 85 %) is conjugated with sulfate or glucuronic acid and safely excreted from the body. However, acetaminophen can be oxidized to N-acetyl-p-benzoquinone imine (NAPQI) by the hepatocytes' CYP450 enzymes. If NAPQI is not detoxified through glutathione (GSH) conjugation, it can bind to proteins and cause hepatotoxicity (Jaeschke et al. 2011).

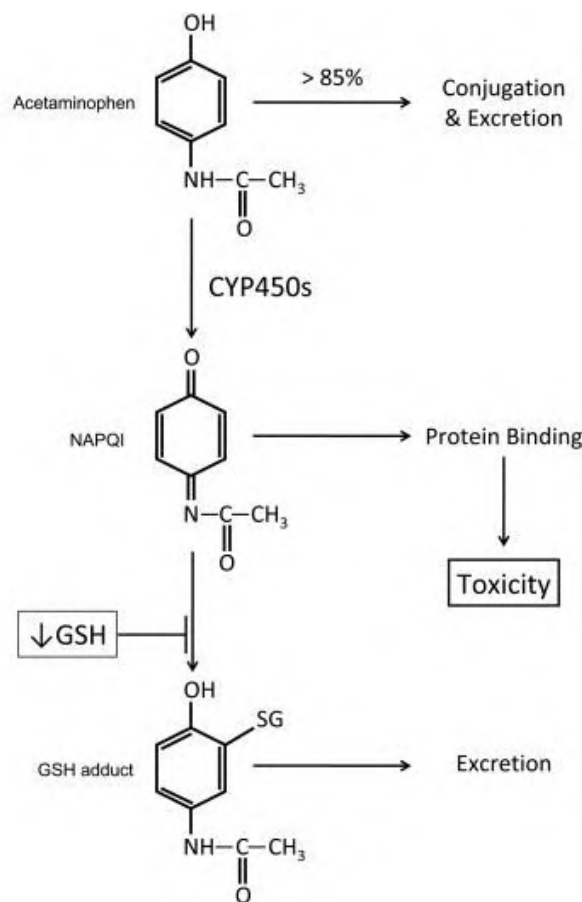


Figure 2.1: Bio-activation of acetaminophen (adapted from Jaeschke et al. 2011).

DILI can be subdivided in three groups, based on the patients' observed LFTs: hepatocellular, cholestatic or a mixed liver toxicity. Drugs can cause damage to the hepatocytes, which is translated to increased serum aminotransferases. Cholestatic liver injury usually results in elevation of alkaline phosphatase and total bilirubin levels in the serum. A mixed form can also occur. More than half of all DILI cases is cholestatic or mixed

hepatocellular/cholestatic in nature (De Valle et al. 2006; de Lima Toccafondo Vieira & Tagliati 2014). These cholestatic injuries account for the most severe cases of DILI (Padda et al. 2011).

2.1.1.2 Drug-induced cholestasis (DIC)

Cholestasis is a disorder that is characterized by a disturbance in bile acid homeostasis. As discussed in Chapter 1, bile acids are steroid derivatives that play an important role in fat digestion due to their detergent-like function. If bile acid homeostasis is disturbed, an accumulation of these molecules in the liver can have a hepatotoxic effect.

Both mechanical or metabolic causes can trigger cholestasis. Mechanical causes may include a tumor, gall stones, or diseases such as primary biliary cirrhosis or primary sclerosing cholangitis that physically block or destroy bile ducts. Formed bile can become trapped in the bile ducts, which can lead to increased bile acid concentrations in the hepatocytes (Zollner & Trauner 2008). Metabolic interference with bile acid homeostasis can occur at the level of bile acid synthesis, detoxification or hepatobiliary transport (de Lima Toccafondo Vieira & Tagliati 2014). Pro-inflammatory cytokines, hormones or drugs (drug-induced cholestasis) can trigger cholestasis (Zollner & Trauner 2008).

Uptake of bile acids in the hepatocyte by OATP or NTCP and their subsequent excretion in bile through BSEP or MRP2 is well regulated, efficient, and prevents the toxic hepatocellular accumulation of bile acids (see Chapter 1). Drugs can have an important influence on this hepatobiliary transport. The mechanism behind it usually involves a direct blockade of the bile acid transport proteins or an indirect alteration of the transporters' expression levels through interaction with the relevant nuclear receptors (Yang et al. 2013). Examples of cholestatic drugs are bosentan, cyclosporin, rifampicin and glibenclamide (de Lima Toccafondo Vieira & Tagliati 2014).

BSEP is the bile acid transport protein that is predominantly responsible for effluxing potentially toxic amounts of bile acids towards the bile ducts. Therefore, drugs (or their metabolites) that are able to inhibit BSEP pose a high risk to trigger drug-induced cholestasis. Examples of drugs that inhibit BSEP are troglitazone, bosentan, cyclosporin A and glibenclamide (Zollner & Trauner 2008; Stieger 2011). MRP2 also contributes to canalicular bile acid efflux, but to a lesser extent. Drug that inhibit MRP2, such as cyclosporin A and

rifampicin, can cause cholestasis and conjugated hyperbilirubinemia (bilirubin is a substrate of MRP2) (Keppler 2011; de Lima Toccafondo Vieira & Tagliati 2014).

Drug inhibition of the OATP or NTCP mediated basolateral uptake, results in prehepatic cholestasis, characterized by elevated serum bile acids (de Lima Toccafondo Vieira & Tagliati 2014; Rodrigues et al. 2014). As OATP is also important for the uptake of a significant amount of drugs and endogenous substrates such as bilirubin, its inhibition can cause increased serum drug levels and hyperbilirubinemia (König 2011; de Lima Toccafondo Vieira & Tagliati 2014).

Several adaptive mechanisms have been uncovered that help the liver cope with the toxic build-up of bile acids during cholestasis (Figure 2.2). The more bile acids present in the hepatocyte, the more stimulation of the pregnane X receptor (PXR), the farnesoid X receptor (FXR) and vitamin D receptor (VDR). These nuclear receptors will respond to the cholestatic conditions by altering the transcription of the bile acid transport proteins, synthesis- and metabolizing enzymes. First of all, OATP and NTCP at the basolateral membrane are downregulated to reduce the reuptake of bile acids. Canalicular efflux by BSEP and MRP2 is preserved. Furthermore, the enzymes responsible for bile acid biosynthesis are downregulated. Upregulation of phase I (hydroxylation) and phase II (sulfation, glucuronidation) metabolizing enzymes will cause faster conversion of bile acids into their more hydrophilic (and less toxic) metabolites. Especially the increased presence of sulfated or glucuronidated bile acids is favorable, because these conjugates undergo renal clearance. Finally, the basolateral efflux transporters MRP3, MRP4 and OST α/β are upregulated dramatically compared to baseline levels. They help shuttle the bile acid excess out of the hepatocyte during cholestatic conditions (Zollner & Trauner 2008; J.G. Marin et al. 2016).

The resulting increase in serum bile acid levels can be counterbalanced by an increased urinary elimination. Renal tubular reuptake of bile acids is reduced by downregulation of ASBT and active tubular secretion is increased by upregulation of MRPs (Zollner & Trauner 2008; J.G. Marin et al. 2016). Renal elimination becomes an important pathway for bile acid detoxification during cholestasis (J.G. Marin et al. 2016).

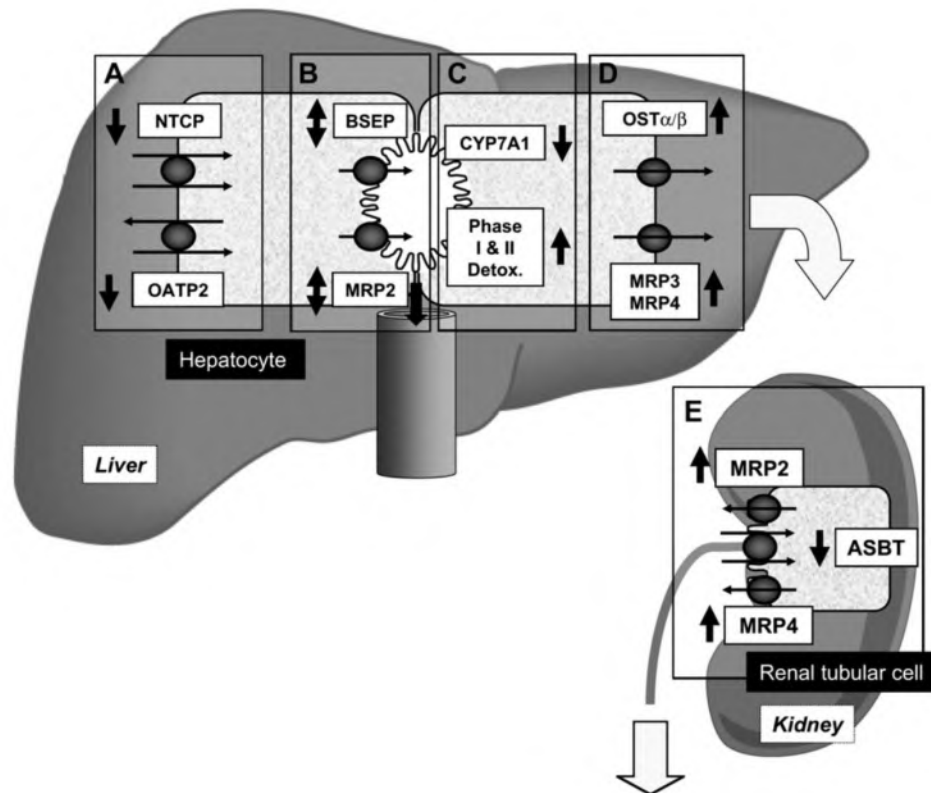


Figure 2.2: Adaptive mechanisms during cholestasis. A: reduced basolateral uptake by downregulation of NTCP and OATP. B: canalicular efflux by BSEP and MRP2 is preserved. C: bile acid biosynthesis is reduced by downregulation of the synthesis enzymes, while phase I and II detoxification enzymes are upregulated. D: upregulation of basolateral efflux by MRP3/4 and OST α/β . E: renal elimination of bile acids is stimulated by downregulation of ASBT and upregulation of MRP2/3/4 (from Zollner & Trauner 2008).

2.1.1.3 Identifying cholestatic drugs

The development of a new drug is a complex, multidisciplinary and expensive process due to its innate hit-and-miss characteristic. It is important to detect drug-induced cholestasis early on in drug development. By faster and more efficient removal of cholestatic drugs from the drug development process, valuable resources and time are saved (Regev 2014). Currently, various *in vitro*, *in silico* and *in vivo* methods are available.

In vitro methods aim to replicate the functionalities of the liver. Because interference with BSEP can cause DIC, membrane vesicles that express BSEP can be of use to very rapidly evaluate a new compound's cholestatic potential. However, recent studies suggest that DIC can not only be triggered by BSEP inhibition alone. Inhibition of other bile acid transporters

such as MRP4 or a complex interplay of multiple mechanisms can also be responsible for DIC (Fukuda et al. 2013; Chatterjee et al. 2014). Sandwich-cultured hepatocytes are therefore ideal to monitor inhibition of both hepatic uptake and biliary efflux by all bile acid transporters involved. Although *in vitro* methods are reproducible, cost-effective and fast, they have the major drawback that they do not mimic the *in vivo* situation completely. Drug transport (and inhibition thereof) in the body for example, is difficult to completely copy to an *in vitro* assay (Brouwer et al. 2013; de Lima Toccafondo Vieira & Tagliati 2014).

Lately, *in silico* methods have gained in importance. They rely on computer modeling algorithms to study the molecular interaction of a certain transporter and its substrates. Various quantitative structure-activity relationship (QSAR) studies have been performed to determine molecular moieties that favor inhibition of BSEP (Saito et al. 2009; Warner et al. 2012; de Lima Toccafondo Vieira & Tagliati 2014). *In silico* methods can aid in the drug discovery process by ruling out high-risk compounds. However, not for every transporter of interest there is QSAR data available. Furthermore, *in silico* methods can guide drug development, but cannot replace *in vitro* and *in vivo* assays that are still mandatory.

Abovementioned drawbacks for *in vitro* and *in silico* methods underline the continuing importance of *in vivo* research to monitor a new drug candidate's cholestatic potential. These studies are invasive, time-consuming and require a lot of lab animals: blood, liver and bile samples have to be acquired, processed and analyzed (Bergman et al. 2010; Sjögren et al. 2014; Shin et al. 2014). The use of non-invasive molecular imaging techniques could shed light on interference with hepatobiliary transport of bile acids *in vivo*.

2.1.2 Cirrhosis

Liver cirrhosis is a chronic liver disease that is characterized histologically by the presence of regenerative nodules that are surrounded by fibrous bands as a response to chronic liver injury. Fibrosis, envelopment or replacement of damaged tissue by collagen fiber scar tissue, is a normal answer of the body to injury. A repeated cycle of liver injury and regeneration however, causes pathological amounts of collagen deposits in liver tissue. Changes in liver microvasculature may hamper exchange between hepatic sinusoids and hepatocytes. Cirrhosis is already an end-stage form of liver fibrosis: the macroscopic anatomy of the liver also changes dramatically (Figure 2.3). As a result, the liver's functional

capacities will deteriorate and portal hypertension can occur due to the increased hepatic resistance. Chronic liver disease can stay asymptomatic for a long time, until clinical decompensation occurs. Symptoms include: ascites, sepsis, variceal bleeding, encephalopathy and non-obstructive jaundice. Cirrhosis is also an important risk-factor for the development of hepatocellular carcinoma (Schuppan & Afdhal 2008; Tsochatzis et al. 2014). In 2010, more than 1 million patients died from the complications of liver cirrhosis (2 % of the global deaths) (Mokdad et al. 2014).



Figure 2.3: Macroscopic anatomy of a cirrhotic liver (from Wiegand & Berg 2013).

The diagnosis can be made by imaging the liver with US, CT or MRI combined with liver function tests. However, early stage cirrhosis is not easy to detect with these conventional imaging modalities (Tsochatzis et al. 2014). Liver stiffness can also be measured by a fibroscan procedure: a soundwave is passed through the liver and its velocity is a measure for liver stiffness (and fibrosis) (Afdhal 2012).

There are several risk factors to develop cirrhosis, of which excessive alcohol consumption is the strongest. Other risk factors include hepatitis virus infections, drug-induced liver injuries and diseases such as auto-immune hepatitis, primary biliary cirrhosis, primary sclerosing cholangitis and non-alcoholic fatty liver disease (NAFLD) (Blachier et al. 2013). Especially NAFLD poses a significant threat to public health, as it has taken up endemic proportions in the western world (approx. 20-30 % of the population!) (Preiss & Sattar 2008). NAFLD is characterized by an increased accumulation of liver fat. It is strongly associated with obesity and metabolic syndrome. If it is left unchecked, NAFLD can progress to non-alcoholic steatohepatitis (NASH) and eventually liver cirrhosis (Michelotti et al. 2013).

Early-stage cirrhosis can be halted or sometimes even reversed by providing the suitable treatment and avoiding further harm to the liver, such as alcohol abstinence in case of alcoholic cirrhosis, antiviral therapy for cirrhosis caused by hepatitis viruses and immune

suppression in auto-immune hepatitis (Wiegand & Berg 2013). Prognosis depends on the underlying cause of cirrhosis and if liver decompensation is already present. If the liver is already decompensated, mortality can be as high as 85 % over 5 years if no liver transplantation is possible. The Child-Pugh-Turcotte (CPT) classification can predict survival rates of cirrhotic patients based on bilirubin and albumin levels in blood, bleeding time (international normalized ratio/INR) and the presence of ascites or hepatic encephalopathy (Schuppan & Afdhal 2008).

2.1.3 Hepatocellular carcinoma (HCC)

Hepatocellular carcinoma (HCC) is the most prevalent primary liver malignancy. It is ranked as the sixth most common cancer and is the third leading cause of cancer death worldwide. The pathogenesis of HCC is complex and involves several phenomena such as hepatocyte necrosis and regeneration, fibrosis, and inflammatory damage (Balogh et al. 2016; Forner et al. 2018). Chronic liver diseases and cirrhosis due to hepatitis B/C or excessive alcohol consumption are the most important risk factors for the development of HCC (Sanyal et al. 2010).

Liver patients that are at risk of HCC development, can be screened for mass formation on ultrasound. Nodules detected on US that are smaller than 1 cm are very hard to diagnose as HCC with the current techniques. Even if it was possible, overdiagnosis of nodules could occur that can cause more harm than good. Nodules larger than 1 cm can be confidently diagnosed as HCC with contrast-enhanced CT or MRI. HCC lesions are characterized by an intense contrast uptake in the arterial phase and a consequent contrast washout during the venous phase. A biopsy can be taken if the imaging results are not conclusive (Forner et al. 2018).

Prognosis should not only bear in mind the tumor stage, but also the remaining liver function in patients that suffer from liver disease. The Barcelona Clinic Liver Cancer (BCLC) classification system is the most commonly used staging tool for HCC. It classifies patients into a very early, early, intermediate, advanced or terminal stage, based on the amount of tumor nodules, their size and remaining liver function. The patient's classification determines the estimation of survival time and proposed treatments such as ablation, resection, transplantation, chemoembolization or systemic therapy (Forner et al. 2018).

2.2 Molecular imaging of hepatobiliary function

The liver plays a vital part in maintaining physiological homeostasis by its synthetic, storage and metabolizing function. An accurate determination of liver functionality in a healthy state and especially during disease is therefore of great importance. To that end, a whole spectrum of classic liver function tests (LFTs) is available by determining concentrations of liver substrates and enzymes in blood. Expanding these LFTs with hepatobiliary molecular imaging techniques can have significant advantages (Keiding & Sorensen 2012; Geisel et al. 2015):

- Molecular imaging can add a spatial component to the liver's function, making it possible to determine regional alterations in liver function.
- Specialized molecular imaging probes can help understand, detect and follow-up on liver disease processes at a molecular level. Anatomical imaging modalities such as ultrasound (US), Computed Tomography (CT) or Magnetic Resonance Imaging (MRI) can miss liver lesions or mild bile duct obstructions, which molecular imaging is able to detect.
- Interference of drugs with liver transporters (such as the bile acid transporters) can be detected during drug development.
- Molecular imaging is superbly suited to provide an estimation of post-operative remnant liver function of patients that underwent liver resection. Nowadays, post-operative liver function (future liver remnant; FLR) is usually estimated by determining the pre-operative liver volume on CT or MRI. However, this liver volume is not necessarily completely functional, especially in liver disease patients. This poses an important risk of triggering liver failure after resection due to insufficient functional liver volume.

An overview of hepatobiliary molecular imaging probes for MRI, Single Photon Emission Computed Tomography (SPECT) and Positron Emission Tomography (PET) is given below.

2.2.1 MRI contrast agents

Magnetic resonance imaging (MRI) is an imaging modality that provides excellent anatomical resolution and soft tissue contrast. Consequently, liver imaging with MRI has become the clinical reference standard. Aided with hepatocyte-specific contrast agents, MRI can offer the clinician both anatomical and functional hepatobiliary information (Frydrychowicz et al. 2012).

The most commonly used MRI hepatobiliary contrast agents are gadolinium based. After their intravenous administration, they can diffuse into the extracellular space of the liver, allowing hepatic arterial and portal venous phase imaging. They can then enter functional hepatocytes through active transport mechanisms, followed by active biliary excretion. Differences in arterial phase, portal venous phase or hepatic phase MRI enhancement can help detect and characterize different liver lesions such as cysts, adenoma, hemangioma, metastases, HCC etc. (Figure 2.4) (Ringe et al. 2010; Frydrychowicz et al. 2012; Geisel et al. 2015).



Figure 2.4: Contrast-enhanced MRI images of a patient with a liver lesion (arrowhead).

Contrast-enhancement in the arterial phase, fast washout in the delayed phase and no uptake in the hepatobiliary phase is characteristic for a HCC lesion

(adapted from Francisco et al. 2014).

The current available gadolinium-based contrast agents (GBCAs) for hepatobiliary imaging are gadobenate dimeglumine (Gd-BOPTA; MultiHance®) and gadoxetic acid (Gd-EOB-DTPA; Primovist®) (Figure 2.5). The pharmacokinetics of these two GBCAs differ significantly. Approximately 50 % of the administered dose of gadoxetic acid is cleared hepatobiliary, whereas this is only 3-5 % for gadobenate dimeglumine. Because it is primarily cleared renally, gadobenate dimeglumine has to be administered in a larger dose than

gadoteric acid. The different pharmacokinetics also have an effect on the optimal scanning time and the length of hepatobiliary contrast enhancement, which is superior for gadoteric acid (Francisco et al. 2014).

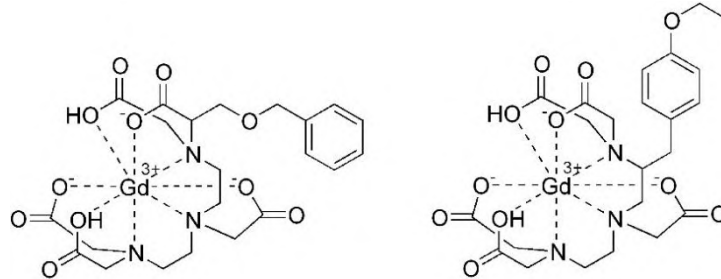


Figure 2.5: Molecular structure of gadobenate (left) and gadoteric acid (right) (adapted from archive.cnx.org).

To generate hepatic contrast, the GBCAs first have to be taken up into the hepatocytes. This happens by the basolateral OATP hepatic uptake transporters. Gadoteric acid is a substrate for OATP1B1 and OATP1B3 (Nassif et al. 2012). Biliary excretion is mediated by MRP2. The knowledge that hepatobiliary transport is mediated by OATPs and MRP2 can be used to employ gadoteric acid MRI as a measure for hepatocyte functionality and biliary excretion efficiency in liver diseases (Frydrychowicz et al. 2012).

As bile acids show very efficient hepatobiliary transport in the healthy liver, attempts have been made to design bile acid-based MRI contrast agents to monitor hepatobiliary transport efficiency. Bile acids have been linked with a bulky gadolinium complex by Anelli et al (Figure 2.6). They differ in degree of biliary clearance and tolerability. No extensive determination of the relevant bile acid transporters involved in their transport was done, although taurocholate appeared to inhibit the hepatobiliary clearance of an investigated compound (Anelli et al. 2004). Fluorinated bile acids for ¹⁹F-MRI have also been developed (Figure 2.7) (Vivian et al. 2013; Vivian et al. 2014). Cholic acid trifluoroacetyl lysine (CA-lys-TFA) and cholylsarcosine trifluoro-N-methyl-acetamide (CA-sar-TFMA) are both potent substrates of ASBT and NTCP and show hepatobiliary transport. CA-sar-TFMA was developed to counter the observed bacterial deconjugation of CA-lys-TFA.

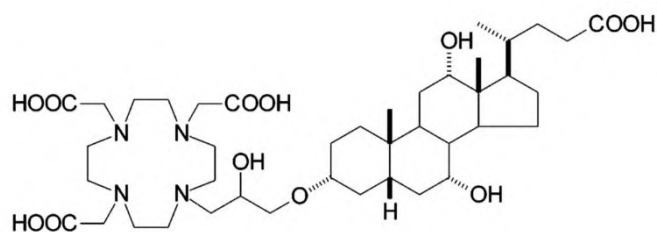


Figure 2.6: Molecular structure of the lead gadolinium bile acid compound by Anelli et al. The bulky complexating structure (gadolinium not shown) is coupled to cholic acid on the 3 α OH function (from Anelli et al. 2004).

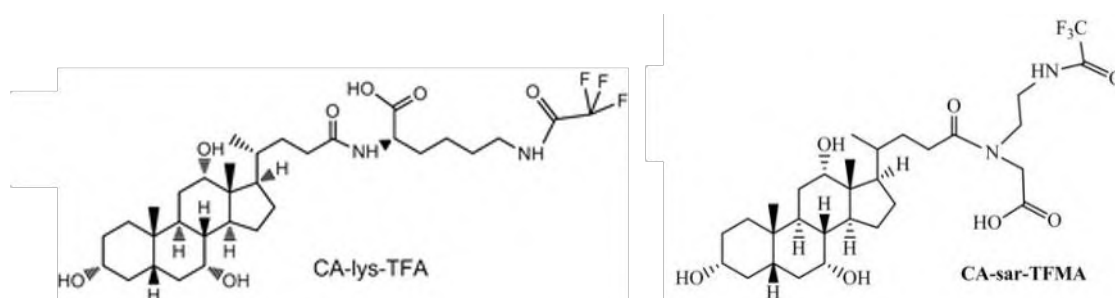


Figure 2.7: Molecular structures of bile acid analogues for ^{19}F MRI imaging (adapted from Vivian et al. 2013; Vivian et al. 2014).

2.2.2 SPECT tracers

Both SPECT and PET are nuclear imaging techniques that rely on administration of trace amounts of radioactively labeled molecular imaging probes (radiotracers). As a result of this high sensitivity, and in contrast to other molecular imaging probes, SPECT and PET radiotracers will generally not disturb the biochemical process under investigation. The most commonly used SPECT tracers for liver function testing are $^{99\text{m}}\text{Tc}$ galactosyl serum albumin ($^{99\text{m}}\text{Tc}$ -GSA) and $^{99\text{m}}\text{Tc}$ -mebrofenin (Bennink et al. 2012).

The $^{99\text{m}}\text{Tc}$ -GSA tracer is composed of human serum albumin, on which a $^{99\text{m}}\text{Tc}$ diethylenetriamine-pentaacetic acid complex and galactosyl groups are linked. After intravenous injection, it binds exclusively on the asialoglycoprotein receptors that are expressed on the hepatocytes' sinusoidal surface. $^{99\text{m}}\text{Tc}$ -GSA is then taken up into the hepatocytes by endocytosis. However, it is not excreted into bile and hence not suited for evaluation of biliary excretion (Hoekstra et al. 2013).

The most commonly used parameters that are determined with $^{99\text{m}}\text{Tc}$ -GSA are the blood clearance ratio and the hepatic extraction efficiency. The ratio of radioactivity in the

heart at 15 and 3 minutes post-injection (HH15) is used as a measure for blood clearance ratio. Hepatic uptake is quantified by the ratio of activity in the liver and liver plus heart, 15 minutes post-injection (LHL15). LHL15 can be measured preoperatively to predict complications after hepatectomy in patients with HCC or chronic liver diseases. Furthermore, cirrhosis patients with a low HH15 or high LHL15 have a higher survival rate (Bennink et al. 2012; Hoekstra et al. 2013; Eo et al. 2014).

^{99m}Tc -mebrofenin is a lidocaine analogue with a high hepatic uptake (approx. 98 %) and a fast biliary excretion (liver excretion half time is approx. 17 minutes) (Frisch & Hofmann 2012) (Figure 2.8). After intravenous injection, ^{99m}Tc -mebrofenin binds to plasma proteins and is transported to the hepatic sinusoids. ^{99m}Tc -mebrofenin is then taken up into the hepatocytes by OATP1B1 and OATP1B3. Excretion in the bile canaliculi is mediated by MRP2 (Ghibellini et al. 2008).

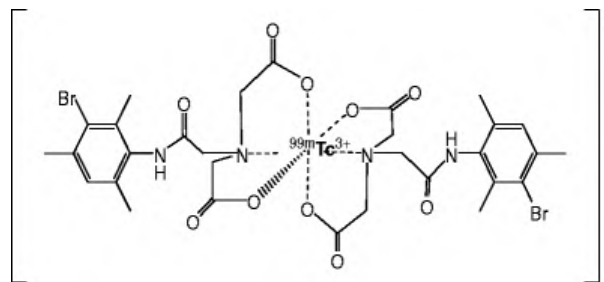


Figure 2.8: Molecular structure of ^{99m}Tc -mebrofenin. The technetium ion is chelated by two lidocaine analogues to form an organic anion (from Ghibellini et al. 2008)

Hepatobiliary function assessment can be done in several ways: visual or fully quantitative using kinetic modelling. However, there are also semi-quantitative metrics available to quantify hepatic function, such as the hepatic extraction fraction, the time it takes to reach maximal radioactivity in the liver (T_{peak}) and the time needed to decrease this peak activity by 50 % ($T_{1/2_{\text{peak}}}$) (Bennink et al. 2012).

Acute cholecystitis is the most common clinical indication for ^{99m}Tc -mebrofenin (Ziessman 2014). Liver or biliary tree disorders will alter the efficient hepatobiliary transport of ^{99m}Tc -mebrofenin. If the tracer does not flow to and accumulate in the gallbladder, the diagnosis of acute cholecystitis can be made with high sensitivity and specificity. The detection of biliary obstruction, especially partial biliary obstruction, is also possible with

^{99m}Tc -mebrofenin. Here, poor tracer clearance from the bile ducts is a characteristic, where the standard examination with ultrasonography may miss small gallstones (Ziessman 2014). Furthermore, ^{99m}Tc -mebrofenin can also serve as a tool to predict post-hepatectomy liver failure in combination with structural MRI (Chapelle et al. 2016).

An extensive preclinical evaluation of ^{99m}Tc -mebrofenin was performed by Neyt et al. 2013. The tracer's ability to detect drug inhibition of the hepatic transport proteins oatp and mrp2 was assessed in mice. It was shown that the tuberculostatic drug rifampicin, a known oatp and mrp2 inhibitor, caused a dose-dependent alteration of ^{99m}Tc -mebrofenin hepatic uptake and biliary excretion. As the rifampicin dose increases, the time to peak of ^{99m}Tc -mebrofenin in the liver increases. More radioactivity is found in the blood compartment as a result of the oatp mediated hepatic uptake. Furthermore, by increasing the rifampicin dose, mrp2 is more potently blocked and ^{99m}Tc -mebrofenin accumulates less in gallbladder and intestines.

Although ^{99m}Tc -mebrofenin offers drug development a valuable tool to measure interference with oatp and mrp2 non-invasively *in vivo*, because the tracer is not a bile acid analogue, no information is gained about the effect of drugs on hepatobiliary transport of endogenous bile acids. For that reason, ^{99m}Tc labeled bile acids were developed and evaluated in mice (Neyt et al. 2016). Cholic (CA) and chenodeoxycholic acid (CDCA) were conjugated with a ^{99m}Tc diethylene triamine penta-acetic acid (^{99m}Tc -DTPA) complex on their carboxyl acid terminus to form [^{99m}Tc]-DTPA-CA and [^{99m}Tc]-DTPA-CDCA, respectively (Figure 2.9). These tracers are substrates of the basolateral transporters OATP1B1 and OATP1B3, but not of NTCP. Canalicular efflux is mediated by MRP2 and not by BSEP. Both [^{99m}Tc]-DTPA-CA and [^{99m}Tc]-DTPA-CDCA showed hepatobiliary clearance *in vivo*, but some renal clearance could be observed. Significant alterations in hepatobiliary transport efficiency were observed in mice dosed with rifampicin. Abovementioned findings can be of interest to detect drug interference with hepatobiliary transport, however, [^{99m}Tc]-DTPA-CA and [^{99m}Tc]-DTPA-CDCA only partly resemble characteristics of endogenous bile acids. Endogenous bile acids show almost exclusively hepatobiliary clearance and are predominantly transported by NTCP and BSEP, and to a lesser extent by OATP and MRP2. The addition of a bulky [^{99m}Tc]-DTPA complex on the carboxylic acid functional group of CA and CDCA is presumably detrimental for substrate recognition by NTCP and BSEP, indicating that the substrate range of these

transporters is rather limited to endogenous bile acids or bile acid derivatives that still retain the anionic moiety on the steroid side chain in their molecular structure (see Chapter 1).

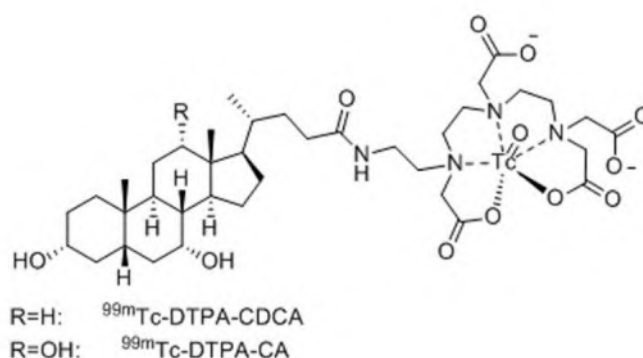


Figure 2.9: Molecular structures of [^{99m}Tc]-DTPA-CA and [^{99m}Tc]-DTPA-CDCA (adapted from Neyt et al. 2016).

2.2.3 PET tracers

Because of its excellent sensitivity, good spatial/temporal resolution and the possibility to develop tracers that closely mimic endogenous substrates, PET is ideally suited for quantification of hepatobiliary transport. Lately, an increased interest in functional imaging of hepatic transporters with PET can be observed (Testa et al. 2015).

2.2.3.1 *Drug derivatives*

Marketed drugs are ideal starting points to develop a PET tracer. Their pharmacokinetics (including the hepatobiliary transporters they might use) have been studied in great detail during the drug development process. A number of drugs or their metabolites have therefore been radiolabeled to study hepatic transporter function (Table 2.1).

The statin-based tracer [^{11}C]rosuvastatin was developed to gain insight in the hepatic concentration and hepatobiliary transport of its non-radiolabeled counterpart (Figure 2.10) (He et al. 2014). Its hepatic uptake is mediated by OATP and NTCP; canalicular efflux by the Breast Cancer Resistance Protein (BCRP). The tracer was evaluated in rats, where it is mainly distributed to the liver. A rifampicin dose had a significant effect on hepatobiliary clearance. Another statin based PET tracer is [^{11}C]dehydropravastatin (Figure 2.10). It was developed to provide an accurate evaluation of oatp and mrp2 activities in hepatobiliary transport

(Shingaki et al. 2013). This can aid in predicting pharmacokinetic properties of drugs. [^{11}C]Dehydropravastatin is distributed to the liver and kidneys *in vivo* in rats. Hepatic uptake is mediated by oatp, biliary excretion by mrp2. Recently, a clinical evaluation with [^{11}C]dehydropravastatin was performed in healthy volunteers that received a rifampicin dose (Kaneko et al. 2018). The drug caused a reduction of [^{11}C]dehydropravastatin's hepatic uptake and canalicular efflux, and consequently, the tracer can be used as a means to monitor OATP and MRP2 function in humans.

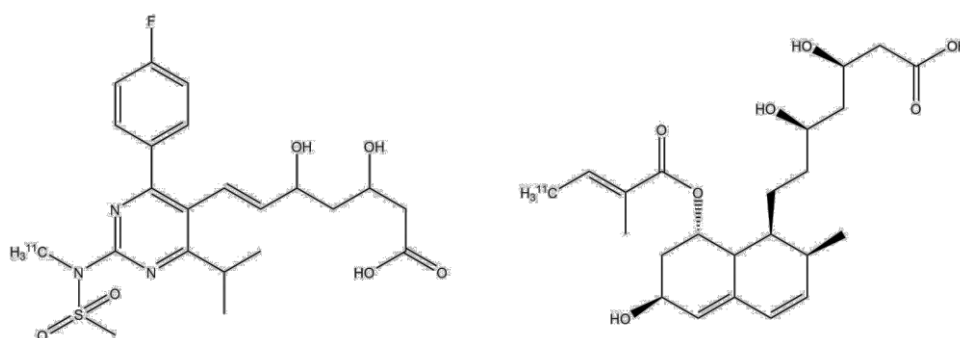


Figure 2.10: Molecular structure of [^{11}C]rosuvastatin (left) and [^{11}C]dehydropravastatin (right) (adapted from He et al. 2014; Shingaki et al. 2013).

Table 2.1: Drug-based PET tracers & transporters they use (adapted from Testa et al. 2015).

PET tracer	Hepatic transporter(s)	Preclinical or clinical?
[^{11}C]Rosuvastatin	OATPs, NTCP, BCRP	Preclinical (rat) and clinical
[^{11}C]Dehydropravastatin	OATPs, MRP2	Preclinical (rat) and clinical
[^{11}C]TIC-Me	OATP1B1, OATP1B3, MRP2	Preclinical (rat) and clinical
[^{11}C]Telmisartan	OATP1B3	Preclinical (rat) and clinical
[^{11}C]Glyburide	OATPs, BCRP, MRPs, P-gp?	Preclinical (mouse, baboon)
[^{11}C]Metformin	OCT1, MATE1	Preclinical (mouse, rat, pig) and clinical

Another ^{11}C labeled tracer that can be used to assess variations in OATP function in humans is (15R)-16-m-tolyl-17,18,19,20-tetranorisocarbacyclin methyl ester ([^{11}C]TIC-Me; Figure 2.11). This tracer is taken up by OATP1B1 and OATP1B3 into the hepatocytes. MRP2 is responsible for canalicular efflux. Kinetic analysis of [^{11}C]TIC-Me's hepatobiliary transport

was performed in healthy human subjects (Takashima et al. 2012). A rifampicin dose significantly reduced the hepatic uptake and biliary excretion of [^{11}C]TIC-Me.

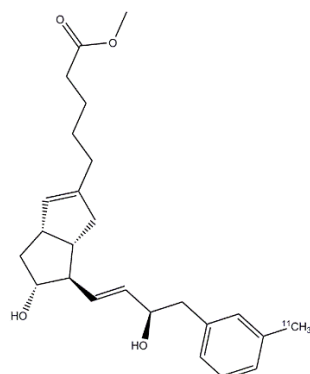


Figure 2.11: Molecular structure of [^{11}C]-TIC-Me (adapted from Takashima et al. 2010).

A ^{11}C radiolabeled telmisartan ([^{11}C]telmisartan) tracer, that is substrate of OATP1B3, was developed to gain information on the whole body pharmacokinetics of telmisartan and assess the OATP1B3 transport function in humans (Figure 2.12) (Shimizu et al. 2012). Hepatobiliary clearance is the dominant clearance pathway for the tracer. Renal clearance was negligible. The safety of human [^{11}C]telmisartan administration was established.

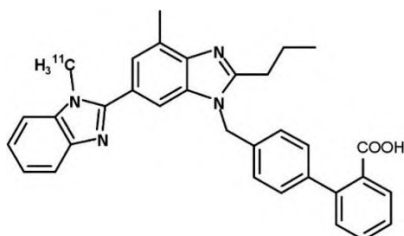


Figure 2.12: Molecular structure of [^{11}C]telmisartan (adapted from Shimizu et al. 2012).

Glyburide (glibenclamide), an oral antidiabetic drug, was radiolabeled with ^{11}C ([^{11}C]glyburide) and evaluated in mice and baboons (Figure 2.13) (Tournier et al. 2013). Glyburide shows hepatobiliary transport: it is taken up into the hepatocytes by OATPs and canalicular export by BCRP, MRPs and possibly also P-glycoprotein (P-gp). PET scans with [^{11}C]glyburide were performed to evaluate the influence of these transporters on glyburide's distribution in the body. The animals were dosed with rifampicin (OATP inhibitor) or cyclosporin (P-gp inhibitor), revealing that OATP transport controls glyburide's distribution in the body, whereas P-gp inhibition had no impact.

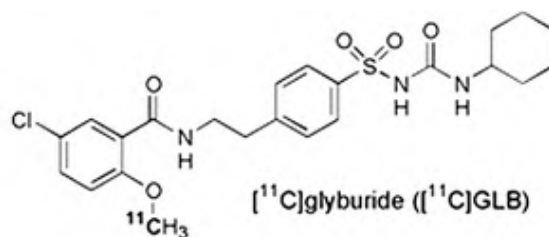


Figure 2.13: Molecular structure of [¹¹C]glyburide (adapted from Tournier et al. 2013).

The oral antidiabetic agent metformin was also radiolabeled with ¹¹C ([¹¹C]metformin) to study hepatobiliary transport and drug-induced alterations thereof (Figure 2.14) (Hume et al. 2013). Its hepatic uptake is mediated by the Organic Cation transporter 1 (OCT1) on the basolateral side of the hepatocytes. Biliary excretion is handled by the Multi-drug And Toxin Extrusion transporter 1 (MATE1). [¹¹C]Metformin was evaluated in healthy mice and mice that were treated with pyrimethamine, a MATE1 inhibitor. Although [¹¹C]metformin shows hepatobiliary transport, renal clearance is the major elimination pathway: uptake of the tracer is highest in kidneys and urinary bladder. The inhibition of MATE1 with pyrimethamine could be detected with [¹¹C]metformin. Recently, [¹¹C]metformin was also evaluated in humans to assess the impact of metformin treatment in patients that have varying metformin transport capacity (Gormsen et al. 2016).

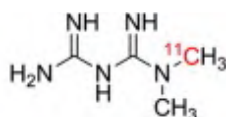


Figure 2.14: Molecular structure of [¹¹C]metformin (adapted from Hume et al. 2013).

2.2.3.2 Bile acid analogues

Because of their exclusive and efficient hepatobiliary clearance, radiolabeled bile acids should be excellent imaging probes to monitor hepatobiliary transport and alterations thereof. Bile acid tracers should have the same *in vivo* characteristics as the endogenous bile acid pool, making them also ideal functional imaging tools to study cholestasis. Various bile acid PET tracers have already been developed (Testa et al. 2015).

Several ¹¹C labeled bile salts have been developed by the same research group (Figure 2.15). Their aim is to use ¹¹C labeled bile salts for studying normal and pathological hepatic excretory function. Frisch et al. developed [¹¹C]cholylsarcosine, which is prepared by

conjugating cholic acid with a N-[^{11}C]methyl glycine molecule. The resulting [^{11}C]cholylsarcosine was evaluated preclinically in pigs (Frisch et al. 2012). The tracer showed fast hepatic uptake and biliary clearance. There was no uptake of [^{11}C]cholylsarcosine in other organs than liver, gallbladder and intestines. Dosing a pig with taurocholate caused an inhibition of [^{11}C]cholylsarcosine's hepatobiliary transport. Although no *in vitro* research was performed to determine the hepatic transporters that are involved in its transport, [^{11}C]cholylsarcosine seems to share the same transporters as taurocholate, an endogenous bile salt.

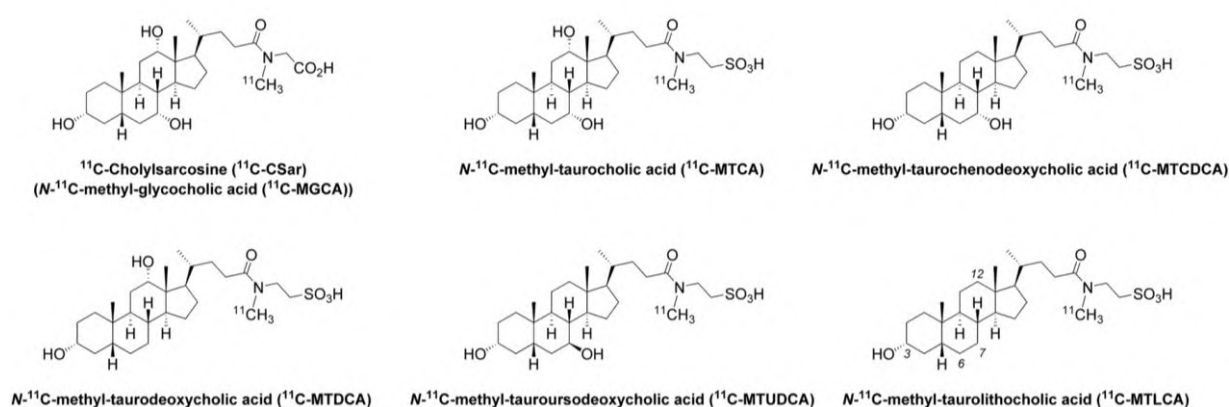


Figure 2.15: Molecular structures of several ^{11}C labeled bile salts
(adapted from Schacht et al. 2016).

Clinical studies with [^{11}C]cholylsarcosine have already been performed (Ørntoft et al. 2017; Ørntoft et al. 2018). Nine healthy subjects and eight patients with cholestasis from different origins (primary biliary cholangitis, primary sclerosing cholangitis, autoimmune hepatitis, alcoholic hepatitis and alcoholic cirrhosis) were examined with [^{11}C]cholylsarcosine. Rate constants for hepatic uptake and excretion in bile were determined by kinetic modelling. Compared to healthy controls, the intrinsic hepatic clearance of [^{11}C]cholylsarcosine was lower for cholestasis patients. The rate constant for biliary excretion was lower in the patient group as well. An increased flux of [^{11}C]cholylsarcosine from the hepatocytes into blood was observed in the cholestasis group. This tracer could be used to reveal whether different liver diseases give rise to different types of cholestasis. Furthermore, [^{11}C]cholylsarcosine may be useful to validate new cholestasis therapeutics.

Several other, taurine conjugated bile acids for ^{11}C PET imaging were also developed and their biodistribution was evaluated in pigs (Schacht et al. 2016). Taurine was radiolabeled with $[\text{C}^{11}]$ methyl iodide to form N- $[\text{C}^{11}]$ methyltaurine. This radiolabeled amino acid was then conjugated with cholic acid, chenodeoxycholic acid, deoxycholic acid, ursodeoxycholic acid or lithocholic acid (Figure 2.15). These tracers show hepatobiliary transport and are not present in urine.

Although abovementioned findings with ^{11}C labeled bile acids are promising, the short half-life of ^{11}C (20 minutes) and challenging ^{11}C radiochemistry may limit its use. Fluorine-18, with its longer half-life (110 minutes) and shorter positron range, can be a better alternative for ^{11}C . For this reason, ^{18}F labeled bile acid analogues have been developed.

Jia et al. developed an ^{18}F labeled bile acid analogue to study the farnesoid-X-receptor (FXR), whose expression is downregulated in liver diseases such as HCC, hepatic adenoma and liver fibrosis (Jia et al. 2014). Hence, their tracer may serve as a tool to detect liver diseases at an early stage. The ^{18}F label is introduced on a chenodeoxycholic acid molecule by a so-called “click reaction”: a 1,3 dipolar cycloaddition of a ^{18}F labeled azide bearing prosthetic group and a terminal alkyne group present on chenodeoxycholic acid (Figure 2.16). However, this modification removes the carboxylic acid moiety of the bile acid, which is critical for recognition by the bile acid transporters (Frisch & Sørensen 2014). So, although this ^{18}F labeled bile acid analogue shows hepatobiliary transport *in vivo* in mice, questions can be raised whether this compound can represent the same transport processes as endogenous bile acids. No *in vitro* research was done to assess this.

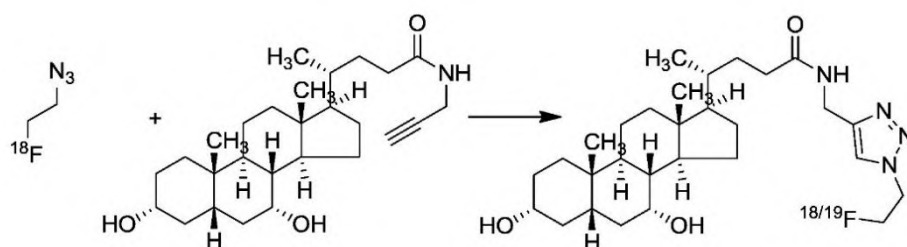


Figure 2.16: “Click reaction” of a ^{18}F labeled azide prosthetic group and a chenodeoxycholic acid analogue that has an alkyne functional group (adapted from Jia et al. 2014).

This click chemistry approach to radiolabel bile acids with ^{18}F was improved by Testa et al. Three different bile acids (cholic, deoxycholic and lithocholic acid) were subjected to the ^{18}F click reaction; but contrary to the study above by Jia et al., the resulting ^{18}F labeled bile acid analogues still contain the important carboxylic acid functional group (Testa et al. 2017). Nevertheless, the introduction of a long 1,2,3, triazole linked fluoroalkyl sidechain on the carboxylic acid terminus still encompasses a substantial addition to the bile acid structure. This might result in altered hepatobiliary transport, compared to endogenous bile acids. Their lead compound is based on lithocholic acid (^{18}F LCATD; Figure 2.17) and was evaluated in rats. It shows exclusive hepatobiliary transport and the authors claim it can be used to study bile acid transporter inhibition.

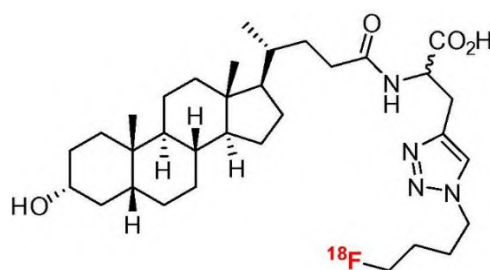


Figure 2.17: Molecular structure of the lithocholic acid based ^{18}F bile acid analogue ^{18}F LCATD (adapted from Testa et al. 2017).

Recently, Frisch et al. developed a ^{18}F labeled bile acid analogue, N-(4- ^{18}F fluorobenzyl)cholyglycine to monitor enterohepatic circulation of bile acids (Frisch et al. 2018) (Figure 2.18). The tracer's molecular structure is significantly expanded with the addition of a fluorobenzyl at the amide moiety. The tracer showed enterohepatic recirculation in rats, yet no *in vitro* research was performed to determine the relevant bile acid transporters the tracer uses.

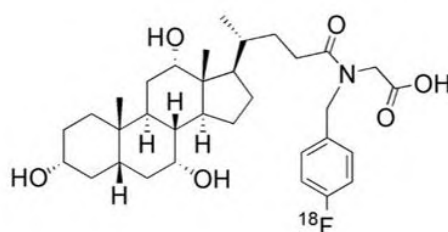


Figure 2.18: Molecular structure of N-(4- ^{18}F fluorobenzyl)cholyglycine (adapted from Frisch et al. 2018)

References

- Afdhal, N.H., 2012. Fibroscan (transient elastography) for the measurement of liver fibrosis. *Gastroenterology and Hepatology*, 8(9), pp.605–607.
- Anelli, P.L. et al., 2004. Conjugates of gadolinium complexes to bile acids as hepatocyte-directed contrast agents for magnetic resonance imaging. *Journal of medicinal chemistry*, 47(14), pp.3629–41.
- Balogh, J. et al., 2016. Hepatocellular carcinoma: a review. *Journal of Hepatocellular Carcinoma*, 3, pp.41–53.
- Bennink, R.J. et al., 2012. Liver function testing with nuclear medicine techniques is coming of age. *Seminars in Nuclear Medicine*, 42(2), pp.124–137.
- Bergman, E. et al., 2010. The effect of acute administration of rifampicin and imatinib on the enterohepatic transport of rosuvastatin in vivo. *Xenobiotica*, 40(8), pp.558–568.
- Bernal, W. & Wendon, J., 2013. Acute Liver Failure. *New England Journal of Medicine*, 369(26), pp.2525–2534.
- Blachier, M. et al., 2013. The burden of liver disease in Europe: A review of available epidemiological data. *Journal of Hepatology*, 58(3), pp.593–608.
- Bleibel, W. et al., 2007. Drug-induced liver injury: Review article. *Digestive Diseases and Sciences*, 52, pp.2463–2471.
- Brouwer, K.L.R. et al., 2013. In vitro methods to support transporter evaluation in drug discovery and development. *Clinical pharmacology and therapeutics*, 94(1), pp.95–112.
- Chapelle, T. et al., 2016. Future remnant liver function estimated by combining liver volumetry on magnetic resonance imaging with total liver function on ^{99m}Tc-mebrofenin hepatobiliary scintigraphy: Can this tool predict post-hepatectomy liver failure? *Hpb*, 18, pp.494–503.
- Chatterjee, S. et al., 2014. Hepatocyte-based in vitro model for assessment of drug-induced cholestasis. *Toxicology and Applied Pharmacology*, 274(1), pp.124–136.

- Corsini, A. & Bortolini, M., 2013. Drug-induced liver injury: the role of drug metabolism and transport. *Journal of clinical pharmacology*, 53(5), pp.463–74.
- Eo, J.S., Paeng, J.C. & Lee, D.S., 2014. Nuclear imaging for functional evaluation and theragnosis in liver malignancy and transplantation. *World Journal of Gastroenterology*, 20(18), pp.5375–5388.
- Forner, A., Reig, M. & Bruix, J., 2018. Hepatocellular carcinoma. *The Lancet*, 391, pp.1301–1314.
- Francisco, F.A. et al., 2014. Hepatobiliary contrast agents: differential diagnosis of focal hepatic lesions, pitfalls and other indications. *Radiol Bras*, 47(5), pp.301–309.
- Frisch, K. et al., 2012. [N-methyl-11C]cholylsarcosine, a novel bile acid tracer for PET/CT of hepatic excretory function: radiosynthesis and proof-of-concept studies in pigs. *Journal of nuclear medicine : official publication, Society of Nuclear Medicine*, 53(5), pp.772–8.
- Frisch, K. et al., 2018. N-(4-[18F]fluorobenzyl) cholyglycine, a novel tracer for PET of enterohepatic circulation of bile acids: Radiosynthesis and proof-of-concept studies in rats. *Nuclear Medicine and Biology*, 61, pp.56–62.
- Frisch, K. & Hofmann, A., 2012. Biliary Secretion. In *Functional Molecular Imaging in Hepatology*. pp. 49–75.
- Frisch, K. & Sørensen, M., 2014. On fluoro-18 labeling of bile acids. *Nuclear medicine and biology*, 41, p.775.
- Frydrychowicz, A. et al., 2012. Hepatobiliary MR imaging with gadolinium-based contrast agents. *Journal of magnetic resonance imaging : JMRI*, 35, pp.492–511.
- Fukuda, Y. et al., 2013. Human Immunodeficiency Virus Protease Inhibitors Interact with ATP Binding Cassette Transporter 4/Multidrug Resistance Protein 4: A Basis for Unanticipated Enhanced Cytotoxicity. *Molecular Pharmacology*, 84(3), pp.361–371.
- Geisel, D. et al., 2015. Imaging-Based Liver Function Tests – Past , Present and Future Bildgestützte Leberfunktionstests – Stand der Technik und zukünftige Entwicklungen. , 187, pp.863–871.

- Ghibellini, G. et al., 2008. Use of tc-99m mebrofenin as a clinical probe to assess altered hepatobiliary transport: integration of in vitro, pharmacokinetic modeling, and simulation studies. *Pharmaceutical research*, 25(8), pp.1851–60.
- Gormsen, L.C. et al., 2016. In Vivo Imaging of Human 11C-Metformin in Peripheral Organs: Dosimetry, Biodistribution, and Kinetic Analyses. *Journal of Nuclear Medicine*, 57(12), pp.1920–1926.
- He, J. et al., 2014. PET imaging of oatp-mediated hepatobiliary transport of [11C] rosuvastatin in the rat. *Molecular Pharmaceutics*, 11, pp.2745–2754.
- Hoekstra, L.T. et al., 2013. Physiological and biochemical basis of clinical liver function tests: a review. *Annals of surgery*, 257(1), pp.27–36.
- Hume, W.E. et al., 2013. The synthesis and biodistribution of [11C]metformin as a PET probe to study hepatobiliary transport mediated by the multi-drug and toxin extrusion transporter 1 (MATE1) in vivo. *Bioorganic and Medicinal Chemistry*, 21(24), pp.7584–7590.
- J.G. Marin, J. et al., 2016. Bile Acids in Physiology, Pathology and Pharmacology. *Current Drug Metabolism*, 17(1), pp.4–29.
- Jaeschke, H. et al., 2011. Current issues with acetaminophen hepatotoxicity - A clinically relevant model to test the efficacy of natural products. *Life Sciences*, 88(17–18), pp.737–745.
- Jia, L. et al., 2014. Synthesis and evaluation of (18)F-labeled bile acid compound: a potential PET imaging agent for FXR-related diseases. *Nuclear medicine and biology*, 41, pp.495–500.
- Kaneko, K.-I. et al., 2018. A clinical quantitative evaluation of hepatobiliary transport of [11C] Dehydropravastatin in humans using positron emission tomography. *Drug Metabolism and Disposition*, 46(5), pp.719–728.
- Keiding, S. & Sorensen, M., 2012. *Functional Molecular Imaging in Hepatology*

- Keppler, D., 2011. *Handbook of Experimental Pharmacology vol 201: Multidrug Resistance Proteins (MRPs, ABCs): Importance for Pathophysiology and Drug Therapy*,
- König, J., 2011. *Handbook of Experimental Pharmacology vol 201: Uptake Transporters of the Human OATP Family*,
- Licata, A. et al., 2017. A focus on epidemiology of drug-induced liver injury: analysis of a prospective cohort. *European Review for Medical and Pharmacological Sciences*, 21(1), pp.112–121.
- de Lima Toccafondo Vieira, M. & Tagliati, C.A., 2014. Hepatobiliary transporters in drug-induced cholestasis: a perspective on the current identifying tools. *Expert opinion on drug metabolism & toxicology*, 10(4), pp.581–97.
- Michelotti, G. a, Machado, M. V & Diehl, A.M., 2013. NAFLD, NASH and liver cancer. *Nature reviews. Gastroenterology & hepatology*, 10(11), pp.656–65.
- Mokdad, A.A. et al., 2014. Liver cirrhosis mortality in 187 countries between 1980 and 2010: A systematic analysis. *BMC Medicine*, 12, pp.1–24.
- Nassif, A. et al., 2012. Visualization of hepatic uptake transporter function in healthy subjects by using gadoxetic acid-enhanced MR imaging. *Radiology*, 264(3), pp.741–50.
- Neyt, S. et al., 2013. In vivo visualization and quantification of (disturbed) Oatp-mediated hepatic uptake and Mrp2-mediated biliary excretion of ^{99m}Tc-mebrofenin in mice. *Journal of Nuclear Medicine*, 54(4), pp.624–630.
- Neyt, S. et al., 2016. Synthesis, in vitro and in vivo small-animal SPECT evaluation of novel technetium labeled bile acid analogues to study (altered) hepatic transporter function. *Nuclear Medicine and Biology*, 43(10).
- Ørntoft, N. et al., 2018. Functional assessment of hepatobiliary secretion by ¹¹C-cholylsarcosine positron emission tomography. *Biochimica et Biophysica Acta - Molecular Basis of Disease*, 1864, pp.1240–1244.

- Ørntoft, N.W. et al., 2017. Hepatobiliary transport kinetics of the conjugated bile acid tracer ¹¹C-CSar quantified in healthy humans and patients by positron emission tomography. *Journal of Hepatology*, 67(2), pp.321–327.
- Ostapowicz, G. et al., 2002. Results of a Prospective Study of Acute Liver Failure at 17 Tertiary Care Centers in the United States. *ann intern med*, 137, pp.947–954.
- Padda, M.S. et al., 2011. Drug-Induced Cholestasis. *Hepatology*, 53, pp.1377–1387.
- Preiss, D. & Sattar, N., 2008. Non-alcoholic fatty liver disease: an overview of prevalence, diagnosis, pathogenesis and treatment considerations. *Clinical science (London, England : 1979)*, 115, pp.141–50.
- Regev, A., 2014. Drug-induced liver injury and drug development: industry perspective. *Seminars in Liver Disease*, 34(2), pp.227–239.
- Ringe, K.I. et al., 2010. Gadoxetate disodium - enhanced MRI of the liver: Part 1, protocol optimization and lesion appearance in the noncirrhotic liver. *American Journal of Roentgenology*, 195, pp.13–28.
- Rodrigues, A.D. et al., 2014. Drug-induced perturbations of the bile acid pool, cholestasis, and hepatotoxicity: Mechanistic considerations beyond the direct inhibition of the bile salt export pump. *Drug Metabolism and Disposition*, 42(4), pp.566–574.
- Roth, A.D. & Lee, M.Y., 2017. Idiosyncratic Drug-Induced Liver Injury (IDILI): Potential Mechanisms and Predictive Assays. *BioMed Research International*, p.23.
- Saito, H. et al., 2009. Technical pitfalls and improvements for high-speed screening and QSAR analysis to predict inhibitors of the human bile salt export pump (ABCB11/BSEP). *The AAPS journal*, 11(3), pp.581–9.
- Sanyal, A.J., Yoon, S.K. & Lencioni, R., 2010. The Etiology of Hepatocellular Carcinoma and Consequences for Treatment. *The Oncologist*, 15, pp.14–22.
- Schacht, A.C. et al., 2016. Radiosynthesis of N-¹¹C-Methyl-Taurine-Conjugated Bile Acids and Biodistribution Studies in Pigs by PET/CT. *Journal of Nuclear Medicine*, 57(4), pp.628–633.

- Schuppan, D. & Afdhal, N.H., 2008. Liver cirrhosis. *The Lancet*, 371(9615), pp.838–851.
- Shimizu, K. et al., 2012. Whole-body distribution and radiation dosimetry of [11C]telmisartan as a biomarker for hepatic organic anion transporting polypeptide (OATP) 1B3. *Nuclear Medicine and Biology*, 39, pp.847–853.
- Shin, D.H. et al., 2014. Hepatic uptake of epirubicin by isolated rat hepatocytes and its biliary excretion after intravenous infusion in rats. *Archives of Pharmacal Research*, 37(12), pp.1599–1606.
- Shingaki, T. et al., 2013. Evaluation of Oatp and Mrp2 activities in hepatobiliary excretion using newly developed positron emission tomography tracer [11C]dehydropravastatin in rats. *The Journal of pharmacology and experimental therapeutics*, 347, pp.193–202.
- Sjögren, E. et al., 2014. Effects of verapamil on the pharmacokinetics and hepatobiliary disposition of fexofenadine in pigs. *European Journal of Pharmaceutical Sciences*, 57(1), pp.214–223.
- Stevens, J.L. & Baker, T.K., 2009. The future of drug safety testing: expanding the view and narrowing the focus. *Drug Discovery Today*, 14(3–4), pp.162–167.
- Stieger, B., 2011. *Handbook of Experimental Pharmacology vol 201: The Role of the Sodium-Taurocholate Cotransporting Polypeptide (NTCP) and of the Bile Salt Export Pump (BSEP) in Physiology and Pathophysiology of Bile Formation*,
- Takashima, T. et al., 2012. PET imaging-based evaluation of hepatobiliary transport in humans with (15R)-11C-TIC-Me. *Journal of Nuclear Medicine*, 53, pp.741–748.
- Takashima, T. et al., 2010. Positron emission tomography studies using (15R)-16-m-[11C]tolyl-17,18,19,20-tetranorisocarbacyclin methyl ester for the evaluation of hepatobiliary transport. *The Journal of pharmacology and experimental therapeutics*, 335(2), pp.314–23.
- Testa, A. et al., 2017. Design, synthesis, in vitro characterization and preliminary imaging studies on fluorinated bile acid derivatives as PET tracers to study hepatic transporters. *Bioorganic and Medicinal Chemistry*, 25, pp.963–976.

- Testa, A. et al., 2015. PET Tracers To Study Clinically Relevant Hepatic Transporters. *Molecular Pharmaceutics*, 12(7), pp.2203–2216.
- Tournier, N. et al., 2013. Effects of selected OATP and/or ABC transporter inhibitors on the brain and whole-body distribution of glyburide. *Aaps J*, 15(4), pp.1082–1090.
- Tsochatzis, E.A., Bosch, J. & Burroughs, A.K., 2014. Liver cirrhosis. *The Lancet*, 383(9930), pp.1749–1761.
- De Valle, M.B. et al., 2006. Drug-induced liver injury in a Swedish University hospital outpatient hepatology clinic. *Alimentary Pharmacology and Therapeutics*, 24, pp.1187–1195.
- Vivian, D. et al., 2013. Design and characterization of a novel fluorinated magnetic resonance imaging agent for functional analysis of bile acid transporter activity. *Pharmaceutical Research*, 30, pp.1240–1251.
- Vivian, D. et al., 2014. Design and evaluation of a novel trifluorinated imaging agent for assessment of bile acid transport using fluorine magnetic resonance imaging. *Journal of Pharmaceutical Sciences*, 103(11), pp.3782–3792.
- Warner, D., Chen, H. & Cantin, L., 2012. Inhibition of Human Bile Salt Export Pump by Drugs: Opportunities Provided by Physicochemical Property Modulation, In-silico Modeling and Structural Modification. *Drug Metabolism and Disposition*, pp.2332–2341.
- Wiegand, J. & Berg, T., 2013. The etiology, diagnosis and prevention of liver cirrhosis: part 1 of a series on liver cirrhosis. *Deutsches Ärzteblatt international*, 110(6), pp.85–91.
- Yang, K. et al., 2013. An Updated Review on Drug-Induced Cholestasis : Mechanisms and Investigation of Physicochemical Properties and Pharmacokinetic Parameters. *Journal of pharmaceutical sciences*, 102(9), pp.3037–3057.
- Ziessman, H. a, 2014. Hepatobiliary Scintigraphy in 2014. *Journal of nuclear medicine : official publication, Society of Nuclear Medicine*, 55, pp.967–975.
- Zollner, G. & Trauner, M., 2008. Mechanisms of cholestasis. *Clinical Liver Disease*, (12), pp.1–26.

CHAPTER 3:

SCOPE AND AIMS

The liver plays a vital role in maintaining homeostasis in the body through essential physiological functions. One of these is the production of bile, a complex fluid containing organic and inorganic solutes. The bulk of the organic constituents is comprised of bile acids, amphiphilic steroid derivatives that are synthesized in the liver and excreted in the small intestine where they help to emulsify fat and solubilize fat-soluble vitamins (Alrefai & Gill 2007). Bile acids are reabsorbed in the small intestine and return to the liver by the portal circulation, where they are taken up in the hepatocytes predominantly by the basolateral uptake transporter Na⁺-dependent Taurocholate Cotransporting Polypeptide (NTCP) and by the Organic Anion Transporting Polypeptide (OATP). Excretion of bile acids towards bile canaliculi is mainly mediated by the Bile Salt Export Pump (BSEP) and by the Multidrug Resistance-associated Protein 2 (MRP2) (Halilbasic et al. 2013). The enterohepatic cycle and hepatobiliary transport of bile acids through these transporters is remarkably efficient, as only 5 % of the total bile acid pool is lost daily in faeces (Vaz & Ferdinandusse 2017).

However, disturbances in hepatobiliary transport of bile acids can occur and lead to a toxic accumulation of bile acids in the liver, termed cholestasis. Cholestasis can be triggered as a result of drug interference with abovementioned bile acid efflux transport proteins (drug-induced cholestasis; DIC). Inhibition of the basolateral bile acid uptake transporters can result in increased bile acid levels in blood (hypercholanemia). It is therefore important to detect this toxicity early on in drug development of new candidate drugs. *In vivo* experiments to monitor a new candidate drug's cholestatic potential are however time-consuming and require invasive sampling of a lot of laboratory animals. Blood, liver and bile samples have to be acquired, processed and analyzed (Bergman et al. 2010; Sjögren et al. 2014; Shin et al. 2014). The use of non-invasive molecular imaging in drug development can help to reduce attrition rates and allow selection of the most promising drug candidate early on in drug development, saving valuable time and resources.

Disturbance in hepatobiliary transport of bile acids cannot only be the result of pharmacological interference with the bile acid transporters, it can also present itself in certain liver diseases that are characterized by altered expression of the bile acid transporters (Thakkar et al. 2017).

In this regard, development of a molecular imaging probe that is transported by these proteins can provide clinicians with a non-invasive imaging tool to assess and follow-up on liver function in liver disease patients. Furthermore, it can add a spatial component to the liver's function, making it possible to determine regional differences.

The aim of this dissertation is to develop ^{18}F labeled bile acid analogues for Positron Emission Tomography (PET) imaging that closely resemble endogenous bile acids in molecular structure, *in vitro* and *in vivo* characteristics. It is hypothesized that these tracers can be used to detect pharmacological interference with the bile acid transporters in preclinical drug development. Secondary to that, we hypothesize that the same tracers can also serve as a functional liver imaging tool in liver disease.

The experimental part of this dissertation is divided into 4 chapters that handle 4 different research questions that have to be answered.

Question 1 (Chapter 4):

Can a set of ^{18}F labeled bile acid analogues be synthesized in sufficient radiochemical yields, that are characterized by minimal modification to the bile acid steroid backbone?

Biochemical processes can be visualized and quantified *in vivo* with PET using radiolabeled substrates of these processes. In order to acquire representative information, it is important to develop PET radiotracers that closely resemble the endogenous substrate of the biochemical pathway to be visualized. In this dissertation, hepatobiliary transport of bile acids will be investigated. Therefore, endogenous bile acids such as cholic-, glycocholic- and chenodeoxycholic acid will be chosen as starting point to develop the ^{18}F labeled bile acids. As fluorine is often used as bioisostere for hydroxyl functions, it was hypothesized that substitution of a bile acid's hydroxyl function with a fluorine atom would not have a major impact on the biological activity of the resulting fluorinated bile acid. Substitution of the 3, 7 and 12 hydroxyl groups of cholic acid will be investigated, as well as substitution of the 3 hydroxyl group of glycocholic acid and chenodeoxycholic acid. Several modifications will have to be made to these molecules before ^{18}F labeling with [^{18}F]fluoride can take place.

Question 2 (Chapter 5):

Are the developed fluorinated bile acid analogues stable and substrates for the relevant hepatobiliary transport proteins *in vitro*?

In this chapter, the stability of the developed ^{18}F labeled bile acid analogues will be determined in its formulation for use, in mouse serum and in presence of primary mouse hepatocytes. Even though fluorine substitution of a bile acid's hydroxyl function is not a major structural change, it is necessary to investigate whether the developed compounds are still substrates of the same hepatobiliary transport proteins that endogenous bile acids use. Therefore, competitive *in vitro* assays will be performed in which a non-radiolabeled (cold) fluorinated bile acid has to displace a tritium labeled model substrate of the transporters. Affinity for the transporters will be determined. Transport by the basolateral uptake transporters NTCP and OATP will be assessed using transfected cell lines. Transport by the canalicular efflux transporters BSEP and MRP2 will be investigated with membrane vesicles.

Question 3 (Chapter 6):

- a) Do the ^{18}F labeled bile acid analogues show hepatobiliary transport in healthy wild-type mice?
- b) Is the inter- and intra-animal variability sufficiently low to assess hepatobiliary transport?
- c) Can disturbed hepatobiliary transport of bile acids be detected *in vivo*?

The developed ^{18}F labeled bile acids will first be evaluated in healthy wild-type mice to assess if they are able to visualize hepatobiliary transport. Quantification of this process is possible by extracting metrics from the tracers' time-activity curves (TACs) in the liver and gallbladder and intestines. A special focus will be put on our lead compound 3β - ^{18}F fluorocholeic acid (3β - ^{18}F FCA) because of its easy precursor synthesis and furthermore, it was historically the first compound to be developed. The inter- and intra-animal variability of 3β - ^{18}F FCA TAC metrics will be assessed. Furthermore, disturbed hepatobiliary transport of bile acids will be monitored with 3β - ^{18}F FCA *in vivo* through the NTCP/OATP and

BSEP/MRP2 transport systems by dosing mice with the OATP(oatp)/MRP2(mrp2) inhibitor rifampicin and the NTCP(ntcp)/BSEP(bsep) inhibitor bosentan.

Question 4 (Chapter 7):

Can ^{18}F labeled bile acid analogues play a role in detection and follow-up of liver diseases?

- a) By detecting direct pharmacological interference with the bile acid transporters.
- b) By providing insight into liver function through altered expression of the bile acid transporters in liver diseases.

Valorization of ^{18}F labeled bile acid analogues as hepatobiliary PET imaging tools will be performed in several mouse models of liver disease. Firstly, the potential to visualize and quantify dose-dependent DIC by direct interference with the bile acid transporters, will be assessed by dosing mice with cyclosporin, a potent ntcp/oatp and bsep/mrp2 inhibitor.

It was hypothesized that ^{18}F labeled bile acid analogues can be used not only to study direct pharmacological interference with ntcp/oatp and bsep/mrp2, but also to monitor (regional) differences in hepatocyte functionality during liver diseases that are characterized by altered expression of these transporters. Therefore, evaluation will take place in several mouse models for liver disease, including acute liver injury, chronic cholangiopathy, non-alcoholic steatohepatitis (NASH), hepatocellular carcinoma (HCC) and fibrosis/cirrhosis.

References

- Alrefai, W. a & Gill, R.K., 2007. Bile acid transporters: structure, function, regulation and pathophysiological implications. *Pharmaceutical research*, 24(10), pp.1803–23.
- Bergman, E. et al., 2010. The effect of acute administration of rifampicin and imatinib on the enterohepatic transport of rosuvastatin in vivo. *Xenobiotica*, 40(8), pp.558–568.
- Halilbasic, E., Claudel, T. & Trauner, M., 2013. Bile acid transporters and regulatory nuclear receptors in the liver and beyond. *Journal of Hepatology*, 58, pp.155–168.
- Shin, D.H. et al., 2014. Hepatic uptake of epirubicin by isolated rat hepatocytes and its biliary excretion after intravenous infusion in rats. *Archives of Pharmacal Research*, 37(12), pp.1599–1606.
- Sjögren, E. et al., 2014. Effects of verapamil on the pharmacokinetics and hepatobiliary disposition of fexofenadine in pigs. *European Journal of Pharmaceutical Sciences*, 57(1), pp.214–223.
- Thakkar, N., Slizgi, J.R. & Brouwer, K.L.R., 2017. Effect of Liver Disease on Hepatic Transporter Expression and Function. *Journal of Pharmaceutical Sciences*, 106(9), pp.2282–2294.
- Vaz, F.M. & Ferdinandusse, S., 2017. Bile acid analysis in human disorders of bile acid biosynthesis. *Molecular Aspects of Medicine*, 56, pp.10–24.

CHAPTER 4:

DEVELOPMENT OF FLUORINATED BILE ACIDS FOR PET IMAGING

This chapter contains parts that have been adapted from:

De Lombaerde S, Kersemans K, Neyt S, Verhoeven J, Vanhove C, De Vos F; *Evaluating Hepatobiliary Transport with ¹⁸F-Labeled Bile Acids: The Effect of Radiolabel Position and Bile Acid Structure on Radiosynthesis and In Vitro and In Vivo Performance*; Contrast Media & Molecular Imaging, Volume 2018, Article ID 6345412, p1-9

De Lombaerde S, Neyt S, Kersemans K, Verhoeven J, Devisscher L, Van Vlierberghe H, et al.; *Synthesis, in vitro and in vivo evaluation of 3β-[¹⁸F]fluorocholeic acid for the detection of drug-induced cholestasis in mice*; PLoS One. 2017;12 (3), p1-14

4.1 Introduction

As described in Chapter 1, bile acids are steroid derivatives that are produced by the hepatocytes of the liver and excreted in bile. These molecules play an important role in micelle formation for lipid digestion and uptake of fat-soluble vitamins in the intestines (Hofmann & Hagey 2008). The majority of bile acids (95 %) is then reabsorbed and transported back to the liver by the portal circulation. Bile acid homeostasis in the liver is maintained by specific bile acid transporters on the hepatocytes. Uptake at the basolateral side relies predominantly on the Na⁺-dependent Taurocholate Cotransporting Polypeptide (NTCP) and the Organic Anion Transporting Polypeptides (OATPs). Once in the hepatocyte, excretion in the bile canaliculi is mainly mediated by the Bile Salt Export Pump (BSEP) (Alrefai & Gill 2007).

However, as revealed in Chapter 2, this highly efficient hepatobiliary transport of bile acids can be disturbed by xenobiotics that inhibit the aforementioned bile acid transporters, or in certain liver diseases such as primary biliary cirrhosis or progressive familial intrahepatic cholestasis (PFIC) (de Lima Toccafondo Vieira & Tagliati 2014; Jüngst et al. 2013; Kubitz et al. 2012). A toxic build-up of bile acids in the hepatocytes, termed cholestasis, can then present itself. Clinical features may consist of nausea, abdominal pain, jaundice and pruritus (Padda et al. 2011). An accurate *in vivo* determination of bile acid transport efficiency can therefore be valuable for detection or evaluation of liver disease in both drug-development and clinic.

To visualize physiological processes on a molecular level *in vivo*, Positron Emission Tomography (PET) is an excellent imaging modality. The possibility for close resemblance of the PET-radiotracer and the endogenous substrate under investigation gives this imaging technique an important asset (Miller et al. 2008). As described in Chapter 2, a number of studies with ¹¹C or ¹⁸F labeled bile acid PET-tracers have been published recently. Frisch et al. and Schacht et al. evaluated ¹¹C labeled bile acids, conjugated with sarcosine or N-methyl taurine in pigs (Frisch et al. 2012; Schacht et al. 2016). These tracers were able to visualize hepatobiliary transport and can provide valuable information in hepatobiliary diseases, although the short half-life of the ¹¹C isotope limit their use. Several ¹⁸F labeled bile acids were developed to overcome this issue. Jia et al. developed a ¹⁸F labeled bile acid for studying Farnesoid X Receptor (FXR)-related diseases, using a click reaction of 1,3-dipolar

cycloaddition of terminal alkynes and organic azides (Jia et al. 2014). However, this modification removes the terminal carboxylic acid moiety that is critical for recognition by the bile acid transporters (Dong et al. 2015). Testa et al. improved this click chemistry approach by retaining the carboxylic acid functional group (Testa et al. 2017). Recently, Frisch et al. developed a ^{18}F labeled bile acid analogue, using a [^{18}F]fluorobenzyl prosthetic group that reacts with the amide function of cholylsarcosine (Frisch et al. 2018). However, all abovementioned recently developed ^{18}F labeled bile acid analogues contain a substantial addition to the steroid backbone. This might result in altered hepatobiliary transport, compared to endogenous bile acids.

Therefore, the aim of this dissertation was to develop and evaluate ^{18}F labeled bile acids with minor modifications on the endogenous bile acid structure. This tracer can represent endogenous bile acid transport and can be used as imaging probe for preclinical evaluation of drug interference with the hepatic bile acid transporters or bile acid transport efficiency in liver diseases.

In many species, including rodents and humans, cholic acid makes up the larger part of the bile acid spectrum (Hofmann & Hagey 2008). As fluorine is often used as a bioisostere for hydroxyl functions in medicinal chemistry, the idea was formed to substitute the hydroxyl functional groups of cholic acid by a fluorine atom. This relatively minor modification keeps the bile acid steroid nucleus and carboxylic acid functional group intact, which is important for recognition by the bile acid transporters (Dong et al. 2015). Furthermore, the 3α -hydroxyl function is not a prerequisite for recognition by the bile acid transporters, so 3α -hydroxyl substitution was focussed (Baringhaus et al. 1999; González et al. 2014). Several ^{18}F labeled bile acids were conceived based on cholic acid, glycocholic acid and chenodeoxycholic acid. (Figure 4.1).

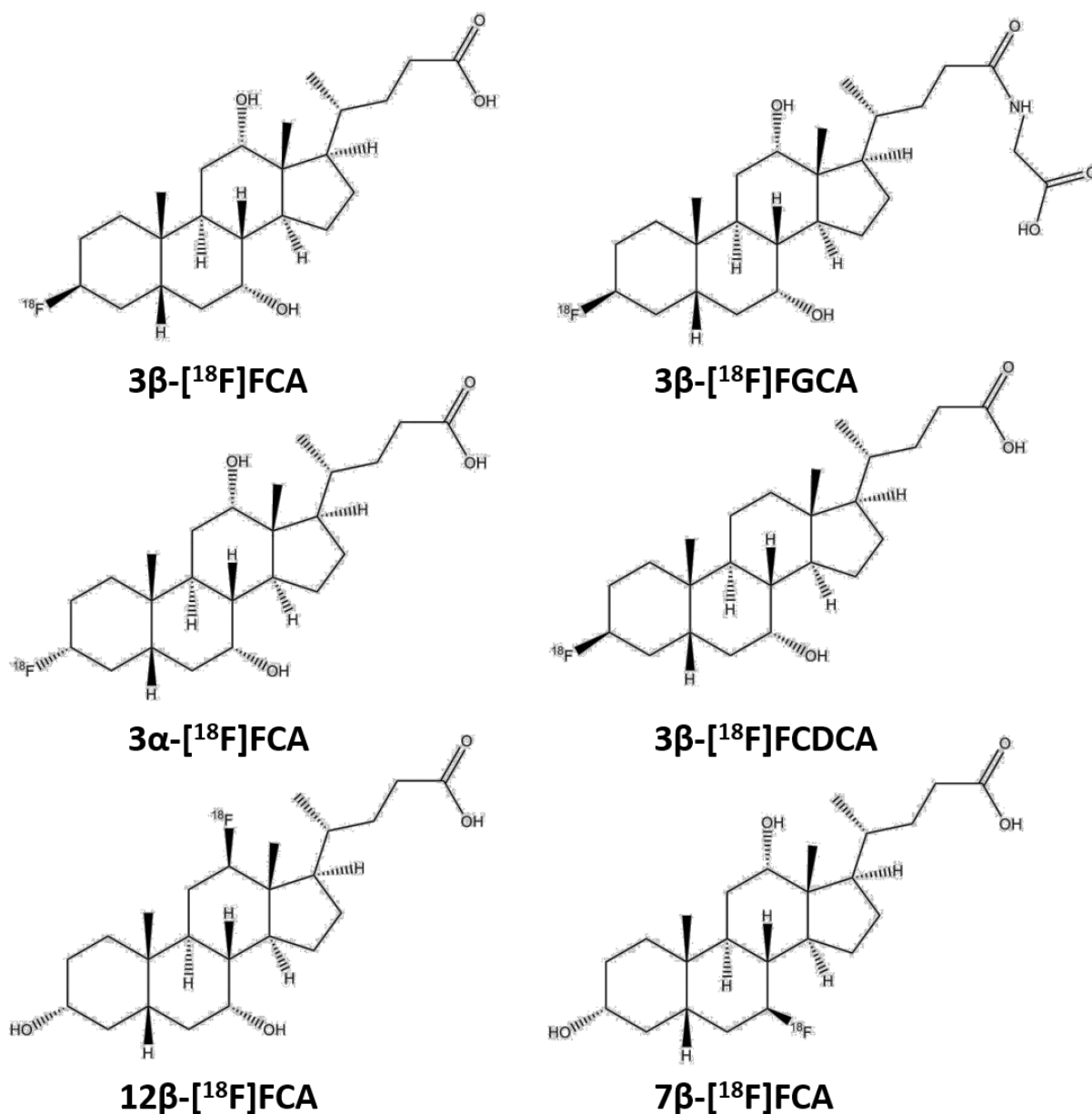


Figure 4.1: Overview of the conceived ^{18}F labeled bile acid analogues in this dissertation. Compounds 3 β -[^{18}F]fluorocholeic acid (3 β -[^{18}F]FCA), 3 α -[^{18}F]fluorocholeic acid (3 α -[^{18}F]FCA), 3 β -[^{18}F]fluorocholedeoxycholeic acid (3 β -[^{18}F]FCDCA), and 3 β -[^{18}F]fluoroglycocholeic acid (3 β -[^{18}F]FGCA) differ in bile acid structure (choleic acid, choledeoxycholeic acid, and glycocholeic acid) or 3 α/β position of the radiolabel. The structures 12 β -[^{18}F]fluorocholeic acid (12 β -[^{18}F]FCA) and 7 β -[^{18}F]fluorocholeic acid (7 β -[^{18}F]FCA) have the same choleic acid structure, but different position of the radiolabel (7 or 12).

The most common ^{18}F radiolabeling strategy is a direct nucleophilic substitution with ^{18}F fluoride ($^{18}\text{F}\text{F}^-$) (Miller et al. 2008). To accommodate this substitution reaction, cholic acid has to first be converted in a suitable precursor for radiolabeling. A good leaving group should be placed on the hydroxyl function that has to be substituted. Furthermore, the other hydroxyl functions and the carboxy function have to be protected, as they can interfere in the substitution reaction. Based on its likely ease of precursor synthesis, 3β - ^{18}F fluorocholeic acid (3β - ^{18}F FCA) was chosen as lead compound (Figure 4.2).

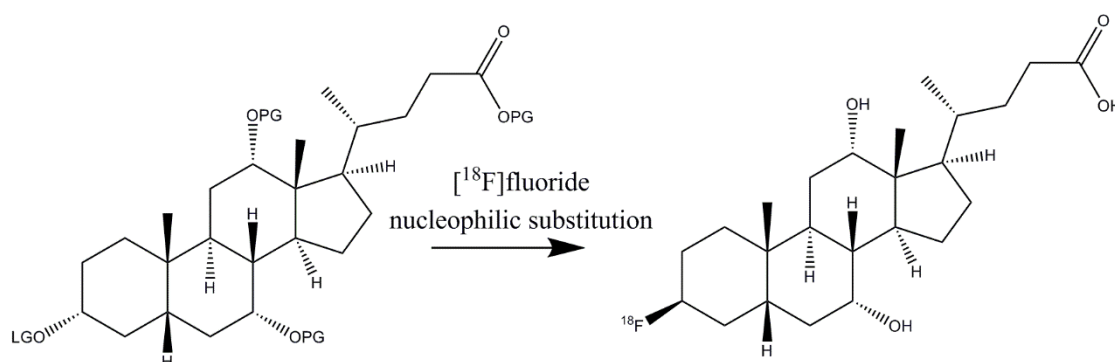


Figure 4.2: Structure of a suitable precursor for radiolabeling to produce 3β - ^{18}F fluorocholeic acid by nucleophilic substitution with ^{18}F fluoride. A leaving group (LG) should be placed on the 3α position, while protecting groups (PG) should be placed on the 7α , 12α hydroxyl functions during the nucleophilic substitution. The carboxylic acid functional group should also be protected.

4.2 Materials and methods

4.2.1 Synthesis of lead compound 3 β -[¹⁸F]fluorocholeic acid

4.2.1.1 *Synthesis of precursor for radiolabeling*

Figure 4.2 displays the molecular structure of the precursor for radiolabeling that should be synthesized to obtain 3 β -[¹⁸F]FCA. The carboxylic acid functional group can be protected by converting it into its methyl ester. As hydroxyl protecting groups, acetyl groups were chosen because of their easy introduction and removal. Furthermore, the reactivity of bile acid hydroxyl functions towards acetylation is not equal and can be used to the chemist's advantage. Acetylation is more efficient in the following order: 3 α -OH > 7 α -OH > 12 α -OH (Kuhajda et al. 2006). When deprotection of the acetyl groups is needed, the 3 α -acetyl group will consequently also be the first group to be cleaved. A leaving group can then be introduced on the free 3 α -OH function. Different leaving groups (mesylate, tosylate, triflate) were tested. The reaction scheme to obtain the precursor for radiosynthesis is presented in Figure 4.3 and the experimental information can be found in the supplementary paragraph 4.6 of this chapter: "experimental section". In short, cholic acid methyl ester (compound **1**) was acetylated to compound **2** (reaction a) and then partially deprotected to compound **3** (reaction b). Mesylation, tosylation or triflation were tested on compound **3** to form compound **4**, **5** or **6** respectively.

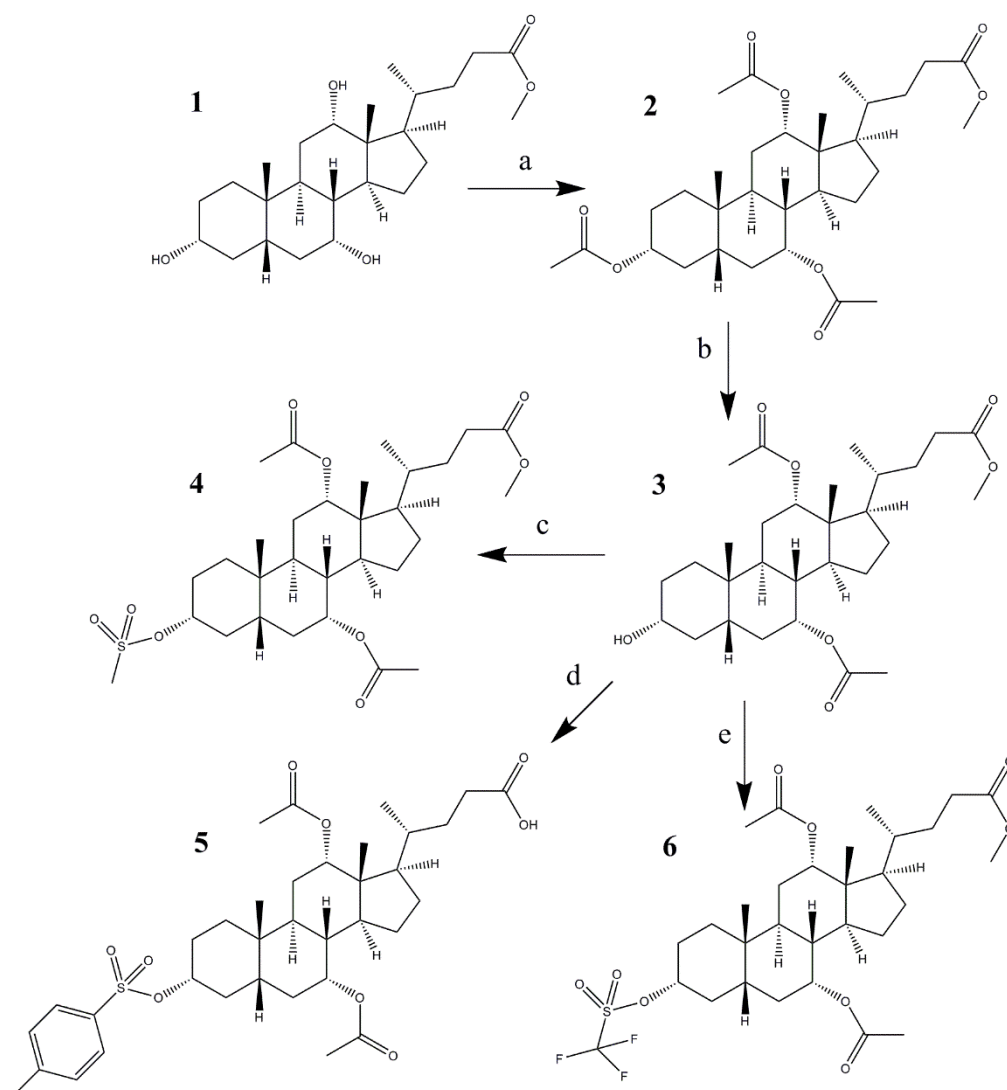


Figure 4.3: Reaction scheme to obtain the precursor for radiosynthesis for 3β -[^{18}F]fluorocholeic acid. a: 4-DMAP, pyridine, Ac_2O , overnight, room temperature (RT); b: AcCl , MeOH, 24 h, 0°C to RT; c: MsCl , pyridine, 6 h, 0°C to RT; d: TsCl , Et_3N , CH_2Cl_2 , 40 h, RT; e: Tf_2O , pyridine, CH_2Cl_2 , RT, 30 min.

4.2.1.2 Synthesis of fluorinated reference compound

A non-radioactive (cold) fluorinated reference compound for 3β -[^{18}F]FCA has to be synthesized. This compound can be used to confirm the identity of its radiolabeled counterpart. Furthermore, it can be employed in *in vitro* assays to examine its affinity as substrate for the bile acid transporters. Introducing a fluorine atom on a molecule can be challenging, and several strategies and reagents are available. Fluorodeoxygenation with diethylaminosulfur trifluoride (DAST) has been commonly used to convert alcohol functional groups into fluorine (Liang et al. 2013). The mechanism of DAST is proposed to be initiated

with the nucleophilic attack of a hydroxyl group on the sulphur atom of DAST. An activated intermediate is formed, on which an *in situ* generated fluoride ion can attack by an S_N2 mechanism. Compound **3** provides an excellent substrate for this strategy, as only the free 3 α -hydroxy group is available for reaction with DAST. The 3 α -hydroxy group is then converted to a 3 β -fluorine atom (Figure 4.4). In a second step, the fluorinated bile acid analogue has to be deprotected. The acetyl protecting groups and the methyl ester can be cleaved in an alkaline environment to provide compound **8**, 3 β -fluorocholeic acid (Figure 4.4).

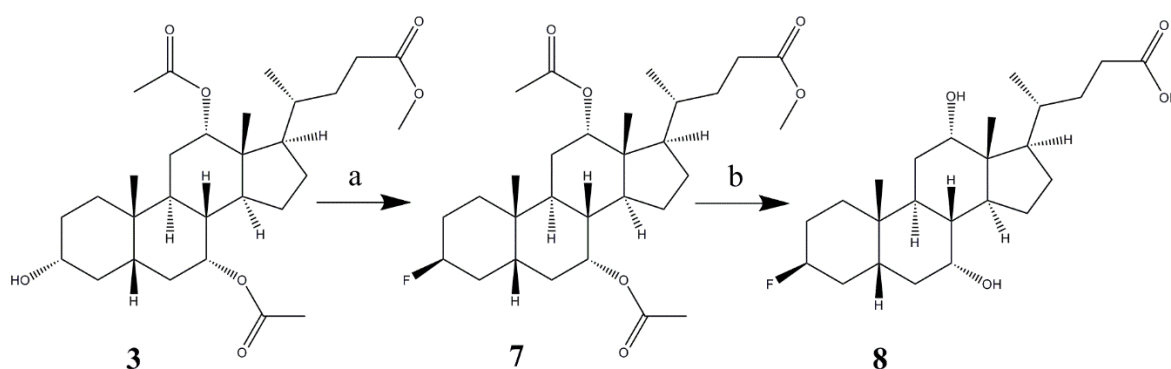


Figure 4.4: Reaction scheme to obtain 3 β -fluorocholeic acid (compound **8**).

a: DAST, CH_2Cl_2 , 3 hours, 0°C to RT; b: NaOH, EtOH, H_2O , 3 hours, reflux.

4.2.1.3 Radiosynthesis of 3 β -[^{18}F]fluorocholeic acid

The radiosynthesis of 3 β -[^{18}F]FCA encompasses two steps (Figure 4.5). In the first step, the precursor for radiosynthesis has to be radiolabeled with a fluorine-18 atom. In the second step, the radiolabeled intermediate has to be deprotected. Finally, 3 β -[^{18}F]FCA is purified from the reaction mixture and prepared in a physiological solution.

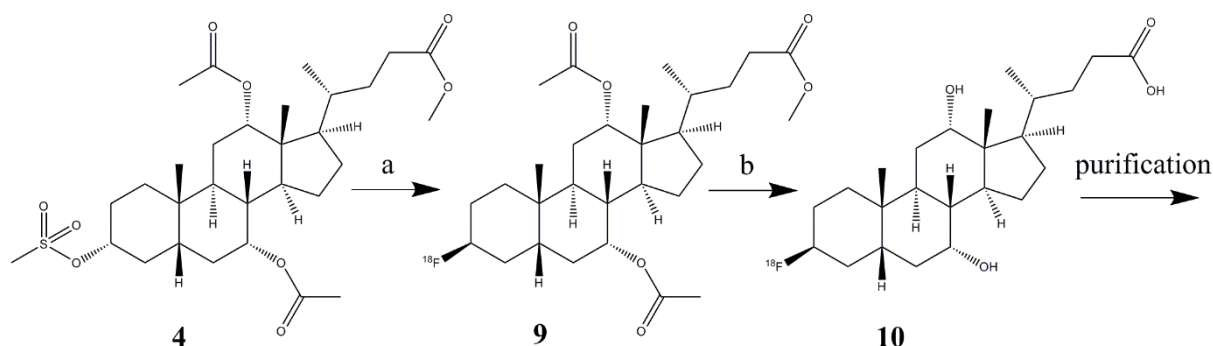


Figure 4.5: Radiosynthesis of 3 β -[^{18}F]fluorocholeic acid. a: [^{18}F]F/ $\text{K}_{222}\text{-K}_2\text{CO}_3$, DMSO; b: NaOH.

Radiolabeling

[¹⁸F]Fluoride was produced by a ¹⁸O(p,n)¹⁸F nuclear reaction with a Cyclone 18/9 cyclotron (IBA). [¹⁸F]Fluoride (approx. 370 MBq) was trapped on a Sep-Pak QMA cartridge (Waters; preconditioned with 5 mL 0.01 M K₂CO₃ and 5 mL ultrapure water) and then eluted in a radiosynthesis vial with 1 mL cryptand-2.2.2./K₂CO₃ solution (0.9 mL acetonitrile (AcN) and 0.1 mL H₂O containing 20 mg cryptand-2.2.2. and 2 mg K₂CO₃ respectively). The solution was azeotropically evaporated to dryness under a gentle nitrogen flow at 100°C, followed by two additional drying steps with 500 µL AcN.

The radiolabeling was examined by variation of three reaction conditions: precursor amount, reaction time and temperature. Precursor compound **4** (1-8 mg) was dissolved in 200 µL anhydrous DMSO and added to azeotropically dried [¹⁸F]fluoride in a radiosynthesis vial. After vigorous shaking, the reaction mixture was heated (80 – 120°C; 5 to 40 minutes). Next, the vial was cooled in an ice bath and samples of the crude reaction mixture were taken to evaluate the ¹⁸F labeling yield (incorporation ratio of fluorinated bile acid on total activity). These yields were determined by radio TLC analysis (silica gel TLC; with 4:1 v/v AcN:H₂O).

Deprotection

To the radiolabeled mixture (see above), 100 µL of 3 M NaOH was added. The deprotection yield was monitored in function of time (5 – 40 minutes) and temperature (room temperature – 120°C) using the same radio TLC conditions as described for radiolabeling.

Purification

After deprotection, the vial was cooled to room temperature, neutralized with HCl and phosphate buffered saline pH 7.4 (PBS). The reaction mixture was purified by semi-preparative HPLC (Grace Econosphere C18 10.0x250 mm, 10 µm; 6 mL/min AcN:H₂O 10:90 v:v ->AcN 100% in 20 minutes as mobile phase; radiodetection (Geiger-Müller tube; Ludlum Measurements Inc)). The desired HPLC-fraction was collected, diluted with 50 mL ultrapure water and loaded onto a Sep-Pak C18 cartridge (Waters; preconditioned with 10 mL EtOH and 10 mL ultrapure water). The cartridge was washed with 10 mL ultrapure water and

eluted with 1 mL EtOH. The solvent was evaporated under a gentle nitrogen flow and 3 β -¹⁸F]FCA was reformulated in 500 μ L phosphate buffered saline (PBS) pH 7.4.

This formulation was subjected to quality control by means of analytical HPLC with radio- and UV detection (205 nm; Waters) using a Grace Alltima C18 (4.6x250 mm; 5 μ m) column and 1 mL/min H₂O:AcN 70:30 v:v as mobile phase. The retention time of 3 β -¹⁸F]FCA was compared to that of a non-radioactive reference compound **8**. Radiochemical purity was determined by abovementioned analytical HPLC and radio-TLC (silica gel TLC; with 10 % MeOH in CH₂Cl₂).

4.2.2 Synthesis of other ^{18}F labeled bile acid analogues

4.2.2.1 Synthesis of precursors for radiolabeling and fluorinated reference compounds

3α - ^{18}F fluorocholeic acid (3α - ^{18}F FCA)

To obtain 3α - ^{18}F FCA, a structure on which the fluorine atom is positioned in the 3α position instead of the 3β position, the precursor for radiosynthesis should contain a 3β -leaving group. Because of the Walden inversion during the $\text{S}_{\text{N}}2$ nucleophilic ^{18}F fluoride attack, the fluorine atom will then be positioned 3α . Compound **1** was therefore first converted into its 3β epimer, compound **12**, by a Mitsunobu esterification. The following reaction steps are analogous to the synthesis of precursor and reference compound of 3β - ^{18}F FCA (Figure 4.6).

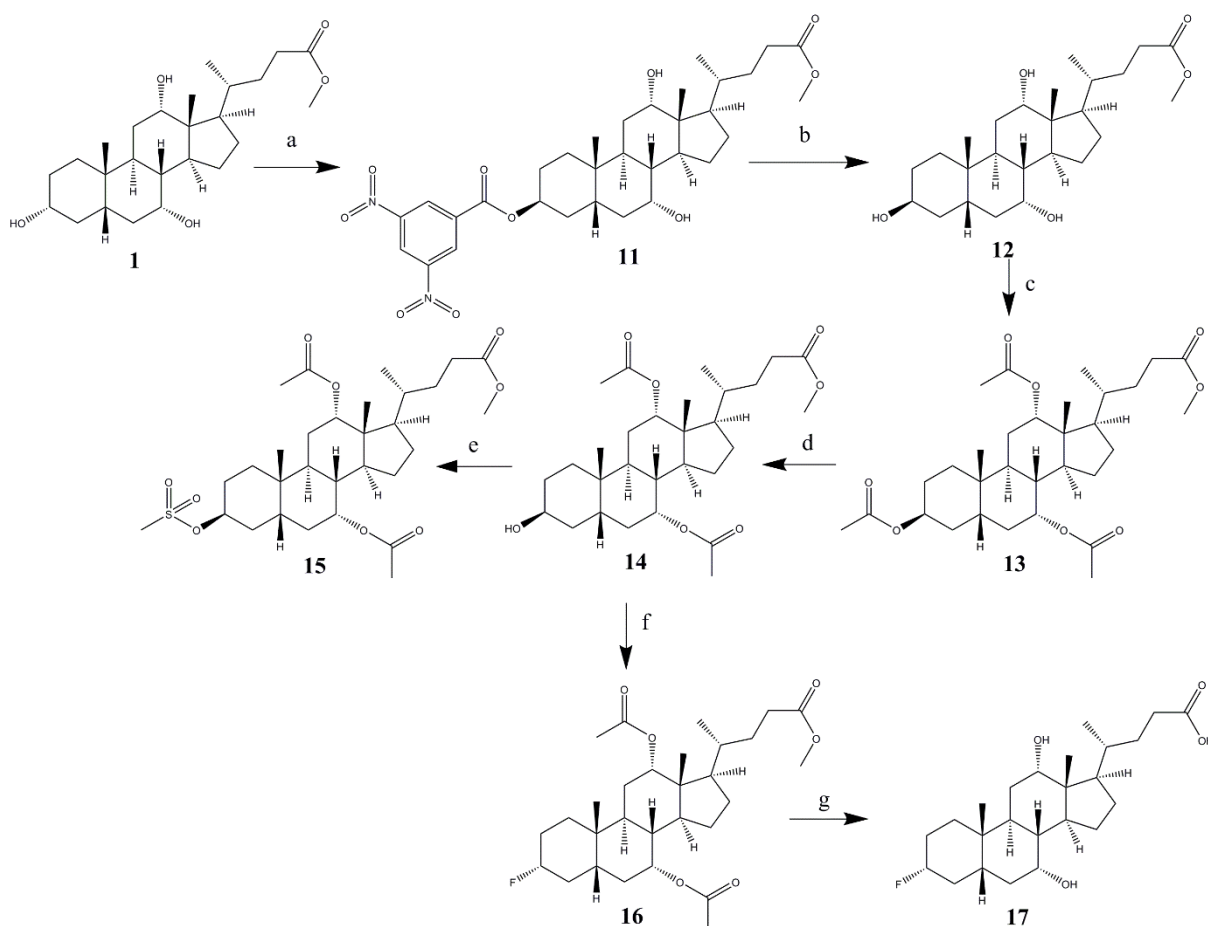


Figure 4.6: Reaction scheme to obtain the precursor for radiosynthesis and reference compound of 3α - ^{18}F FCA. a: 3,5-Dinitrobenzoic acid, PPh_3 , DIAD, THF, 50°C , 48h; b: NaOMe, MeOH, THF, RT, 15 min; c: 4-DMAP, Ac_2O , pyridine, RT, overnight; d: AcCl , MeOH, 0°C -> RT, 32h; e: MsCl , pyridine, 0°C -> RT; f: DAST, CH_2Cl_2 , RT, 15 min; g: KOH , MeOH, reflux, 45 min.

3β-[¹⁸F]fluoroglycocholic acid (3β-[¹⁸F]FGCA)

Compound **18** (cholic acid) was first conjugated with a carboxyl protected glycine group to form compound **19**, which was then further used to obtain the precursor for radiosynthesis (compound **22**) and the 3β-FGCA cold reference product (compound **24**) (Figure 4.7).

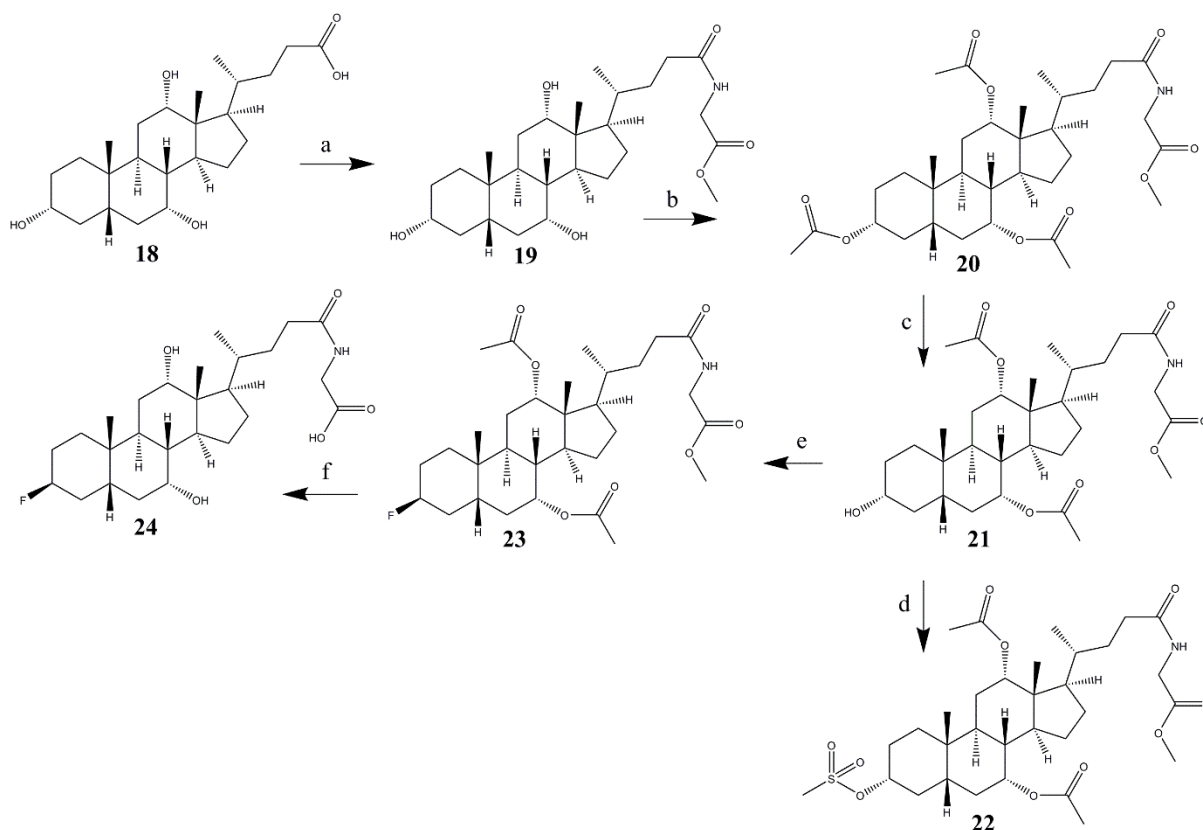


Figure 4.7: Reaction scheme to obtain the precursor for radiosynthesis and reference compound of 3β-[¹⁸F]FGCA. a: glycine methylester, EEDQ, Et₃N, EtOAc, reflux, overnight; b: 4-DMAP, Ac₂O, pyridine, RT, overnight; c: AcCl, MeOH, 0°C → RT, 32h; d: MsCl, pyridine, 0°C → RT; e: DAST, CH₂Cl₂, RT, 15 min; f: KOH, MeOH, reflux, 45 min.

3β-[¹⁸F]fluorochenodeoxycholic acid (3β-[¹⁸F]FCDCA)

The precursor and reference compound of 3β-[¹⁸F]FCDCA was synthesized in the same manner as 3β-[¹⁸F]FCA, but with chenodeoxycholic acid instead of cholic acid methyl ester as starting point (Figure 4.8).

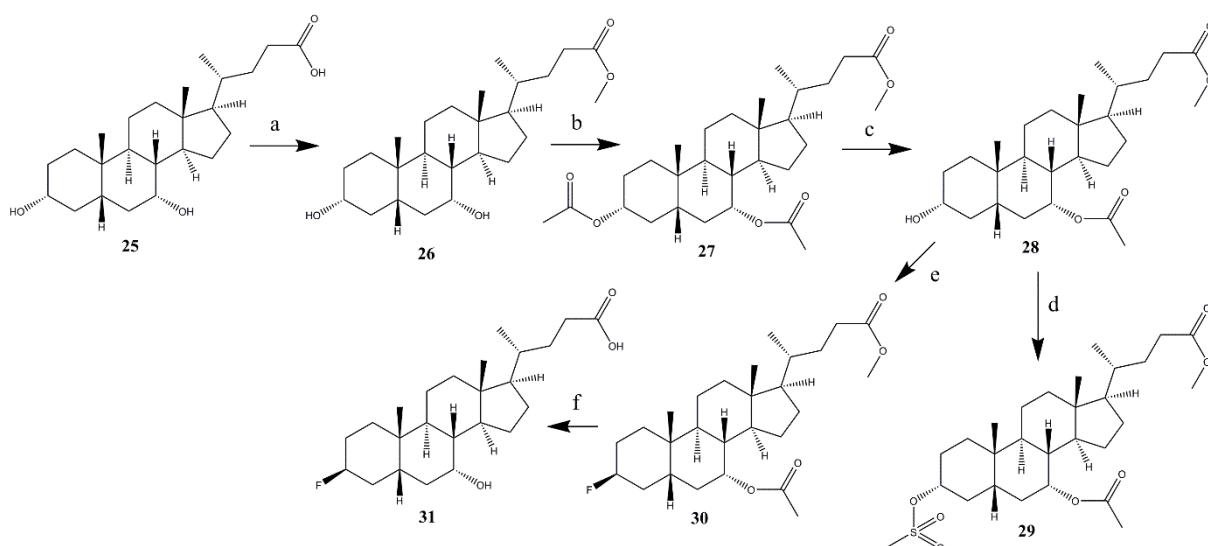


Figure 4.8: Reaction scheme to obtain the precursor for radiosynthesis and reference compound of 3β-[¹⁸F]FCDCA. a: HCl, MeOH, reflux, overnight; b: 4-DMAP, Ac₂O, pyridine, RT, overnight; c: AcCl, MeOH, 0°C → RT, 32h; d: MsCl, pyridine, 0°C → RT; e: DAST, CH₂Cl₂, RT, 15 min; f: KOH, MeOH, reflux, 45 min.

7β-[¹⁸F]fluorocholeic acid (7β-[¹⁸F]FCA)

Introducing a leaving group or fluorine atom on the 7 position of cholic acid is not that straightforward, as it relies on protecting the 3 and 12 hydroxyl function, but not the 7 hydroxyl function. However, the difference in oxidation efficiency of 3, 7 and 12 hydroxyl functional groups can be exploited. The reactivity towards oxidation follows this order: 7 > 12 > 3 (Kuhajda et al. 2006). By first oxidizing compound **18**, cholic acid, to compound **32**, 7-oxo cholic acid, the free 3 and 12 hydroxyl groups can be acetylated (preceded by first converting 7-oxo cholic acid to 7-oxo cholic acid methyl ester (compound **33**). Afterwards, the keto function can be reduced to compound **35** in a stereospecific manner. The leaving group or fluorine atom can then be introduced on the free 7 hydroxyl function (Figure 4.9).

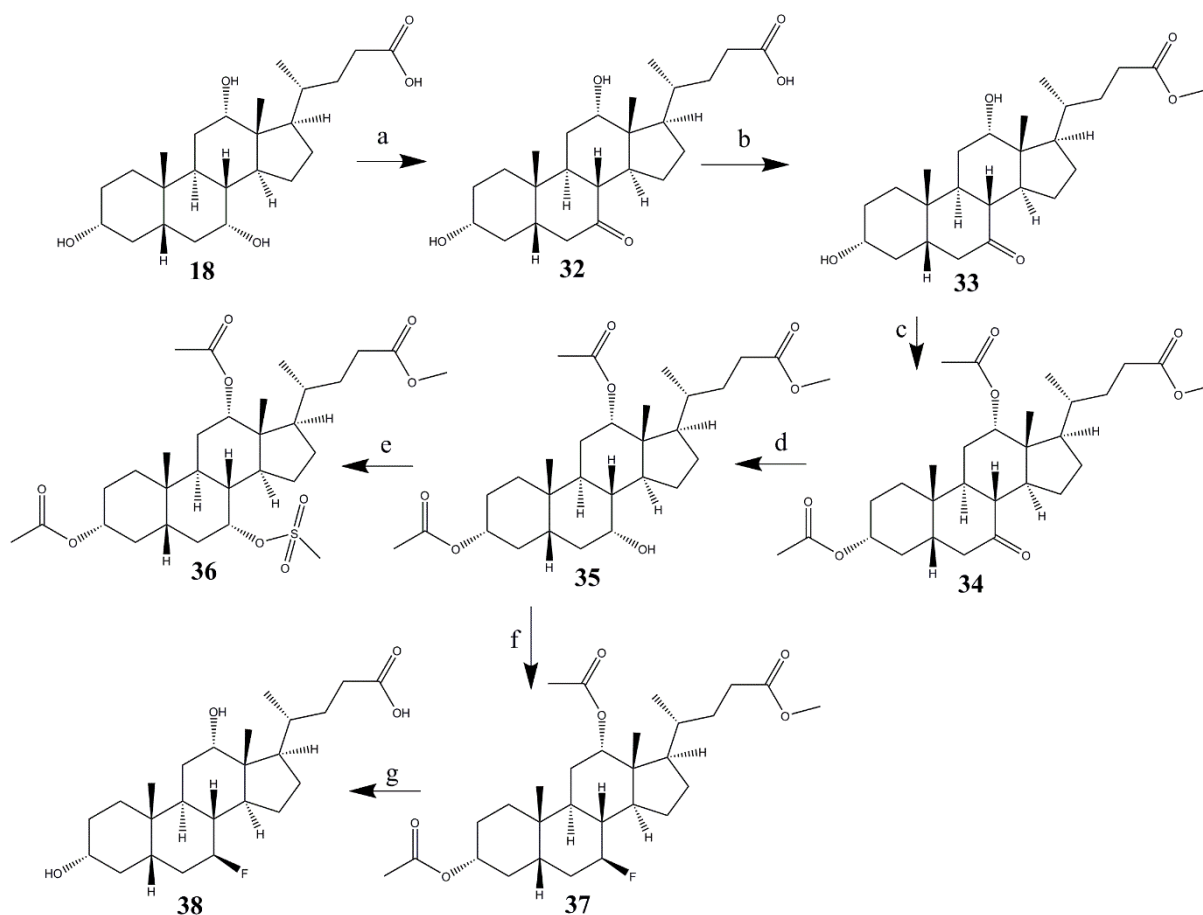


Figure 4.9: Reaction scheme to obtain the precursor for radiosynthesis and reference compound of 7β -[^{18}F]FCA. a: NBS, NaHCO_3 , H_2O , RT, 24h; b: HCl, dimethoxypropane, MeOH, RT, 24h; c: 4-DMAP, Ac_2O , pyridine, RT, overnight; d: NaBH_4 , THF, MeOH, RT, 4h; e: MsCl, pyridine, $0^\circ\text{C} \rightarrow \text{RT}$; f: DAST, CH_2Cl_2 , RT, 15 min; g: KOH, MeOH, reflux, 45 min.

12β -[^{18}F]fluorocholeic acid (12β -[^{18}F]FCA)

The synthesis of precursor and reference compound of 12β -[^{18}F]FCA relied on obtaining a partially protected cholic acid intermediate. The difference in reactivity of the hydroxyl functions towards acetylation ($3 > 7 > 12$) can be exploited to synthesize compound **40**, which still has a free 12 hydroxyl group (Figure 4.10).

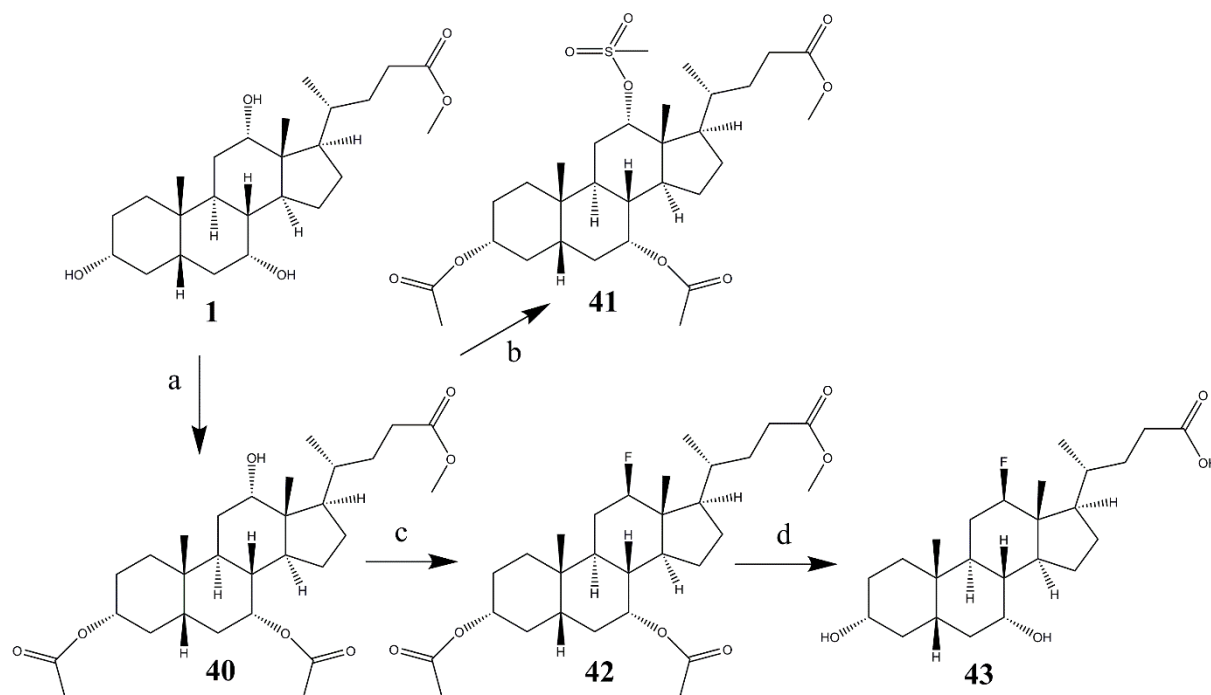


Figure 4.10: Reaction scheme to obtain the precursor for radiosynthesis and reference compound of 12β-[¹⁸F]FCA. a: Ac₂O, toluene, pyridine, RT, overnight; b: MsCl, pyridine, 0°C -> RT; c: DAST, CH₂Cl₂, RT, 15 min; d: KOH, MeOH, reflux, 45 min.

4.2.2.2 Radiosynthesis

Production and work-up of [¹⁸F]fluoride was performed as described in paragraph 4.2.1.3. The precursor for radiosynthesis was dissolved in 200 μL anhydrous DMSO and added to the radiosynthesis vial. A fixed amount (6.84 μmol; 3.4 - 4.4 mg) of precursor for 3α-[¹⁸F]FCA, 7β-[¹⁸F]FCA, 12β-[¹⁸F]FCA, 3β-[¹⁸F]FGCA and 3β-[¹⁸F]FCDCA was used. The vial was sealed, shaken and heated for 20 minutes at 120°C. Afterwards, the vial was cooled and 100 μL 5 M NaOH was added. The mixture was shaken and heated again at 120°C for 10 minutes. After cooling and neutralization of the basic reaction mixture, purification was performed by a semi-preparative HPLC-system (Grace Econosphere C18 10.0 x 250 mm, 10 μm; 6 mL/min 10 % AcN in H₂O -> 100 % AcN in 20 minutes; radiodetection (Ludlum Measurements Inc.)). The desired HPLC-fraction was collected, diluted with 50 mL ultrapure water and loaded on a Sep-Pak C18 Plus short cartridge (preconditioned with 10 mL EtOH and 10 mL ultrapure water). After washing with 10 mL ultrapure water, the ¹⁸F-labeled bile acid was eluted off the column with 1 mL EtOH in a separate vial. This fraction was evaporated under a gentle N₂-flow and heating. Finally, 500 μL phosphate buffered saline was added to reformulate the tracer.

The identity of the tracer was assessed as described earlier (paragraph 4.2.1.3). Radiochemical purity and percentage ^{18}F -labeling of precursor was determined by radio-TLC (silica gel TLC; with 10 % MeOH in CH_2Cl_2 and 4:1 AcN:H $_2$ O respectively).

4.3 Results

4.3.1 Synthesis of lead compound 3β - $[^{18}\text{F}]$ fluorocholeic acid

Compound **4**, the mesylated precursor for radiosynthesis of 3β - $[^{18}\text{F}]$ FCA, was obtained in a total yield of 66.0 %. The introduction of a tosylate leaving group on the free 3α -OH group of compound **3** was unsuccessful. Formation of the triflate precursor was possible, yet the resulting compound **6** proved to be too unstable to reliably use for radiolabeling. Reference compound **8** was obtained in a total yield of 43.9 %.

Several radiolabeling experiments with compound **4** were performed. The effects of precursor amount, reaction time and temperature on radiolabeling yield (^{18}F incorporation on precursor) were determined (Figure 4.11). At least 4 mg of precursor had to be dissolved in 200 μL of DMSO to obtain the largest yield possible. A radiolabeling time of 20 minutes was optimal: no further increase in yield was observed by extending it to 40 minutes. On the contrary, the longer radiolabeling time reduced radiolabeling yield. The temperature had to be at least 100°C to obtain noticeable labeling; the optimal temperature was established at 120°C . By combining the optima for these parameters (4 mg in 200 μL DMSO, 20 minutes, 120°C), an average $[^{18}\text{F}]$ F $^-$ radiolabeling yield of 31.07 ± 3.65 % ($n = 10$) was obtained.

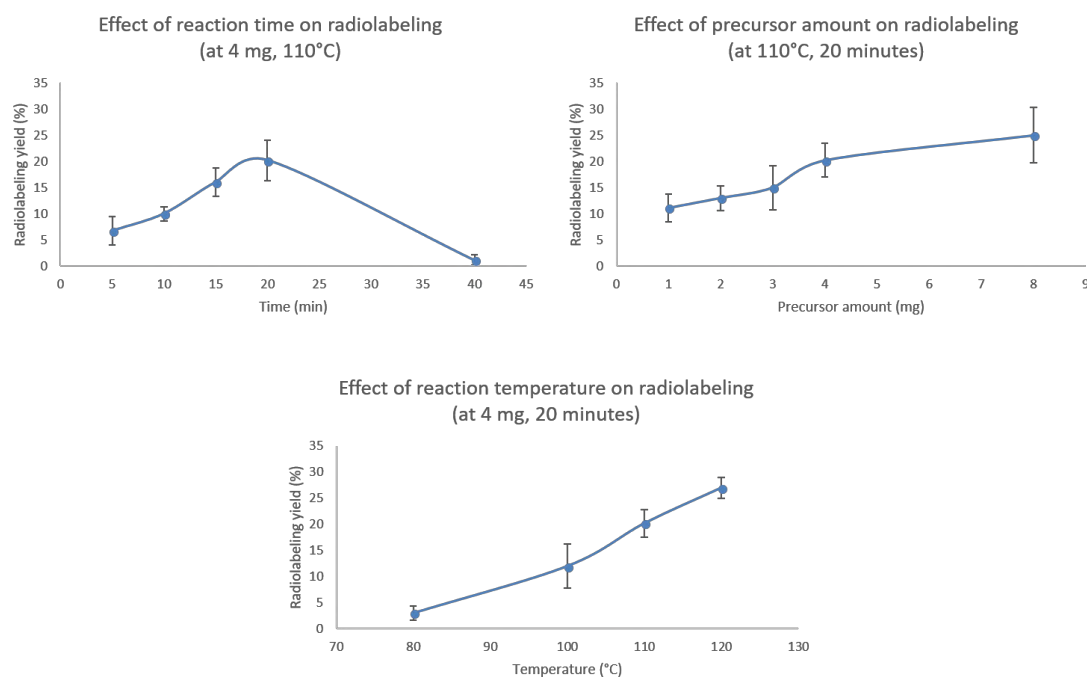


Figure 4.11: Radiolabeling yield of compound **4**, in function of precursor amount, time and temperature (Data: mean \pm SD; $n = 3$ per reaction).

The deprotection of radiolabeled compound **9** did not proceed at room temperature. To achieve complete deprotection, it was necessary to increase the reaction temperature to 120°C for 10 minutes.

The deprotected compound **9**, 3β-[¹⁸F]FCA, was purified with semi-preparative HPLC. The radiochromatogram of the injected reaction mixture after deprotection showed three prominent peaks. A representative radio chromatogram is shown in Figure 4.12. The first peak (retention time ≈ 2.5 min) was [¹⁸F]F, which shows no retention on the C18 stationary phase. The second peak (retention time ≈ 6-7 minutes) was 3β-[¹⁸F]FCA. This was verified by coinjection with the cold reference compound. The last and smallest peak (retention time ≈ 11 minutes) was probably a partially deprotected radiolabeled compound.

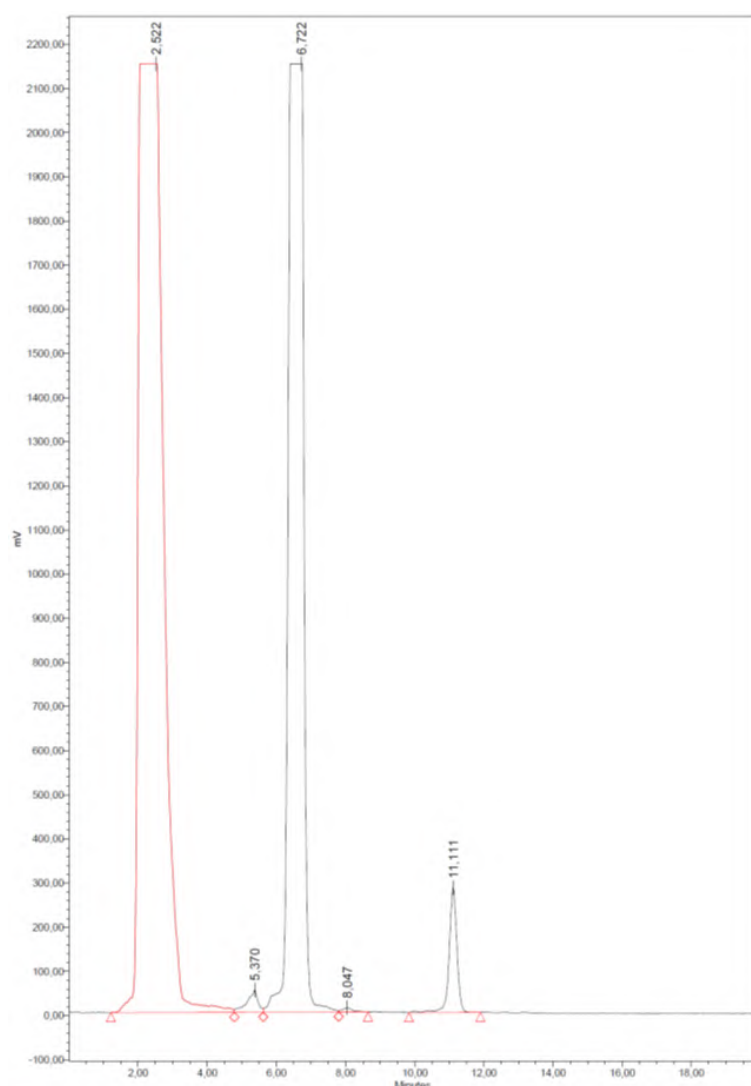


Figure 4.12: A representative radio chromatogram of the 3β-[¹⁸F]FCA reaction mixture after deprotection on semi-preparative HPLC. Peak 1: 59.81 %; peak 2: 36.99 %; peak 3: 2.48 %.

In summary, the ideal radiosynthesis of 3β - ^{18}F FCA consisted of labeling 4 mg precursor compound **4** in 200 μL DMSO with $^{18}\text{F}^-$ for 20 minutes at 120°C , followed by deprotection at 120°C for 10 minutes. The total radiosynthesis and subsequent purification was achieved in 100 minutes with 8.11 ± 1.94 % non-decay corrected radiochemical yield (mean \pm SD; $n = 10$). Radiochemical purity was assessed by analytical HPLC (retention time 3β - ^{18}F FCA = 3.3 min) and was >99 %. The identity of 3β - ^{18}F FCA was confirmed by coinjection of the cold reference compound.

4.3.2 Synthesis of other ^{18}F labeled bile acid analogues

All the mesylated precursor and fluorinated reference compounds of the conceived ^{18}F labeled bile acid analogues were synthesized in a good to moderate total yield (Table 4.1). However, the cold reference compound of 7β - ^{18}F FCA could not be synthesized. Fluorination of compound **40** with DAST to obtain the 12β - ^{18}F FCA reference compound also showed low yield, yet was still achievable.

Table 4.1: Overview of the total synthesis yields to obtain the mesylated precursors for radiosynthesis and the reference compounds of the conceived ^{18}F labeled bile acid analogues.

Total yield (%)	3β - ^{18}F FCA	3α - ^{18}F FCA	3β - ^{18}F FGCA	3β - ^{18}F FCDCA	7β - ^{18}F FCA	12β - ^{18}F FCA
Mesylated precursor	66.0	29.6	38.5	69.9	27.5	36.1
Reference compound	43.9	23.6	24.2	39.0	/	9.28

Differences in radiolabeling yield of the precursors for radiosynthesis with $^{18}\text{F}^-$ were observed (Table 4.2). The precursors for 3α - ^{18}F FCA and 3β - ^{18}F FCDCA had approximately the same labeling yield (30 %) and non-decay corrected yield (10 %). The precursor for 3β - ^{18}F FGCA was only labeled for 11.51 ± 2.55 %, which also resulted in a lower total yield of 4.28 ± 0.39 %. Both the precursors for 12β - ^{18}F FCA and 7β - ^{18}F FCA provided minimal radiolabeling: generating a significant amount of completed product proved troublesome for these two products.

Table 4.2: Radiosynthesis characteristics of the different ^{18}F labeled bile acids. The overall synthesis time was 100 minutes. N.d.c. RY: non-decay corrected radiochemical yield. RP: radiochemical purity. Data are mean \pm SD.

	^{18}F labeling of precursor (%) (n = 3)	n.d.c. RY (%) (n = 3)	RP (%)
3β-[^{18}F]FCA	31.07 \pm 3.65	8.11 \pm 1.94	> 99
3α-[^{18}F]FCA	30.31 \pm 1.28	10.56 \pm 2.02	> 99
3β-[^{18}F]FGCA	11.51 \pm 2.55	4.28 \pm 0.39	> 99
3β-[^{18}F]FCDCA	28.27 \pm 5.02	9.57 \pm 1.51	> 99
12β-[^{18}F]FCA	2.82 \pm 1.14	< 0.50	N.A.
7β-[^{18}F]FCA	1.23 \pm 0.26	< 0.50	N.A.

4.4 Discussion

Cholestasis, a toxic accumulation of bile acids in the liver or blood, may occur in certain liver diseases or can be triggered as the result of a xenobiotic interfering with the hepatobiliary transport of bile acids (Zollner & Trauner 2008). It is therefore important to have an adequate tool to evaluate the efficiency of bile acid transport *in vivo* for clinical use or in drug development. To that end, PET-imaging of hepatobiliary transport with radiolabeled bile acids is gaining importance. A number of studies have been published in which bile acids were labeled with either ^{11}C or ^{18}F on different bile acid structures (Frisch et al. 2012; Schacht et al. 2016; Jia et al. 2014; Testa et al. 2017). However, these compounds lack a long half-life (in the case of the ^{11}C compounds) or only partly resemble an endogenous bile acid (^{18}F labeled bile acid analogues).

To accurately follow hepatobiliary transport and possible accumulation of endogenous bile acids *in vivo*, our research group conceived a set of ^{18}F labeled bile acids with remarkable structural resemblance to their endogenous counterparts. They are cholic acid derivatives of which the 3, 7 and 12 OH functions were replaced with a fluorine atom, a 3 β -fluorine labeled chenodeoxycholic acid and 3 β -fluorine labeled glycocholic acid.

The first ^{18}F labeled bile acid to be developed by our research group was lead compound 3 β -[^{18}F]FCA, which only differs from cholic acid by the substitution of a 3 α -OH with a 3 β -fluorine-18 atom. A suitable precursor for radiosynthesis had to be developed. Only a mesylated precursor could be obtained, as the tosyl leaving group could not be introduced and the triflated compound was not stable enough. Tosylation of a 3 α -OH steroid structure has already been described in literature and should therefore have been possible, yet repeated attempts with multiple tosylation protocols proved unsuccessful (Herrmann et al. 2008). It is possible that the partially deprotected compound **3** presents too much steric hindrance for the introduction of a relatively large tosyl group. A mesyl group was successfully introduced and does not contain the large benzene ring, but still retains approximately the same leaving group ability as a tosylate. A triflate leaving group has the highest leaving group ability for nucleophilic fluorination but as a consequence, is also much more prone to stability issues (Jacobson et al. 2014).

The radiofluorination of precursor compound **4** with $[^{18}\text{F}]\text{F}^-$ was investigated in function of precursor amount, reaction time and temperature. Lower precursor amounts resulted in lower labeling yields. Increasing the precursor amount to 4 – 8 mg resulted in a maximum ^{18}F incorporation yield of approx. 25 %. The labeling yield did not improve drastically by doubling the amount of precursor from 4 mg to 8 mg in 200 μL DMSO. To label compound **4** in a cost-effective way, 4 mg was chosen as optimal precursor amount. The labeling yield was optimal at 20 minutes reaction. No more labeling was observed at 40 minutes, probably due to breakdown of the radiolabeled intermediates by extended exposure to the relatively harsh reaction conditions. The reaction temperature had an influence on labeling yield: from 100°C onwards there was effective radiolabeling. This is in line with the temperature requirements for other $\text{S}_{\text{N}}2$ nucleophilic substitutions with $[^{18}\text{F}]\text{F}^-$ (Jacobson et al. 2014). A maximum temperature of 120°C was chosen as optimum, because heating the reaction mixture further beyond this value increases the risk of ineffective $\text{S}_{\text{N}}2$ nucleophilic substitution with $[^{18}\text{F}]\text{F}^-$ due to the harsh reaction conditions (Miller et al. 2008). Precursor compound **4** showed an incorporation yield of 31.07 ± 3.65 % at optimized radiolabeling conditions, which is in line with radiofluorination of a secondary mesylate directly attached to a cyclohexane ring (Seo et al. 2007). This moderate yield can be attributed to the sterically hindered environment of the leaving group.

The deprotection of radiolabeled intermediate **9** did not proceed at room temperature. $[^{11}\text{C}]\text{Cholylsarcosine}$, a ^{11}C labeled bile acid which also needs deprotection, can however be deprotected at room temperature in less time (2 minutes) (Frisch et al. 2012). However, $[^{11}\text{C}]\text{cholylsarcosine}$ only has one methyl ester function to cleave, whereas intermediate **9** has to be stripped from its methyl ester and two additional acetyl protecting groups. Furthermore, the reaction solvents are not the same (ethanolic NaOH solution vs. DMSO and NaOH solution). Heating at 120°C for 10 minutes was needed to achieve full deprotection.

Abovementioned optimal parameters for radiolabeling and deprotection of 3β - $[^{18}\text{F}]\text{FCA}$ were applied to the other ^{18}F labeled bile acids that were developed. Of the other conceived ^{18}F labeled bile acids, only 3α - $[^{18}\text{F}]\text{FCA}$, 3β - $[^{18}\text{F}]\text{FGCA}$ and 3β - $[^{18}\text{F}]\text{FCDCA}$ could be obtained in suitable radiochemical yields. The ^{18}F labeling yield of the precursor molecules for 3α - $[^{18}\text{F}]\text{FCA}$ and 3β - $[^{18}\text{F}]\text{FCDCA}$ was comparable to that of 3β - $[^{18}\text{F}]\text{FCA}$ described earlier

(approx. 30 %). Labeling of the 3β - ^{18}F FGCA precursor was only 11.51 ± 2.55 %. This reduced yield could be attributed to the presence of a more polar amide group on the precursor, which can reduce the $^{18}\text{F}^-$ nucleophilic substitution efficiency.

The mesylated precursors for 12β - ^{18}F FCA and 7β - ^{18}F FCA could not be substituted efficiently with $^{18}\text{F}^-$ and can therefore not be included in the *in vivo* evaluation part of this dissertation. The 7α - and 12α - mesylgroups on cholic acid are positioned axially on steroid rings B and C, respectively. Coupled to the presence of neighboring hydrogen atoms that can be removed by a base, these positions are more prone to elimination than substitution with $^{18}\text{F}^-$. This observation was also made in the attempted synthesis of the 12β - ^{18}F FCA and 7β - ^{18}F FCA reference compounds. The 7β -FCA synthesis with DAST resulted exclusively in the formation of elimination product. However, it was possible to synthesize the 12β -FCA reference compound in low yield, as there are less protons available for elimination by a base due to the 18-methylgroup present near the 12α -mesyl-group.

Four ^{18}F labeled bile acids whose molecular structures closely resemble their endogenous counterparts could thus be developed: 3β - ^{18}F FCA, 3α - ^{18}F FCA, 3β - ^{18}F FGCA and 3β - ^{18}F FCDCA. Their total non-decay corrected radiosynthesis yields can be considered moderate (approx. 10 %). The synthesized reference compounds can be used *in vitro* to assess the bile acid transporters that these fluorinated bile acids use. The PET tracers can be evaluated *in vivo* for their ability to monitor hepatobiliary transport of bile acids and possible alterations thereof in liver disease.

4.5 Conclusion

A number of ^{18}F labeled bile acids were conceived to monitor (disturbed) hepatobiliary transport of bile acids in liver disease with PET. Suitable precursors for radiosynthesis and cold fluorinated reference compounds were synthesized. The radiosynthesis encompassed a $\text{S}_{\text{N}}2$ nucleophilic substitution with $^{18}\text{F}^-$ on a mesylated, protected precursor, followed by an alkaline deprotection step and HPLC purification. Four PET tracers were successfully synthesized in moderate radiochemical yields: 3β - ^{18}F FCA, 3α - ^{18}F FCA, 3β - ^{18}F FGCA and 3β - ^{18}F FCDCA. The precursors for 12β - ^{18}F FCA and 7β - ^{18}F FCA could not be labeled with sufficient radiochemical yield and therefore cannot be used further for *in vivo* evaluation.

4.6 Experimental section: precursor and reference compound synthesis

4.6.1 General synthesis information

All used chemicals were bought from Sigma Aldrich (Bornem, Belgium) and were at least reagent grade. Cholic acid methyl ester was acquired from TCI Europe (Zwijndrecht, Belgium). All solvents were obtained from Acros (Geel, Belgium) and were at least of HPLC-grade. TLC analysis during and after each synthesis step was performed on aluminium sheets, coated with silica gel (silica gel 60; Sigma Aldrich, Bornem, Belgium). Spots were visualized by spraying a 50% phosphoric acid solution on the plates and heating them.

Purification of the crude reaction products was achieved by silica gel column chromatography (Sigma Aldrich, Bornem, Belgium). A mixture of ethyl acetate and hexane was used as mobile phase unless specified otherwise. Fractions were collected and analyzed by aforementioned TLC method to isolate the desired compound. ^1H NMR spectra were recorded with a Varian Mercury BB 300 MHz (Palo Alto, CA, USA). Mass spectra were obtained by ESI with a Waters LCT-premier XE, TOF high resolution mass spectrometer (Milford, MA, USA).

4.6.2 Synthesis of precursor for radiosynthesis and reference compound of 3 β - ^{18}F fluorocholeic acid

3 α ,7 α ,12 α -Triacetoxy-5 β -Cholanic acid methyl ester (compound 2)

Acetyl protecting groups were introduced on the hydroxyl functions of 3 α ,7 α ,12 α -trihydroxy 5 β -cholanic acid methyl ester based on a similar reaction described in literature (Májér et al. 2014). To a stirred solution of 3 α ,7 α ,12 α -trihydroxy 5 β -cholanic acid methyl ester (4 g, 9,465 mmol) and 4-DMAP (240 mg, 1.964 mmol) in anhydrous pyridine (30 mL), acetic acid anhydride (28 mL, 296 mmol) was added. The reaction mixture was stirred overnight at room temperature, after which the mixture was poured into water (200 mL) and extracted with EtOAc (3x 200 mL). The organic phase was washed with 1 M HCl (200 mL), brine (200 mL), and water (200 mL). The washed solvent was dried with Na_2SO_4 and evaporated. The remaining residue was subjected to column chromatography using EtOAc:hexane (50:50 v/v). The desired fractions were combined and evaporated, yielding a white solid (100 %). Theoretical MS [$\text{M}+\text{NH}_4$]: 566.3693; Found MS [$\text{M}+\text{NH}_4$]: 566.3677. ^1H

NMR (DMSO- d_6 ; 300 MHz): 4.93 (1H, m); 4.75 (1H, m); 4.42 (1H, m); 3.54 (3H, s); 2.04 (3H, s); 1.97 (3H, s); 1.95 (3H, s).

3 α -Hydroxy-7 α ,12 α -Diacetoxy-5 β -Cholanic acid methyl ester (compound 3)

The partial deprotection of 3 α ,7 α ,12 α -trihydroxy 5 β -cholanic acid methyl ester was based on a similar reaction described in literature (Májér et al. 2014). 3 α ,7 α ,12 α -trihydroxy 5 β -cholanic acid methyl ester (2 g; 3.645 mmol) was dissolved in anhydrous MeOH (20 mL). The solution was cooled to 0°C. AcCl (340 μ L), dissolved in anhydrous MeOH (3 mL), was slowly added. The mixture was stirred for 24h at room temperature. The reaction was stopped by adding saturated NaHCO₃ (50 mL) and extracted with EtOAc (3x 100 mL). The organic phase was dried over Na₂SO₄, concentrated *in vacuo* and subjected to column chromatography using EtOAc:hexane (1:3 v/v). The desired fractions were combined and evaporated, yielding a white solid (75.0 %). Theoretical MS [M+NH₄]: 524.3588; found MS [M+NH₄]: 524.3576. ¹H NMR (DMSO- d_6 ; 300 MHz): 4.92 (1H, m); 4.73 (1H, m); 4.44 (1H, m); 3.54 (3H, s); 3.19 (1H, m); 2.03 (3H, s); 1.97 (3H, s).

3 α -Mesyl-7 α ,12 α -Diacetoxy-5 β -Cholanic acid methyl ester (Compound 4)

The introduction of the mesyl leaving group was based on a similar reaction described in literature (Rohacova, J. et al., 2009). 3 α -hydroxy-7 α ,12 α -dihydroxy 5 β -cholanic acid methyl ester (150 mg, 0.296 mmol) was dissolved in anhydrous pyridine (5 mL). The solution was cooled to 0°C and MsCl (69 μ L; 0.888 mmol) was slowly added. The mixture was stirred for 6h at room temperature. Then, the reaction mixture was diluted with 50 mL 6 M HCl in brine and extracted with CH₂Cl₂ (3x 50 mL). The organic phase was dried with MgSO₄ and concentrated *in vacuo*. This residue was purified by column chromatography using EtOAc:hexane (2:3 v/v). The desired fractions were combined and evaporated, yielding a white solid (88.0 %). Theoretical MS [M+NH₄]: 602.3363; found MS [M+NH₄]: 602.3380. ¹H NMR (DMSO- d_6 ; 300 MHz): 4.95 (1H, m); 4.78 (1H, m); 4.41 (1H, m); 3.55 (3H, s); 3.13 (3H, s); 2.05 (3H, s); 1.99 (3H, s).

3 α -Tosyl-7 α ,12 α -Diacetoxy-5 β -Cholanic acid methyl ester (Compound 5)

The introduction of a tosylate leaving group was based on a reaction described by Wang et al. (Wang et al. 2011). Compound **3** (200 mg, 0.395 mmol) was dissolved in 10 mL CH₂Cl₂. Triethylamine (172 μ L; 1.23 mmol) and tosyl chloride (113 mg, 0.593 mmol, 1.5

equivalent) were added. The reaction was monitored at room temperature for 40 hours, yet no reaction products were observed.

3 α -Triflyl-7 α ,12 α -Diacetoxy-5 β -Cholanic acid methyl ester (Compound 6)

The introduction of a triflate leaving group was based on a reaction described in literature (Májér et al. 2014). Compound **3** (200 mg, 0.395 mmol) was dissolved in 6 mL CH₂Cl₂ and 79 μ L pyridine was added. Trifluoromethane sulfonic anhydride (Tf₂O; 1.5 equivalent) was added and the reaction took place for 30 minutes at room temperature. Ice-cold saturated NaHCO₃ was added (50 mL) and an extraction was performed with CH₂Cl₂ (3 x 50 mL). The organic phase was dried with MgSO₄ and concentrated *in vacuo*. On TLC, degradation of the end product was visible.

3 β -Fluoro-7 α ,12 α -Diacetoxy-5 β -Cholanic acid methyl ester (compound 7)

The fluorination of a partially deprotected bile acid methyl ester was based on a similar reaction in literature (Xia et al. 2003). Compound **3** (400 mg; 0.789 mmol) was dissolved in anhydrous CH₂Cl₂ (10 mL). The solution was cooled to 0°C and DAST (200 μ L; 1.514 mmol) was slowly added. The mixture was stirred for 3 h at room temperature and then diluted with CH₂Cl₂ (30 mL) and saturated NaHCO₃ (50 mL). The organic phase was washed with water (3x100 mL), dried with MgSO₄ and concentrated *in vacuo*. The residue was purified by column chromatography, using EtOAc:hexane (3:7 v/v). The desired fractions were combined to yield a white solid (77.0 %). Theoretical MS [M+NH₄]: 526.3544; Found MS [M+NH₄]: 526.3530. ¹H NMR (DMSO-d₆; 300 MHz): 4.93-4.73 (3H, m); 3.54 (3H, s); 2.02 (3H, s); 1.99 (3H, s).

3 β -Fluoro-7 α ,12 α -Dihydroxy-5 β -Cholanic acid (compound 8)

A solution of 3 β -fluoro-7 α ,12 α -dihydroxy 5 β -cholanic acid methyl ester (260 mg; 0.511 mmol) in 1 M NaOH and EtOH (20 mL) was refluxed for 3 hours. Then, the reaction mixture was acidified with 1 M HCl and extracted with CH₂Cl₂ (3x 50 mL). The organic phase was washed with brine (50 mL), saturated NaHCO₃ (50 mL), water (50 mL). Finally, the organic phase was dried over MgSO₄ and evaporated, yielding a white solid (76.0 %). Purity was assessed by TLC-analysis, and no further purification was performed. Theoretical MS [M+NH₄]: 428.3176; found MS [M+NH₄]: 428.3193. ¹H NMR (DMSO-d₆; 300 MHz): 11.98 (1H, s); 4.85-4.69 (1H, d); 4.12 (2x 1H overlap; m) 3.76 (1H, s); 3.60 (1H, s).

4.6.3 Synthesis of other ^{18}F labeled bile acid analogues

Procedure A: introduction of acetyl protecting groups

The acetylation of the free hydroxyl functions on a bile acid methyl ester was based on similar reactions described in literature (Májér et al. 2014). In a roundbottom flask, 2 mmol of bile acid (compounds **12**, **19**, **26**, **33**) and 0.4 mmol 4-DMAP was dissolved in 10 mL of pyridine. Acetic anhydride (58 mmol; 5.5 mL) was added and the reaction mixture was stirred overnight under inert atmosphere at room temperature. The reaction mixture was then poured into 100 mL 6 M HCl. The aqueous phase was extracted three times with 100 mL EtOAc. The organic fractions were combined and washed with 300 mL 6 M HCl, brine and water, after which it was dried over Na_2SO_4 , filtered and concentrated *in vacuo*. This crude reaction product was then subjected to silicagel column chromatography.

Procedure B: partial deprotection of acetyl group

The partial deprotection of the acetyl protecting group on the 3 position of the bile acid methyl ester was based on similar reactions described in literature (Májér et al. 2014). The acetyl protected bile acid methyl ester (1 mmol; compounds **13**, **20**, **27**) was dissolved in 7 mL MeOH and the solution was cooled to 0°C. A solution of AcCl (94 μL) in MeOH (3 mL) was slowly added. The mixture was stirred at room temperature until full consumption of the starting product (24-32 h). A saturated NaHCO_3 solution (50 mL) was added to quench the reaction. The aqueous phase was extracted three times with 100 mL EtOAc. The organic phases were combined, dried over Na_2SO_4 , concentrated *in vacuo*. The residue was further purified by silicagel column chromatography.

Procedure C: mesylation

The mesylation of the free OH-function of the bile acid analogue was based on similar reactions described in literature (Rohacova et al. 2009). The partially deprotected bile acid methyl ester (0.3 mmol; compounds **14**, **21**, **28**, **35**, **40**) was dissolved in anhydrous pyridine (5 mL) under inert atmosphere. The solution was cooled to 0°C and MsCl (70 μL ; 0.9 mmol) was slowly added. The mixture was stirred at room temperature until the starting product was consumed. Then, the content of the flask was emptied in 50 mL 6 M HCl and extracted three times with 50 mL CH_2Cl_2 . The organic phases were combined and washed with 150 mL

6 M HCl, brine and water. Following this washing step, the organic phase was dried over MgSO_4 and concentrated *in vacuo*. The residue was further purified by silicagel column chromatography.

Procedure D: fluorination with DAST

The fluorination of a partially deprotected bile acid methyl ester was based on a similar reaction in literature (Xia et al. 2003). The bile acid analogue (0.3 mmol; compounds **14, 21, 28, 35, 40**) was dissolved in 10 mL anhydrous CH_2Cl_2 and DAST (79 μL ; 0.6 mmol) was added slowly. The reaction mixture was allowed to stir for 15 minutes at room temperature, after which it was diluted with 40 mL CH_2Cl_2 and 50 mL saturated NaHCO_3 . The organic phase was washed with 50 mL brine and water, dried over MgSO_4 and concentrated *in vacuo*. The residue was purified by silicagel column chromatography.

Procedure E: alkaline deprotection

The deprotection of the fluorinated bile acid analogue was carried out in alkaline environment. The bile acid (0.2 mmol; compounds **16, 23, 30, 42**) was dissolved in 10 mL 5 % KOH in MeOH solution and refluxed for 45 minutes. The solvent was evaporated and the residue was transferred to a separatory funnel with 50 mL 6 M HCl and 50 mL CH_2Cl_2 . The aqueous phase was extracted twice more with 50 mL CH_2Cl_2 . The combined organic phases were washed with 150 mL saturated NaHCO_3 , brine and water. Finally, the CH_2Cl_2 was dried over MgSO_4 and concentrated *in vacuo*. No further purification was performed.

3 β ,5-Dinitrobenzoate-7 α ,12 α -Dihydroxy-5 β -Cholanic acid methyl ester (Compound 11)

The Mitsunobu esterification with 3, 5-dinitrobenzoic acid was based on a similar reaction described in literature (Zhao & Zhong 2005). Cholic acid methyl ester (CAME, 5 g, 11.83 mmol) 3, 5-dinitrobenzoic acid (5 g, 23.57 mmol) and PPh₃ (9 g, 34.31 mmol) were dissolved in anhydrous THF under inert atmosphere. The mixture was warmed to 50°C and DIAD (2.1 mL, 10.67 mmol) was slowly added. After 48 hours at 50°C, the solvent was removed by rotary evaporation. Methanol was added to the residue and the desired product was precipitated. The precipitate was washed with water and subjected to silica gel column chromatography to afford a slightly yellow solid (78.57 %). Theoretical MS [M+NH₄]: 634.3340; found MS [M+NH₄]: 634.3326. ¹H NMR (DMSO-d₆; 300 MHz): 9.01 (1H, s); 8.87 (2H, s); 5.26 (1H, m); 4.20 (1H, m); 4.16 (1H, m); 3.78 (1H, s); 3.63 (1H, s); 3.56 (3H, s)

3 β ,7 α ,12 α -Trihydroxy-5 β -Cholanic acid methyl ester (Compound 12)

This reaction was based on a similar reaction in the article of Gunasekara et al (Gunasekara & Zhao 2015). A solution was made of compound **11** (1 g, 1.622 mmol) in 10 mL THF. A 10 % NaOMe solution in methanol was added. The reaction mixture was stirred for 15 minutes at room temperature, after which the solvents were removed by rotary evaporation. The residue was redissolved in 100 mL EtOAc and was washed with 100 mL saturated NaHCO₃-solution, brine and water. The organic layer was dried over Na₂SO₄ and finally evaporated to yield a white solid (100 %). Theoretical MS [M+NH₄]: 440.3376; found MS [M+NH₄]: 440.3362. ¹H NMR (DMSO-d₆; 300 MHz): 4.84 (1H, m); 4.10 (1H, m); 4.02 (2H, m overlap); 3.76 (1H, s); 3.61 (1H, s); 3.55 (3H, s)

3 β ,7 α ,12 α -Triacetoxo-5 β -Cholanic acid methyl ester (Compound 13)

Compound **13** was synthesized by subjecting **12** to procedure A, yielding a white solid (53.94 %). Theoretical MS [M+NH₄]: 566.3696; found MS [M+NH₄]: 566.3700. ¹H NMR (DMSO-d₆; 300 MHz): 4.94 (1H, m); 4.88 (1H, m); 4.76 (1H, m); 3.55 (3H, s); 2.04 (3H, s); 1.99 (3H, s); 1.96 (3H, s)

3 β -Hydroxy-7 α ,12 α -Diacetoxy-5 β -Cholanic acid methyl ester (Compound 14)

Compound **14** was synthesized by subjecting **13** to procedure B, yielding a white solid (96.84 %). Theoretical MS [M+FA-H]: 551.3287; found MS [M+FA-H]: 551.3215. ^1H NMR (DMSO- d_6 ; 300 MHz): 4.93 (1H, m); 4.75 (1H, m); 4.16 (1H, m); 3.81 (1H, m); 3.55 (3H, s); 2.03 (3H, s); 1.97 (3H, s)

3 β -Mesyl-7 α ,12 α -Diacetoxy-5 β -Cholanic acid methyl ester (Compound 15)

Compound **15** was synthesized by subjecting **14** to procedure C, yielding a white solid (72.0 %). Theoretical MS [M+NH $_4$]: 602.3363; found MS [M+NH $_4$]: 602.3379. ^1H NMR (DMSO- d_6 ; 300 MHz): 4.95 (1H, m); 4.89 (1H, m); 4.78 (1H, m); 3.55 (3H, s); 3.10 (3H, s); 2.04 (3H, s); 2.00 (3H, s)

3 α -Fluoro-7 α ,12 α -Diacetoxy-5 β -Cholanic acid methyl ester (Compound 16)

Compound **14** was subjected to procedure D, yielding a white solid (62.6 %). Theoretical MS [M+Cl]: 543.2870; found MS [M+Cl]: 543.2856. ^1H NMR (DMSO- d_6 ; 300 MHz): 4.93 (1H, m); 4.80 (1H, m); 4.68 (1H, m); 3.54 (3H, s); 2.02 (3H, s); 1.92 (3H, s)

3 α -Fluoro-7 α ,12 α -Dihydroxy-5 β -Cholanic acid (Compound 17)

Compound **16** was subjected to procedure E, yielding a white solid (92.0 %). Theoretical MS [M-H]: 409.2800; found MS [M-H]: 409.2757. ^1H NMR (DMSO- d_6 ; 300 MHz): 11.93 (1H, s); 5.48 (2H, m overlap); 4.07 (1H, m); 3.77 (1H, s); 3.58 (1H, s)

3 α ,7 α ,12 α -Trihydroxy-5 β -glycocholic acid methyl ester (Compound 19)

Cholic acid (compound **18**) was esterified with glycine methyl ester according to a literature procedure (Tserng et al. 1977). A white solid was obtained (100 %). Theoretical MS [M+H]: 480.3247; found MS [M+H]: 480.3327. ^1H NMR (DMSO- d_6 ; 300 MHz): 8.21 (1H, s); 4.32 (1H, m); 4.09 (1H, m); 4.00 (1H, m); 3.77 (2H, m, overlap); 3.59 (3H, s)

3 α ,7 α ,12 α -Triacetoxy-5 β -glycocholic acid methyl ester (Compound 20)

Compound **19** was subjected to procedure A, yielding a white solid (70.0 %). Theoretical MS [M+H]: 606.3637; found MS [M+H]: 606.3627. ^1H NMR (DMSO- d_6 ; 300 MHz): 8.22 (1H, s);

4.96 (1H, m); 4.77 (1H, m); 4.44 (1H, m); 3.77 (2H, m); 3.59 (3H, s); 2.05 (3H, s); 1.98 (3H, s); 1.96 (3H, s)

3 α -Hydroxy-7 α ,12 α -Diacetoxy-5 β -glycocholic acid methyl ester (Compound 21)

Compound **20** was subjected to procedure B, yielding a white solid (72.8 %). Theoretical MS [M+H]: 564.3531; found MS [M+H]: 564.3547. ¹H NMR (DMSO-d₆; 300 MHz): 8.22 (1H, s); 4.94 (1H, m); 4.74 (1H, m); 4.47 (1H, m); 3.77 (2H, m); 3.59 (3H, s); 2.05 (3H, s); 1.99 (3H, s)

3 α -Mesyl-7 α ,12 α -Diacetoxy-5 β -glycocholic acid methyl ester (Compound 22)

Compound **21** was subjected to procedure C, yielding a white solid (75.5 %). Theoretical MS [M+H]: 642.3307; found MS [M+H]: 642.3317. ¹H NMR (DMSO-d₆; 300 MHz): 8.22 (1H, s); 4.96 (1H, m); 4.77 (1H, m); 4.41 (1H, m); 3.78 (2H, m); 3.59 (3H, s); 3.14 (3H, s); 2.05 (3H, s); 1.99 (3H, s)

3 β -Fluoro-7 α ,12 α -Diacetoxy-5 β -glycocholic acid methyl ester (Compound 23)

Compound **21** was subjected to procedure D, yielding a white solid (63.0 %). Theoretical MS [M+H]: 566.3488; found MS [M+H]: 566.3504. ¹H NMR (DMSO-d₆; 300 MHz): 8.19 (1H, s); 4.95 (1H, m); 4.75 (2H, m overlap); 3.77 (2H, d); 3.59 (3H, s); 2.03 (3H, s); 1.99 (3H, s)

3 β -Fluoro-7 α ,12 α -Dihydroxy-5 β -glycocholic acid (Compound 24)

Compound **23** was subjected to procedure E, yielding a white solid (75.5%). Theoretical MS [M+H]: 468.3120; found MS [M+H]: 468.3135. ¹H NMR (DMSO-d₆; 300 MHz): 8.01 (1H, s); 5.00 (1H, m); 4.70 (1H, m); 4.11 (2H, s overlap); 3.77 (1H, s); 3.65 (2H, d)

3 α ,7 α -Dihydroxy-5 β -Cholanic acid methyl ester (Compound 26)

Compound **25** (chenodeoxycholic acid) was esterified as described earlier in literature (Májér et al. 2014). A white solid (100 %) was obtained. Theoretical MS [M+Cl]: 441.2777; found MS [M+Cl]: 441.2774. ¹H NMR (DMSO-d₆; 300 MHz): 4.28 (1H, m); 4.08 (1H, m); 3.61 (2H, s overlap); 3.55 (1H, s)

3 α ,7 α -Diacetoxy-5 β -Cholanic acid methyl ester (Compound 27)

Compound **26** was subjected to procedure A, yielding a white solid (97.3 %). Theoretical MS [M+NH₄]: 508.3638; found MS [M+NH₄]: 508.3628. ¹H NMR (DMSO-d₆; 300 MHz): 4.74 (1H, m); 4.45 (1H, m); 3.55 (3H, s); 1.96 (3H, s); 1.94 (3H, s)

3 α -Hydroxy-7 α -Acetoxy-5 β -Cholanic acid methyl ester (Compound 28)

Compound **27** was subjected to procedure B, yielding a white solid (96.7 %). Theoretical MS [M+Cl]: 483.2883; found MS [M+Cl]: 483.2885. ¹H NMR (DMSO-d₆; 300 MHz): 4.71 (1H, m); 4.38 (1H, m); 3.55 (3H, s); 1.96 (3H, s)

3 α -Mesityl-7 α -Acetoxy-5 β -Cholanic acid methyl ester (Compound 29)

Compound **28** was subjected to procedure C, yielding a white solid (74.3 %). Theoretical MS [M+NH₄]: 544.3308; found MS [M+NH₄]: 544.3317. ¹H NMR (DMSO-d₆; 300 MHz): 4.75 (1H, m); 4.41 (1H, m); 3.55 (3H, s); 3.13 (3H, s); 1.97 (3H, s)

3 β -Fluoro-7 α -Acetoxy-5 β -Cholanic acid methyl ester (Compound 30)

Compound **28** was subjected to procedure D, yielding a white solid (53.3%). Theoretical MS [M+NH₄]: 468.3489; found MS [M+NH₄]: 468.3473. ¹H NMR (DMSO-d₆; 300 MHz): 4.88 (1H, m); 4.75 (1H, m); 3.55 (3H, s); 1.97 (3H, s)

3 β -Fluoro-7 α -Hydroxy-5 β -Cholanic acid (Compound 31)

Compound **30** was subjected to procedure E, yielding a white solid (77.7 %). Theoretical MS [M-H]: 393.2810; found MS [M-H]: 393.2913. ¹H NMR (DMSO-d₆; 300 MHz): 11.92 (1H, s); 4.83 (m, 1H); 4.20 (1H, m); 3.63 (s, 1H)

3 α ,12 α -Dihydroxy-7-oxo 5 β -Cholanic acid (Compound 32)

Compound **18** was selectively oxidized according to a literature procedure (LF & S 1949). A white-yellowish solid was obtained (100 %) and was used without further purification.

3 α ,12 α -Dihydroxy-7-oxo 5 β -Cholanic acid methyl ester (Compound 33)

Compound **32** was esterified based on a method described in literature (Neyt et al. 2016). Compound **32** (3 g, 7.379 mmol) was dissolved in a mixture of 0.75 mL 37 % HCl, 7.5 mL

dimethoxypropane and 15 mL MeOH. The reaction mixture was stirred for 24h at room temperature, after which the solvents were evaporated and the residue subjected to silica gel column chromatography to afford a white solid (100%). Theoretical MS [M+NH₄]: 438.3220; found MS [M+NH₄]: 438.3241. ¹H NMR (DMSO-d₆; 300 MHz): 4.50 (1H, m); 4.30 (1H, m); 3.55 (3H, s)

3 α ,12 α -Diacetoxy-7-oxo 5 β -Cholanic acid methyl ester (Compound 34)

Compound **33** was subjected to procedure A, yielding a white solid (65.6 %). Theoretical MS [M+NH₄]: 522.3431; found MS [M+NH₄]: 522.3414. ¹H NMR (DMSO-d₆; 300 MHz): 4.95 (1H, m); 4.55 (1H, m); 3.55 (3H, s) 2.02 (3H, s); 1.94 (3H, s)

3 α ,12 α -Diacetoxy-7 α -Hydroxy 5 β -Cholanic acid methyl ester (Compound 35)

Compound **34** was reduced based on a method described in literature (Iuliano et al. 2006). Compound **34** (200 mg; 0.3961 mmol) and NaBH₄ (28 mg; 0.740 mmol) were dissolved in 5 mL 20% THF in methanol. The reaction mixture was stirred for 4 hours at room temperature under inert atmosphere. Then, the solvents were evaporated and the residue redissolved in 100 mL EtOAc. The organic phase was washed with 100 mL NaHCO₃, 100 mL brine and 100 mL water. It was then dried over MgSO₄, concentrated *in vacuo* and subjected to column chromatography to yield a white solid (49.8%). Theoretical MS [M+NH₄]: 524.3588; found MS [M+NH₄]: 524.3609. ¹H NMR (DMSO-d₆; 300 MHz): 4.93 (1H, m); 4.41 (1H, m); 4.25 (1H, m); 3.63 (1H, s) 3.55 (3H, s); 2.02 (3H, s); 1.94 (3H, s)

3 α ,12 α -Diacetoxy-7 α -Mesyl 5 β -Cholanic acid methyl ester (Compound 36)

Compound **35** was subjected to procedure C, yielding a white solid (84.3%). Theoretical MS [M+NH₄]: 602.3363; found MS [M+NH₄]: 602.3384. ¹H NMR (DMSO-d₆; 300 MHz): 4.95 (1H, m); 4.75 (1H, m); 4.48 (1H, m); 3.55 (3H, s); 3.14 (3H, s); 2.04 (3H, s); 1.97 (3H, s)

3 α ,12 α -Diacetoxy-7 β -Fluoro 5 β -Cholanic acid methyl ester (Compound 37)

Compound **35** was subjected to procedure D, but no fluorinated reaction product was formed. MS- and NMR-analysis showed formation of elimination side product.

3 α ,12 α -Dihydroxy-7 β -Fluoro 5 β -Cholanic acid (Compound 38)

Compound **38** could not be synthesized out of compound **37**.

3 α ,7 α -Diacetoxy-12 α -Hydroxy 5 β -Cholanic acid methyl ester (Compound 40)

The synthesis of compound **40** was based on a literature procedure (Ito et al. 2010). To compound **1** (1 g, 2.366 mmol), 1.25 mL pyridine, 5 mL toluene and Ac₂O (1.25 mL, 13.2 mmol) was added. The reaction mixture was stirred overnight at room temperature. Then 40 mL of toluene and 50 mL water was added. The organic phase was washed with 50 mL 6 M HCl, 50 mL brine and 50 mL water, after which it was dried with CaCl₂ and evaporated. The residue was subjected to silica gel column chromatography to afford a white solid (58.2 %). Theoretical MS [M+FA-H]: 551.3214; found MS [M+FA-H]: 551.3215. ¹H NMR (DMSO-d₆; 300 MHz): 4.73 (1H, m); 4.46 (1H, m); 4.25 (1H, m); 3.77 (1H, m); 3.55 (3H, s); 1.96 (6H, s; overlap)

3 α ,7 α -Diacetoxy-12 α -Mesyl 5 β -Cholanic acid methyl ester (Compound 41)

Compound **40** was subjected to procedure C, yielding a white solid (62.0%) Theoretical MS [M+NH₄]: 602.3363; found MS [M+NH₄]: 602.3403. ¹H NMR (DMSO-d₆; 300 MHz): 4.96 (1H, m); 4.77 (1H, m); 4.43 (1H, m); 3.55 (3H, s); 3.18 (3H, s); 1.99 (3H, s); 1.94 (3H, s)

3 α ,7 α -Diacetoxy-12 β -Fluoro 5 β -Cholanic acid methyl ester (Compound 42)

Compound **40** was subjected to procedure D, yielding a white solid (27.3 %). Theoretical MS [M+Na]: 531.3092; found MS [M+Na]: 531.3121. ¹H NMR (DMSO-d₆; 300 MHz): 4.95 (1H, m); 4.77 (1H, m); 4.47 (1H, m); 3.54 (3H, s); 1.97 (3H, s); 1.94 (3H, s)

3 α ,7 α -Dihydroxy-12 β -Fluoro 5 β -Cholanic acid (Compound 43)

Compound **42** was subjected to procedure E, yielding a white solid (58.4 %). Theoretical MS [M-H]: 409.2759; found MS [M-H]: 409.2743. ¹H NMR (DMSO-d₆; 300 MHz): 11.92 (1H, s); 4.93 (1H, m); 4.37 (1H, m); 4.26 (1H, m); 3.75 (1H, s); 3.64 (1H, s)

4.7 References

- Alrefai, W. a & Gill, R.K., 2007. Bile acid transporters: structure, function, regulation and pathophysiological implications. *Pharmaceutical research*, 24(10), pp.1803–23.
- Baringhaus, K.H. et al., 1999. Substrate specificity of the ileal and the hepatic Na(+)/bile acid cotransporters of the rabbit. II. A reliable 3D QSAR pharmacophore model for the ileal Na(+)/bile acid cotransporter. *Journal of lipid research*, 40(12), pp.2158–2168.
- Dong, Z., Ekins, S. & Polli, J.E., 2015. A substrate pharmacophore for the human sodium taurocholate co-transporting polypeptide. *International Journal of Pharmaceutics*, 478, pp.88–95.
- Frisch, K. et al., 2012. [N-methyl-11C]cholylsarcosine, a novel bile acid tracer for PET/CT of hepatic excretory function: radiosynthesis and proof-of-concept studies in pigs. *Journal of nuclear medicine : official publication, Society of Nuclear Medicine*, 53(5), pp.772–8.
- Frisch, K. et al., 2018. N-(4-[18F]fluorobenzyl) cholyglycine, a novel tracer for PET of enterohepatic circulation of bile acids: Radiosynthesis and proof-of-concept studies in rats. *Nuclear Medicine and Biology*, 61, pp.56–62.
- González, P.M. et al., 2014. Structural requirements of the human sodium-dependent bile acid transporter (hASBT): Role of 3- and 7-OH moieties on binding and translocation of bile acids. *Molecular Pharmaceutics*, 11, pp.588–598.
- Gunasekara, R.W. & Zhao, Y., 2015. Conformationally switchable water-soluble fluorescent bischolate foldamers as membrane-curvature sensors. *Langmuir*, 31(13), pp.3919–3925.
- Herrmann, P. et al., 2008. Synthesis of Fluorinated Steroids Using a Novel Fluorinating Reagent Tetrabutylammonium Difluorodimethylphenylsilicate (TAMPS). *Collection of Czechoslovak Chemical Communications*, 73(12), pp.1825–1834.
- Hofmann, a. F. & Hagey, L.R., 2008. Bile Acids: Chemistry, Pathochemistry, Biology, Pathobiology, and Therapeutics. *Cellular and Molecular Life Sciences*, 65(16), pp.2461–2483.

- Ito, A., Ishizaka, S. & Kitamura, N., 2010. A ratiometric TICT-type dual fluorescent sensor for an amino acid. *Phys. Chem. Chem. Phys.*, 12, pp.6641–6649.
- Iuliano, A., Facchetti, S. & Uccello-Barretta, G., 2006. Asymmetric induction by the cholestanic moiety on Tropos species: Synthesis and stereochemical characterization of bile acid-based biphenyl phosphites. *Journal of Organic Chemistry*, 71(13), pp.4943–4950.
- Jacobson, O., Kiesewetter, D.O. & Chen, X., 2014. Fluorine-18 Radiochemistry, Labeling Strategies and Synthetic Routes. *Bioconjugate chemistry*, 26(1), pp.1–18.
- Jia, L. et al., 2014. Synthesis and evaluation of (18)F-labeled bile acid compound: a potential PET imaging agent for FXR-related diseases. *Nuclear medicine and biology*, 41, pp.495–500.
- Jüngst, C. et al., 2013. Intrahepatic cholestasis in common chronic liver diseases. *European journal of clinical investigation*, 43(10), pp.1069–83.
- Kubitz, R. et al., 2012. The bile salt export pump (BSEP) in health and disease. *Clinics and Research in Hepatology and Gastroenterology*, 36(6), pp.536–553.
- Kuhajda, K. et al., 2006. Chemical and metabolic transformations of selected bile acids. *European journal of drug metabolism and pharmacokinetics*, 31(3), pp.179–235.
- LF, F. & S, R., 1949. Selective Oxidation with N-Bromosuccinimide: cholic acid. *Journal of the American Chemical Society*, 71, pp.3935–3938.
- Liang, T., Neumann, C.N. & Ritter, T., 2013. Introduction of Fluorine and Fluorine-Containing Functional Groups. *Angew Chem Int Edit*, 52(32), pp.8214–8264.
- de Lima Toccafondo Vieira, M. & Tagliati, C.A., 2014. Hepatobiliary transporters in drug-induced cholestasis: a perspective on the current identifying tools. *Expert opinion on drug metabolism & toxicology*, 10(4), pp.581–97.
- De Lombaerde, S. et al., 2017. Synthesis, in vitro and in vivo evaluation of 3β-[18F]fluorocholeic acid for the detection of drug-induced cholestasis in mice. *Plos One*, 12(3), pp.1–14.

- Májér, F. et al., 2014. New highly toxic bile acids derived from deoxycholic acid, chenodeoxycholic acid and lithocholic acid. *Bioorganic and Medicinal Chemistry*, 22, pp.256–268.
- Miller, P.W. et al., 2008. Synthesis of ^{11}C , ^{18}F , ^{15}O , and ^{13}N Radiolabels for Positron Emission Tomography. *Angew. Chem*, 47, pp.8998–9033.
- Neyt, S. et al., 2016. Synthesis, in vitro and in vivo small-animal SPECT evaluation of novel technetium labeled bile acid analogues to study (altered) hepatic transporter function. *Nuclear Medicine and Biology*, 43, pp.642–649.
- Padda, M.S. et al., 2011. Drug-Induced Cholestasis. *Hepatology*, 53, pp.1377–1387.
- Rohacova, J. et al., 2009. Synthesis of new, UV-photoactive dansyl derivatives for flow cytometric studies on bile acid uptake. *Organic & biomolecular chemistry*, 7, pp.4973–80.
- Schacht, A.C. et al., 2016. Radiosynthesis of N- ^{11}C -Methyl-Taurine-Conjugated Bile Acids and Biodistribution Studies in Pigs by PET/CT. *Journal of Nuclear Medicine*, 57(4), pp.628–633.
- Seo, J.W. et al., 2007. Synthesis and biodistribution of fluorine-18-labeled fluorocyclofenils for imaging the estrogen receptor. *Nuclear Medicine and Biology*, 34, pp.383–390.
- Testa, A. et al., 2017. Design, synthesis, in vitro characterization and preliminary imaging studies on fluorinated bile acid derivatives as PET tracers to study hepatic transporters. *Bioorganic and Medicinal Chemistry*, 25, pp.963–976.
- Tserng, K., Hachey, D.L. & Klein, P.D., 1977. An improved procedure for the synthesis of glycine and taurine conjugates of bile acids. *Journal of Lipid Research*, 18, pp.404–407.
- Wang, L. et al., 2011. Synthesis, uptake mechanism characterization and biological evaluation of ^{18}F labeled fluoroalkyl phenylalanine analogs as potential PET imaging agents. *Nuclear Medicine and Biology*, 38, pp.53–62.
- Xia, J. et al., 2003. The application of diethylaminosulfur trifluoride in the synthesis of fluorinated sterols and bile acids. *Tetrahedron Letters*, 44(52), pp.9295–9297.

Zhao, Y. & Zhong, Z., 2005. Oligomeric cholates: Amphiphilic foldamers with nanometer-sized hydrophilic cavities. *Journal of the American Chemical Society*, 127(50), pp.17894–17901.

Zollner, G. & Trauner, M., 2008. Mechanisms of cholestasis. *Clinical Liver Disease*, (12), pp.1–26.

CHAPTER 5:

IN VITRO EVALUATION OF FLUORINATED BILE ACIDS

This chapter contains parts that have been adapted from:

De Lombaerde S, Kersemans K, Neyt S, Verhoeven J, Vanhove C, De Vos F; *Evaluating Hepatobiliary Transport with ¹⁸F-Labeled Bile Acids: The Effect of Radiolabel Position and Bile Acid Structure on Radiosynthesis and In Vitro and In Vivo Performance*; Contrast Media & Molecular Imaging, Volume 2018, Article ID 6345412, p1-9

De Lombaerde S, Neyt S, Kersemans K, Verhoeven J, Devisscher L, Van Vlierberghe H, et al.; *Synthesis, in vitro and in vivo evaluation of 3β-[¹⁸F]fluorocholeic acid for the detection of drug-induced cholestasis in mice*; PLoS One. 2017;12 (3), p1-14

5.1 Introduction

Bile acids show highly efficient hepatobiliary transport and enterohepatic cycling. Only 5 % of the bile acid pool is lost daily in the faeces (Vaz & Ferdinandusse 2017). This effective transport is warranted by specialized bile acid transport proteins, which were discussed in detail in Chapter 1. In short, hepatic uptake of bile acids is primarily mediated by the basolateral Na⁺-dependent Taurocholate Cotransporting Polypeptide (NTCP). However, the Organic Anion Transporting Polypeptide (OATP) is also capable of transporting bile acids into the hepatocyte. Hepatic efflux of bile acids towards the bile canaliculi is mediated mainly by the Bile Salt Export Pump (BSEP) and to a minor extent by the Multidrug Resistance-associated Protein 2 (MRP2) (Trauner & Boyer 2003).

The fluorinated bile acid compounds that were developed (Chapter 4) need to be assessed *in vitro*. Although only minor changes to the bile acid structure were made, there is a need for *in vitro* confirmation that these compounds are substrates for the bile acid transporters. The fluorinated bile acid PET probes can subsequently provide functional information of bile acid hepatobiliary transport efficiency *in vivo*.

Several *in vitro* assay types are available to evaluate whether a specific compound shows hepatic uptake or biliary efflux by specific transporters (Brouwer et al. 2013). First of all, recombinant cell lines that express a single hepatic uptake transporter such as NTCP or OATP are of considerable interest, as they allow investigation of uptake by a single transporter. Furthermore, they can easily be cryopreserved and therefore be used multiple times. Secondly, plated hepatocytes or hepatocytes in suspension can also be applied. These cells express a broad spectrum of uptake transporters. They allow assessment of contribution of several hepatic uptake transporters in the same experiments. Thirdly, sandwich-cultured hepatocytes offer simultaneous information on both hepatic uptake and biliary clearance, because the hepatocytes are cultured in a way that promotes the development of bile canaliculi (same as *in vivo*). However, the organization of the canalicular network takes several days and the assay is hence not readily available. Furthermore, transporter expression may be modulated by culture conditions (Brouwer et al. 2013). Finally, membrane vesicles assays are not cell-based and can be used to evaluate a substrate's efflux through a specific transporter of interest (such as BSEP or MRP2).

In this chapter, the previously synthesized fluorinated bile acids (3β - ^{18}F FCA, 3α - ^{18}F FCA, 3β - ^{18}F FGCA and 3β - ^{18}F FCDCA) will be evaluated *in vitro* (Figure 5.1). Their hepatic uptake by the bile acid transport proteins NTCP and OATP1B1 will be assessed using cell lines expressing recombinant proteins. Their biliary efflux will be investigated with membrane vesicles that express BSEP or MRP2. The uptake and efflux of the developed compounds will be evaluated in a competitive way with tritium labeled model substrates that are displaced by the synthesized, cold reference compounds. K_i -values of their transport will be determined. Finally, the stability of the developed PET tracers will be assessed in formulation for use, mouse serum and in the presence of primary hepatocytes. Their $\text{LogD}(7.4)$ value will also be determined.

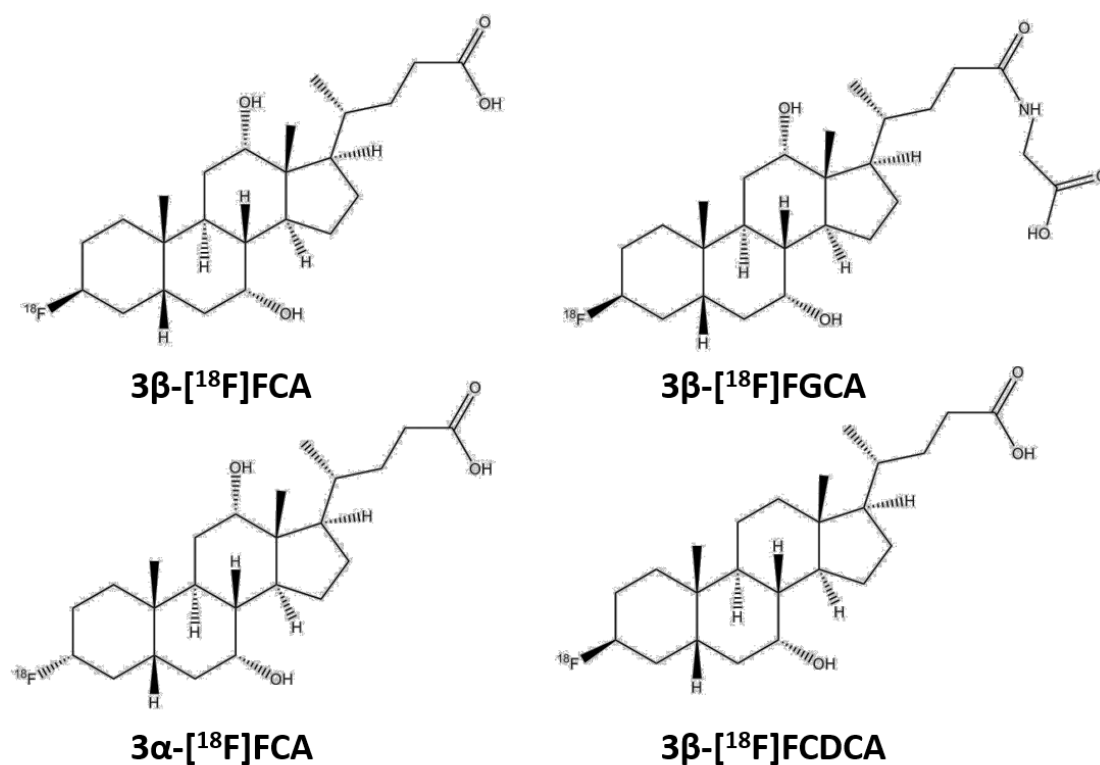


Figure 5.1: Overview of the ^{18}F labeled bile acid analogues that will be evaluated *in vitro*: compounds 3β - ^{18}F fluorocholeic acid (3β - ^{18}F FCA), 3α - ^{18}F fluorocholeic acid (3α - ^{18}F FCA), 3β - ^{18}F fluorochenodeoxycholeic acid (3β - ^{18}F FCDCA), and 3β - ^{18}F fluoroglycocholeic acid (3β - ^{18}F FGCA).

5.2 Materials and methods

5.2.1 Radiosynthesis of ^{18}F labeled bile acids

The radiosynthesis of each ^{18}F labeled bile acid (3β - ^{18}F FCA, 3α - ^{18}F FCA, 3β - ^{18}F FGCA and 3β - ^{18}F FCDCA) has been described in detail in Chapter 4.

5.2.2 LogD(7.4) determination

The LogD value describes the lipophilicity of an ionizable structure at a certain pH. Of the ^{18}F labeled bile acids, 1 MBq was used to spike an octanol/PBS 50:50 v:v pH 7.4 mixture in a test tube. After mixing and centrifugation (5 min; 1100 g), aliquots were taken from each layer and radioactivity was measured in a NaI (TI) scintillation counter (Capintec; Ramsey, NJ, USA). The LogD(7.4) value was calculated as the logarithm of the ratio of counts in octanol and PBS pH 7.4. Values were determined in triplicate.

5.2.3 *In vitro* investigation of stability

The stability and metabolization of the different ^{18}F labeled bile acids was assessed in its PBS formulation for use at room temperature, in mouse serum at 37°C and in presence of primary mouse hepatocytes at 37°C. The stability of the PET tracer in PBS after radiosynthesis was monitored for a period up to 6 hours. Mouse serum (Sigma Aldrich, Bornem, Belgium) was spiked with 37 MBq of ^{18}F labeled bile acid (1.0 mL total volume) and incubated at 37°C for 5, 10, 30 and 60 minutes.

Primary mouse hepatocytes were isolated as described in literature (Severgnini et al. 2012), formulated in Dulbecco's modified Eagle's medium (DMEM) medium (supplemented with 0.1 g/L taurine) at 1 million cells/mL and immediately incubated with 37 MBq of PET tracer (1.0 mL total volume) at 37°C, 5 % CO_2 for 5, 10, 30 and 60 minutes. A control sample without hepatocytes was included.

At the indicated timepoints, 100 μL serum or hepatocyte incubation medium was withdrawn and 100 μL AcN was added. Samples were then centrifuged at 13000 g for 5 minutes and the supernatant was analyzed by radio-TLC (silica gel TLC; with 10 % MeOH in CH_2Cl_2) and by a semi-preparative RP-HPLC method (Grace Econosphere C18 10.0x250 mm, 10 μm ; 6 mL/min AcN:H₂O 10:90 v:v ->AcN 100 % in 20 minutes as mobile phase; radiodetection (Ludlum Measurements Inc)).

5.2.4 *In vitro* uptake assay

Transport of 3 β -FCA, 3 α -FCA, 3 β -FGCA and 3 β -FCDCA by NTCP and OATP1B1 was assessed using stable transfected cell lines. Chinese hamster ovary (CHO) parent cells and Human Embryonic Kidney (HEK 293) control cells were purchased from Solvo Biotechnologies; CHO-NTCP and HEK293-OATP1B1 cells were a kind gift from the same company. CHO cells were cultured in DMEM/F12 with 10 % fetal calf serum, 0.3 mM L-proline, 2 mM glutamine and penicilline/streptomycine (50 U/mL). HEK cell lines were cultured in DMEM glutamax (high glucose/pyruvate) with 10 % fetal calf serum, MEM non-essential amino acid supplement and penicilline/streptomycine (50 U/mL). All cell lines were cultured in a 37°C 5 % CO₂ environment.

For cell assays, cells were seeded in 24-well plates at 400,000 cells per well. After 24 hours, the culture medium was removed and cells were washed twice with 1 mL 10 mM HEPES-Hank's Balanced Salt Solution (HBSS; with Ca and Mg; 37 °C pH 7.4) washing buffer. Dosing solutions were prepared by supplementing the washing buffer with the appropriate concentrations of fluorinated bile acid analogues and tritium labeled model substrates for NTCP ([³H]taurocholate; [³H]TC; Perkin Elmer) or OATP1B1 ([³H]estradiol-17 β -glucuronide; [³H]EbG; Perkin Elmer) (see following paragraphs). Cholic acid (CA) was added to the test panel. Of the dosing solution, 250 μ L was added to the washed cells and incubation took place at 37 °C for the specified time. The plates were subsequently cooled on ice and 1 mL 1 % BSA ice-cold HBSS (with Ca and Mg) was added. Cells were washed twice with 2 mL ice-cold HBSS (with Ca and Mg) and were finally lysed with 250 μ L 0.1 M NaOH. The plates were shaken for 15 minutes at 37 °C. Of the lysate, 150 μ L was used for liquid scintillation counting (TriCarb 2900 TR; Perkin Elmer) and 25 μ L was subjected to a bicinchoninic acid (BCA) assay (ThermoFisher Scientific) to determine protein content. Measurements were performed in triplicate and three independent experiments were performed.

A kinetic profile of the uptake of the tritium labeled model substrates was first determined. CHO parent and CHO-NTCP cells were incubated with 1 μ M [³H]TC for 1, 3, 5, 10, 15 or 30 minutes. HEK control and HEK-OATP1B1 cells were incubated with 1 μ M [³H]EbG for 1, 3, 5, 10, 15 or 30 minutes at 37°C.

The Michaelis-Menten constants (K_m) of [^3H]TC and [^3H]EbG for NTCP and OATP1B1 respectively were determined by incubating the appropriate cells with 0 – 150 μM [^3H]TC (NTCP) or [^3H]EbG (OATP1B1) for 10 minutes at 37°C. Transport of the fluorinated bile acids was assessed by the inhibition of the uptake of the tritium labeled model substrates. IC50-values were acquired by incubating the cells with 0 – 1000 μM cold fluorinated bile acid and 1 μM [^3H]TC (NTCP) or [^3H]EbG (OATP1B1) for 15 minutes at 37°C. Competitive inhibition was assumed and K_i -values of the different bile acids were calculated using the experimentally determined IC50-and K_m -parameters and the Cheng-Prusoff equation (Graphpad Prism v5.00 Software) (Eq. 1).

$$K_i = \frac{IC_{50}}{1 + \frac{[S]}{K_m}} \text{ (Eq. 1)}$$

K_i: inhibition constant; IC₅₀: concentration of fluorinated bile acid that causes a 50 % decrease in ^3H labeled substrate uptake; [S] = concentration of ^3H labeled substrate; K_m: Michaelis-Menten constant of ^3H labeled substrate.

5.2.5 *In vitro* efflux assay

Transport of the fluorinated bile acids by BSEP and MRP2 was evaluated by the inhibition of [^3H]TC uptake in BSEP membrane vesicles or [^3H]EbG in MRP2 vesicles (Pharmtox). Cholic acid (CA) was added to the test panel. K_i -values of the different bile acids were calculated using the experimentally determined IC50-and K_m -parameters in the Cheng-Prusoff equation (Graphpad Prism v5.00 Software) (Eq. 1). Only for cholic acid and lead compound 3 β -FCA, K_i values for MRP2 were also determined. The assay was performed in V-tip 96-well plates; each well contained 3.75 μg membrane vesicle, 10 mM MgCl_2 , 10 mM Tris, 4 mM adenosinetriphosphate (ATP) and 250 mM sucrose. A concentration range of 0 – 50 μM [^3H]TC (BSEP) or 0 – 350 μM [^3H]EbG (MRP2) was included for K_m -determination. To determine the IC50s, 0 – 2500 μM of bile acid was used with 0.65 μM [^3H]TC or 2.00 μM [^3H]EbG. All dosing was performed in triplicate. The plates were suspended in a 37°C water bath 1 minute before the incubation. Incubation was started by adding 10 μL of the ATP solution or buffer solution (negative control). Each well contained a final volume of 30 μL and the plates were incubated for 10 minutes at 37°C. Three independent experiments were performed.

Transport was stopped by placing the plates on ice and adding 150 μL ice-cold buffer solution. The contents of each well were pipetted in a glass fiber filter plate (Multiscreen HTS plates; Merck Millipore) and washed 3 times with 200 μL ice-cold buffer solution. Finally, 100 μL 0.1 M NaOH was added: lysis of the vesicles took place for 10 minutes at room temperature. An aliquot (80 μL) was taken for liquid scintillation counting.

5.3 Results

5.3.1 LogD(7.4) determination

The determined LogD(7.4) values are listed in Table 5.1, along with literature logD(7.4) values of the endogenous bile acid counterparts.

Table 5.1: Overview of the acquired LogD(7.4) values for 3 α -[¹⁸F]FCA, 3 β -[¹⁸F]FCA, 3 β -[¹⁸F]FGCA and 3 β -[¹⁸F]FCDCA. Data are mean \pm SD (n = 3). CA: cholic acid; GCA: glycocholic acid; CDCA: chenodeoxycholic acid.

	LogD(7.4)
3 α -[¹⁸ F]FCA	0.92 \pm 0.17
3 β -[¹⁸ F]FCA	1.19 \pm 0.10
3 β -[¹⁸ F]FGCA	0.011 \pm 0.037
3 β -[¹⁸ F]FCDCA	1.42 \pm 0.16
CA	1.1*
GCA	-0.4*
CDCA	2.25*
*From: Roda et al. 1990	

5.3.2 In vitro investigation of stability

The tracers 3 α -[¹⁸F]FCA, 3 β -[¹⁸F]FCA, 3 β -[¹⁸F]FGCA and 3 β -[¹⁸F]FCDCA were found to be stable in their PBS formulation for at least 6 hours at room temperature. No degradation or metabolization products were detected at any examined time point in the presence of mouse serum or primary mouse hepatocytes. No defluorination was observed.

5.3.3 In vitro uptake assay

The NTCP transfected CHO cell lines showed uptake of [³H]TC in a time-dependent manner (Figure 5.2). After 15 minutes of incubation, the uptake of [³H]TC was 101-fold higher in the CHO-NTCP cells than in CHO parent cells (135.5 pmol/mg protein vs. 1.3 pmol/mg protein respectively). [³H]EbG was taken up in the HEK-OATP1B1, but not in control (Figure 5.2). After 15 minutes, uptake of [³H]EbG was 115 times higher in HEK-OATP1B1 (163.9 pmol/mg protein vs. 1.62 pmol/mg protein).

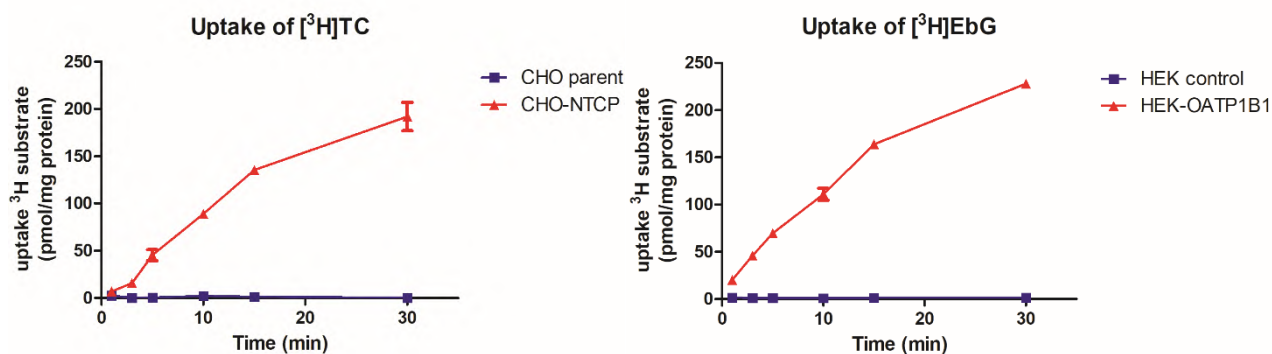


Figure 5.2: Uptake of 1 μM [^3H]TC in CHO-NTCP and CHO parent cells in function of incubation time (left). Uptake of 1 μM [^3H]EbG in HEK-OATP1B1 and HEK control cells in function of incubation time (right). Values are expressed as mean \pm SD ($n = 3$).

A Michaelis-Menten curve was made for [^3H]TC and [^3H]EbG for the CHO-NTCP and HEK-OATP1B1 cells respectively (Figure 5.4). For the CHO-NTCP cells, the K_m of [^3H]TC was $15.27 \pm 2.46 \mu\text{M}$ and the V_{max} $200.4 \pm 9.77 \text{ pmol/min.mg protein}$. For the HEK-OATP1B1 cells, the K_m of [^3H]EbG was $11.72 \pm 1.59 \mu\text{M}$ and the V_{max} $146.4 \pm 5.52 \text{ pmol/min.mg protein}$.

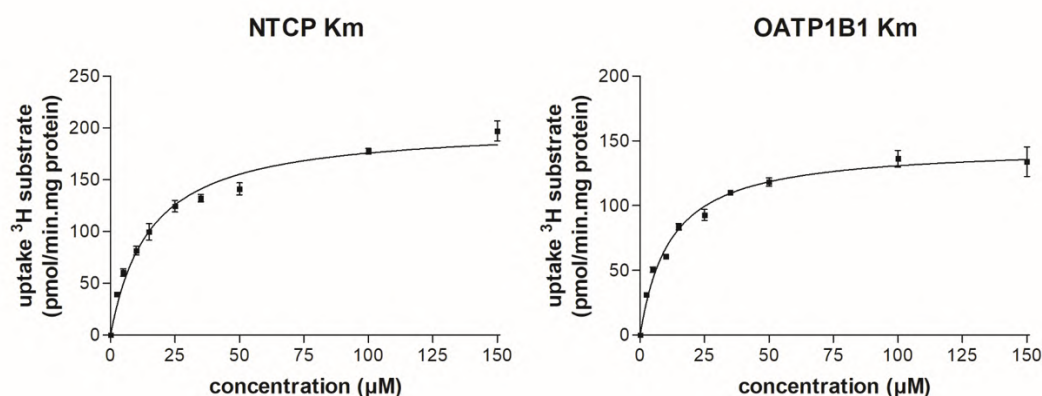


Figure 5.4: Graphs of the concentration dependent uptake of [^3H]TC in CHO-NTCP cells (left) and [^3H]EbG in HEK-OATP1B1 cells (right). All data are mean \pm SD ($n = 3$).

The fluorinated bile acid analogues and cholic acid caused a dose-dependent decrease in the uptake of [^3H]TC and [^3H]EbG for NTCP and OATP1B1. A sigmoidal dose-response curve was fitted on the acquired data points to determine the IC_{50} and calculate the K_i -value (Figure 5.5, Table 5.2 and Table 5.3).

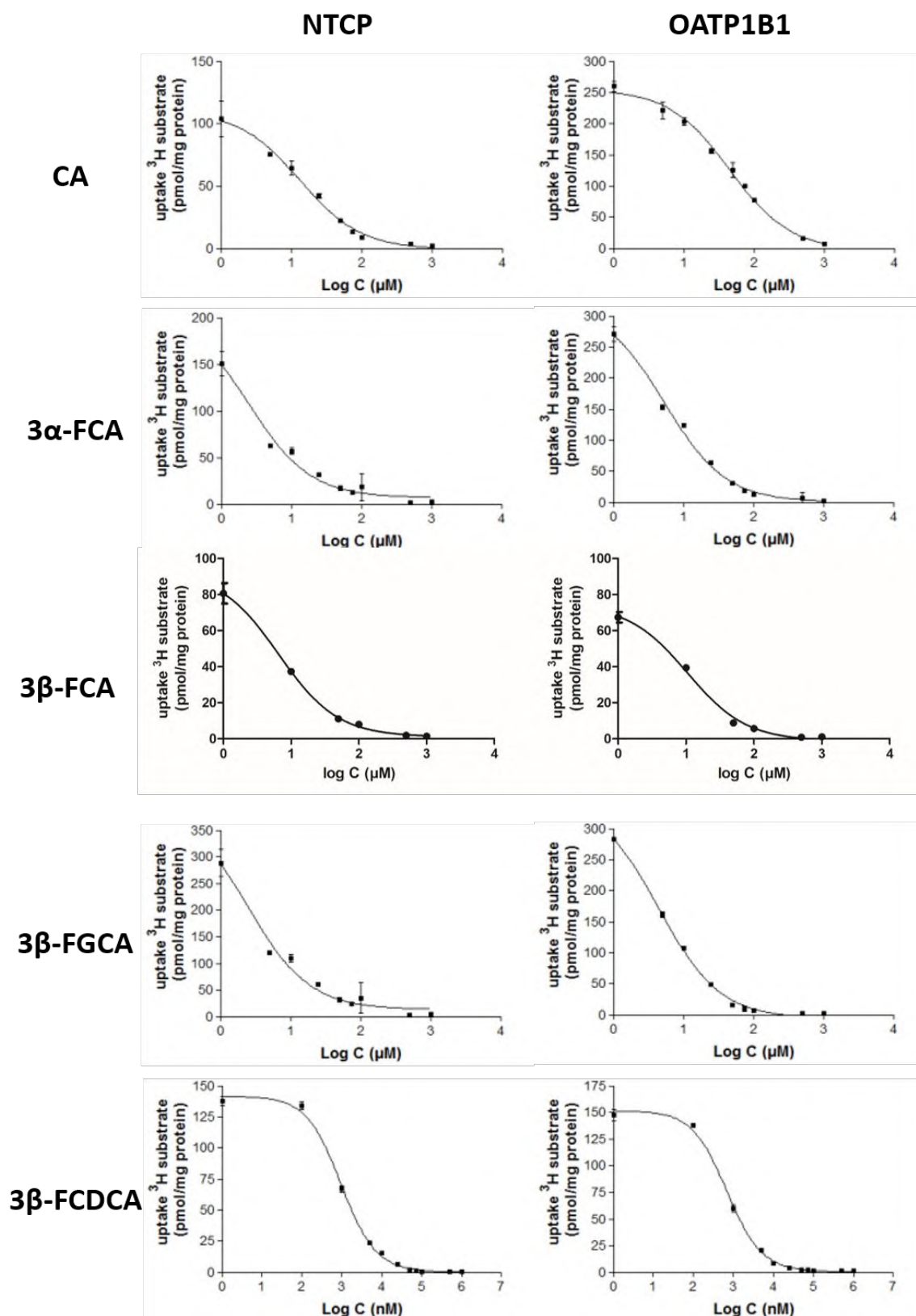


Figure 5.5: Graphs of the concentration dependent decrease in uptake of tritium labeled substrate ($[^3\text{H}]\text{TC}$ for NTCP, $[^3\text{H}]\text{EbG}$ for OATP1B1). IC_{50} s were determined by Graphpad, their respective K_i -values can be found in Table 5.2. Data are mean \pm SD ($n = 3$).

Table 5.2: Calculated K_i -values of the fluorinated bile acid analogues for NTCP and literature data of their endogenous bile acid counterparts (Dong et al. 2015; González et al. 2014; Kolhatkar et al. 2012). Data are mean \pm SD ($n = 3$). CA: cholic acid; GCA: glycocholic acid; CDCA: chenodeoxycholic acid.

	Ki for NTCP (μM)	Affinity endogenous counterpart (μM)
CA	12.96 \pm 4.26	Ki CA: 41.6 \pm 5.3
3α-FCA	2.53 \pm 0.76	Ki 3 α OH-CA (ASBT): 17.7 \pm 1.4
3β-FCA	6.18 \pm 0.59	Ki 3 β -OH-CA (ASBT): 53.8 \pm 14
3β-FGCA	1.09 \pm 0.34	Ki GCA: 29.6 \pm 1.7
3β-FCDCA	0.91 \pm 0.02	Ki CDCA (NTCP): 0.939 \pm 0.057

Table 5.3: Calculated K_i -values of the fluorinated bile acid analogues for OATP1B1 and literature data of their endogenous bile acid counterparts (Suga et al. 2017). Data are mean \pm SD ($n = 3$). CA: cholic acid; GCA: glycocholic acid.

	Ki for OATP1B1 (μM)	Affinity endogenous counterpart (μM)
CA	42.70 \pm 0.16	Km CA: 47.1 \pm 0.6
3α-FCA	5.22 \pm 0.56	N/A
3β-FCA	9.67 \pm 0.83	N/A
3β-FGCA	4.24 \pm 0.16	Km GCA: 14.7 \pm 2.7
3β-FCDCA	0.64 \pm 0.07	N/A

5.3.4 *In vitro* efflux assay

A Michaelis-Menten curve of [3 H]TC and [3 H]EbG was made for BSEP and MRP2 respectively (Figure 5.6). The K_m of [3 H]TC was 3.89 μ M \pm 1.44 μ M and the V_{max} 34.97 \pm 3.57 pmol/min.mg protein, while the K_m and V_{max} of [3 H]EbG for MRP2 was 23.66 \pm 11.91 μ M and 1271.3 \pm 128.0 pmol/min.mg protein. Cholic acid and the fluorinated bile acid analogues caused a dose-dependent decrease in the uptake of [3 H]TC in the BSEP membrane vesicles. Lead compound 3 β -FCA and cholic acid caused a dose-dependent decrease in uptake of [3 H]EbG in MRP2 vesicles. A sigmoidal dose-response curve was fitted on the

acquired data points to determine the IC₅₀ and calculate the K_i-value (Figure 5.7 and Table 5.4 and Table 5.5).

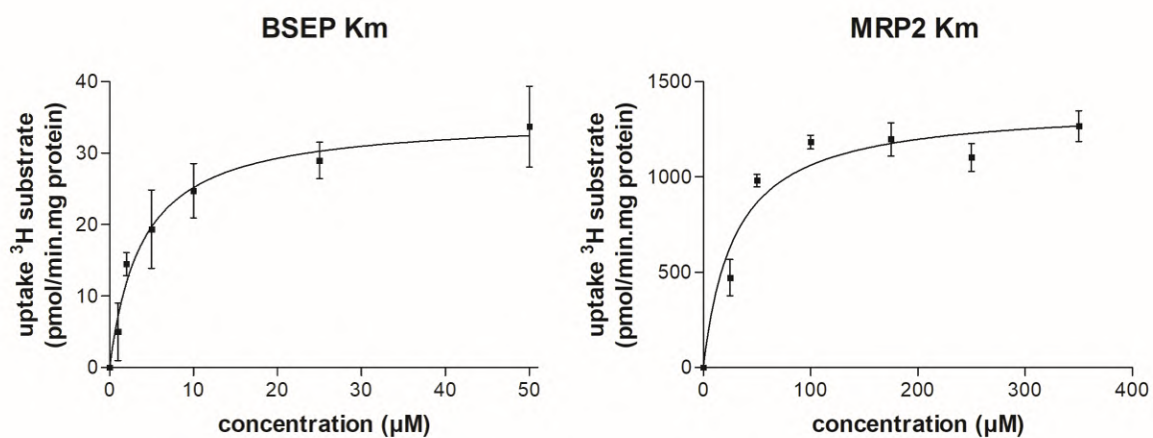


Figure 5.6: Graphs of the concentration dependent uptake of [³H]TC in BSEP membrane vesicles and [³H]EbG in MRP2 vesicles. All data are mean ± SD (n = 3).

Table 5.4: Calculated K_i-values of the fluorinated bile acid analogues for BSEP and literature data of their endogenous bile acid counterparts (Van Beusekom et al. 2013).

Data are mean ± SD (n = 3). CA: cholic acid; GCA: glycocholic acid.

	K _i for BSEP (µM)	Affinity endogenous counterpart (µM)
CA	95.46 ± 33.97	Km CA: 11.3 ± 4.3
3α-FCA	198.9 ± 39.5	N/A
3β-FCA	216.3 ± 53.0	N/A
3β-FGCA	87.38 ± 14.61	Km GCA: 9.0 ± 2.0
3β-FCDC	48.24 ± 3.94	N/A

Table 5.5: Calculated K_i-values of cholic acid (CA) and 3β-FCA for MRP2.

Data are mean ± SD (n = 3). No literature data was found.

	K _i for MRP2 (µM)
CA	95.46 ± 33.97
3β-FCA	216.3 ± 53.0

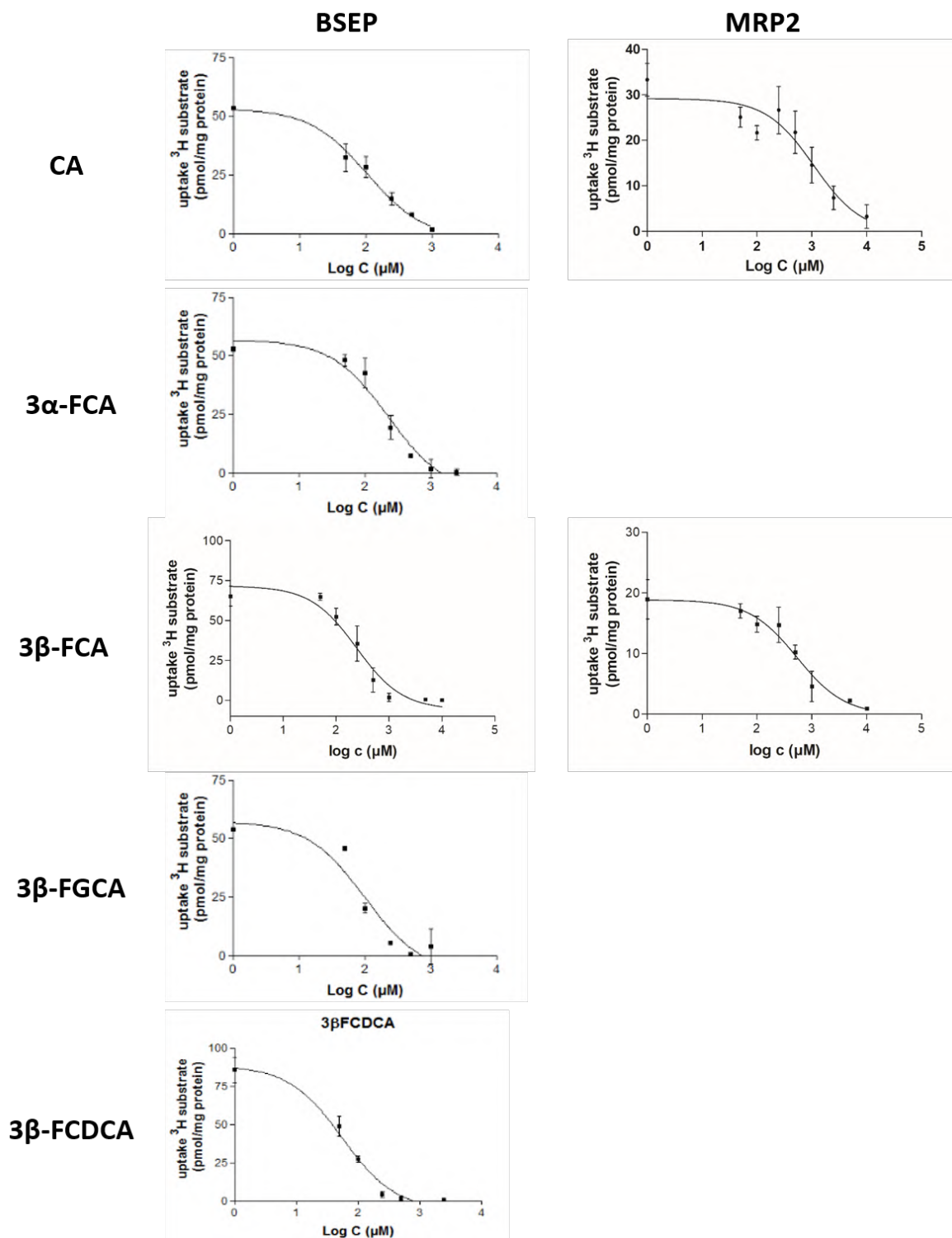


Figure 5.7: Graphs of the concentration dependent decrease in uptake of tritium labeled substrate ($[^3\text{H}]$ TC for BSEP, $[^3\text{H}]$ EbG for MRP2). IC₅₀s were determined by Graphpad, their respective K_i-values can be found in Table 5.3. Data are mean \pm SD (n = 3).

5.4 Discussion

A number of ^{18}F labeled bile acids have been developed (see Chapter 4) and were evaluated *in vitro* for their $\text{LogD}(7.4)$, (metabolic) stability and recognition by the relevant bile acid transporters. These results can help determine if the developed PET bile acid tracers are suitable (i.e.: resemble endogenous bile acids) to monitor (disturbed) hepatobiliary transport of bile acids *in vivo* with a PET scan.

The $\text{LogD}(7.4)$ values of the ^{18}F labeled bile acids were determined at pH 7.4 and compared to their endogenous bile acid counterparts (Roda et al. 1990). The $\text{logD}(7.4)$ values of $3\alpha\text{-}^{18}\text{F}\text{FCA}$ and $3\beta\text{-}^{18}\text{F}\text{FCA}$ (0.92 ± 0.17 and 1.19 ± 0.10 resp.) were in accordance with the $\text{logD}(7.4)$ value of cholic acid at pH 7.4 ($\text{logD}(7.4) = 1.1$). The glycine conjugate of $3\beta\text{-}^{18}\text{F}\text{FCA}$, $3\beta\text{-}^{18}\text{F}\text{FGCA}$, showed a much lower $\text{LogD}(7.4)$ of 0.011 ± 0.10 , which is in line with the fact that conjugated bile acids have a lower pK_a and are therefore more ionized at physiological pH ($\text{LogD}(7.4)$ glycocholic acid pH 7.4: -0.4). The $\text{LogD}(7.4)$ of $3\beta\text{-}^{18}\text{F}\text{FCDCA}$ (1.42 ± 0.16) was higher than $3\beta\text{-}^{18}\text{F}\text{FCA}$ and comparable to the $\text{logD}(7.4)$ value of chenodeoxycholic acid at pH 7.4 (2.25). This can be explained by the absence of a 12-hydroxy functional group on the fluorinated chenodeoxycholic acid molecule that results in a higher lipophilicity. Overall, the ^{18}F labeled bile acids resemble their endogenous counterparts well regarding $\text{LogD}(7.4)$ value and ionizability. This is important for substrate recognition by the bile acid transporters, as one of the key elements for recognition is a negatively ionized moiety (Dong et al. 2015).

The stability of the fluorinated PET tracers was assessed in presence of primary mouse hepatocytes: no radiometabolites were detected in a time period up to 1 hour. Considering the fact that the overwhelming majority of bile acids are conjugated in the liver (with glycine or taurine) *in vivo*, the dominant radiometabolites were hypothesized to be conjugates of the ^{18}F labeled bile acids (but not $3\beta\text{-}^{18}\text{F}\text{FGCA}$, which is already conjugated with glycine) (Chiang 2013). For example, a dose of ursodeoxycholate or chenodeoxycholate is conjugated for more than 97 % after a single pass through rat liver (Gurantz et al. 1991; Yeh et al. 1997). However, the developed compounds are remarkably stable. It might be possible that the introduction of a fluorine atom on the 3 position of the bile acid has an effect on substrate recognition by the enzymes responsible for conjugating bile acids: bile acid coenzyme A (CoA) ligase and bile acid CoA amino acid N-acyltransferase. To our

knowledge, no in-depth quantitative structure-activity relationship (QSAR) study has been conducted to evaluate the substrate requirements of abovementioned enzymes, and thus link this result to literature data.

Uptake of the fluorinated bile acids 3 α -FCA, 3 β -FCA, 3 β -FGCA and 3 β -FCDCA by NTCP and OATP1B1 was assessed with competition assays, using model substrates [³H]TC for NTCP and [³H]EbG for OATP1B1. Km and Vmax values of these model substrates was in accordance with literature data. For NTCP, [³H]TC had a Km and Vmax of 15.27 \pm 2.46 μ M and 200.4 \pm 9.77 pmol/min.mg respectively (literature Km: 5.4 \pm 1.8 μ M; literature Vmax: 229 \pm 24 pmol/min.mg; Gozalpour et al. 2014). For OATP1B1, [³H]EbG had a Km and Vmax of 11.72 \pm 1.59 μ M and 146.4 \pm 5.52 pmol/min.mg respectively (literature Km: 10 \pm 3.4 μ M; literature Vmax: 151 \pm 14 pmol/min.mg; Gozalpour et al. 2014).

Transport of the tritium labeled model substrates was reduced by increasing concentrations of the developed compounds, which means that they are substrates of NTCP and OATP1B1. Their affinity was quantified by Ki values. Because the inhibitors are in this case also substrates of the transporters under investigation, Ki and Km values are theoretically equal and can be compared (Vivian & Polli 2014).

The substitution of the 3-OH function by a more lipophilic fluorine atom on the 3 α - and 3 β -position of CA causes an increase in affinity for NTCP and OATP1B1, compared to CA. Although both 3-FCA epimers are a substrate for the bile acid transporters, 3 α -FCA displays a slightly higher affinity than 3 β -FCA for NTCP and OATP1B1 (2.53 \pm 0.76 μ M and 5.22 \pm 0.56 μ M resp. versus 6.18 \pm 0.59 and 9.67 \pm 0.83 μ M resp.). This difference in affinity for 3 α / β cholic acid epimers of bile acid transporters was already uncovered in cell lines that express the Apical Sodium-dependent Bile acid Transporter (ASBT; responsible for basolateral uptake of bile acids in the enterocytes). It was found that 3 β -OH-bile acids have a lower affinity than 3 α OH-bile acids for ASBT (González et al. 2014). In the present study, the hepatic basolateral uptake transporters NTCP and OATP1B1 also reveal a slight preference in affinity for the 3 α -FCA epimer.

Compound 3 β -FGCA, showed an increase in affinity for NTCP and OATP1B1 compared to the non-conjugated 3 β -FCA (1.09 \pm 0.34 and 4.24 \pm 0.16 μ M versus 6.18 \pm 0.59 and 9.67 \pm 0.83 μ M resp.). This is in line with literature data: conjugated bile acids have a higher affinity

for NTCP and OATP and BSEP than non-conjugated bile acids (Alrefai & Gill 2007; Suga et al. 2017). The acquired K_i values of 3β -FGCA are in accordance with the low micromolar K_m values of glycocholic acid that are found for NTCP (15.8 μ M; Dong et al. 2015) and OATP1B1 (14.7 μ M; Suga et al. 2017). Compound 3β -FCDCA was also a high affinity substrate of NTCP and OATP1B1, which is in line with literature data that chenodeoxycholic acid also uses NTCP and OATP1B1 (Dong et al. 2015; Suga et al. 2017).

All fluorinated compounds under investigation were able to inhibit the uptake of [3 H]TC by BSEP vesicles in a concentration dependent fashion. K_m of model substrate [3 H]TC was in line with literature: $3.89 \pm 1.44 \mu$ M (literature: 4.1 ± 0.5 ; Van Beusekom et al. 2013). The introduction of a fluorine atom on the 3 position of the CA backbone caused a decrease in affinity for the BSEP transporter, compared to the endogenous bile acid CA ($198.9 \pm 39.5 \mu$ M for 3α -FCA, 216.3 ± 53.0 for 3β -FCA; versus $95.46 \pm 33.97 \mu$ M for CA). Between the 3-FCA epimers, no difference in affinity for canalicular efflux by BSEP was observed, whereas basolateral uptake by NTCP and OATP1B1 does show a slight preference for 3α -FCA. Lead compound 3β -FCA was also evaluated in MRP2 vesicles and showed, just as CA, relatively low affinity for the transporter. Just as with basolateral uptake by NTCP and OATP1B1, 3β -FGCA showed greater affinity than its non-conjugated counterpart (3β -FCA) for BSEP. This is in accordance with literature data: conjugated bile acids have a higher affinity for BSEP than unconjugated bile acids (Stieger 2011).

5.5 Conclusion

The fluorine labeled bile acid analogues 3α -FCA, 3β -FCA, 3β -FGCA and 3β -FCDCA are found to be stable for use *in vivo*. Fluorine substitution possibly hampers metabolization, but does not have a considerable effect on substrate recognition by the transporters: they are substrates with low micromolar affinity for the relevant bile acid transport proteins NTCP, OATP1B1 and BSEP. The $\text{LogD}(7.4)$ values of the fluorinated bile acids are also in accordance with endogenous bile acids. The developed compounds are therefore deemed suitable to monitor (disturbed) hepatobiliary transport of bile acids *in vivo* with PET.

5.6 References

- Alrefai, W. a & Gill, R.K., 2007. Bile acid transporters: structure, function, regulation and pathophysiological implications. *Pharmaceutical research*, 24(10), pp.1803–23.
- Brouwer, K.L.R. et al., 2013. In vitro methods to support transporter evaluation in drug discovery and development. *Clinical pharmacology and therapeutics*, 94(1), pp.95–112.
- Chiang, J., 2013. Bile Acid Metabolism and Signalling. *Compr Physiol*, 3(3), pp.1191–1212.
- Dong, Z., Ekins, S. & Polli, J.E., 2015. A substrate pharmacophore for the human sodium taurocholate co-transporting polypeptide. *International Journal of Pharmaceutics*, 478, pp.88–95.
- González, P.M. et al., 2014. Structural requirements of the human sodium-dependent bile acid transporter (hASBT): Role of 3- and 7-OH moieties on binding and translocation of bile acids. *Molecular Pharmaceutics*, 11, pp.588–598.
- Gozalpour E, Greupink R, Wortelboer HM, Bilos A, Schreurs M, Russel FGM, Koenderink JB (2014) Interaction of digitalis-like compounds with liver uptake transporters NTCP, OATP1B1, and OATP1B3. *Mol Pharm* 11:1844–1855.
- Gurantz, D. et al., 1991. Hypercholeresis induced by unconjugated bile acid infusion correlates with recovery in bile of unconjugated bile acids. *Hepatology*, 13(3), pp.540–550.
- Kolhatkar V, Polli JE (2012) Structural requirements of bile acid transporters: C-3 and C-7 modifications of steroidal hydroxyl groups. *Eur J Pharm Sci* 46:86–99.
- Roda, a et al., 1990. Bile acid structure-activity relationship: evaluation of bile acid lipophilicity using 1-octanol/water partition coefficient and reverse phase HPLC. *Journal of lipid research*, 31, pp.1433–1443.
- Severgnini, M. et al., 2012. A rapid two-step method for isolation of functional primary mouse hepatocytes: Cell characterization and asialoglycoprotein receptor based assay development. *Cytotechnology*, 64(2), pp.187–195.
- Stieger, B., 2011. *Handbook of Experimental Pharmacology vol 201: The Role of the Sodium-*

Taurocholate Cotransporting Polypeptide (NTCP) and of the Bile Salt Export Pump (BSEP) in Physiology and Pathophysiology of Bile Formation,

Suga, T. et al., 2017. Preference of Conjugated Bile Acids over Unconjugated Bile Acids as Substrates for OATP1B1 and OATP1B3. *Plos One*, 12(1), p.e0169719.

Trauner, M. & Boyer, J.L., 2003. Bile Salt Transporters : Molecular Characterization , Function , and Regulation. *Physiol Rev*, 83, pp.633–671.

Van Beusekom CD, van den Heuvel JJMW, Koenderink JB, Schrickx JA, Russel FGM (2013) The feline bile salt export pump: A structural and functional comparison with canine and human Bsep/BSEP. *BMC Vet Res* 9:1–10.

Vaz, F.M. & Ferdinandusse, S., 2017. Bile acid analysis in human disorders of bile acid biosynthesis. *Molecular Aspects of Medicine*, 56, pp.10–24.

Vivian, D. & Polli, J., 2014. Mechanistic Interpretation of Conventional Michaelis-Menten Parameters in a Transporter System. *eur j pharm sci*, (60), pp.44–52.

Yeh, H.Z. et al., 1997. Effect of side chain length on biotransformation, hepatic transport, and choleric properties of chenodeoxycholy homologues in the rodent: Studies with dinorchenodeoxycholic acid, norchenodeoxycholic acid, and chenodeoxycholic acid. *Hepatology*, 26(2), pp.374–385.

CHAPTER 6:

IN VIVO EVALUATION OF ^{18}F LABELED BILE ACIDS IN WILD-TYPE MICE

This chapter contains parts that have been adapted from:

De Lombaerde S, Kersemans K, Neyt S, Verhoeven J, Vanhove C, De Vos F; *Evaluating Hepatobiliary Transport with ^{18}F -Labeled Bile Acids: The Effect of Radiolabel Position and Bile Acid Structure on Radiosynthesis and In Vitro and In Vivo Performance*; Contrast Media & Molecular Imaging, Volume 2018, Article ID 6345412, p1-9

De Lombaerde S, Neyt S, Kersemans K, Verhoeven J, Devisscher L, Van Vlierberghe H, et al.; *Synthesis, in vitro and in vivo evaluation of 3 β -[^{18}F]fluorocholeic acid for the detection of drug-induced cholestasis in mice*; PLoS One. 2017;12 (3), p1-14

6.1 Introduction

The synthesis and hepatobiliary transport of bile acids has been discussed extensively in Chapter 1. As reported in Chapter 2, the highly efficient hepatobiliary transport of bile acids can be disturbed in liver disease (de Lima Toccafondo Vieira & Tagliati 2014; Jüngst et al. 2013; Kubitz et al. 2012). Drug-induced liver injury (DILI) for example, is an acquired liver disorder responsible for a significant amount of hospitalizations and a prime cause of rejecting new drug candidates during drug development (Bleibel et al. 2007; Regev 2014). A major part of DILI is represented by drug-induced cholestasis (DIC), which can result from inhibition of the bile acid transporters by drugs, leading to a toxic accumulation of bile acids in the liver (Padda et al. 2011; Pauli-Magnus & Meier 2006). Clinical features may consist of nausea, abdominal pain, jaundice and pruritus (Padda et al. 2011).

It is important to detect drug-induced cholestasis early on in drug development. In this regard, nuclear imaging is a powerful tool to investigate interference with the bile acid transporters on a molecular level (Testa et al. 2015). Various radiotracers have already been developed that show hepatobiliary transport by these transporters. Single Photon Emission Computed Tomography (SPECT)-tracers such as $^{99\text{m}}\text{Tc}$ -mebrofenin, [$^{99\text{m}}\text{Tc}$]-DTPA-CDCA and [$^{99\text{m}}\text{Tc}$]-DTPA-CA are substrates of OATP1B1, OATP1B3 and MRP2 (Ghibellini et al. 2008; Neyt et al. 2016). Although the latter two are bile acid analogues, no transport by NTCP or BSEP was observed. [^{11}C]dehydropravastatin, [^{11}C]rosuvastatin, [^{11}C]TIC-Me, [^{11}C]glyburide and [^{11}C]telmisartan are Positron Emission Tomography (PET)-tracers that provide insight into (altered) transport function by OATP, NTCP or MRP2 (Shingaki et al. 2013; He et al. 2014; Takashima et al. 2012; Tournier et al. 2013; Shimizu et al. 2012). However, in order to study bile acid transport and the corresponding disturbances, the desired tracer would be a radiolabeled bile acid, predominantly transported by NTCP, BSEP, and also by OATP and MRP2 (de Lima Toccafondo Vieira & Tagliati 2014).

The synthesis and *in vivo* evaluation of different ^{11}C labeled bile acid analogues such as [^{11}C]choly sarcosine was described (Frisch et al. 2012; Schacht et al. 2016). Although the results are promising, the half-life of the ^{11}C -isotope can limit its use. Consequently, two ^{18}F labeled bile acids were developed and evaluated *in vivo* in mice (Jia et al. 2014; Testa et al. 2017). In these studies, the molecular structures of the bile acid PET tracers were expanded

significantly by the addition of substantial ^{18}F radiolabeled groups. Due to these major structural modifications, questions were raised whether the transport mechanism was still comparable to endogenous bile acids (Frisch & Sørensen 2014).

As described in the previous chapters, the aim of this dissertation was to develop and evaluate ^{18}F labeled bile acids with minor modifications on the endogenous bile acid structure. These tracers can represent endogenous bile acid transport and can be used as imaging probe for preclinical evaluation of drug interference with the hepatic bile acid transporters or in other liver diseases. In Chapter 4, four ^{18}F labeled bile acids were synthesized: 3β - ^{18}F FCA, 3α - ^{18}F FCA, 3β - ^{18}F FGCA and 3β - ^{18}F CDCA. In Chapter 5, *in vitro* assays were performed to determine the bile acid transporters involved for uptake in, and efflux out of, the liver. All synthesized tracers are substrates of the relevant bile acid transporters *in vitro*.

In this Chapter, the *in vivo* pharmacokinetics of the developed tracers will be investigated in healthy wild-type mice. Moreover, 3β - ^{18}F FCA will be used as a tool to evaluate the inter- and intra-animal variability to quantify the tracer's hepatobiliary transport characteristics. Finally, 3β - ^{18}F FCA will be used to monitor disturbed hepatobiliary transport of bile acids *in vivo* through the NTCP/OATP and BSEP/MRP2 transport systems by dosing mice with the OATP(oatp)/MRP2(mrp2) inhibitor rifampicin (Vavricka et al. 2002; Shingaki et al. 2013; Kaneko et al. 2018) and the NTCP(ntcp)/BSEP(bsep) inhibitor bosentan (Fattinger et al. 2001; Leslie et al. 2007; Lepist et al. 2014).

6.2 Materials and methods

6.2.1 Radiosynthesis

The radiosynthesis of each ^{18}F labeled bile acid (3β - ^{18}F FCA, 3α - ^{18}F FCA, 3β - ^{18}F FGCA and 3β - ^{18}F FCDCA) has been described in detail in Chapter 4.

6.2.2 PET imaging protocol and animal experiments

The *in vivo* transport characteristics of the ^{18}F labeled bile acids were evaluated in wild-type FVB-mice (female, 5 weeks old). The animals were housed and handled in accordance with the European Ethics Committee guidelines and the experiments were approved by the Animal Experimental Ethical Committee of Ghent University (ECD 15/69). Food and water was provided *ad libitum*, but animals were fasted overnight before the PET-scan. Mice were anesthetized with 1.5 v:v % isoflurane in 100 % O_2 for the duration of the experiment. An intravenous polyethylene line was inserted in the lateral tail vein and fixated. The animals were placed in the small animal PET/CT-scanner (FLEX Triumph II small animal PET/CT-scanner; PET field of view: 7.5 cm axial; 1.3 mm spatial resolution; TriFoil Imaging) on a heated bed. A CT-scan was acquired for anatomical correlation.

6.2.2.1 *Evaluation of lead compound 3β - ^{18}F FCA*

In vivo pharmacokinetics of 3β - ^{18}F FCA were investigated by a 1 hour dynamic PET scan, started directly after intravenous injection of 30 MBq 3β - ^{18}F FCA in three mice. Four and six hours post-injection, a 30 minutes static PET scan was acquired to evaluate tracer distribution.

The inter- and intra-animal variability of 3β - ^{18}F FCA was evaluated to assess the tracer's reproducibility. For inter-animal variability, three mice were scanned with 3β - ^{18}F FCA on the same day. For intra-animal variability, the same mouse was scanned with 3β - ^{18}F FCA on three different days. Mean, standard deviation and coefficient of variation (CV) were determined of the tracer's kinetic characteristics (see PET data analysis).

The interaction of rifampicin (Sigma Aldrich) and bosentan (Activate Scientific) on *in vivo* 3β - ^{18}F FCA transport was examined to confirm that the tracer is transported by ntcp/oatp and bsep/mrp2. FVB-mice were divided into 3 different groups (n=3 per group): rifampicin, bosentan, and a control, DMSO vehicle treated, group. Both drugs were

administered in doses of 100 mg/kg, intra-peritoneal in DMSO:PBS 70:30 v:v (rifampicin) or DMSO (bosentan) 1 hour before the start of the PET-scan. An additional dose (25 mg/kg for rifampicin in DMSO:PBS 40:60 v:v, 50 mg/kg for bosentan in DMSO) was co-injected intravenously with the tracer. For each scan, 10 MBq of 3β - ^{18}F]FCA was administered intravenously and a 1 hour dynamic scan was started. Immediately after the dynamic scan, 18 MBq ^{18}F]fluorodeoxyglucose (^{18}F]FDG) was injected intravenously. After 20 minutes, a 20 minutes static scan was taken.

6.2.2.2 Comparison of the different ^{18}F labeled bile acids

Each ^{18}F labeled bile acid (3β - ^{18}F]FCA, 3α - ^{18}F]FCA, 3β - ^{18}F]FGCA and 3β - ^{18}F]FCDCA) was evaluated in a group of three healthy wild-type mice. Approx. 9 MBq tracer was injected intravenously after starting a 1 hour dynamic PET scan. Following this PET-scan, 9 MBq ^{18}F]FDG was injected and twenty minutes later, a second PET-scan with a 20 minutes acquisition time was started. Tracer kinetics (see PET data analysis) were compared to 3β - ^{18}F]FCA as a reference.

6.2.2.3 PET data analysis

All PET-scans were acquired in list-mode and were iteratively reconstructed (50 iterations). Unless specified otherwise, the 1 hour dynamic scans were reconstructed in the following frames: 8 x 15 s; 16 x 30 s; 10 x 60 s; 20 x 120 s. For presentation purposes, maximum intensity projections (MIPs) of the PET/CT images were generated in Amide (A Medical Imaging Data Examiner) (Loening & Gambhir 2003). The data were further analyzed using Pmod software v3.405 (PMOD Technologies): Regions of interest (ROIs) were drawn manually over the liver, gallbladder and intestines. On the static ^{18}F]FDG scan, the left ventricle was delineated and this ROI was pasted on the dynamic scan to obtain an image-derived arterial blood concentration (Moerman et al. 2011). The uptake of radioactivity in liver, gallbladder and intestines was expressed as a percentage of the injected dose (injected radioactivity; % ID) and normalized for the weight of a 20 g mouse. The % ID in these organs was monitored in function of time to obtain time-activity curves (TACs). Hepatic and biliary clearance of the tracers was determined with equation 1 and 2 from Ghibellini et al. 2004.

$$\text{Hepatic clearance} = \frac{\text{cumulative amount of tracer in liver}}{\text{AUC bloodconcentration}_{0 \rightarrow 60 \text{ min}}} \text{ Eq.1}$$

$$\text{Biliary clearance} = \frac{\text{cumulative amount of tracer in gallbladder\&intestines}}{\text{AUC bloodconcentration}_{0 \rightarrow 60 \text{ min}}} \text{Eq. 2}$$

The area under the curve (AUC), % ID and time-to-peak values of the TACs were determined in Graphpad Prism v5.00 Software. The obtained parameters of the different groups were compared with SPSS Statistics 23 Software. Differences between two groups were analyzed with the non-parametric Mann-Whitney U test. A p-value ≤ 0.05 was considered significant.

6.3 Results

6.3.1 Evaluation of lead compound 3β - ^{18}F FCA

Figure 6.1 shows a PET/CT image of 3β - ^{18}F FCA in a wild-type FVB mouse at different time points. After intravenous injection, the PET tracer accumulated rapidly and exclusively in the liver. Biliary clearance of the tracer was observed: radioactivity was visible in gallbladder and intestines. After 1 hour, almost all radioactivity was found in the gallbladder and intestines. No uptake was observed in the urinary bladder or other organs for a period up to 6 hours post-injection.

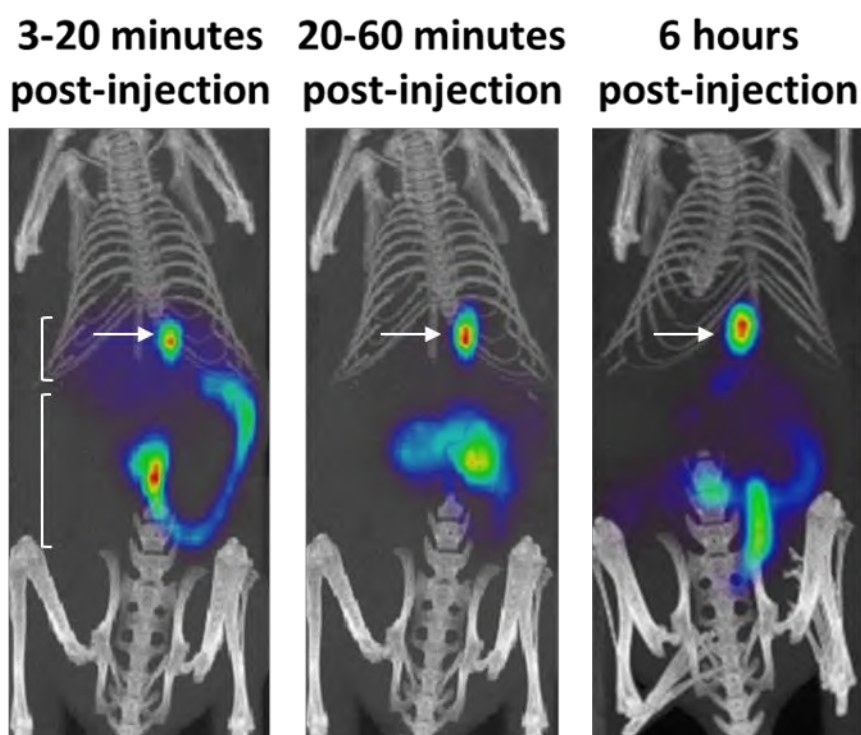


Figure 6.1: Maximum intensity projection PET/CT images of 3β - ^{18}F FCA in a wild-type FVB-mouse at different time points. Images were generated in AMIDE with a slice thickness of 12 mm. In the early phase (3-20 minutes post-injection), the liver (upper white accolade), gallbladder (white arrow) and intestines (lower white accolade) are visible on PET. In a later phase (20-60 minutes post-injection), all radioactivity is excreted from the liver to the gallbladder and intestines. The late phase PET/CT images (6 hours post-injection) show that 3β - ^{18}F FCA remains present only in gallbladder and intestines: visual analysis of all images showed no uptake in other organs than liver, gallbladder and intestines.

The inter- and intra-animal variation of 3β - ^{18}F FCA's hepatobiliary transport is visualized in Figure 6.2 and Figure 6.3; the corresponding metrics can be found in Table 6.1 and Table 6.2. The maximum coefficient of variance observed for all determined kinetic parameters inter-and intra-animal was 15.5 %.

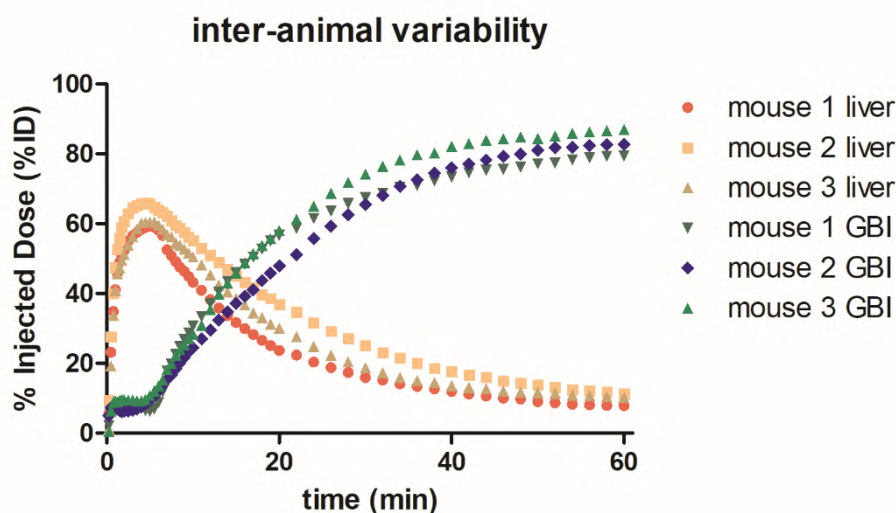


Figure 6.2: Inter-animal variability of 3β - ^{18}F FCA's time-activity curves in liver and gallbladder and intestines (GBI).

Table 6.1: Inter-animal variability of the determined kinetic parameters of 3β - ^{18}F FCA's hepatobiliary transport. SD: standard deviation; CV: coefficient of variance; GBI: gallbladder and intestines; AB: arterial blood; HC: hepatic clearance; BC: biliary clearance.

	Mouse 1	Mouse 2	Mouse 3	Mean	SD	CV (%)
AUC liver (% ID.min)	1345	1829	1539	1571	244	15.5
Max % ID liver (%)	59.28	65.86	60.50	61.88	3.50	5.7
Time-to-peak liver (min)	5.00	4.50	5.50	5.00	0.50	10
AUC GBI (% ID.min)	3444	3377	3738	3520	192	5.46
Max % ID GBI (%)	79.48	82.74	86.92	83.05	3.73	4.49
AUC AB concentration (kBq.min/mL)	11920	13289	12322	12510	704	5.62
HC (mL/min)	0.42	0.34	0.40	0.39	0.04	10.8
BC (mL/min)	0.55	0.49	0.50	0.51	0.03	6.3

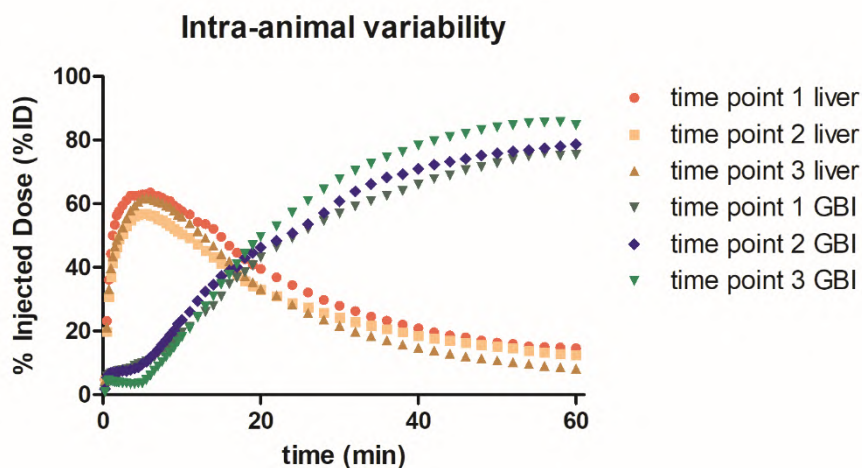


Figure 6.3: Intra-animal variability of 3β - ^{18}F FCA's time-activity curves in liver and gallbladder and intestines (GBI).

Table 6.2: Intra-animal variability of the determined kinetic parameters of 3β - ^{18}F FCA's hepatobiliary transport. SD: standard deviation; CV: coefficient of variance; GBI: gallbladder and intestines; AB: arterial blood; HC: hepatic clearance; BC: biliary clearance.

	Timepoint 1	Timepoint 2	Timepoint 3	Mean	SD	CV (%)
AUC liver (% ID.min)	1967	1710	1650	1776	168	9.5
Max % ID liver (%)	63.52	56.85	61.79	60.72	3.46	5.7
Time-to-peak liver (min)	6.00	5.50	5.50	5.67	0.29	5.1
AUC GBI (% ID.min)	2984	3179	3399	3187	208	6.51
Max % ID GBI (%)	75.87	78.75	85.67	80.10	5.04	6.29
AUC AB concentration (kBq.min/mL)	12542	14521	11620	12894	1482	11.5
HC (mL/min)	0.38	0.33	0.39	0.37	0.03	8.8
BC (mL/min)	0.50	0.45	0.55	0.50	0.05	10.0

The hepatobiliary transport of 3β - ^{18}F FCA was also studied in mice that were dosed with oatp/mrp2 inhibitor rifampicin or ntcp/bsep inhibitor bosentan. TACs of 3β - ^{18}F FCA distribution in bosentan- and rifampicin-treated mice are depicted in Figure 6.4 and Figure 6.5 respectively. The metrics derived from these TACs are summarized in Table 6.3. Rifampicin and bosentan treated mice showed altered pharmacokinetics of 3β - ^{18}F FCA compared to control animals. The time-to-peak of the liver TACs significantly increased 2.9- and 1.7-fold compared to control mice for rifampicin and bosentan, respectively ($p = 0.0073$ and $p = 0.021$ resp.). The maximum % ID in the liver was significantly lower than control for both compounds ($49.7 \pm 1.6\%$ and $54.4 \pm 1.7\%$ for rifampicin and bosentan respectively, compared to $71.2 \pm 3.5\%$ for control) ($p = 0.007$ and $p = 0.015$ resp.). Efflux towards the gallbladder and intestines was impaired: the AUC-value of the gallbladder & intestines TACs was 3.1 times lower for rifampicin and 1.7 times lower for bosentan, compared to the control animals ($p = 0.0007$ and $p = 0.025$ resp.). The AUC of the arterial blood TACs was 2-fold and 2.4-fold higher than control for rifampicin and bosentan, respectively ($p = 0.031$ and $p = 0.017$ resp.) (see Figure 6.6). Hepatic clearance and biliary clearance values were significantly lower compared to control. Figure 6.7 shows representative MIPs of the altered hepatobiliary transport of 3β - ^{18}F FCA in rifampicin-treated mice.

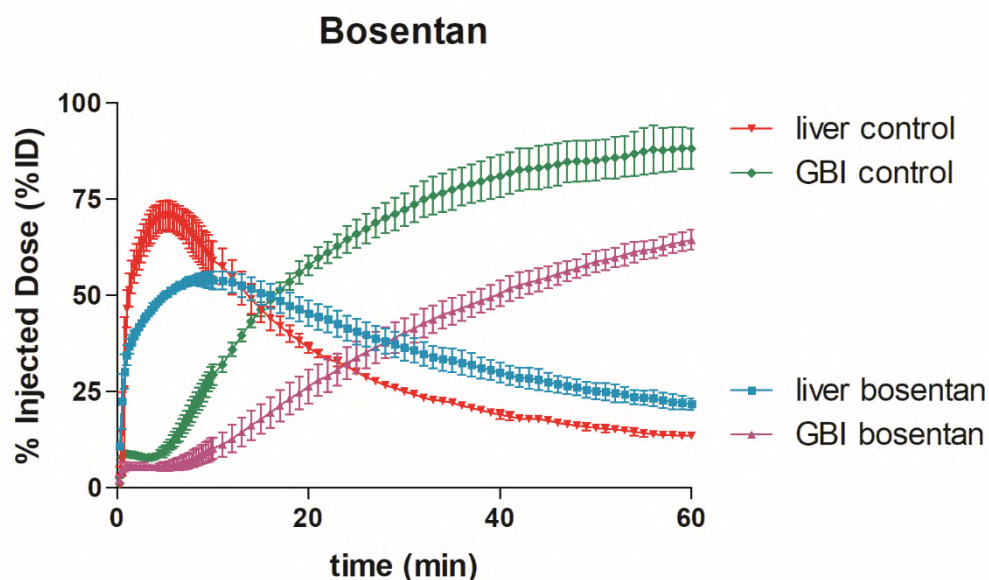


Figure 6.4: Liver and gallbladder & intestines (GBI) TACs of 3β - ^{18}F FCA in control and bosentan treated FVB-mice ($n=3$ per group). Uptake of 3β - ^{18}F FCA is expressed as % injected dose (% ID) and normalized for a 20 g mouse. Values are expressed as mean \pm SD.

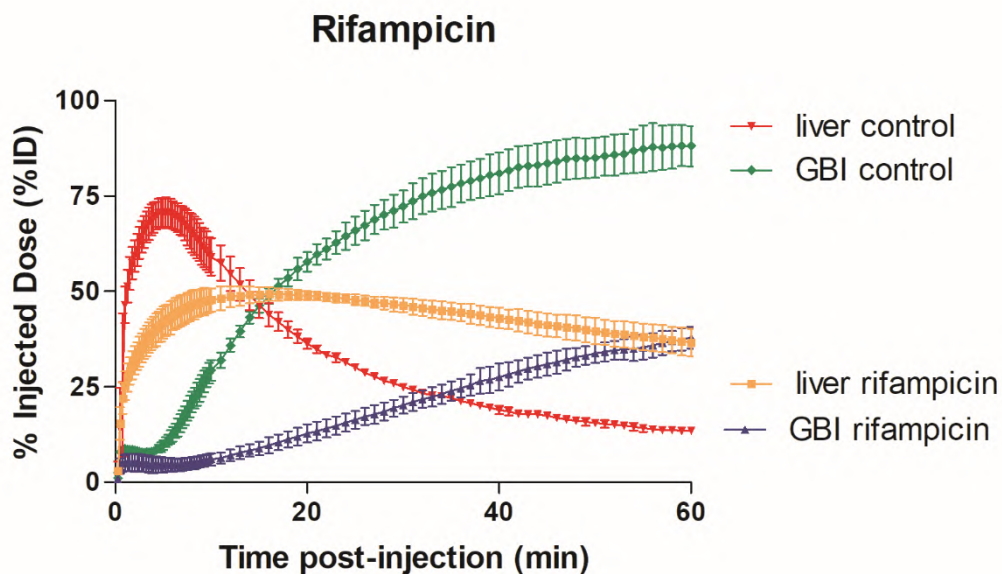


Figure 6.5: Liver and gallbladder & intestines (GBI) TACs of 3β - ^{18}F FCA in control and rifampicin treated FVB-mice ($n=3$ per group). Uptake of 3β - ^{18}F FCA is expressed as % injected dose (% ID) and normalized for a 20 g mouse. Values are expressed as mean \pm SD.

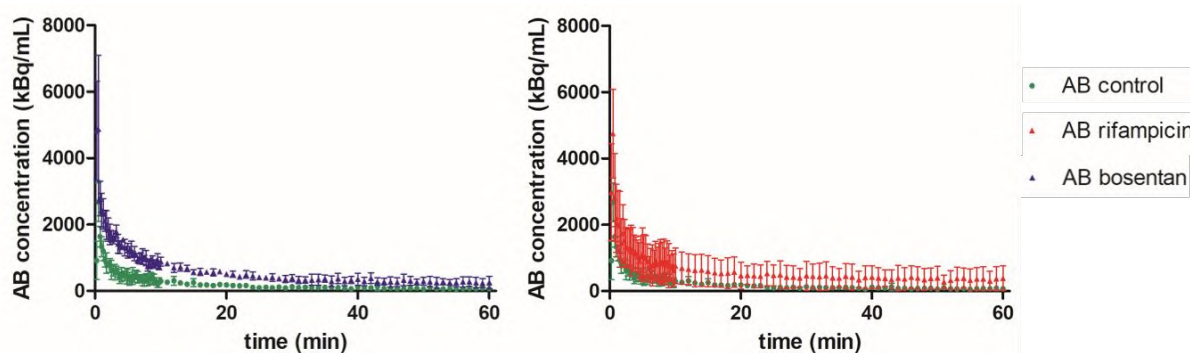


Figure 6.6: TACs of 3β - ^{18}F FCA in arterial blood (AB) for vehicle (green), rifampicin (red) and bosentan (blue) treated mice ($n=3$ per group). Values are expressed as mean \pm SD.

Table 6.3: Metrics obtained from TACs of 3β-[¹⁸F]FCA in control, rifampicin and bosentan treated animals (n=3 per group). Values are expressed as mean ± SD. *: significant difference compared to control group (*p<0.05; **p<0.01; ***p<0.001).

GBI: gallbladder and intestines; AB: arterial blood.

	Control	Rifampicin 100 mg/kg IP + 25 mg/kg IV	Bosentan 100 mg/kg IP + 50 mg/kg IV
AUC liver (% ID.min)	1909 ± 20	2591 ± 86**	2209 ± 133*
Max % ID liver (%)	71.23 ± 3.57	49.70 ± 1.64**	54.37 ± 1.73*
Time-to-peak liver (min)	5.50 ± 1.15	16.00 ± 5.00*	9.25 ± 1.64*
AUC GBI (% ID.min)	3718 ± 182	1208 ± 132***	2196 ± 181*
Max % ID GBI (%)	88.57 ± 5.80	37.94 ± 2.89**	64.41 ± 2.56*
AUC AB concentration (kBq.min/mL)	14023 ± 3060	29023 ± 7893*	34187 ± 4493*
Hepatic clearance (mL/min)	0.38 ± 0.08	0.21 ± 0.07*	0.16 ± 0.01*
Biliary clearance (mL/min)	0.47 ± 0.12	0.16 ± 0.05**	0.19 ± 0.01**

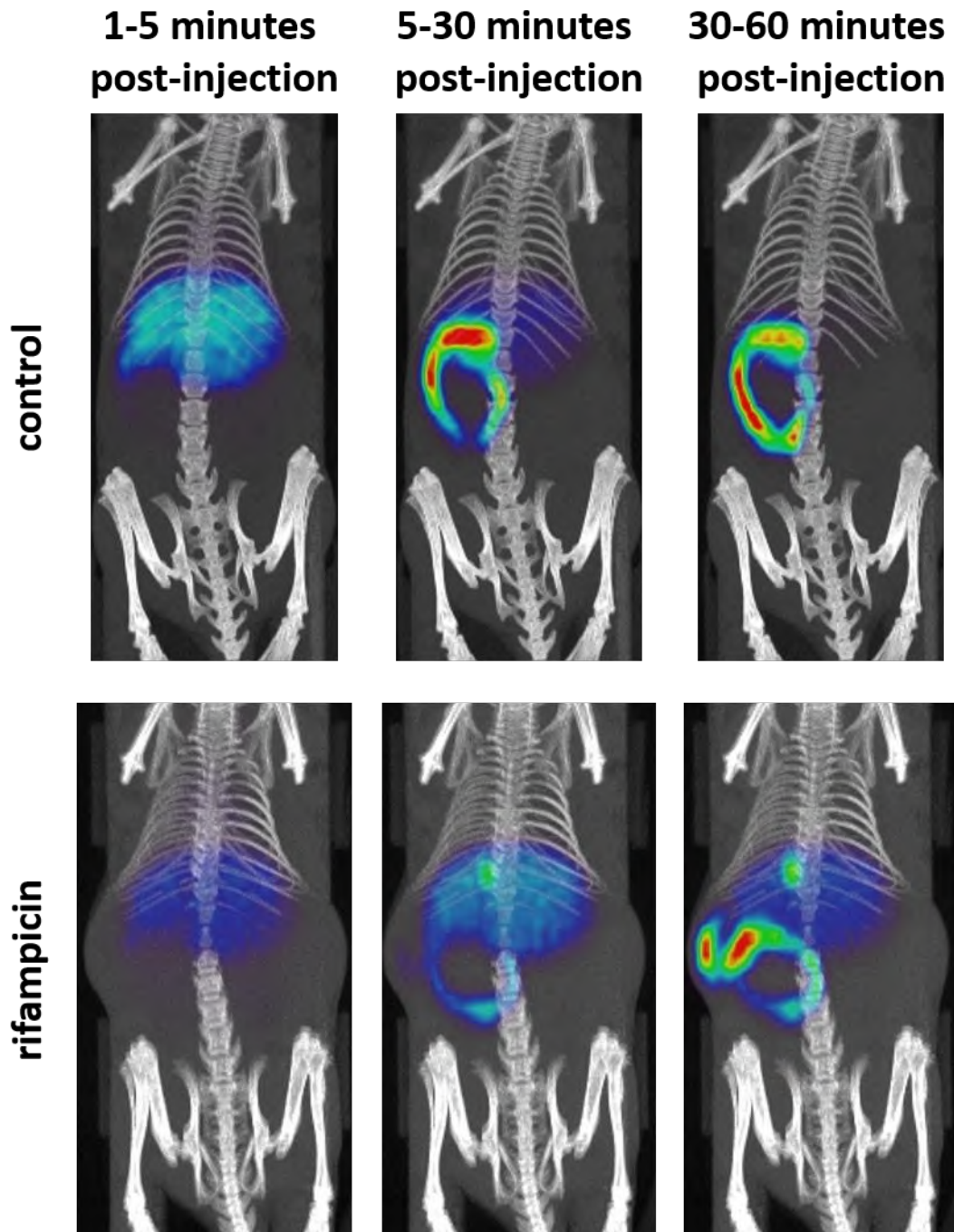


Figure 6.7: MIP PET/CT images of $3\beta\text{-}[^{18}\text{F}]\text{FCA}$ in control and rifampicin-treated wild-type FVB-mice at different time points (slice thickness: 15 mm). Compared to control, the tracer accumulates slower in the liver of rifampicin-treated mice. The subsequent biliary excretion of $3\beta\text{-}[^{18}\text{F}]\text{FCA}$ is also impaired: the radioactivity accumulates more in the liver of rifampicin-treated mice than control.

6.3.2 Comparison of the different ^{18}F labeled bile acids

The ^{18}F labeled bile acids 3α - ^{18}F FCA, 3β - ^{18}F FCA, 3β - ^{18}F FGCA and 3β - ^{18}F FCDCA were evaluated in wild-type mice and their TACs were compared to reference tracer 3β - ^{18}F FCA (Figure 6.8; Table 6.4). Compounds 3β - ^{18}F FCA, 3α - ^{18}F FCA, 3β - ^{18}F FGCA and 3β - ^{18}F FCDCA showed exclusive hepatic uptake after intravenous injection. The hepatic uptake of reference tracer 3β - ^{18}F FCA was slightly, yet significantly slower than 3α - ^{18}F FCA (5.33 ± 0.24 vs. 3.33 ± 0.62 minutes; $p = 0.041$), but significantly faster than 3β - ^{18}F FCDCA (5.33 ± 0.24 vs. 10.17 ± 0.62 minutes; $p = 0.007$). There was no significant difference in the time-to-peak and AUC of the liver TACs between 3β - ^{18}F FGCA and 3β - ^{18}F FCA.

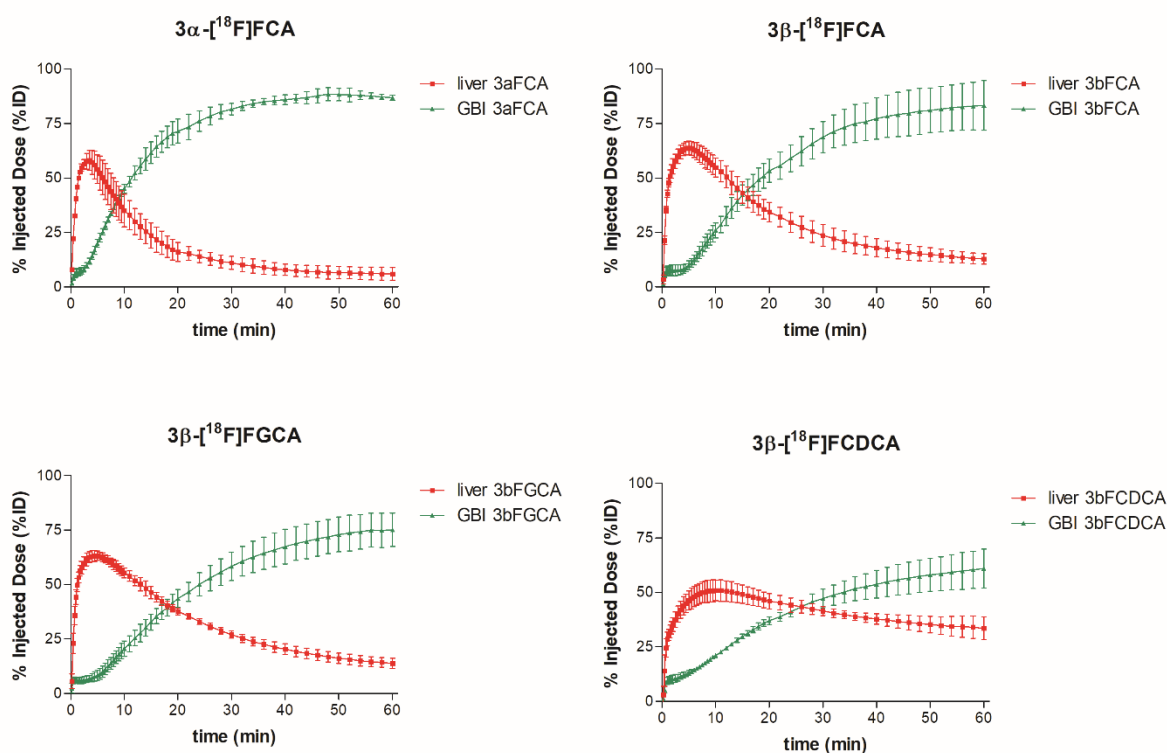


Figure 6.8: TACs of 3α - ^{18}F FCA, 3β - ^{18}F FCA, 3β - ^{18}F FGCA and 3β - ^{18}F FCDCA in liver (red curve) and gallbladder and intestines (GBI; green curve) of wild-type mice. Uptake of the tracers was expressed as % injected dose (% ID) and normalized for a 20 g mouse.

Data are mean \pm SD ($n = 3$ per group)

Once in the liver, the tracers were excreted in gallbladder and intestines. Almost all of the injected activity (approx. 80 %) of 3α - ^{18}F FCA, 3β - ^{18}F FCA and 3β - ^{18}F FGCA was found in gallbladder and intestines after 1 hour. Due to slower excretion of 3β - ^{18}F FCDCA

from the liver, only 60 % of the injected dose was found in gallbladder and intestines after 1 hour. Of the four tracers, only the hepatic and biliary clearance of 3β - ^{18}F FCDCA (0.15 ± 0.04 mL/min and 0.18 ± 0.04 mL/min resp.) was significantly lower compared to 3β - ^{18}F FCA (0.35 ± 0.04 mL/min and 0.46 ± 0.08 mL/min resp.; $p = 0.008$ and $p = 0.005$ resp.). No uptake was observed in other organs for all tracers under investigation. Representative PET/CT images of 3α - ^{18}F FCA, 3β - ^{18}F FGCA and 3β - ^{18}F FCDCA are displayed in Figure 6.9.

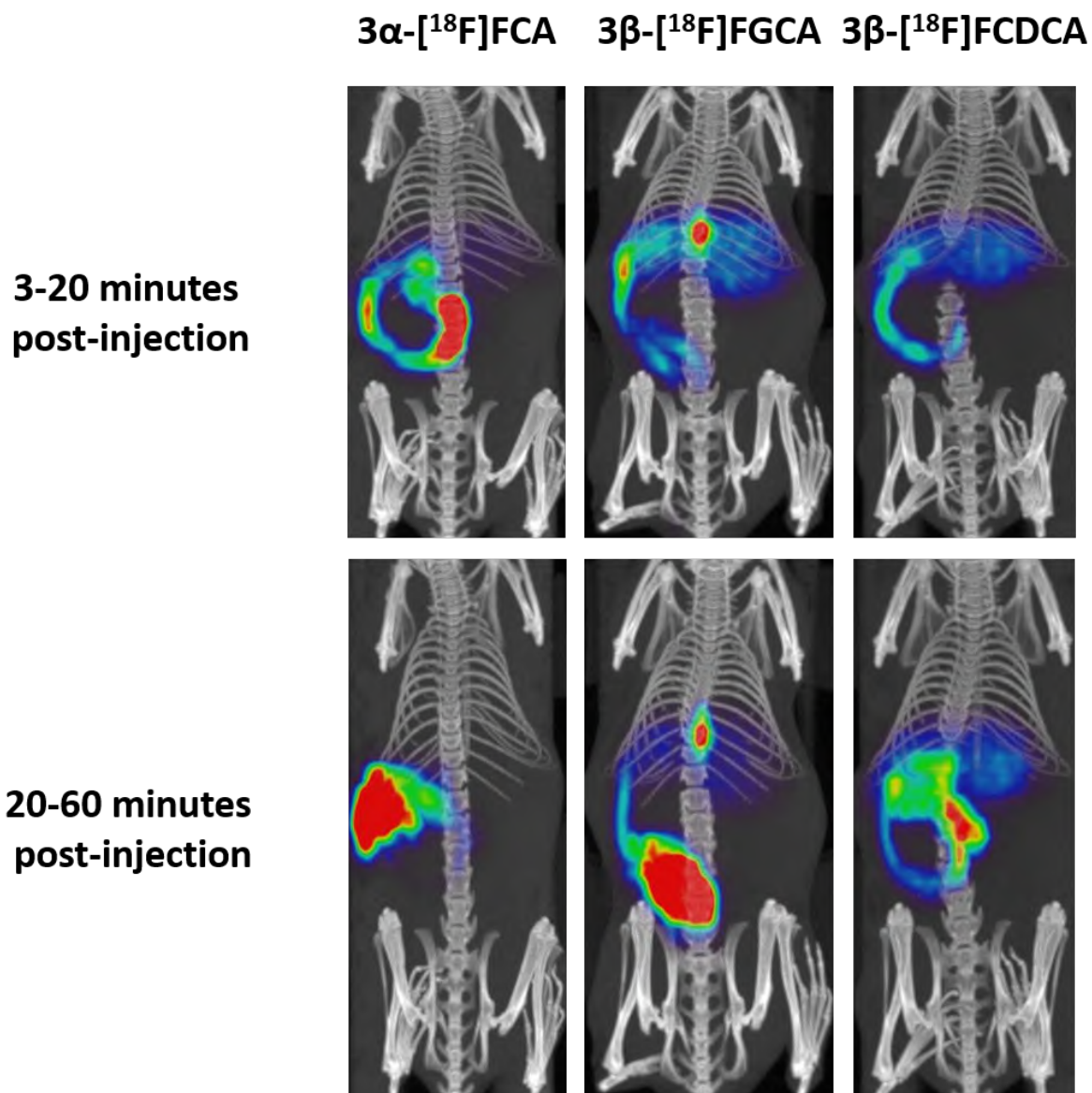


Figure 6.9: Representative MIP PET/CT of 3α - ^{18}F FCA, 3β - ^{18}F FGCA and 3β - ^{18}F FCDCA in a wild-type mouse (slice thickness: 15 mm). After intravenous injection, the tracers showed exclusive uptake in the liver and some biliary excretion (3-20 minutes). The ^{18}F labeled bile acids accumulate in gallbladder and intestines (20-60 minutes post injection).

Biliary excretion of 3β - ^{18}F FCDCA is visually slower.

Table 6.4: Metrics of the ¹⁸F labeled bile acids' TACs. The values are expressed as mean \pm SD (n = 3). Significant differences compared to the 3 β -[¹⁸F]FCA values are marked with * (*p<0.05; **p<0.01; ***p<0.001). GBI: gallbladder and intestines; AB = arterial blood.

	3 β -[¹⁸ F]FCA	3 α -[¹⁸ F]FCA	3 β -[¹⁸ F]FGCA	3 β -[¹⁸ F]FCDCA
AUC liver (% ID.min)	1785 \pm 194	1065 \pm 171*	1907 \pm 58	2449 \pm 111*
Max % ID liver (%)	63.80 \pm 2.61	58.58 \pm 3.19	63.58 \pm 1.84	51.01 \pm 3.94*
Time-to-peak liver (min)	5.33 \pm 0.24	3.33 \pm 0.62*	5.17 \pm 0.62	10.17 \pm 0.62**
AUC GBI (% ID.min)	3499 \pm 340	4184 \pm 109*	3021 \pm 276	2515 \pm 189*
Max % ID GBI (%)	83.44 \pm 9.27	88.70 \pm 2.38	75.32 \pm 6.30	60.93 \pm 7.29*
AUC AB concentration (kBq.min/mL)	13003 \pm 1032	14007 \pm 2150	10192 \pm 1404	28437 \pm 4380*
Hepatic clearance (mL/min)	0.35 \pm 0.04	0.32 \pm 0.06	0.40 \pm 0.04	0.15 \pm 0.04**
Biliary clearance (mL/min)	0.46 \pm 0.08	0.49 \pm 0.10	0.47 \pm 0.07	0.18 \pm 0.04**

6.4 Discussion

A set of ^{18}F labeled bile acids was synthesized to monitor hepatobiliary transport efficiency of bile acids *in vivo*. Compounds 3α - ^{18}F FCA, 3β - ^{18}F FCA, 3β - ^{18}F FGCA and 3β - ^{18}F FCDCa show remarkable structural resemblance to their endogenous bile acid counterparts cholic acid and chenodeoxycholic acid. It was hypothesized that the substitution of the 3-OH group by a fluorine atom would not have a major effect on transport by the bile acid transporters, as fluorine is isosteric and iso-electronic with a OH-group. Moreover, the 3α -OH group is not an absolute requisite for active bile acid transport (Baringhaus et al. 1999; González et al. 2014). In Chapter 5, *in vitro* assays confirmed that abovementioned tracers are transported by the relevant bile acid transporters NTCP, OATP, BSEP and MRP2. In this Chapter, the *in vivo* characteristics of the developed tracers was investigated in wild-type mice.

Lead compound 3β - ^{18}F FCA showed fast and exclusive hepatic uptake after intravenous injection, followed by biliary excretion in gallbladder and intestines. TACs of 3β - ^{18}F FCA in the liver, gallbladder and intestines and arterial blood were generated of which several kinetic parameters could be derived. Hepatic uptake can be quantified by the time it takes to reach maximum tracer concentration in the liver (time-to-peak; maximum % ID liver). The AUC of the liver TACs can be used to measure accumulation of tracer in the liver. The AUC and the maximum % ID of the gallbladder and intestines TAC can be employed as a measure for biliary excretion. The inter- and intra-animal variability of these (and other) metrics for 3β - ^{18}F FCA PET scans was investigated. The results are reproducible between different animals and within the same animal with a maximum observed coefficient of variation of 15.5 %. This is in line with the preclinical variability of the commonly used hepatobiliary SPECT tracer $^{99\text{m}}\text{Tc}$ -mebrofenin (12 %; Neyt 2016).

The *in vivo* evaluation of 3β - ^{18}F FCA in wild-type FVB mice showed that the tracer is rapidly and exclusively taken up into the liver after intravenous injection (approx. 5 min to reach approx. 60 maximum % ID). This is in accordance with literature on rodent bile acid uptake: intravenously injected ^{14}C taurocholate was almost completely taken up in the liver of rats after 10 minutes (Crawford et al. 1988). The hepatic uptake of 3β - ^{18}F FCA is slightly slower compared to $^{99\text{m}}\text{Tc}$ -mebrofenin in FVB-mice, but reaches a comparable % ID (2.2 minutes to reach 51.8 maximum % ID) (Neyt et al. 2013). This behavior is similar to ^{11}C

labeled bile acid analogues that also show a fast and exclusive hepatic uptake (<7 minutes), in pigs (Frisch et al. 2012; Schacht et al. 2016). On the other hand, $^{99\text{m}}\text{Tc}$ labeled bile acids [$^{99\text{m}}\text{Tc}$]-DTPA-CDCA and [$^{99\text{m}}\text{Tc}$]-DTPA-CA reach a lower peak value in the liver at a reduced rate (12.7 minutes to reach 37.3 max % ID and 12.0 minutes to reach 25.7 max % ID respectively) (Neyt et al. 2016), probably as a result of the addition of DTPA that has a substantial effect on the molecular structure of the bile acids.

Following rapid uptake into the liver, 3β -[^{18}F]FCA is excreted into the bile ducts, gallbladder and finally accumulates in the intestines. There was no accumulation of tracer visible in other organs for up to 6 hours post-injection. After 1 hour, activity in the gallbladder and intestines reached a plateau of approx. 80 % ID. This value is comparable to that of $^{99\text{m}}\text{Tc}$ -mebrofenin (78.1 % ID) and higher than the maximal % ID in gallbladder and intestines of the $^{99\text{m}}\text{Tc}$ labeled bile acids (62.2 % ID for [$^{99\text{m}}\text{Tc}$]-DTPA-CDCA; 47.8 % for [$^{99\text{m}}\text{Tc}$]-DTPA-CA) (Neyt et al. 2016). Because they are only transported by oatp/mrp2 and show partial urinary clearance, $^{99\text{m}}\text{Tc}$ bile acids show a lower uptake into the liver and a lower accumulation in gallbladder and intestines.

Mice that were dosed with rifampicin or bosentan confirmed that 3β -[^{18}F]FCA uses the ntcp/oatp and bsep/mrp2 transporters *in vivo*. Both rifampicin and bosentan caused a significant delay in hepatic uptake and lower maximum % ID in the liver. Both drugs gave rise to an increased amount of 3β -[^{18}F]FCA in arterial blood, which is in line with an observed increase in serum bile acids after administration of these drugs (Chen et al. 2009; Fattinger et al. 2001). When an identical dose of rifampicin was administered to FVB-mice scanned with $^{99\text{m}}\text{Tc}$ -mebrofenin (Neyt et al. 2013), a complete block of canalicular efflux was observed on the SPECT-scan, whereas 3β -[^{18}F]FCA excretion into bile is only hindered. This difference in excretion can be attributed to the maximal blocking effect of rifampicin on $^{99\text{m}}\text{Tc}$ -mebrofenin transport, as this tracer is an exclusive oatp and mrp2 substrate (Ghibellini et al. 2008), whereas 3β -[^{18}F]FCA can still be excreted into bile by bsep. The observed *in vivo* inhibition is in line with our *in vitro* findings (cfr. Chapter 5) that 3β -[^{18}F]FCA uses the OATP and NTCP transport systems as the basolateral hepatic uptake systems; for canalicular hepatic efflux, BSEP and MRP2 are the bile acid transporters involved. Consequently, pharmacologic interference with these transporters can be studied *in vivo* with 3β -[^{18}F]FCA.

The developed ^{18}F labeled bile acids 3α - ^{18}F FCA, 3β - ^{18}F FGCA and 3β - ^{18}F FCDCA were evaluated in healthy wild-type FVB mice and compared to reference tracer 3β - ^{18}F FCA. All tracers showed exclusive hepatobiliary transport after intravenous injection. Fairly similar TACs were obtained for 3α - ^{18}F FCA, 3β - ^{18}F FCA, 3β - ^{18}F FGCA, whereas 3β - ^{18}F FCDCA had the most aberrant curves. Compared to 3β - ^{18}F FCA, 3β - ^{18}F FCDCA shows a significantly slower liver uptake from the blood compartment. Both the time-to-peak of the liver TACs and the AUC of tracer in arterial blood increased approximately two-fold. Furthermore, a significant drop in excretion towards gallbladder and intestines was observed. Although *in vitro* results indicated that this fluorinated bile acid has a very high affinity for the bile acid transporters (cfr. Chapter 5), the slower *in vivo* hepatobiliary clearance implies that 3β -FCDCA acts as slow substrate for the bile acid transporters *in vivo*. A slow substrate is characterized by a very high affinity for the transporter it uses, but this tight binding to the transporter can also cause slower release from it. Because 3β - ^{18}F FCDCA already shows slower hepatobiliary transport in healthy wild-type mice, this tracer is less suited to detect possible alterations of bile acids transport by pharmacological interference or in liver disease.

Considering the $3\alpha/\beta$ - ^{18}F FCA epimers, it was found that 3α - ^{18}F FCA shows a slight, yet significant decrease in time-to-peak of the liver TACs and excretion to gallbladder and intestines proceeded faster. This is reflected in a decrease of the liver TACs AUC-value and modest increase in AUC of the gallbladder and intestines TACs compared to 3β - ^{18}F FCA. These results illustrate that there is not only an observable difference in affinity of the $3\alpha/\beta$ FCA epimers for bile acid transporters *in vitro* (Chapter 5), but also in hepatobiliary transport *in vivo*. There is a slight preference for 3α - ^{18}F FCA compared to 3β - ^{18}F FCA, probably because the fluorine atom is in the same 3α -configuration as the 3α -OH on the endogenous cholic acid molecule.

Conjugation of 3β - ^{18}F FCA with glycine did not have a significant impact on its *in vivo* hepatobiliary transport, although the affinity of 3β FGCA for NTCP, OATP1B1 and BSEP rises compared to 3β FCA *in vitro* (Chapter 5). This means that glycine conjugation of a bile acid is not a prerequisite for faster or more efficient hepatobiliary transport in mice. However, the majority of the murine bile acid spectrum is composed of taurine conjugated bile acids (Alnouti et al. 2008). The observed identical transport efficiency of 3β - ^{18}F FCA and its

glycine conjugate 3β - ^{18}F FGCA could be different if taurine conjugation was explored. A conjugated bile acid tracer could have an advantage over a non-conjugated bile acid with regards to enterohepatic circulation. Conjugated bile acids are more efficiently taken up by ASBT, the ileal bile acid transport protein. Recently, Frisch et al. developed a ^{18}F labeled conjugated bile acid to assess deviations from efficient enterohepatic uptake of bile acids (Frisch et al. 2018). Conjugated bile acid tracers could for example be useful to assess bile acid malabsorption in patients suffering from inflammatory bowel diseases.

The hepatic and biliary clearance values of 3α - ^{18}F FCA, 3β - ^{18}F FCA and 3β - ^{18}F FGCA were not significantly different and similar to $^{99\text{m}}\text{Tc}$ -mebrofenin in wild-type FVB mice (Neyt 2016). A much lower hepatic and biliary clearance was observed for the $^{99\text{m}}\text{Tc}$ labeled bile acids due to their partial urinary clearance.

6.5 Conclusion

Three out of four newly developed PET tracers (3α - ^{18}F FCA, 3β - ^{18}F FCA and 3β - ^{18}F FGCA) display fast and exclusive hepatobiliary transport and can therefore be employed as a probe for bile acid transport *in vivo*. Lead compound 3β - ^{18}F FCA showed good inter- and intra-animal reproducibility in mice and was confirmed as an *in vivo* ntcp/oatp and bsep/mrp2 substrate by coadministration of the tracer with rifampicin or bosentan. Therefore, 3β - ^{18}F FCA can be used as a probe for evaluation of *in vivo* bile acid uptake, biliary efflux, and related disturbances. This tracer can for example be a valuable tool to detect drug-induced cholestasis during preclinical evaluation of new drugs *in vivo*.

6.6 References

- Alnouti, Y., Csanaky, I. & Klaassen, C., 2008. Quantitative profiling of bile acids and their conjugates in mouse liver, bile, plasma and urine using LC-MS/MS. *J Chromatogr B Analyt*, 873(2), pp.209–217.
- Baringhaus, K.H. et al., 1999. Substrate specificity of the ileal and the hepatic Na(+)/bile acid cotransporters of the rabbit. II. A reliable 3D QSAR pharmacophore model for the ileal Na(+)/bile acid cotransporter. *Journal of lipid research*, 40(12), pp.2158–2168.
- Bleibel, W. et al., 2007. Drug-induced liver injury: Review article. *Digestive Diseases and Sciences*, 52, pp.2463–2471.
- Chen, X. et al., 2009. Altered integrity and decreased expression of hepatocyte tight junctions in rifampicin-induced cholestasis in mice. *Toxicology and Applied Pharmacology*, 240, pp.26–36.
- Crawford, J.M., Berken, C.A. & Gollan, J.L., 1988. Role of the hepatocyte microtubular system in the excretion of bile salts and biliary lipid: implications for intracellular vesicular transport. *The Journal of Lipid Research*, 29, pp.144–156.
- Fattinger, K. et al., 2001. The endothelin antagonist bosentan inhibits the canalicular bile salt export pump: a potential mechanism for hepatic adverse reactions. *Clinical pharmacology and therapeutics*, 69(4), pp.223–31.
- Frisch, K. et al., 2012. [N-methyl-11C]cholylsarcosine, a novel bile acid tracer for PET/CT of hepatic excretory function: radiosynthesis and proof-of-concept studies in pigs. *Journal of nuclear medicine : official publication, Society of Nuclear Medicine*, 53(5), pp.772–8.
- Frisch, K. & Sørensen, M., 2014. On fluoro-18 labeling of bile acids. *Nuclear medicine and biology*, 41, p.775.
- Frisch, K. et al., 2018. N-(4-[18F]fluorobenzyl) cholyglycine, a novel tracer for PET of enterohepatic circulation of bile acids: Radiosynthesis and proof-of-concept studies in rats. *Nuclear Medicine and Biology*, 61, pp.56–62.

- Ghibellini, G. et al., 2004. A Novel Method for the Determination of Biliary Clearance in Humans. *The AAPS journal*, 6(1), pp.45–56.
- Ghibellini, G. et al., 2008. Use of tc-99m mebrofenin as a clinical probe to assess altered hepatobiliary transport: integration of in vitro, pharmacokinetic modeling, and simulation studies. *Pharmaceutical research*, 25(8), pp.1851–60.
- González, P.M. et al., 2014. Structural requirements of the human sodium-dependent bile acid transporter (hASBT): Role of 3- and 7-OH moieties on binding and translocation of bile acids. *Molecular Pharmaceutics*, 11, pp.588–598.
- He, J. et al., 2014. PET imaging of oatp-mediated hepatobiliary transport of [11C] rosuvastatin in the rat. *Molecular Pharmaceutics*, 11, pp.2745–2754.
- Jia, L. et al., 2014. Synthesis and evaluation of (18)F-labeled bile acid compound: a potential PET imaging agent for FXR-related diseases. *Nuclear medicine and biology*, 41, pp.495–500.
- Jüngst, C. et al., 2013. Intrahepatic cholestasis in common chronic liver diseases. *European journal of clinical investigation*, 43(10), pp.1069–83.
- Kaneko, K.-I. et al., 2018. A clinical quantitative evaluation of hepatobiliary transport of [11C] Dehydropravastatin in humans using positron emission tomography. *Drug Metabolism and Disposition*, 46(5), pp.719–728.
- Kubitz, R. et al., 2012. The bile salt export pump (BSEP) in health and disease. *Clinics and Research in Hepatology and Gastroenterology*, 36(6), pp.536–553.
- Lepist, E.I. et al., 2014. Evaluation of the endothelin receptor antagonists ambrisentan, bosentan, macitentan, and sitaxsentan as hepatobiliary transporter inhibitors and substrates in sandwich-cultured human hepatocytes. *PLoS ONE*, 9(1).
- Leslie, E.M. et al., 2007. Differential Inhibition of Rat and Human Na^+ -Dependent Taurocholate Cotransporting Polypeptide (NTCP / SLC10A1) by Bosentan : A Mechanism for Species Differences in Hepatotoxicity. *The Journal of pharmacology and experimental therapeutics*, 321(3), pp.1170–1178.

- de Lima Toccafondo Vieira, M. & Tagliati, C.A., 2014. Hepatobiliary transporters in drug-induced cholestasis: a perspective on the current identifying tools. *Expert opinion on drug metabolism & toxicology*, 10(4), pp.581–97.
- Loening, A. & Gambhir, S., 2003. AMIDE: a free software tool for multimodality medical image analysis. *Molecular Imaging*, 2(3), pp.131–137.
- Moerman, L. et al., 2011. P-glycoprotein at the blood-brain barrier: kinetic modeling of 11C-desmethyloperamide in mice using a 18F-FDG μ PET scan to determine the input function. *EJNMMI Research*, 1(1), p.12.
- Neyt, S. et al., 2013. In vivo visualization and quantification of (disturbed) Oatp-mediated hepatic uptake and Mrp2-mediated biliary excretion of 99mTc-mebrofenin in mice. *Journal of Nuclear Medicine*, 54(4), pp.624–630.
- Neyt, S., 2016. *Non-invasive visualization and quantification of (disturbed) hepatobiliary transport - PhD dissertation*
- Neyt, S. et al., 2016. Synthesis, in vitro and in vivo small-animal SPECT evaluation of novel technetium labeled bile acid analogues to study (altered) hepatic transporter function. *Nuclear Medicine and Biology*, 43, pp.642–649.
- Padda, M.S. et al., 2011. Drug-Induced Cholestasis. *Hepatology*, 53, pp.1377–1387.
- Pauli-Magnus, C. & Meier, P.J., 2006. Hepatobiliary transporters and drug-induced cholestasis. *Hepatology (Baltimore, Md.)*, 44, pp.778–87.
- Regev, A., 2014. Drug-induced liver injury and drug development: industry perspective. *Seminars in Liver Disease*, 34(2), pp.227–239.
- Schacht, A.C. et al., 2016. Radiosynthesis of N-11C-Methyl-Taurine-Conjugated Bile Acids and Biodistribution Studies in Pigs by PET/CT. *Journal of Nuclear Medicine*, 57(4), pp.628–633.
- Shimizu, K. et al., 2012. Whole-body distribution and radiation dosimetry of [11C]telmisartan as a biomarker for hepatic organic anion transporting polypeptide (OATP) 1B3. *Nuclear Medicine and Biology*, 39, pp.847–853.

- Shingaki, T. et al., 2013. Evaluation of Oatp and Mrp2 activities in hepatobiliary excretion using newly developed positron emission tomography tracer [11C]dehydropravastatin in rats. *The Journal of pharmacology and experimental therapeutics*, 347, pp.193–202.
- Takashima, T. et al., 2012. PET imaging-based evaluation of hepatobiliary transport in humans with (15R)-11C-TIC-Me. *Journal of Nuclear Medicine*, 53, pp.741–748.
- Testa, A. et al., 2017. Design, synthesis, in vitro characterization and preliminary imaging studies on fluorinated bile acid derivatives as PET tracers to study hepatic transporters. *Bioorganic and Medicinal Chemistry*, 25, pp.963–976.
- Testa, A. et al., 2015. PET Tracers To Study Clinically Relevant Hepatic Transporters. *Molecular Pharmaceutics*, 12(7), pp.2203–2216.
- Tournier, N. et al., 2013. Effects of selected OATP and/or ABC transporter inhibitors on the brain and whole-body distribution of glyburide. *Aaps J*, 15(4), pp.1082–1090.
- Trauner, M. & Boyer, J.L., 2003. Bile Salt Transporters: Molecular Characterization, Function, and Regulation. *Physiol Rev*, 83, pp.633–671.
- Vavricka, S.R. et al., 2002. Interactions of rifamycin SV and rifampicin with organic anion uptake systems of human liver. *Hepatology*, 36(1), pp.164–172.

CHAPTER 7:

VALORIZATION OF 3β -[^{18}F]FCA IN LIVER DISEASE MODELS

7.1 Introduction

As illustrated in Chapter 1, the liver synthesizes bile acids that play a vital role in lipid digestion. Their hepatobiliary transport and enterohepatic cycle is warranted by bile acid transport proteins. However, disturbances in hepatobiliary transport of bile acids are present in certain liver diseases or can be triggered by xenobiotic interference with abovementioned bile acid transporters (Padda et al. 2011; Jüngst et al. 2013). Alterations in bile acid transport can lead to toxic accumulation of bile acids (cholestasis) and eventually liver inflammation. Therefore, it is important to have an accurate assessment of liver functionality with regards to bile acid transport. To monitor physiological processes on a molecular level *in vivo*, nuclear imaging techniques are the preferred methods. The radiolabeled tracer that should be used to visualize hepatobiliary transport of bile acids, would preferably be structurally similar to endogenous bile acids.

Recently, bile acid Positron Emission Tomography (PET) imaging has gained considerable interest: development and *in vivo* evaluation of several ^{11}C and ^{18}F has already been described (Frisch et al. 2012; Schacht et al. 2016; Ørntoft et al. 2018; Jia et al. 2014; Testa et al. 2017; Frisch et al. 2018). In Chapter 6 of this dissertation, we evaluated several ^{18}F labeled bile acid analogues that closely resemble endogenous bile acids and show hepatobiliary transport. Interference of the drugs rifampicin and bosentan with the bile acid transporters and the resulting cholestasis could be detected *in vivo* with 3β - ^{18}F FCA PET.

In this Chapter, valorization of 3β - ^{18}F FCA as a hepatobiliary PET imaging tool will be performed in several mouse models of liver disease. The potential of 3β - ^{18}F FCA to visualize and quantify dosage-dependent drug-induced cholestasis by direct interference with the bile acid transporters, will be assessed by dosing mice with cyclosporin, a potent ntcp/oatp and bsep/mrp2 inhibitor (Hofmann et al. 2011).

It was hypothesized that 3β - ^{18}F FCA could be used not only to study direct pharmacological interference with ntcp/oatp and bsep/mrp2, but also to monitor (regional) differences in hepatocyte functionality during liver diseases that are characterized by altered expression of these transporters (Thakkar et al. 2017). To the best of our knowledge, no single PET bile acid has been evaluated in preclinical liver disease models, other than direct pharmacological inhibition of the bile acid transporters. In this chapter, 3β - ^{18}F FCA will also

be evaluated in five well-established mouse models for liver diseases. Firstly, acute liver injury will be induced by an acute overdose of acetaminophen (APAP) ingestion which results in severe liver injury and centrilobular necrosis within 6-24 hours (Jaeschke et al. 2013). Secondly, chronic cholangiopathy will be evoked by feeding mice 3,5-diethoxycarbonyl-1,4-dihydrocollidine (DDC). DDC feed results in formation of porphyrin plugs in the bile ducts which leads to cholestasis, ductular reaction and fibrosis (Fickert et al. 2007; Delire et al. 2015). Thirdly, non-alcoholic steatohepatitis (NASH) will be mimicked in mice by feeding them a methionine and choline deficient (MCD) diet for 8 weeks, resulting in steatosis and associated liver inflammation (Rinella et al. 2008). Fourthly, 3β - ^{18}F FCA will be evaluated in a mouse model for hepatocellular carcinoma (HCC), induced by administration of diethylnitrosamine (DEN) for 23 weeks (Tolba et al. 2015). Finally, the tracer will also be evaluated in a mouse model for alcoholic cirrhosis by dosing mice with carbon tetrachloride (CCl_4) and providing them alcohol spiked drinking water. Expressions levels of *ntcp*, *oatp*, *bsep* and *mrp2* mRNA will be determined in these models.

7.2 Materials and methods

7.2.1 Animal models

The animals were housed and handled in accordance with the European Ethics Committee guidelines. All experiments were approved by the Animal Experimental Ethical Committee of Ghent University (ECD 15/69 and ECD 17/30). Food and water was presented ad libitum, yet before a PET/CT scan, the animals were fasted overnight. A timeline of the different chronic liver disease experiments is given in Figure 7.1.

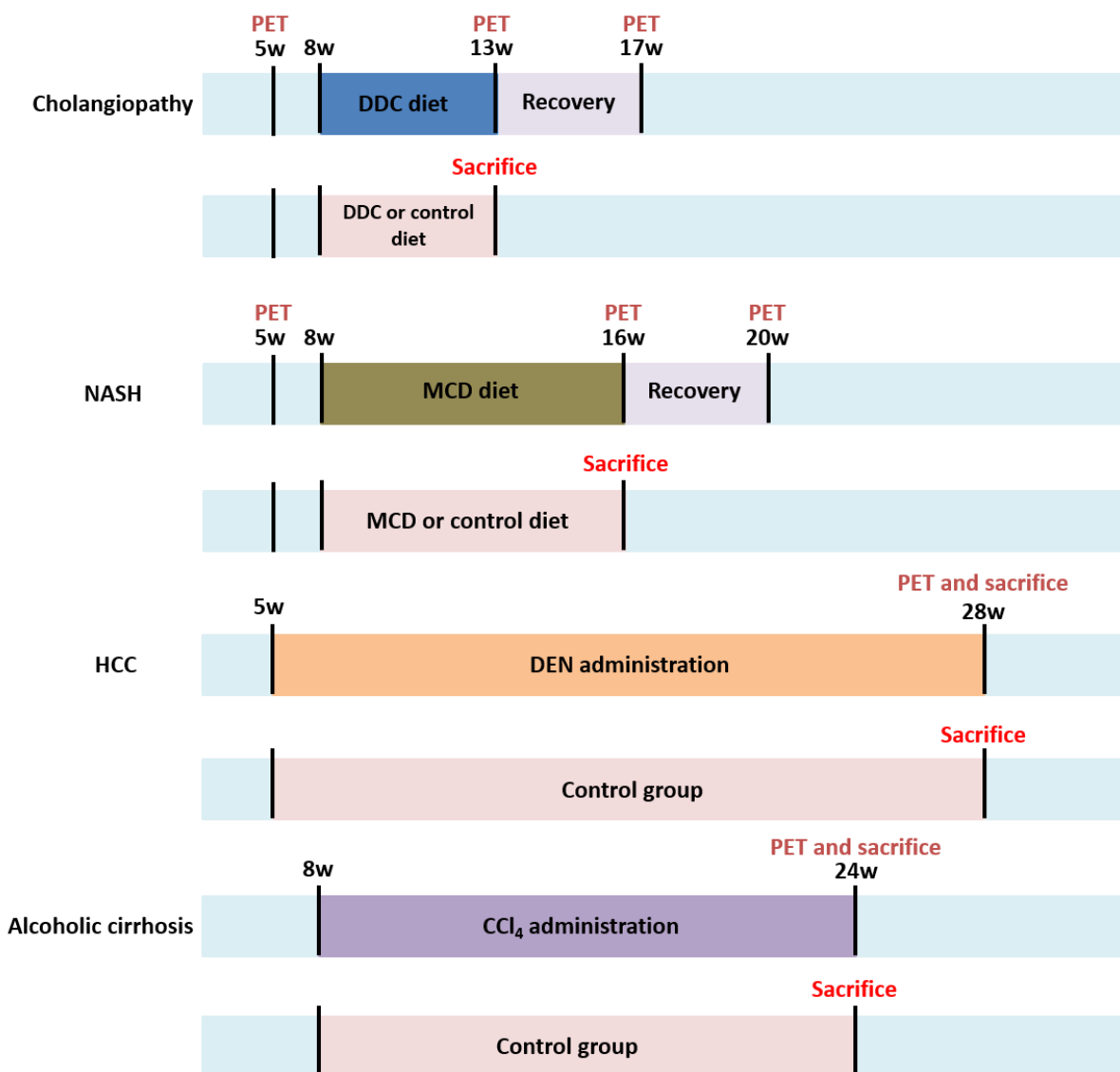


Figure 7.1: Overview of the timelines for the different chronic liver disease experiments. To determine mRNA levels, animals were sacrificed at indicated timepoints in separate groups that received either the same treatment as the PET imaging group or were a control group.

7.2.1.1 Drug-induced cholestasis by cyclosporin administration

Different dosages of cyclosporin A (5, 10, 20, 30 and 50 mg/kg; Sigma Aldrich) were administered intravenously to wild-type FVB mice (female; 5 weeks of age; n = 3 per dosage group; Janvier). The drug was dissolved in 40 μL of DMSO. A control group was included that received a DMSO injection only. Twenty minutes after the intravenous administration, a 3β - ^{18}F FCA PET scan was acquired.

7.2.1.2 Acute liver injury by APAP overdose

Wild-type C57Bl/6 mice (male; 8 weeks of age; n = 4; Janvier) underwent a 3β - ^{18}F FCA PET scan (cfr. infra) to establish baseline 3β - ^{18}F FCA parameters. Two days later and after overnight fasting, the animals received an APAP overdose (300 mg/kg; Sigma-Aldrich) by oral gavage. Retro-orbital blood sampling was performed 4 hours after dosing and aspartate transaminase/alanine transaminase (AST/ALT) levels were determined to confirm acute liver injury. A second 3β - ^{18}F FCA PET scan was performed 24 hours after APAP administration and compared to baseline. A different group of animals also received an APAP overdose, after which they were sacrificed for gene expression analysis, which was compared to a control group that received oral gavage of physiological solution.

7.2.1.3 Cholangiopathy by DDC diet

Wild-type 129/Sv mice (male; 5 weeks of age; n = 6; Janvier) underwent a baseline 3β - ^{18}F FCA PET scan. At the age of 8 weeks, mice received the DDC diet ad libitum (Envigo). A second 3β - ^{18}F FCA PET scan was acquired after 5 weeks of DDC diet, after which the animals were allowed to recover for 4 weeks. A third 3β - ^{18}F FCA PET scan was then acquired. A different group of animals was also fed the DDC diet for 5 weeks, after which they were sacrificed to obtain paraffin liver sections for histology (Sirius Red staining) and gene expression analysis. Control mice received a standard diet.

7.2.1.4 NASH by MCD diet

A group of wild-type C57Bl/6 mice (female; 5 weeks of age; n = 6; Janvier) underwent a baseline 3β - ^{18}F FCA PET scan. At the age of 8 weeks, the mice received the MCD diet (Envigo) ad libitum for 8 weeks and underwent a second 3β - ^{18}F FCA PET scan. After 8 weeks MCD diet feeding, the diet was replaced by normal chow and the animals were allowed to recover for 4 weeks. A final 3β - ^{18}F FCA PET scan was then acquired. A different group of

animals was also fed the MCD diet for 8 weeks, after which they were sacrificed to obtain paraffin liver sections for histology (hematoxylin and eosin stain) and gene expression analyses. Control mice received the same diet in which methionine and choline was added.

7.2.1.5 HCC by DEN administration

HCC was induced in wild-type 129/Sv mice (male; 5 weeks of age; n = 20; Janvier) by injecting them once a week with 35 mg/kg DEN (Sigma-Aldrich) intraperitoneally. Injections were started at 5 weeks of age and were continued for 23 weeks. At that time, the animals were subjected to a 3β - ^{18}F FCA PET/CT scan. The quantitative information obtained from this scan was compared to the baseline 3β - ^{18}F FCA scans for the DDC diet. The DEN-treated mice were sacrificed after the scanning procedure and their livers were isolated for histology (hematoxylin and eosin stain) and gene expression analyses. Control mice received weekly intraperitoneal injections of physiological solution for 23 weeks.

7.2.1.6 Alcoholic cirrhosis by CCl_4 administration

Alcoholic cirrhosis was induced in wild-type Sv129 mice (male; 8 weeks of age; n = 15; Janvier) by injecting them twice a week subcutaneously with 1.0 mL/kg CCl_4 (dissolved in olive oil; 1/1 v/v) for 16 weeks. Drinking water was spiked with 4 % ethanol for the duration of the experiment. After 16 weeks of CCl_4 administration, a 3β - ^{18}F FCA PET scan was acquired. The quantitative information obtained from this scan was compared to the baseline 3β - ^{18}F FCA scans for the DDC diet. After the scan, the animals were sacrificed to obtain paraffin liver sections for histology (Sirius Red stain) and hepatic gene expression analyses that was compared to a control group.

7.2.2 RNA extraction and RT-qPCR (Real-time quantitative polymerase chain reaction)

RNA was extracted from 10 mg of frozen liver tissue preserved in RNA-later (Ambion, Thermo Fisher Life Technologies, Ghent, Belgium), according to the manufacturer's guidelines (Rneasy Mini Kit, Quiagen, Venlo, the Netherlands) and measured for purity and quantity by spectrophotometry (Nanodrop, Thermo Scientific, Waltham, USA). cDNA was made out of one microgram of mRNA by reverse transcription using the iScript cDNA synthesis kit (BioRad, Temse, Belgium) according to the manufacturer's instructions. Diluted cDNA was subjected to 45 cycles of quantitative PCR amplification using SYBR Green mix (Sensimix, Bioline Reagents Ltd, London, UK) and 2 μM of each primer. A two-step program

was run on a LightCyclerR 480 (Roche, Vilvoorde, Belgium). Melting curve analysis confirmed primer specificities. All reactions were run in duplicate and normalized to reference genes that showed stable expression in all samples (GAPDH, SDHA and HPRT). Differences between groups were analyzed with the Mann-Whitney U test (SPSS Statistics 23 Software). A p-value < 0.05 was considered significant.

The PCR efficiency of each primer pair was calculated using a standard curve of reference cDNA. Amplification efficiency was determined using the formula $10^{-1/\text{slope}} - 1$. The primer set sequences are listed in Table 7.1.

Table 7.1: Primers that were used to determine gene expression of *ntcp*, *oatp4*, *bsep* and *mrp2* in liver samples by RT-qPCR.

Gene	Forward Primer 5'-3'	Reverse Primer 3'-5'	Efficiency	R ²
<i>Ntcp</i>	CACCATGGAGTTCAGCAAGA	AGCACTGAGGGGCATGATAC	0.99	100.2
<i>Oatp4</i>	GATCCTTCACTTACCTGTTCAA	CCTAAAAACATTCCACTTGCCATA	0.99	97
<i>Bsep</i>	GAGTGGTGGACAGAAGCAAA	TGAGGTAGCCATGTCCAGAA	0.99	102
<i>Mrp2</i>	GCTTCCCATGGTGATCTCTT	ATCATCGCTTCCCAGGTACT	0.99	95

7.2.3 PET imaging protocol

The radiosynthesis and quality control of 3β - $[^{18}\text{F}]$ FCA was performed as described previously in Chapter 4. Imaging was performed with a small animal PET/CT scanner (Trifoil Imaging; FLEX Triumph II; axial field of view: 75 mm; 1.3 mm spatial resolution). All mice underwent the same imaging protocol, unless specified otherwise in the following section.

Just before the PET/CT scan, mice were anesthetized on a heated bed using an isoflurane in oxygen mixture (5 % v/v isoflurane for induction; 1.5 % v/v for maintenance of anesthesia). A polyethylene intravenous line was placed in the lateral tail vein and fixated for tracer injection. The animals were then transferred to the heated animal bed of the PET/CT scanner.

A CT acquisition was performed, followed by a one hour PET scan that was started just before intravenous injection of 9 MBq of 3β - $[^{18}\text{F}]$ FCA. Following this scan, 9 MBq of $[^{18}\text{F}]$ FDG was injected intravenously. Twenty minutes later, a twenty minutes PET acquisition

was done. Both PET scans were acquired in list-mode and were reconstructed iteratively (50 iterations). The 3β - ^{18}F FCA scan was reconstructed dynamically using the following time frames: 8 x 15 s; 16 x 30 s; 10 x 60 s; 20 x 120 s. A static reconstruction of the ^{18}F FDG PET scan was made. The data were analyzed using Pmod software v3.405 (PMOD Technologies). Regions of Interest (ROIs) were drawn manually on the PET data over the liver, gallbladder and intestines (GBI). The ^{18}F FDG scan was used to delineate the left ventricle. This ROI was pasted on the 3β - ^{18}F FCA data to obtain an image-derived input function to quantify the arterial blood concentration of 3β - ^{18}F FCA. The tracer's uptake in liver, gallbladder and intestines was expressed as a percentage of injected dose (injected radioactivity; % ID) and monitored in function of time to obtain time-activity curves (TACs). The Area Under the Curve (AUC), % ID and time-to-peak values of the acquired TACs were determined in Graphpad Prism v5.00 Software. Differences between groups were analyzed with the appropriate non-parametric paired or unpaired statistical test (SPSS Statistics 23 Software). A p-value < 0.05 was considered significant. Hepatic and biliary clearance of 3β - ^{18}F FCA was calculated with equation 1 and 2 from Ghibellini et al (Ghibellini et al. 2004).

$$\text{Hepatic clearance} = \frac{\text{cumulative amount of tracer in liver}}{\text{AUC bloodconcentration}_{0 \rightarrow 60 \text{ min}}} \text{ Eq. 1}$$

$$\text{Biliary clearance} = \frac{\text{cumulative amount of tracer in gallbladder\&intestines}}{\text{AUC bloodconcentration}_{0 \rightarrow 60 \text{ min}}} \text{ Eq. 2}$$

Abovementioned data analysis was expanded for DEN-treated mice. For CT visualization of possible HCC nodules, DEN-treated mice received an intravenous bolus injection of 100 μL Exitron Nano 6000TM (Miltényi Biotec) 24 hours before the 3β - ^{18}F FCA scan. HCC lesions were marked with a ROI on the Exitron CT scan and then pasted on the PET scan. The tumor-to-background ratio (TBR) was calculated as the ratio of the average uptake in the tumor lesions and the uptake in the remaining liver tissue. The TBR was determined at maximal liver uptake of 3β - ^{18}F FCA.

7.3 Results

7.3.1 Drug-induced cholestasis by cyclosporin administration

The determined metrics of 3β - ^{18}F FCA TACs in groups of mice that were treated with a different dose of cyclosporin are displayed in Table 7.2. Cyclosporin caused significant alterations in hepatobiliary transport of 3β - ^{18}F FCA, compared to control. Dose-dependent differences in liver time-to-peak, AUC of gallbladder and intestines and AUC of the liver were observed (Figure 7.2). Time-to-peak in the liver and AUC liver increased significantly as the cyclosporin dose was raised, but reached a plateau at 20 mg/kg. Biliary excretion (AUC gallbladder and intestines) decreased significantly compared to control as the cyclosporin dose increased. No further decrease was observed if the dosage was higher than 20 mg/kg. At a dosage of 20 mg/kg, the activity in arterial blood increased 2.5-fold ($p = 0.015$). Hepatic and biliary clearance were significantly lower compared to control ($p = 0.019$ & $p = 0.011$ resp.).

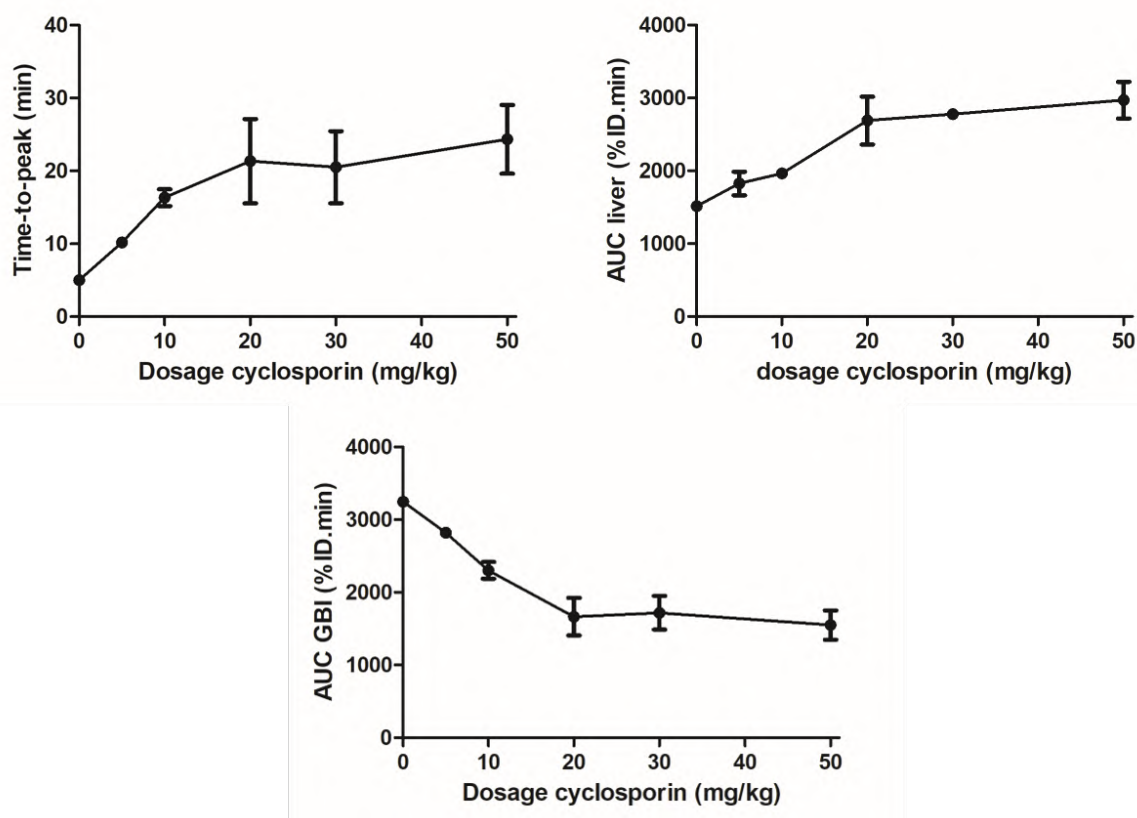


Figure 7.2: Dosage-dependent alterations in liver time-to-peak, liver AUC and gallbladder and intestines (GBI) AUC. Data are presented as mean \pm SD ($n = 3$ per dose).

Table 7.2: Metrics of the 3β-[¹⁸F]FCA TACs for cyclosporin-treated mice. The values are expressed as mean ± SD (n = 3 per group).

Significant differences compared to control are marked with * (*p<0.05; **p<0.01; ***p<0.001). GBI = gallbladder and intestines.

	Control	5 mg/kg cyclosporin	10 mg/kg cyclosporin	20 mg/kg cyclosporin	30 mg/kg cyclosporin	50 mg/kg cyclosporin
AUC liver (% ID.min)	1515 ± 43	1827 ± 161*	1965 ± 39*	2690 ± 329*	2777 ± 9***	2970 ± 251**
Max % ID liver (%)	49.86 ± 3.23	47.53 ± 5.58	44.33 ± 1.92	51.28 ± 6.65	54.26 ± 0.45	55.38 ± 4.86
Time-to-peak liver (min)	5.00 ± 0.50	10.17 ± 0.62**	16.33 ± 0.94**	21.33 ± 4.71*	20.50 ± 3.50**	24.33 ± 3.86**
AUC GBI (% ID.min)	3249 ± 29	2820 ± 21*	2303 ± 95*	1666 ± 210**	1720 ± 164**	1550 ± 163**
Max % ID GBI (%)	78.69 ± 0.86	75.58 ± 2.19	70.46 ± 1.80*	49.59 ± 5.15*	52.73 ± 1.15*	45.22 ± 3.08*
AUC blood (kBq.min/mL)	15422 ± 4328	ND	ND	37852 ± 5286*	ND	ND
Hepatic clearance (mL/min)	0.32 ± 0.07	ND	ND	0.15 ± 0.02**	ND	ND
Biliary clearance (mL/min)	0.44 ± 0.09	ND	ND	0.17 ± 0.04**	ND	ND

7.3.2 Acute liver injury by APAP overdose

Although APAP overdose caused a marked increase in serum AST and ALT levels (ALT: 2062.8 ± 101.7 IU/L; AST: 1935.9 ± 113.1 IU/L; $n = 4$), no significant change in expression of *ntcp*, *oatp4*, *bsep* or *mrp2* was observed ($p = 0.34$; 0.89 ; 0.89 and 0.20 resp.). Furthermore, no significant difference in hepatic uptake or biliary excretion of 3β - ^{18}F FCA was observed between baseline and APAP overdose (Figure 7.3 and Table 7.3).

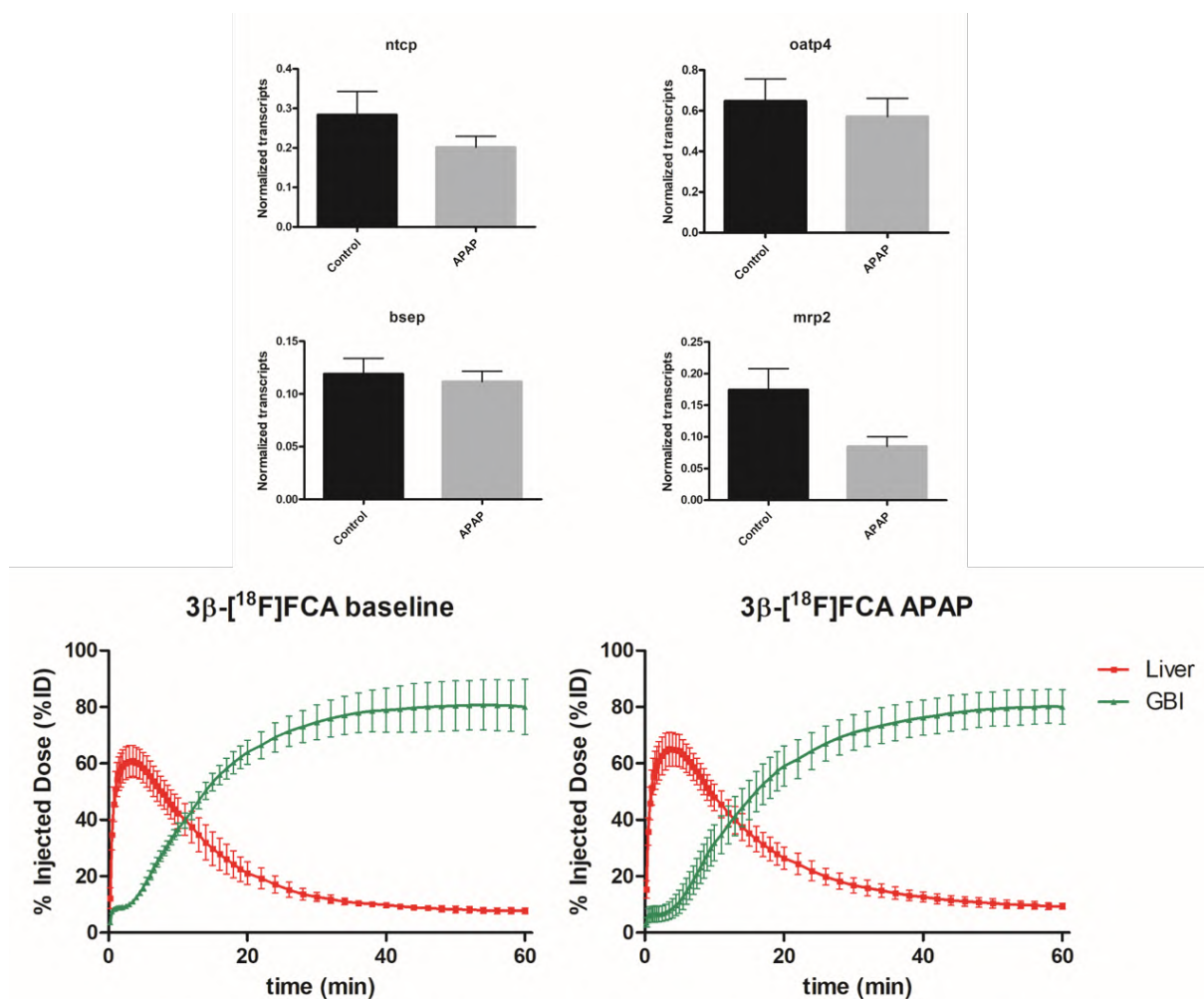


Figure 7.3: Top: mRNA expression of *ntcp*, *oatp4*, *bsep* and *mrp2* in control and APAP overdose. Bottom: TACs of 3β - ^{18}F FCA for baseline and APAP overdose.

Data are mean \pm SD ($n = 4$). GBI = gallbladder and intestines.

Table 7.3: Metrics of the 3β - ^{18}F FCA time-activity curves for baseline and APAP overdose.

The values are expressed as mean \pm SD (n = 4). There were no significant differences in the calculated parameters, compared to baseline. GBI = gallbladder and intestines.

	Baseline	APAP overdose
AUC liver (% ID.min)	1265 \pm 147	1393 \pm 107
Max % ID liver (%)	61.08 \pm 5.56	65.26 \pm 5.94
Time-to-peak liver (min)	3.60 \pm 0.37	4.38 \pm 0.65
AUC GBI (% ID.min)	3778 \pm 329	3579 \pm 351
Max % ID GBI (%)	81.14 \pm 8.83	80.43 \pm 5.90
AUC blood (kBq.min/mL)	14439 \pm 5078	16553 \pm 5488
Hepatic clearance (mL/min)	0.30 \pm 0.09	0.29 \pm 0.05
Biliary clearance (mL/min)	0.39 \pm 0.11	0.36 \pm 0.06

7.3.3 Cholangiopathy by DDC diet

Histology results showed that, after 5 weeks of DDC feeding, the 129/Sv mice developed F1-F2 portal fibrosis with ductular reaction (Figure 7.4 B). A significant decrease in both *ntcp* and *oatp4* mRNA expression was observed ($p = 0.004$ and 0.0006 resp.), whereas *mrp2* was increased ($p = 0.007$) (Figure 7.4).

Baseline 3β - ^{18}F FCA scans indicated a fast and efficient hepatic uptake and biliary excretion of the tracer in healthy 129/Sv mice. In mice fed DDC for 5 weeks, hepatobiliary transport of 3β - ^{18}F FCA was changed significantly (Figure 7.5 and Table 7.4). Hepatic uptake was markedly slower: the time-to-peak of the tracer in the liver increased two-fold from 4.92 ± 0.73 to 11.00 ± 2.12 minutes ($p = 0.02$), while the AUC of the 3β - ^{18}F FCA arterial blood concentration TAC increased approx. 2.9-fold ($p = 0.002$). The biliary excretion of the tracer was reduced significantly: the AUC of the GBI TAC decreased from 3516 ± 338 to 1414 ± 373 %ID.min ($p = 0.002$) and the maximum activity that was found in GBI dropped from 82.52 ± 4.88 to 36.18 ± 10.97 % ($p = 0.002$). After 4 weeks of recovery, the same animals were scanned again with 3β - ^{18}F FCA and the tracer's kinetics returned to baseline values (Table 7.4).

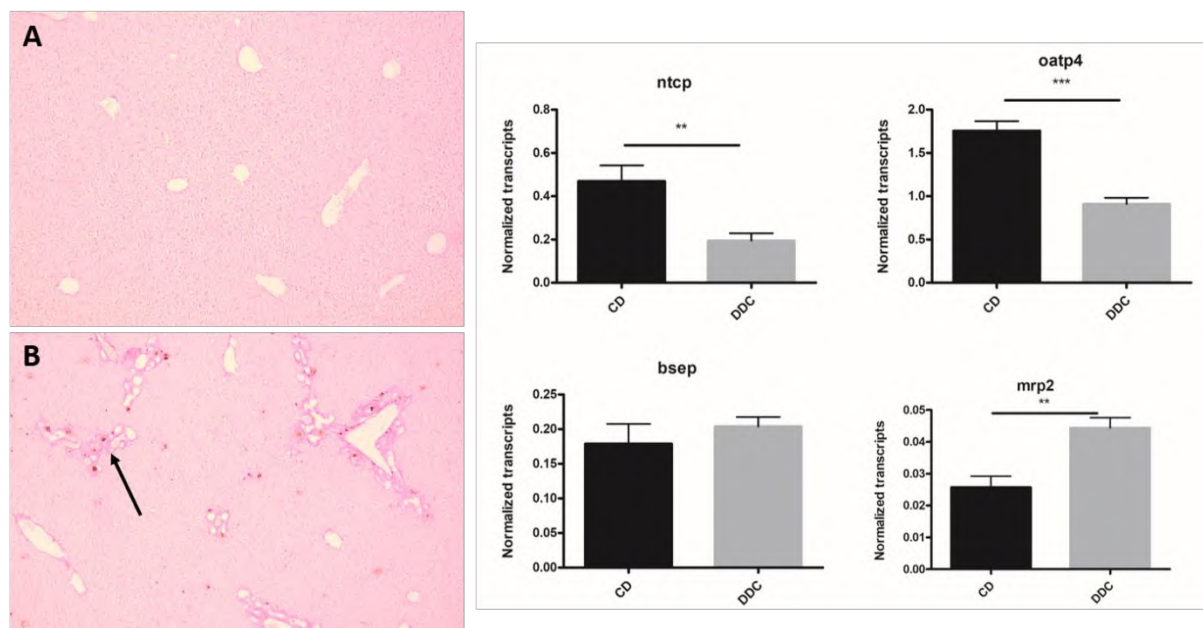


Figure 7.4: Left: Sirius red stained liver sections of mice fed control diet (A) and DDC diet for 5 weeks (B). Mice that were fed the DDC diet for 5 weeks developed F1-F2 portal fibrosis with ductular reaction (arrow). Right: mRNA expression of ntcp, oatp4, bsep and mrp2 in mice fed control diet (CD) or DDC. Data are presented as mean \pm SD and significant differences are marked by * (* p <0.05; ** p <0.01; *** p <0.001).

Table 7.4: Metrics of the 3β - ^{18}F FCA time-activity curves for the DDC experiment at baseline, disease and recovery. The values are expressed as mean \pm SD ($n = 6$). Significant differences towards baseline are marked with a * (* p <0.05; ** p <0.01; *** p <0.001).

	Baseline	DDC-induced cholangiopathy	Recovery
AUC liver (% ID.min)	1595 \pm 409	2907 \pm 386*	1645 \pm 352
Max % ID liver (%)	62.01 \pm 6.81	54.35 \pm 6.79	60.67 \pm 6.35
Time-to-peak liver (min)	4.92 \pm 0.73	11.00 \pm 2.12*	4.75 \pm 0.63
AUC GBI (% ID.min)	3516 \pm 338	1414 \pm 373**	3827 \pm 377
Max % ID GBI (%)	82.52 \pm 4.88	36.18 \pm 10.97**	88.47 \pm 6.20
AUC blood (kBq.min/mL)	19721 \pm 4286	57137 \pm 10893**	14963 \pm 4193
Hepatic clearance (mL/min)	0.33 \pm 0.11	0.10 \pm 0.03**	0.38 \pm 0.12
Biliary clearance (mL/min)	0.46 \pm 0.20	0.066 \pm 0.034*	0.55 \pm 0.17

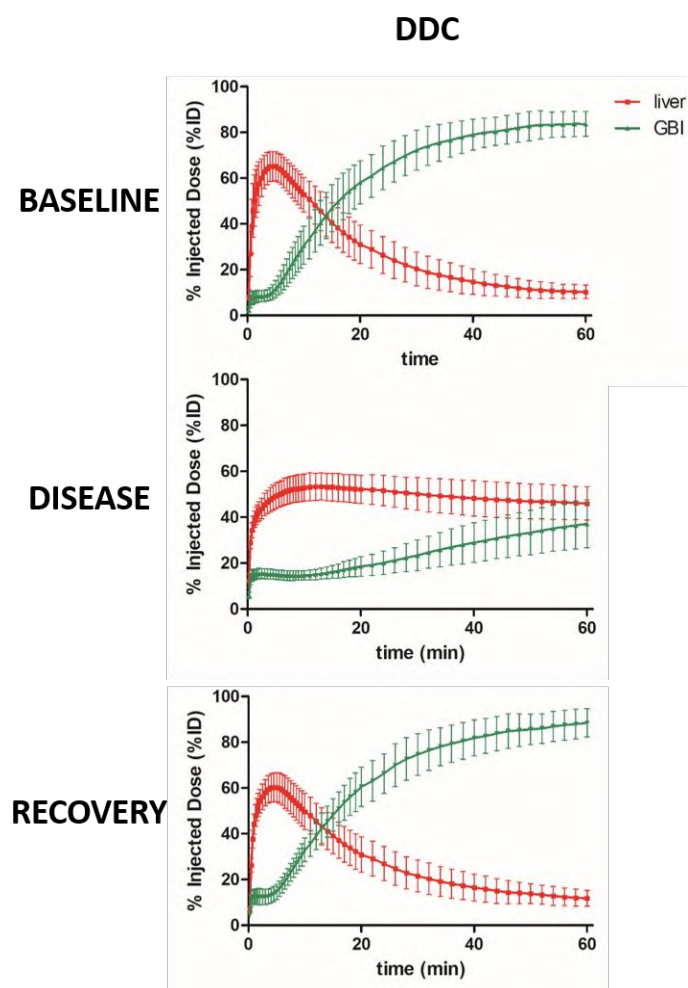


Figure 7.5: Liver (red) and gallbladder and intestines (GBI; green) TACs of 3β - ^{18}F FCA for DDC diet at baseline, disease and recovery. Data are mean \pm SD (n = 6).

7.3.4 NASH by MCD diet

Animals that were fed the MCD diet for 8 weeks developed non-alcoholic steatohepatitis, which is characterized by fat accumulation in the hepatocytes (steatosis), hepatocyte ballooning and inflammation (Figure 7.6 B). MCD-induced steatohepatitis resulted in a significant decrease in *ntcp*, *oatp4* and *mrp2* mRNA expression ($p = 0.0001$; 0.01 ; 0.0005 resp.) compared to control diet fed mice, whereas no difference could be observed for *bsep* expression.

Baseline 3β - ^{18}F FCA scans showed a fast and efficient hepatic uptake and biliary excretion of the tracer in C57Bl/6 mice. The hepatic uptake of 3β - ^{18}F FCA was significantly lower and slower in MCD-fed animals, compared to baseline (Figure 7.7 and Table 7.5). A lower liver maximum % ID was observed (62.10 ± 3.58 versus 35.61 ± 4.85 ; $p = 0.009$), and

the time-to-peak increased from 4.33 ± 0.47 minutes to 12.50 ± 1.50 minutes ($p = 0.01$). There was a significant increase in 3β - ^{18}F FCA presence in arterial blood ($p = 0.02$). The biliary clearance value decreased significantly from 0.48 ± 0.10 mL/min to 0.11 ± 0.02 mL/min ($p = 0.01$). After 4 weeks of recovery, the same animals were scanned again with 3β - ^{18}F FCA and the tracer's kinetics returned to their baseline values (Table 7.5).

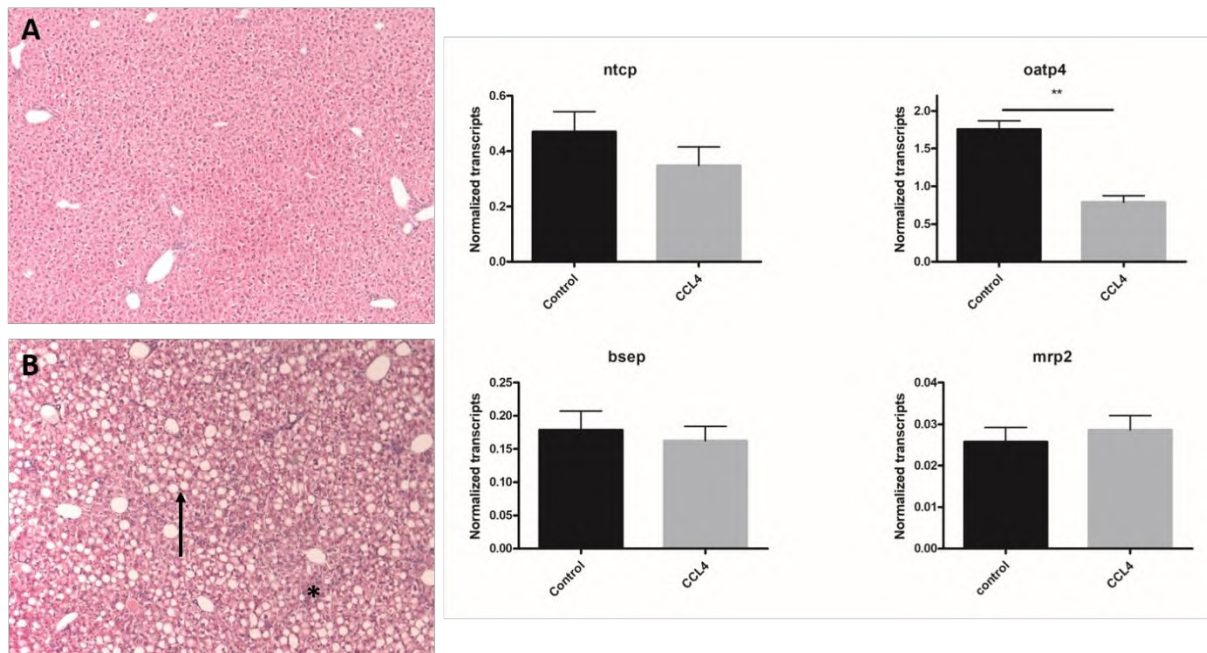


Figure 7.6: Left: hematoxylin & eosin (H&E) stained liver sections of mice fed control diet (A) and MCD diet for 8 weeks (B). Liver sections of MCD fed mice showed macrovesicular steatosis (arrow), ballooning hepatocytes and inflammatory infiltrate (asterix): hallmarks of non-alcoholic steatohepatitis. Right: mRNA expression of ntcp, oatp4, bsep and mrp2 in control diet fed animals (CD) or MCD-fed animals. Data are presented as mean \pm SD and significant differences are marked by * ($p < 0.05$; ** $p < 0.01$; *** $p < 0.001$).

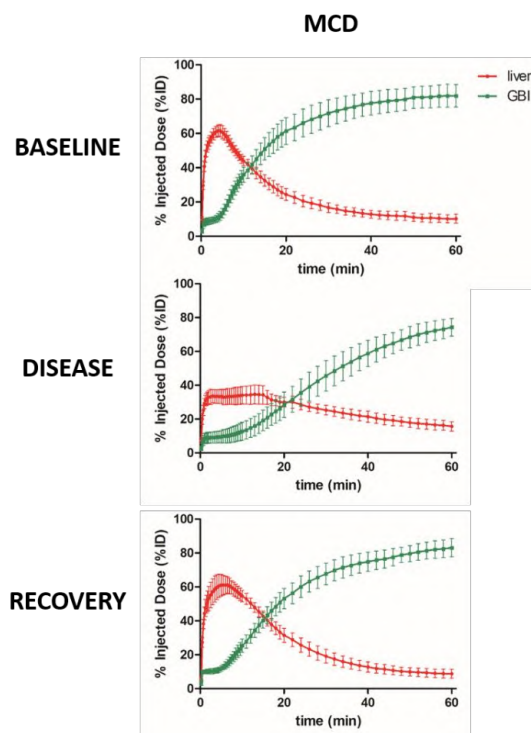


Figure 7.7: Liver (red) and gallbladder and intestines (GBI; green) TACs of 3β - $[^{18}\text{F}]$ FCA for MCD diet at baseline, disease and recovery. Data are mean \pm SD (n = 6).

Table 7.5: Metrics of the 3β - $[^{18}\text{F}]$ FCA time-activity curves for the MCD experiment at baseline, disease and recovery. The values are expressed as mean \pm SD (n = 6). Significant differences towards baseline are marked with a * (* p <0.05; ** p <0.01; *** p <0.001).

GBI = gallbladder and intestines.

	Baseline	MCD-induced NASH	Recovery
AUC liver (% ID.min)	1423 \pm 139	1519 \pm 169	1579 \pm 151
Max % ID liver (%)	62.10 \pm 3.58	35.61 \pm 4.85**	61.95 \pm 5.55
Time-to-peak liver (min)	4.33 \pm 0.47	12.50 \pm 1.50*	5.6 \pm 0.89
AUC GBI (% ID.min)	3696 \pm 347	2543 \pm 371*	3454 \pm 286
Max % ID GBI (%)	82.38 \pm 6.56	74.26 \pm 5.30	83.15 \pm 5.37
AUC blood (kBq.min/mL)	13837 \pm 3721	54260 \pm 9311*	13188 \pm 1823
Hepatic clearance (mL/min)	0.24 \pm 0.05	0.05 \pm 0.01*	0.35 \pm 0.08
Biliary clearance (mL/min)	0.48 \pm 0.10	0.11 \pm 0.02*	0.51 \pm 0.06

7.3.5 HCC by DEN administration

Twenty 129/Sv mice were weekly injected with DEN for 23 weeks. Fourteen mice developed liver lesions that were macroscopically visible after liver isolation (post-scan). Liver sections confirmed the presence of HCC (Figure 7.8). A significant decrease in mRNA expression of *ntcp*, *oatp4* and *bsep* was observed in the HCC lesions ($p = 0.006$; 0.04 ; 0.0005 resp.), whereas *mrp2* mRNA expression was increased compared to control ($p = 0.01$) (Figure 7.8). The liver lesions showed negative contrast on the ExitronTM CT images and could be delineated. However, most HCC nodules were too small to accurately analyze with PET, as a result of the limited spatial resolution. To minimize spill-in effects in the tumor ROIs, only tumors with a radius two times larger than the spatial resolution were considered (1.3 mm for the PET system in this study). Three mice beared a tumor that was large enough for further analysis.

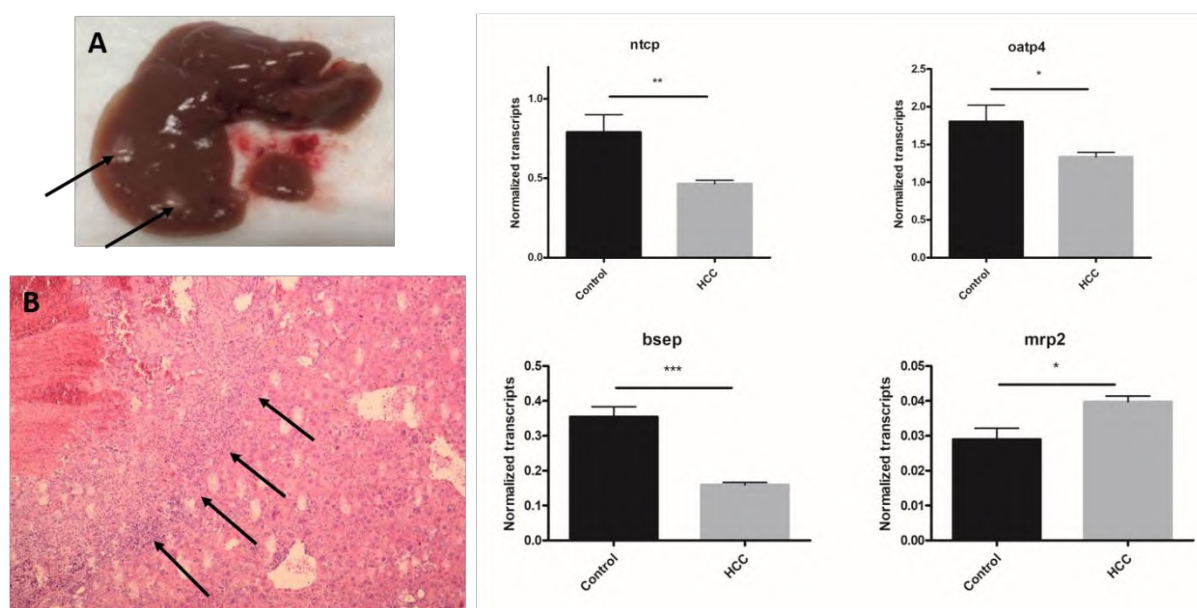


Figure 7.8: Left: isolated liver of a DEN-treated mouse that shows macroscopically visible HCC nodules (arrows; A). Hematoxylin & eosin (H&E) stained liver section, arrows indicate tumor burden; B). Right: mRNA expression of *ntcp*, *oatp4*, *bsep* and *mrp2* in control liver and HCC lesions. Data are presented as mean \pm SD and significant differences are marked by * (* $p < 0.05$; ** $p < 0.01$; *** $p < 0.001$).

A representative PET/CT image of a mice bearing a large HCC is displayed in Figure 7.9. The concentration of 3β - ^{18}F FCA in the HCC tumors was lower than the concentration of 3β - ^{18}F FCA in the surrounding liver tissue for the early phase of the PET scan (0-5 minutes) (see Figure 7.10). The hepatobiliary transport in the surrounding liver tissue was not significantly different compared to the control group, except for the maximum % ID (Table 7.6), which was also the case for mice with small HCC lesions. At 5 minutes post-injection, when the tracer reaches maximum liver uptake, the tumor to background ratio was 0.45 ± 0.13 .

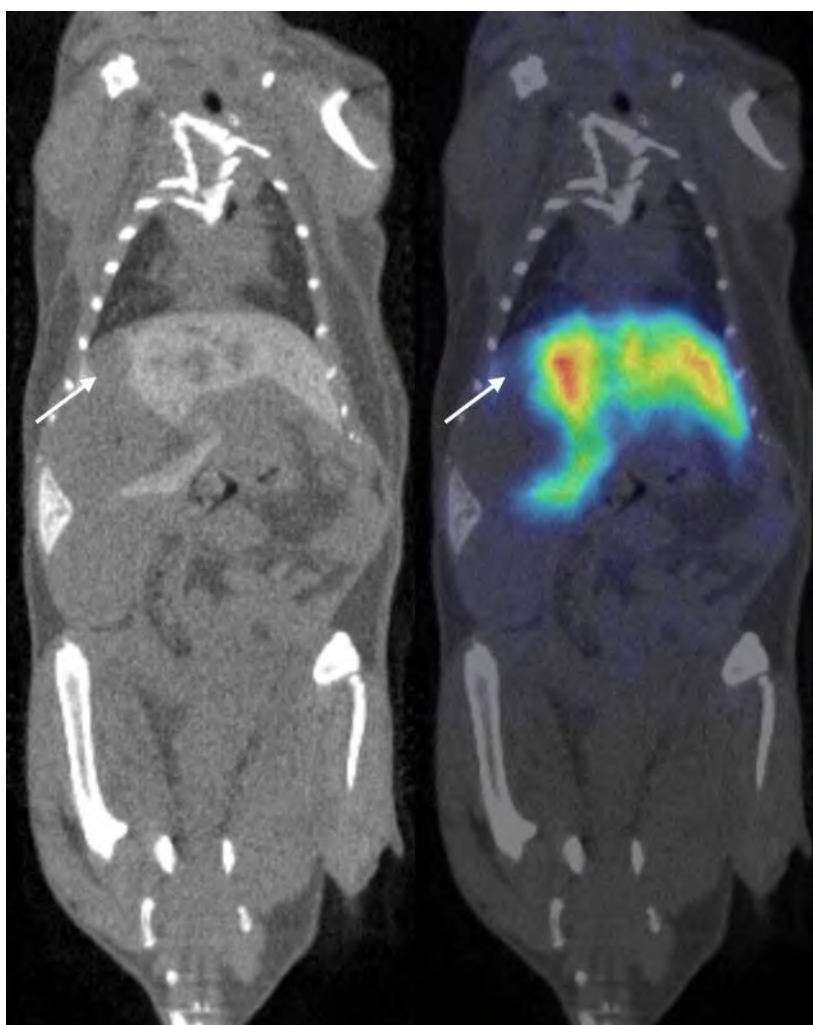


Figure 7.9: Left: coronal CT slice of a DEN-treated mouse that beared a large HCC tumor. The contrast agent Exitron 6000TM was taken up into the liver and caused hyperintensity on CT. The tumor (marked with a white arrow) did not take up the contrast agent. Right: fused PET/CT image (1-5 minutes post-injection tracer). There is less uptake of 3β - ^{18}F FCA in the tumor than in the surrounding liver tissue.

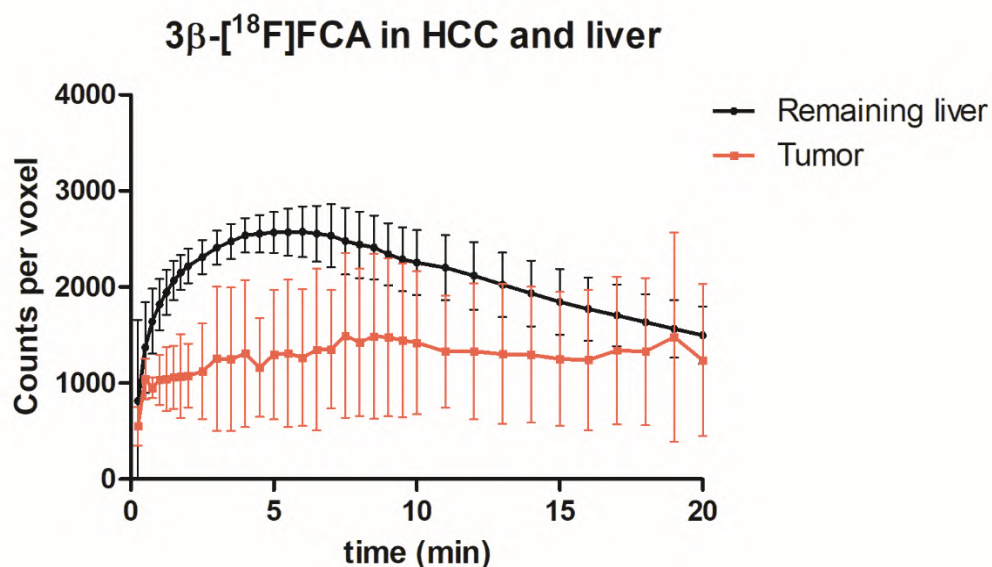


Figure 7.10: Concentration of 3β - $[^{18}\text{F}]\text{FCA}$ in HCC tumor tissue and remaining liver in function of time. Data are mean \pm SD (n = 3).

Table 7.6: Metrics of the 3β - $[^{18}\text{F}]\text{FCA}$ time-activity curves for the DEN experiment. The values are expressed as mean \pm SD (n = 6 for control; n = 3 for large HCC; n = 11 for small HCC).

Significant differences towards control are marked with a * (*p<0.05; **p<0.01; ***p<0.001). GBI = gallbladder and intestines.

	Control	Large HCC-bearing mice	Small HCC-bearing mice
AUC liver (% ID.min)	1595 \pm 409	1470 \pm 193	1473 \pm 226
Max % ID liver (%)	62.01 \pm 6.81	47.78 \pm 0.80*	49.91 \pm 4.39*
Time-to-peak liver (min)	4.92 \pm 0.73	5.67 \pm 1.25	5.41 \pm 2.21
AUC GBI (% ID.min)	3516 \pm 338	3361 \pm 161	3455 \pm 446
Max % ID GBI (%)	82.52 \pm 4.88	80.88 \pm 2.22	81.22 \pm 8.19
AUC blood (kBq.min/mL)	19721 \pm 4286	15566 \pm 6200	19187 \pm 5268
Hepatic clearance (mL/min)	0.33 \pm 0.11	0.22 \pm 0.02	0.21 \pm 0.05
Biliary clearance (mL/min)	0.46 \pm 0.20	0.40 \pm 0.07	0.34 \pm 0.08

7.3.6 Alcoholic cirrhosis by CCl_4 administration

After 16 weeks of CCl_4 administration, the mice developed severe liver fibrosis and suffered from liver decompensation, which resulted in only 5 animals (of the 15) that could undergo a PET scan. Histology showed that these mice had F3 (severe) fibrosis, however no alcoholic steatohepatitis could be observed (Figure 7.11 left). No significant alterations in mRNA expression of the bile acid transporters was detected, except for *oatp4* mRNA expression that was reduced.

Hepatobiliary transport of 3β - ^{18}F FCA in the CCl_4 -treated animals was not significantly altered compared to the control group (Table 7.7).

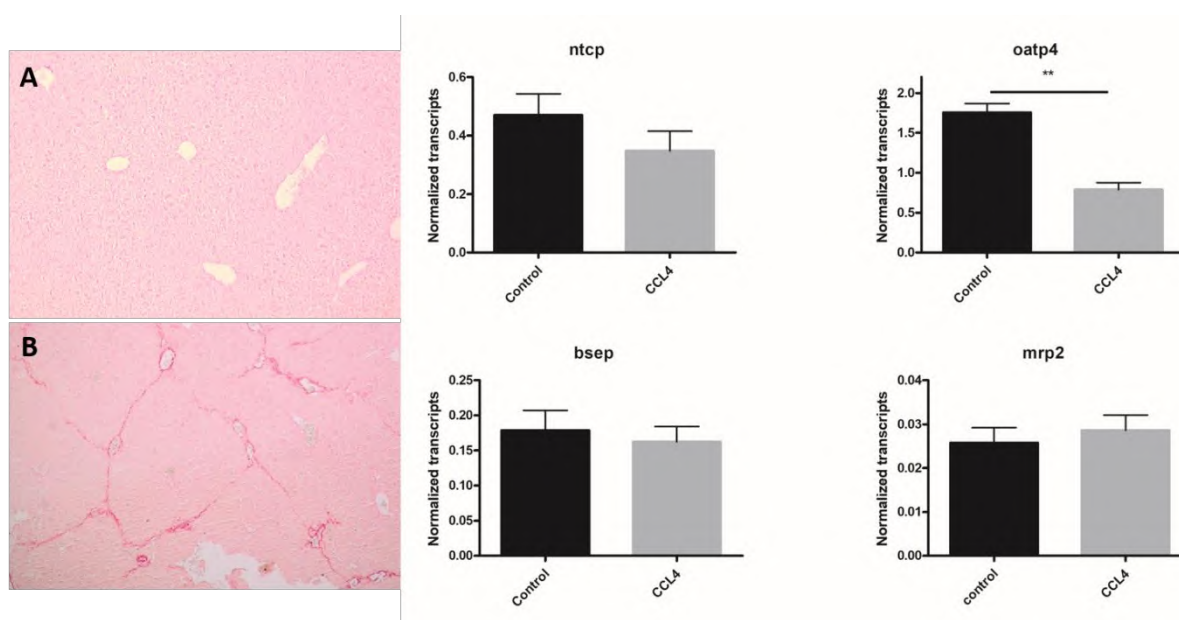


Figure 7.11: Left: Sirius Red stained liver sections, showing dark-red collagen fiber bands around liver lobules on section B (F3 fibrosis), which are absent in control mice (A). Right: mRNA expression of *ntcp*, *oatp4*, *bsep* and *mrp2* in CCl_4 -treated animals and controls. Data are presented as mean \pm SD and significant differences are marked by * (* $p < 0.05$; ** $p < 0.01$; *** $p < 0.001$).

Table 7.7: Metrics of the 3β - ^{18}F FCA TACs for the CCl_4 experiment. The values are expressed as mean \pm SD (n = 6 for control; n = 5 for CCl_4). Significant differences towards control are marked with a *(*p<0.05; **p<0.01; ***p<0.001). GBI = gallbladder and intestines.

	Control	CCl_4 -induced cirrhosis
AUC liver (% ID.min)	1595 \pm 409	1664 \pm 381
Max % ID liver (%)	62.01 \pm 6.81	53.59 \pm 6.33
Time-to-peak liver (min)	4.92 \pm 0.73	6.4 \pm 1.07
AUC GBI (% ID.min)	3516 \pm 338	3551 \pm 483
Max % ID GBI (%)	82.52 \pm 4.88	85.92 \pm 8.09
AUC blood (kBq.min/mL)	19721 \pm 4286	24290 \pm 8154
Hepatic clearance (mL/min)	0.33 \pm 0.11	0.22 \pm 0.09
Biliary clearance (mL/min)	0.46 \pm 0.20	0.35 \pm 0.09

7.4 Discussion

Recently, different research groups have made important contributions to ^{11}C and ^{18}F labeled bile acid PET tracers (Frisch et al. 2012; Schacht et al. 2016; Ørntoft et al. 2018; Jia et al. 2014; Testa et al. 2017; Frisch et al. 2018). In this dissertation, ^{18}F labeled bile acids were developed with only minimal modifications to the endogenous bile acid structure that are transported by the relevant bile acid transporters. In this chapter, lead compound 3β - ^{18}F FCA was evaluated in several mouse models of acute and chronic liver disease to determine the (pre)clinical scope in which this tracer can be employed.

Because interference of new candidate drugs with the bile acid transporters can lead to drug-induced cholestasis, it is important to detect this toxicity early on in preclinical drug development, saving valuable resources and time. PET imaging with 3β - ^{18}F FCA could aid in this task, by providing a non-invasive imaging platform to evaluate interference with the bile acid transporters *in vivo*. Therefore, 3β - ^{18}F FCA was first evaluated in mice that were dosed with cyclosporin, a immunosuppressive drug that is known to competitively inhibit the bile acid transporters *ntcp*, *oatp*, *bsep* and *mrp2* (Hofmann et al. 2011). Hepatobiliary transport metrics of 3β - ^{18}F FCA were determined in groups of mice that were administered a different dosage of cyclosporin. The drug caused significant, dosage-dependent changes in hepatobiliary transport of 3β - ^{18}F FCA: as the dosage rose, slower hepatic uptake and less biliary excretion was observed. Moreover, a higher cyclosporin dosage caused a higher accumulation of 3β - ^{18}F FCA in the liver, which is in accordance with endogenous bile acids that accumulate in the liver during cholestasis. The parameters for hepatic uptake (time-to-peak), biliary excretion (AUC gallbladder and intestines) and accumulation in the liver (AUC liver) reached a plateau from 20 mg/kg onwards. At 20 mg/kg, the activity of 3β - ^{18}F FCA in blood was significantly increased, which is in line with the observed increase in serum bile acids after cyclosporin administration (Stone et al. 1987; Elamiri et al. 2003). The acquired results show that 3β - ^{18}F FCA can be used to detect dosage-dependent interference of drugs with the hepatobiliary transporters *ntcp*, *oatp*, *mrp2* and *bsep* *in vivo*. The tracer could therefore be a valuable tool to evaluate a new candidate drug's cholestatic potential during drug development.

Hepatobiliary transport of 3β - ^{18}F FCA was also evaluated in the well-known APAP model for acute liver injury in mice. Contrary to cyclosporin mentioned in the previous

paragraph, APAP does not interfere with the bile acid transporters directly, but triggers significant liver injury and centrilobular necrosis when an overdose is administered (Jaeschke et al. 2013). Literature data shows that approximately 50 % of the hepatocytes are necrotic 24 hours post-administration of APAP (Uzi et al. 2013; Zhang et al. 2017). However, in our study, no significant differences in mRNA expression of the bile acid transporters and hepatic uptake or biliary excretion of 3β - ^{18}F FCA was detected between baseline and APAP-treated mice. This preserved hepatobiliary transport of 3β - ^{18}F FCA can possibly be attributed to remaining healthy parts of the liver that are still able to efficiently transport bile acids, such as 3β - ^{18}F FCA. The result can be used as an illustration of the tracer's excellent transport capacity, yet at the same time, it shows that 3β - ^{18}F FCA may have limited use in evaluating global liver function in diseases that only affect a part of the liver. Furthermore, another limitation of 3β - ^{18}F FCA is presented in the APAP model: hepatotoxic drugs that are not cholestatic, cannot be detected by 3β - ^{18}F FCA.

The utility of 3β - ^{18}F FCA was assessed in a model of chronic cholangiopathy by feeding mice the DDC-diet. DDC causes the formation of obstructing porphyrin plugs within bile ducts, which leads to cholestatic liver injury (Fickert et al. 2007; Sarnova & Gregor 2017). In this study, mice that were fed the DDC diet for 5 weeks showed a significantly lower hepatic mRNA expression of the basolateral bile acid uptake transporters *ntcp* and *oatp4* compared to control. This downregulation of *ntcp* and *oatp* is a known adaptive response to cholestasis to reduce bile acid accumulation in hepatocytes (Zollner & Trauner 2008; Fickert et al. 2007). Hepatic expression of *bsep* did not change, whereas *mrp2* was significantly higher compared to control. In cholestasis, expression of *bsep* and *mrp2* is indeed preserved or can even be increased (Zollner & Trauner 2008; Klaassen & Aleksunes 2014). Hepatobiliary transport of 3β - ^{18}F FCA in DDC-fed mice was significantly altered compared to baseline. Although the expression of canalicular efflux transporters is preserved or even increased (in the case of *mrp2*), a significant decrease of tracer excretion in gallbladder and intestines was noticed. This is probably caused by the physical obstruction of bile ducts with porphyrin plugs that limits biliary excretion. A slower hepatic uptake and increased arterial activity of 3β - ^{18}F FCA were also observed and can be linked to the reduced expression of basolateral uptake transporters *ntcp* and *oatp4* as an adaptive response to obstructive cholestasis. After a recovery period, hepatobiliary transport parameters returned to normal

baseline levels. These findings show that 3β - $[^{18}\text{F}]$ FCA can give valuable insight for the *in vivo* longitudinal follow-up of bile acid transport in chronic cholestatic liver disease.

Evaluation of 3β - $[^{18}\text{F}]$ FCA was also performed in a chronic liver disease model of NASH. Steatohepatitis was successfully induced in mice by 8 weeks of MCD diet feeding. The mRNA expression of the basolateral uptake transporters *ntcp* and *oatp4* was significantly reduced compared to control, and expression of the canalicular efflux transporter *bsep* was preserved. These results are in line with literature data on altered bile acid transporter expression in NASH (Tanaka et al. 2012). However, in this study, mRNA levels of *mrp2* were reduced after 8 weeks of MCD diet, whereas they remained unaltered in a previous report (Tanaka et al. 2012). The hepatobiliary transport characteristics of 3β - $[^{18}\text{F}]$ FCA in mice with steatohepatitis could be linked to the altered gene expression of the bile acid transporters. Hepatic uptake was significantly slower and reduced compared to baseline. The arterial blood concentration of 3β - $[^{18}\text{F}]$ FCA was also higher, which is in accordance with the higher plasma bile acid concentrations found in NASH patients (Ferslew et al. 2015). With regards to biliary efflux, there was a slight decrease in tracer presence in gallbladder and intestines compared to baseline. After a recovery period, hepatobiliary transport metrics of 3β - $[^{18}\text{F}]$ FCA returned to baseline. This confirms the observation that MCD diet-induced steatohepatitis is reversible after four weeks of recovery (Itagaki et al. 2013). Therefore, it could be possible to use 3β - $[^{18}\text{F}]$ FCA as a means to assess and follow-up on the functionality of hepatocytes in NASH, with regards to bile acid transport efficiency.

PET tracer 3β - $[^{18}\text{F}]$ FCA was also evaluated in a HCC mouse model. Based on the macro- and microscopic findings, HCC was successfully induced by DEN administration. Expression analysis of the HCC lesions revealed that *ntcp*, *oatp4* and *bsep* were significantly reduced, whereas *mrp2* was increased. To the best of our knowledge, no data are available in literature on bile acid transporter expression in a rodent HCC model to be compared with. However, the present results are in accordance with the observed dysregulation of the bile acid transporters in human HCC tissue (Zollner et al. 2005; Cui et al. 2003; Chen et al. 2013). Although 23 weeks of DEN administration resulted in HCC formation in almost every animal, the inherent randomness of tumor formation and growth only led to three animals with a tumor that was large enough to evaluate with PET. In these mice, 3β - $[^{18}\text{F}]$ FCA showed a decreased hepatic uptake in the tumor compared to the surrounding liver tissue,

corresponding with the lower expression of the bile acid basolateral uptake transporters in HCC. The global hepatobiliary transport efficiency of 3β - ^{18}F FCA in a HCC liver was not significantly affected. This confirms the findings from the APAP model that, due to the efficiency of the tracer's transport, it is less suited to determine global liver function in liver diseases that only affect a portion of the liver. However, abovementioned results show that it is possible to detect regional differences in liver functionality through reduced expression of *ntcp* and *oatp* with 3β - ^{18}F FCA PET. These promising results could potentially lead to a functional imaging tool to monitor HCC pre-and post-therapy, in support of CT and MRI techniques that are most commonly used to evaluate liver disease.

Finally, 3β - ^{18}F FCA was also evaluated in a mouse model of alcoholic cirrhosis. Subcutaneous administration of 1 mL/kg CCl_4 twice a week for 16 weeks resulted in the generation of severe F3 fibrosis, but not the expected cirrhosis with moderate steatosis (Geerts et al. 2008). The diseased animals showed no altered mRNA expression of the dominant bile acid transporters *ntcp* and *bsep*. *Mrp2* mRNA expression was also not significantly altered but *oatp4* mRNA was reduced. To the best of our knowledge, no preclinical data is available in literature on mouse bile acid transporter expression in liver fibrosis to compare the present results to. Nonetheless, despite severely fibrotic liver tissue (but retained mRNA expression of the dominant bile acid transporters), no significant alteration of 3β - ^{18}F FCA's hepatobiliary transport was observed. Therefore, it can be said that the utility of the tracer is limited if there are no significant differences in bile acid transporter expression in the liver disease under investigation.

In conclusion and to the best of our knowledge, 3β - ^{18}F FCA is the first PET bile acid that has been evaluated in different mouse models for liver diseases. The obtained results can help to define the (pre)clinical applications of 3β - ^{18}F FCA as a PET tracer to monitor and longitudinally follow-up altered liver functionality in chronic liver diseases through differences in expression of the bile acid transporters.

7.5 Conclusion

The bile acid PET tracer 3β - ^{18}F FCA was evaluated in different mouse models of liver disease. Dosage-dependent alterations in the tracer's hepatobiliary transport metrics could be observed in mice that were dosed with cyclosporine, an immunosuppressive drug that is known to directly inhibit the hepatic bile acid transporters. This way, drug-induced cholestasis can be detected in preclinical drug development. Acute liver toxicity by APAP overdose did not result in significant change of the tracer's hepatobiliary transport. Chronic liver disease models of cholangiopathy and NASH were generated by feeding mice DDC or MCD diet respectively. In both models, 3β - ^{18}F FCA was able to detect altered liver functionality, including recovery. Gene expression data of the bile acid transport proteins could be linked to the altered hepatobiliary transport of 3β - ^{18}F FCA in NASH. HCC development was triggered in mice that received DEN. The tracer showed reduced uptake in HCC compared to the surrounding liver tissue, which could be linked to lower expression of the basolateral uptake transporters in HCC. Finally, repeated CCl_4 injections in mice resulted in severe liver fibrosis, yet no significant changes in expression of the dominant bile acid transporters. In this model, no difference in hepatobiliary transport of 3β - ^{18}F FCA was observed compared to a control group.

The acquired results imply that 3β - ^{18}F FCA can have a broad application range in preclinical drug development and the (pre)clinical evaluation of liver function through the tracer's (regionally altered) hepatobiliary transport by the bile acid transporters.

7.6 References

- Chen, Y. et al., 2013. Bile salt export pump is dysregulated with altered farnesoid X receptor isoform expression in patients with hepatocellular carcinoma. *Hepatology*, 57(4), pp.1530–1541.
- Cui, Y. et al., 2003. Detection of the human organic anion transporters SLC21A6 (OATP2) and SLC21A8 (OATP8) in liver and hepatocellular carcinoma. *Laboratory Investigation*, 83(4), pp.527–538.
- Delire, B., Stärkel, P. & Leclercq, I., 2015. Animal Models for Fibrotic Liver Diseases: What We Have, What We Need, and What Is under Development. *Journal of Clinical and Translational Hepatology*, 3, pp.53–66.
- Elamiri, A. et al., 2003. Effect of mdr2 mutation with combined tandem disruption of canalicular glycoprotein transporters by cyclosporine A on bile formation in mice. *Pharmacological Research*, 48(5), pp.467–472.
- Ferslew, B.C. et al., 2015. Altered Bile Acid Metabolome in Patients with Nonalcoholic Steatohepatitis. *Digestive Diseases and Sciences*, 60, pp.3318–3328.
- Fickert, P. et al., 2007. A New Xenobiotic-Induced Mouse Model of Sclerosing Cholangitis and Biliary Fibrosis. *The American Journal of Pathology*, 171(2), pp.525–536.
- Frisch, K. et al., 2012. [N-methyl- ^{11}C]cholylsarcosine, a novel bile acid tracer for PET/CT of hepatic excretory function: radiosynthesis and proof-of-concept studies in pigs. *Journal of nuclear medicine : official publication, Society of Nuclear Medicine*, 53(5), pp.772–8.
- Frisch, K. et al., 2018. N-(4- $[^{18}\text{F}]$ fluorobenzyl) cholyglycine, a novel tracer for PET of enterohepatic circulation of bile acids: Radiosynthesis and proof-of-concept studies in rats. *Nuclear Medicine and Biology*, 61, pp.56–62.
- Geerts, A.M. et al., 2008. Comparison of three research models of portal hypertension in mice: Macroscopic, histological and portal pressure evaluation. *International Journal of Experimental Pathology*, 89(4), pp.251–263.

- Ghibellini, G. et al., 2004. A Novel Method for the Determination of Biliary Clearance in Humans. *The AAPS journal*, 6(1), pp.45–56.
- Hofmann, F., Fromm, M. & Kim, R., 2011. *Handbook of Experimental Pharmacology vol 201*,
- Itagaki, H. et al., 2013. Morphological and functional characterization of non-alcoholic fatty liver disease induced by a methionine-choline-deficient diet in C57BL/6 mice. *Int J Clin Exp Pathol*, 6(12), pp.2683–2696.
- Jaeschke, H. et al., 2013. Models of drug-induced liver injury for evaluation of phytotherapeutics and other natural products. *Food and Chemical Toxicology*, 55, pp.279–289.
- Jia, L. et al., 2014. Synthesis and evaluation of (18)F-labeled bile acid compound: a potential PET imaging agent for FXR-related diseases. *Nuclear medicine and biology*, 41, pp.495–500.
- Jüngst, C. et al., 2013. Intrahepatic cholestasis in common chronic liver diseases. *European journal of clinical investigation*, 43(10), pp.1069–83.
- Klaassen, C.D. & Aleksunes, L.M., 2014. Xenobiotic , Bile Acid , and Cholesterol Transporters: Function and Regulation. *Pharmacological Reviews*, 62(1), pp.1–96.
- Ørntoft, N. et al., 2018. Functional assessment of hepatobiliary secretion by ^{11}C -choly sarcosine positron emission tomography. *Biochimica et Biophysica Acta - Molecular Basis of Disease*, 1864, pp.1240–1244.
- Padda, M.S. et al., 2011. Drug-Induced Cholestasis. *Hepatology*, 53, pp.1377–1387.
- Rinella, M.E. et al., 2008. Mechanisms of hepatic steatosis in mice fed a lipogenic methionine choline-deficient diet. *Journal of Lipid Research*, 49, pp.1068–1076.
- Sarnova, L. & Gregor, M., 2017. Biliary system architecture: experimental models and visualization techniques. *Physiological research*, 66, pp.383–390.
- Schacht, A.C. et al., 2016. Radiosynthesis of N- ^{11}C -Methyl-Taurine-Conjugated Bile Acids and Biodistribution Studies in Pigs by PET/CT. *Journal of Nuclear Medicine*, 57(4), pp.628–633.

- Stone, B. et al., 1987. Cyclosporin A-induced cholestasis: The mechanism in a rat model. *Gastroenterology*, 93(2), pp.344–351.
- Tanaka, N. et al., 2012. Disruption of phospholipid and bile acid homeostasis in mice with nonalcoholic steatohepatitis. *Hepatology*, 56(1), pp.118–129.
- Testa, A. et al., 2017. Design, synthesis, in vitro characterization and preliminary imaging studies on fluorinated bile acid derivatives as PET tracers to study hepatic transporters. *Bioorganic and Medicinal Chemistry*, 25, pp.963–976.
- Thakkar, N., Slizgi, J.R. & Brouwer, K.L.R., 2017. Effect of Liver Disease on Hepatic Transporter Expression and Function. *Journal of Pharmaceutical Sciences*, 106(9), pp.2282–2294.
- Tolba, R. et al., 2015. Diethylnitrosamine (DEN)-induced carcinogenic liver injury in mice. *Laboratory animals*, 49(S1), pp.59–69.
- Uzi, D. et al., 2013. CHOP is a critical regulator of acetaminophen-induced hepatotoxicity. *Journal of Hepatology*, 59(3), pp.495–503.
- Zhang, J. et al., 2017. Astaxanthin pretreatment attenuates acetaminophen-induced liver injury in mice. *International Immunopharmacology*, 45, pp.26–33.
- Zollner, G. et al., 2005. Hepatobiliary transporter expression in human hepatocellular carcinoma. *Liver international : official journal of the International Association for the Study of the Liver*, 25(2), pp.367–79.
- Zollner, G. & Trauner, M., 2008. Mechanisms of cholestasis. *Cl Liver Disease*, (12), pp.1–26.

CHAPTER 8:

GENERAL CONCLUSIONS

The aim of this dissertation was to develop ^{18}F labeled bile acid analogues for Positron Emission Tomography (PET) imaging that closely resemble endogenous bile acids in molecular structure, *in vitro* and *in vivo* characteristics. It was hypothesized that these tracers can be used to detect pharmacological interference with the bile acid transporters (drug-induced cholestasis; DIC) in preclinical drug development and can serve as a functional liver imaging tool in liver disease through altered expression of the bile acid transporters. To the best of our knowledge, this is the first time that a bile acid PET tracer is extensively evaluated in preclinical mouse models of liver diseases.

Four research questions were postulated in Chapter 3 of this dissertation and each of them was covered in a different chapter.

Question 1 (Chapter 4):

Can a set of ^{18}F labeled bile acid analogues be synthesized in sufficient radiochemical yields, that are characterized by minimal modification to the bile acid steroid backbone?

A number of ^{18}F labeled bile acid analogues were developed to monitor (disturbed) hepatobiliary transport of bile acids in liver disease with PET. These analogues differed in bile acid backbone (cholic acid, chenodeoxycholic acid and glycocholic acid) and in the position of the radiolabel (substitution of different hydroxyl functions of cholic acid).

Suitable precursors for radiosynthesis and cold fluorinated reference compounds were synthesized. The radiosynthesis encompassed a $\text{S}_{\text{N}}2$ nucleophilic substitution with $^{18}\text{F}^-$ on a mesylated, protected precursor, followed by an alkaline deprotection step and HPLC purification. Four PET tracers were successfully synthesized in moderate radiochemical yields: 3β - ^{18}F fluorocholeic acid (3β - ^{18}F FCA), 3α - ^{18}F fluorocholeic acid (3α - ^{18}F FCA), 3β - ^{18}F fluorocholedeoxycholeic acid (3β - ^{18}F FCDCA), and 3β - ^{18}F fluoroglycocholeic acid (3β - ^{18}F FGCA) (Figure 8.1). The precursors for 12β - ^{18}F fluorocholeic acid (12β - ^{18}F FCA) and 7β - ^{18}F fluorocholeic acid (7β - ^{18}F FCA) could not be labeled with sufficient radiochemical yield and therefore could not be used for further *in vivo* evaluation.

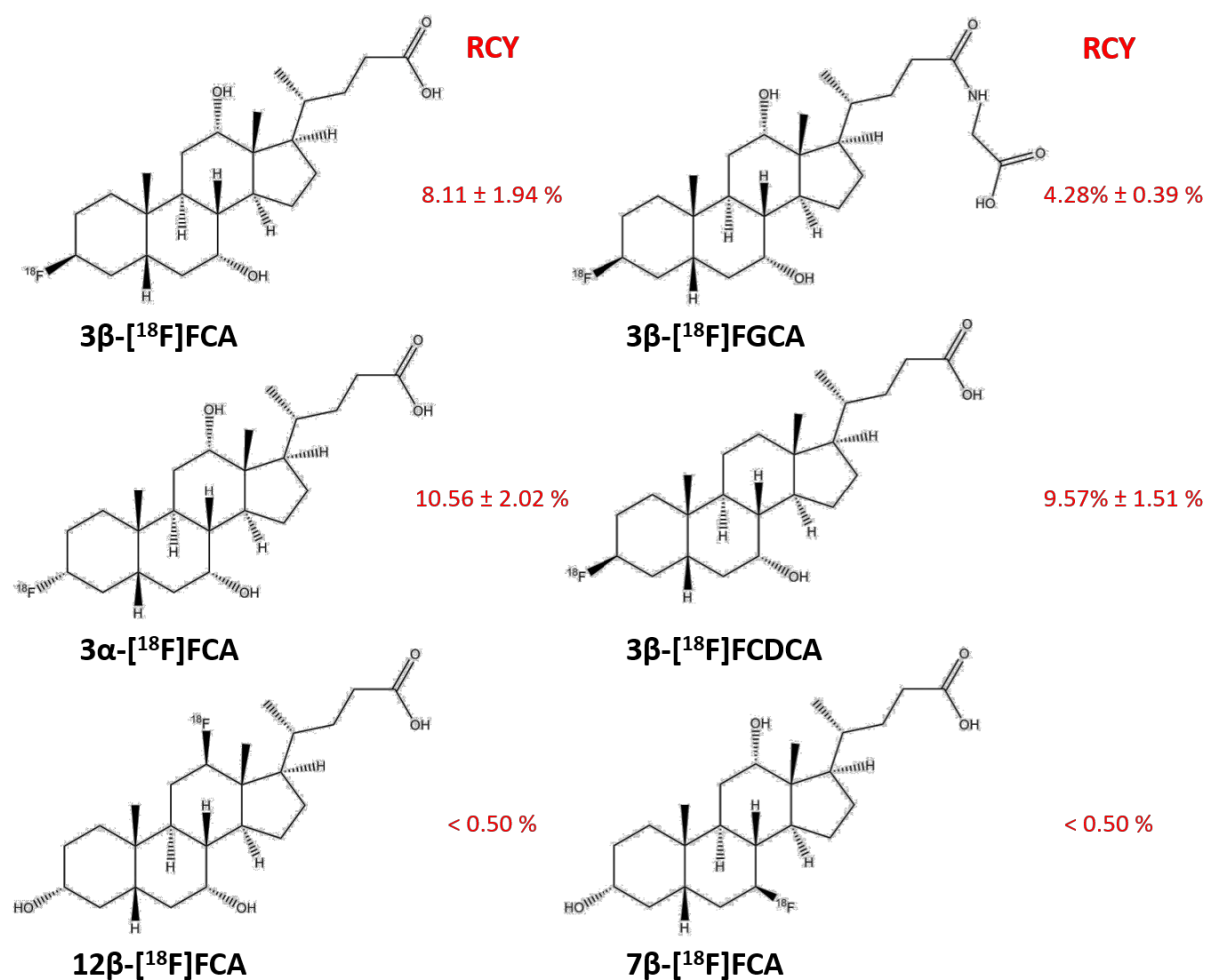


Figure 8.1: overview of the synthesized ^{18}F labeled bile acids, with the corresponding non-decay-corrected radiochemical yields (RCY).

Question 2 (Chapter 5):

Are the developed fluorinated bile acid analogues stable and substrates for the relevant hepatobiliary transport proteins *in vitro*?

The stability of 3β -[^{18}F]FCA, 3α -[^{18}F]FCA, 3β -[^{18}F]FGCA and 3β -[^{18}F]FCDCA was assessed in their formulation, in mouse serum and in presence of primary mouse hepatocytes and found to be stable for *in vivo* use. Fluorine substitution possibly hampers metabolism but does not have a considerable effect on substrate recognition by the relevant bile acid transporters: they are substrates with low micromolar affinity for NTCP, OATP1B1 and BSEP, which is also the case for endogenous bile acids. MRP2 is also used by 3β -[^{18}F]FCA. The LogD(7.4) values of the fluorinated bile acids were also in accordance with

endogenous bile acids. Therefore, the developed compounds were deemed suitable to monitor (disturbed) hepatobiliary transport of bile acids *in vivo* with PET.

Question 3 (Chapter 6):

- a) Do the ^{18}F labeled bile acid analogues show hepatobiliary transport in healthy wild-type mice?
- b) Is the inter- and intra-animal variability sufficiently low to assess hepatobiliary transport?
- c) Can disturbed hepatobiliary transport of bile acids be detected *in vivo*?

The developed ^{18}F labeled bile acids (3α - ^{18}F FCA, 3β - ^{18}F FCA, 3β - ^{18}F FCDCA and 3β - ^{18}F FGCA) were evaluated in healthy wild-type mice to evaluate their pharmacokinetics after intravenous administration. All tracers showed exclusive hepatic uptake and were subsequently excreted in gallbladder and intestines. No uptake in other organs was observed. Time-activity curves (TACs) were determined for the liver, gallbladder and intestines, and arterial blood. It was found that three out of four newly developed PET tracers (3α - ^{18}F FCA, 3β - ^{18}F FCA and 3β - ^{18}F FGCA) displayed fast and efficient hepatobiliary transport. There was a slight, yet significant difference in hepatobiliary transport efficiency of the 3α - ^{18}F FCA and 3β - ^{18}F FCA epimers. Glycine conjugation of 3β - ^{18}F FCA (to form 3β - ^{18}F FGCA) did not have an impact on *in vivo* hepatobiliary transport. The chenodeoxycholic acid derivate 3β - ^{18}F FCDCA had the most aberrant TACs, showing both slower and lower hepatic uptake and biliary excretion. Because it already displays impaired transport, 3β - ^{18}F FCDCA is less suited to monitor (disturbed) hepatobiliary transport of bile acids.

Lead compound 3β - ^{18}F FCA showed good inter-and intra-animal reproducibility in mice (maximum observed coefficient of variation: 15.5 %) that is comparable with the preclinical variability of the commonly used hepatobiliary SPECT tracer $^{99\text{m}}\text{Tc}$ -mebrofenin.

Furthermore, lead compound 3β - ^{18}F FCA was validated as an *in vivo* ntcp/oatp and bsep/mrp2 substrate by coadministration of the tracer with rifampicin or bosentan. Both drugs caused a significant decrease in hepatobiliary transport efficiency of the tracer. Therefore, 3β - ^{18}F FCA can be used as a probe for *in vivo* detection of disturbances in bile acid uptake and biliary efflux.

Question 4 (Chapter 7):

Can ^{18}F labeled bile acid analogues play a role in detection and follow-up of liver diseases?

- a) By detecting direct pharmacological interference with the bile acid transporters.
- b) By providing insight into liver function through altered expression of the bile acid transporters in liver diseases.

Valorization of $3\beta\text{-}[^{18}\text{F}]\text{FCA}$ as a hepatobiliary imaging probe was performed in different mouse models of liver disease. Table 8.1 lists the liver diseases that could be visualized.

Table 8.1: Different mouse models of liver disease in which $3\beta\text{-}[^{18}\text{F}]\text{FCA}$ was evaluated.

Liver disease	Visualization possible?
Drug-induced cholestasis (pharmacological inhibition of transporters)	+
Acute liver toxicity (APAP)	-
Chronic cholangiopathy	+
NASH	+
HCC	+
Fibrosis	-

Dose-dependent alterations in the tracer's hepatobiliary transport metrics could be observed in mice that were dosed with cyclosporine, an immunosuppressive drug that is known to directly inhibit the hepatic bile acid transporters. Consequently, PET imaging with this tracer offers a valuable research platform to evaluate drug-induced cholestasis in preclinical drug development.

Several well-described mouse models for liver disease were generated to validate 3β -[^{18}F]FCA.

- Acute liver toxicity by acetaminophen (APAP) overdose did not result in significant change of the tracer's global hepatobiliary transport. This was probably due to the remaining healthy liver tissue that is still able to efficiently transport 3β -[^{18}F]FCA.
- Chronic liver disease models of cholangiopathy and non-alcoholic steatohepatitis (NASH) were generated by feeding mice 3,5-diethoxycarbonyl-1,4-dihydrocollidine (DDC) or methionine and choline deficient (MCD) diet, respectively. In both models, 3β -[^{18}F]FCA was able to detect altered liver functionality, including the subsequent recovery. Gene expression data of the bile acid transport proteins could be linked to the altered hepatobiliary transport of 3β -[^{18}F]FCA in the NASH model.
- Hepatocellular carcinoma (HCC) development was triggered in mice that received repeated diethylnitrosamine (DEN). The tracer showed reduced uptake in HCC compared to the surrounding liver tissue, which could be linked to lower expression of the basolateral uptake transporters in HCC.
- Finally, repeated CCl_4 injections in mice resulted in mouse model for severe liver fibrosis, yet no significant changes in expression of the dominant bile acid transporters were observed. In this model, no difference in hepatobiliary transport of 3β -[^{18}F]FCA was noticed compared to a control group.

In conclusion, the acquired results imply that 3β -[^{18}F]FCA can have a broad application range in preclinical drug development and the (pre)clinical evaluation of liver function through the tracer's (regionally altered) hepatobiliary transport by the bile acid transporters. The bile acid PET tracer 3β -[^{18}F]FCA can be useful to monitor and longitudinally follow-up altered liver functionality in chronic liver diseases through differences in expression of the bile acid transporters.

CHAPTER 9:

**BROADER INTERNATIONAL CONTEXT, RELEVANCE
AND FUTURE PERSPECTIVES**

9.1 Development of radiolabeled bile acids for molecular imaging of the liver

Molecular imaging can be defined as “*the visual representation, characterization and quantification of biological processes at the cellular and subcellular levels within intact living organisms*” (quote from: Massoud et al. 2003). The past two decades, the field of molecular imaging has evolved into a valuable tool to comprehend certain biological phenomena, identify regions of pathology and explore the molecular origins, progression and follow-up of a disease. In this regard, molecular imaging can give important insight in the functionality of organs and can be an extension of the commonly used anatomical liver imaging modalities Computed Tomography (CT), Magnetic Resonance Imaging (MRI) and Ultrasound (US).

Molecular imaging relies on the administration of a molecular imaging probe, which determines the biological process or phenomenon that will be visualized (and quantified). In this dissertation, we focused imaging probes based on bile acids: amphiphilic steroid derivatives that are exclusively synthesized in the liver, show biliary excretion and are subsequently taken up again in the liver by portal recirculation. This transport is warranted by the function of specific hepatobiliary bile acid transport proteins. Therefore, bile acids form an ideal probe to assess the viability of hepatocytes *in vivo* through their function of active bile acid transport in- and out of the hepatocytes. Furthermore, alterations in bile acid transport can be detected and monitored: a toxic accumulation of bile acids (cholestasis) can occur as a result of drug interference with the efficient hepatobiliary transport process, or in certain liver diseases that are characterized by impeded bile flow, such as primary biliary cirrhosis or sclerosing cholangitis (de Lima Toccafondo Vieira & Tagliati 2014; Jüngst et al. 2013; Kubitz et al. 2012).

Multiple efforts have been made to develop a bile acid probe in the fields of MRI, Single Photon Emission Computed Tomography (SPECT) and Positron Emission Tomography (PET). These probes are discussed in greater detail in Chapter 2 of this dissertation. In short, it was found that contrast agents for functional MRI imaging of the liver require administration of a considerable amount of contrast agent, which can potentially interfere with normal bile acid homeostasis. Although these MRI probes show hepatobiliary transport, they do not use the relevant bile acid transporters (no transport through NTCP and BSEP), which limits the use they can have as an *in vivo* representation of endogenous bile acids to detect possible alterations in bile acid transport efficiency.

Nuclear imaging techniques such as SPECT and PET are of considerable interest in functional imaging, as they are tracer techniques. This means that the radiolabeled probe is only administered in extremely minute quantities (nmol-pmol range). Consequently, there is a reduced risk of interference with the process under investigation. SPECT tracers to study hepatobiliary transport have already been described. The lidocaine analogue ^{99m}Tc -mebrofenin can be used to detect liver or biliary tree disorders. An extensive preclinical evaluation of ^{99m}Tc -mebrofenin was performed by our research group (Neyt et al. 2013). This study concluded that ^{99m}Tc -mebrofenin enters and exits the hepatocytes by the OATP and MRP2 transport systems respectively, which is not in accordance with the bile acid transporters that endogenous bile acids can use (NTCP/OATP and BSEP/MRP2). Although ^{99m}Tc -mebrofenin has clinical use in liver function assessment, it offers no information about endogenous bile acids' *in vivo* behavior. Therefore, our research group developed ^{99m}Tc labeled bile acid analogues (Neyt et al. 2016). Due to the large ^{99m}Tc complex attached to the bile acid backbone, these radiotracers were also no substrates of NTCP and BSEP.

In 2014, at the start of this PhD project, no radiolabeled bile acid was available that was a confirmed *in vitro* and *in vivo* as a substrate of the bile acid transporters. Our research group hypothesized that the development of a ^{18}F labeled bile acid for PET imaging could provide the desired radiotracer to study hepatobiliary transport of bile acids in liver disease. In this dissertation, the development of several ^{18}F labeled bile acids that closely mimic their endogenous counterparts, is presented. *In vitro* results confirm that the tracers are substrates of the relevant bile acid transporters. *In vivo* evaluation revealed that these compounds display favorable hepatobiliary kinetics. Finally, our lead compound, 3 β - ^{18}F fluorocholeic acid (3 β - ^{18}F FCA), was evaluated in several liver disease models and was proven to be valuable to detect and follow-up on altered functionality of hepatocytes *in vivo*, with regards to bile acid transport.

Since 2014, other researchers have also attempted to cater to the unmet need of a PET bile acid. Three other research groups have also developed PET bile acids, indicating the increasing interest in functional liver imaging. Firstly, Jia et al. developed a ^{18}F labeled bile acid compound to study farnesoid-X-receptor (FXR) related diseases (Jia et al. 2014). Preclinical evaluation in mice revealed that this compound showed hepatobiliary transport. However, no *in vitro* evaluation was performed to answer the raised questions on the

possibly altered transport mechanism compared to endogenous bile acids and the molecular structure was significantly larger than an endogenous bile acid (Frisch & Sørensen 2014). Secondly, the group of Testa et al. preclinically developed several ^{18}F labeled bile acid analogues to study drug-drug interactions and drug-induced toxicity by OATP1B1, NTCP and BSEP transporters (Testa et al. 2017). *In vitro* and *in vivo* analysis was performed, however, the molecular structures of Testa's PET bile acid analogues were also significantly larger than an endogenous bile acid, with potentially altered transport as a result. Finally, the group from Aarhus University Hospital (Denmark) has the largest scientific output with regards to PET bile acids. They developed several ^{11}C labeled conjugated bile acids that were evaluated *in vivo* in pigs (Frisch et al. 2012; Schacht et al. 2016; Sorensen et al. 2016). A clinical trial was also performed with their lead compound, N- ^{11}C methyl-cholylysarcosine (Ørntoft et al. 2017). Nine healthy individuals and eight patients with varying degrees of cholestasis from different etiology (alcoholic hepatitis, primary biliary cholangitis, primary sclerosing cholangitis, alcoholic cirrhosis, autoimmune hepatitis) were examined. It was found that N- ^{11}C methyl-cholylysarcosine was able to detect and quantify reduced hepatic uptake, biliary excretion and increased backflux to blood. These findings may improve understanding of cholestatic liver diseases and may support therapeutic decisions. Recently, the Aarhus University Hospital Research group developed a ^{18}F labeled bile acid to detect enterohepatic recirculation in rats (Frisch et al. 2018). The tracer bears a large, additional ^{18}F labeled benzene ring and therefore differs substantially from endogenous bile acids. Moreover, no *in vitro* evaluation was performed on the ^{11}C and ^{18}F labeled bile acids.

The development and evaluation of our ^{18}F labeled bile acid analogues can be placed in the recent, increasing interest in functional imaging of the liver with PET (Figure 9.1). A pivotal advantage of our compounds over abovementioned tracers, is the molecular structure of our ^{18}F labeled bile acids. Whereas other groups used large ^{18}F labeled prosthetic groups for radiolabeling, we developed tracers with only minimal structural difference with endogenous bile acids. This approach warranted low micromolar affinities of the tracers for the relevant bile acid transporters. Moreover, an extensive *in vitro* and *in vivo* evaluation of our compounds was performed. Due to absence of *in vitro* data for most of the compounds mentioned in the previous paragraph, no definitive answer can be given

whether the major changes in molecular structure also cause changes in the hepatic transport systems that are used.

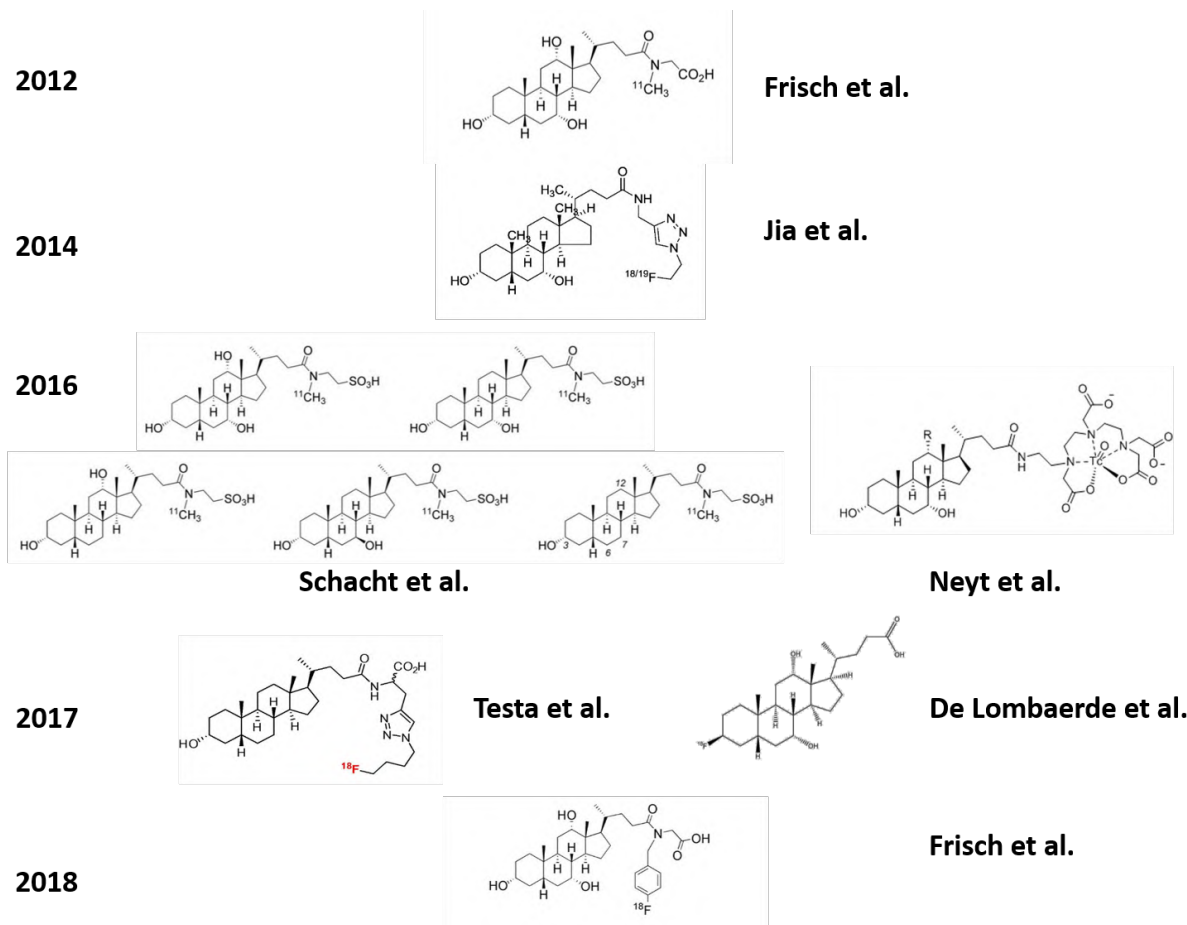


Figure 9.1: Overview of the recently developed bile acid tracers for SPECT and PET imaging.

Although our developed tracers represent endogenous bile acids well by their transport through both NTCP/OATP and BSEP/MRP2, no selective information on NTCP and BSEP transport activity alone can be gained from them. Therefore, future research on radiolabeled substrates for the bile acid transporters could focus on the development of selective radiotracers for NTCP or BSEP, to gain fundamental knowledge on transport through these proteins. However, by using bile acid analogues, there is a large probability that these are also transported by other broad substrate specificity transporters such as OATP and MRP2. Consequently, it is possible that tracers based on the bile acid steroid backbone have to be sidelined. The tracer [^{11}C]rosuvastatin for example, is a statin that uses NTCP to enter the hepatocytes (He et al. 2014). It is nonetheless also a substrate of OATP, illustrating the challenging task of developing a tracer that exclusively uses NTCP.

Another future research interest, is scaling up the radiosynthesis of our developed ^{18}F labeled bile acids. Currently, all radiosyntheses are done manually on the bench. This puts a strain on how much radiotracer can be safely produced and how many animals can be scanned in one day. Furthermore, if a first-in-human application would ever be considered, not enough finished radiotracer can be produced. An automated radiosynthesis module in a lead shielded container (hot cell) allows remotely controlled radiosynthesis of larger activities with minimal radiation dose for the user. However, converting a manual radiosynthesis into an automated one is not always a straightforward task. Differences in radiolabeling yield and purification efficiency might be observed.

9.2 (Future) application areas

9.2.1 Preclinical drug development

Development of a drug is a lengthy and costly undertaking, spanning approximately 14 years and costing an approx. 2 billion dollar (Willmann et al. 2008). This can be explained by the inherent hit-and-miss strategy in development of new drug candidates: Hundreds of compounds are screened for a specific function, yet only a couple pass through preclinical drug development (Figure 9.2). The use of molecular imaging in drug development can help to reduce attrition rates and allow selection of the most promising drug candidate early on in drug development, saving valuable time and resources.

Toxicity is a leading cause of attrition at all stages of the drug development process (Kramer et al. 2007). Because of its essential role in metabolism and detoxification, the liver can be especially prone to injury. Drug-induced liver injury (DILI) is a major issue for the pharmaceutical industry and healthcare. It accounts for the majority of acute liver failure, is a prime cause of attrition for new candidate drugs in the drug development process and responsible for drug withdrawal from the market (Ostapowicz et al. 2002; Bernal & Wendon 2013). About 32 % of all drug withdrawals in the period 1975-2007 were due to hepatotoxicity (Stevens & Baker 2009) (Regev 2014).

A major part of DILI is represented by drug-induced cholestasis (Yang et al. 2013), which results from inhibition of the bile acid transporters on the hepatocyte. It is important to detect this drug-induced cholestasis early on in drug development. Several *in vitro* techniques are available to detect interference with the bile acid transporters such as

transfected cell lines, membrane vesicles or sandwich-cultured hepatocytes (de Lima Toccafondo Vieira & Tagliati 2014). Although these assays are cost-effective and fast, they do not mimic the *in vivo* situation completely. *In vivo* research to monitor a new candidate drug's cholestatic potential is still relevant, yet is time-consuming and requires invasive sampling of a lot of laboratory animals. Blood, liver and bile samples have to be acquired, processed and analyzed (Bergman et al. 2010; Sjögren et al. 2014; Shin et al. 2014).

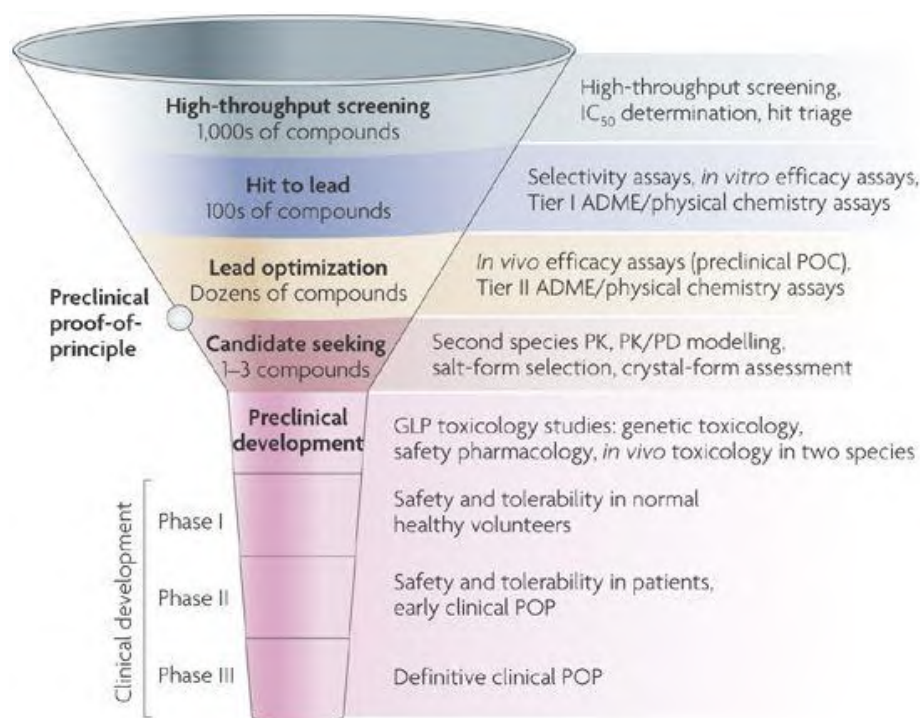


Figure 9.2: A typical testing scheme for a small-molecule drug discovery program
(From: Kramer et al. 2007).

Our developed ^{18}F labeled bile acids can be used as a non-invasive *in vivo* research platform in the lead optimization phase of a preclinical drug development program. Interference of new drug candidates with the bile acid transporters can be detected *in vivo* and a dose-response curve can be acquired (see Chapter 7). Because of their close structural resemblance to endogenous bile acids, the ^{18}F labeled bile acids can give valuable insight in drug-induced cholestasis. It would also be possible to monitor the toxicity longitudinally, by scanning the same animal at several timepoints without compromising statistical significance, whereas traditional studies require the sacrifice of multiple animal groups at all different timepoints (Cunha et al. 2014). This way, PET bile acid scans can help reduce

laboratory animal usage, which is in line with the 3R principle to reduce the use of laboratory animals in research.

9.2.2 Clinical research

Assessing the (remaining) liver function of liver disease patients is of utmost importance to monitor disease status. This is usually achieved with conventional laboratory blood tests (liver function tests; LFTs). Table 9.1 lists commonly determined biochemical substances that relate to liver function. However, LFTs only provide a limited reflection of liver function. The determined concentrations are for example dependent on the volume of distribution, availability of the substance to target liver cells and elimination (Bennink et al. 2012). The use of molecular imaging might provide some advantages over LFTs, as it offers insight in a precise biochemical pathway at a molecular level. Furthermore, it can add a spatial component to the liver's function, making it possible to determine regional differences.

Table 9.1: Conventional laboratory tests reflecting liver function or injury (from: Bennink et al. 2012). *: part of the so-called liver function tests (LFTs)

Blood assay	Main significance
Albumin	Synthetic function
Alanine transaminase (ALT)*	Hepatocyte injury/necrosis
Aspartate transaminase (AST)*	Hepatocyte injury/necrosis
Alkaline phosphatase (ALP)*	Bile duct obstruction/cholestasis
Bilirubin, total*	Uptake, conjugation, excretion
Bilirubin, direct (eg. Conjugated)*	Bile excretion
Gamma glutamyl transpeptidase (GGT)*	Cholestasis, alcohol abuse
Serum bile acids	Excretion, shunting
Coagulation tests	Synthetic function (coagulation factors)
5' Nucleotidase (5'NTD)	Cholestasis, biliary injury
Serum glucose	Synthetic function (gluconeogenesis)
Lactate dehydrogenase (LDH)	Liver cells injury/necrosis

Possible future clinical applications of our ^{18}F labeled bile acids can be situated in assessment of liver function in liver disease patients, pre- and post-therapy (surgery, radio-embolization, ablation, pharmacological treatment) For example, post-operative liver function (future liver remnant; FLR) is usually estimated by determining the pre-operative liver volume on CT or MRI. However, this liver volume is not necessarily completely functional, especially in liver disease patients (Geisel et al. 2015). This poses an important risk of triggering liver failure after resection due to insufficient functional liver volume. By performing a pre-treatment PET scan with our ^{18}F labeled bile acids, information could be acquired on the true (remaining) functional liver capacity, which could help to identify and better cater to a specific liver patient's needs. The effect of therapy on liver function could then be monitored by PET imaging.

In a clinical setting, PET imaging offers higher sensitivity, better spatial resolution and better temporal resolution, compared to SPECT imaging. These advantages, together with the inherent tomographic nature of PET, make PET imaging much more suitable for dynamic imaging, and thus to visualize hepatobiliary transport, compared to SPECT. Furthermore, the quantitative potential of PET has advanced elegantly during the last two decades and is now reaching the maturity required for clinical exploitation. Quantitative dynamic PET opens the way towards kinetic modeling, the current gold standard of quantification in molecular imaging, and parametric imaging.

Compared to the clinically used hepatobiliary SPECT tracer $^{99\text{m}}\text{Tc}$ -mebrofenin, our ^{18}F labeled bile acids can offer the advantages that are related to the advantages of PET over SPECT that were discussed in the previous paragraph and listed in Table 9.2. Furthermore, our tracer could not only provide general information on hepatocyte functionality, it could also give valuable insight in bile acid homeostasis in the body. This is because our tracers are also substrates of NTCP and BSEP, which is not the case for $^{99\text{m}}\text{Tc}$ -mebrofenin.

Table 9.2: Side-by-side comparison of characteristics of our lead compound, 3β - $[^{18}\text{F}]\text{FCA}$, and $^{99\text{m}}\text{Tc}$ -mebrofenin. Kinetic data of $^{99\text{m}}\text{Tc}$ -mebrofenin was determined by Neyt, 2016.

	3β - $[^{18}\text{F}]\text{FCA}$	$^{99\text{m}}\text{Tc}$ mebrofenin
Quantification	+++	+
Temporal resolution	+++	+
Spatial resolution	+++ (3D images)	+ (usually 2D images)
Cost	€€€	€€
Transporters involved	NTCP and OATP1B1 BSEP and MRP2	OATP1B1/1B3 MRP2
Tmax liver (min)	5.33 ± 0.24	2.33 ± 0.63
Hepatic clearance (mL/min)	0.35 ± 0.04	0.82
Biliary clearance (mL/min)	0.46 ± 0.08	1.22

If further preclinical testing confirms the utility of ^{18}F labeled bile acids in liver disease, a first-in-human application can be considered. To that end, an investigational medicinal product dossier (IMPD) has to be prepared. An IMPD includes detailed information on tracer synthesis and quality control according to Good Manufacturing Practice (GMP). Furthermore, the IMPD file must contain a preclinical pharmacology section, in which the mode of action of the tracer is described in detail. The acquired results in this dissertation can already be included in this section. Finally, preclinical toxicity studies (extended single dose toxicity) have to be included, which show that no toxic effects after a single microdosing study can be expected (Koziorowski et al. 2017).

9.3 References

- Bennink, R.J. et al., 2012. Liver function testing with nuclear medicine techniques is coming of age. *Seminars in Nuclear Medicine*, 42(2), pp.124–137.
- Bergman, E. et al., 2010. The effect of acute administration of rifampicin and imatinib on the enterohepatic transport of rosuvastatin in vivo. *Xenobiotica*, 40(8), pp.558–568.
- Bernal, W. & Wendon, J., 2013. Acute Liver Failure. *New England Journal of Medicine*, 369(26), pp.2525–2534.
- Cunha, L. et al., 2014. Preclinical imaging: An essential ally in modern biosciences. *Molecular Diagnosis and Therapy*, 18(2), pp.153–173.
- Frisch, K. et al., 2012. [N-methyl-11C]cholylsarcosine, a novel bile acid tracer for PET/CT of hepatic excretory function: radiosynthesis and proof-of-concept studies in pigs. *Journal of nuclear medicine*, 53(5), pp.772–8.
- Frisch, K. et al., 2018. N-(4-[18F]fluorobenzyl) cholyglycine, a novel tracer for PET of enterohepatic circulation of bile acids: Radiosynthesis and proof-of-concept studies in rats. *Nuclear Medicine and Biology*, 61, pp.56–62.
- Frisch, K. & Sørensen, M., 2014. On fluoro-18 labeling of bile acids. *Nuclear medicine and biology*, 41, p.775.
- Geisel, D. et al., 2015. Imaging-Based Liver Function Tests – Past , Present and Future Bildgestützte Leberfunktionstests – Stand der Technik und zukünftige Entwicklungen. , 187, pp.863–871.
- He, J. et al., 2014. PET imaging of oatp-mediated hepatobiliary transport of [11C] rosuvastatin in the rat. *Molecular Pharmaceutics*, 11, pp.2745–2754.
- Jia, L. et al., 2014. Synthesis and evaluation of (18)F-labeled bile acid compound: a potential PET imaging agent for FXR-related diseases. *Nuclear medicine and biology*, 41, pp.495–500.
- Jüngst, C. et al., 2013. Intrahepatic cholestasis in common chronic liver diseases. *European journal of clinical investigation*, 43(10), pp.1069–83.

- Koziorowski, J. et al., 2017. Position paper on requirements for toxicological studies in the specific case of radiopharmaceuticals. *EJNMMI Radiopharmacy and Chemistry*, 1(1), pp.1–6.
- Kramer, J. a, Sagartz, J.E. & Morris, D.L., 2007. The application of discovery toxicology and pathology towards the design of safer pharmaceutical lead candidates. *Nature reviews. Drug discovery*, 6, pp.636–649.
- Kubitz, R. et al., 2012. The bile salt export pump (BSEP) in health and disease. *Clinics and Research in Hepatology and Gastroenterology*, 36(6), pp.536–553.
- de Lima Toccafondo Vieira, M. & Tagliati, C.A., 2014. Hepatobiliary transporters in drug-induced cholestasis: a perspective on the current identifying tools. *Expert opinion on drug metabolism & toxicology*, 10(4), pp.581–97.
- Massoud, T.F. et al., 2003. Molecular imaging in living subjects: seeing fundamental biological processes in a new light. *Genes & Development*, 17, pp.545–580.
- Neyt, S. et al., 2013. In vivo visualization and quantification of (disturbed) Oatp-mediated hepatic uptake and Mrp2-mediated biliary excretion of ^{99m}Tc-mebrofenin in mice. *Journal of Nuclear Medicine*, 54(4), pp.624–630.
- Neyt, S., 2016. *Non-invasive visualization and quantification of (disturbed) hepatobiliary transport - PhD dissertation*
- Neyt, S. et al., 2016. Synthesis, in vitro and in vivo small-animal SPECT evaluation of novel technetium labeled bile acid analogues to study (altered) hepatic transporter function. *Nuclear Medicine and Biology*, 43(10).
- Ørntoft, N.W. et al., 2017. Hepatobiliary transport kinetics of the conjugated bile acid tracer ¹¹C-CSar quantified in healthy humans and patients by positron emission tomography. *Journal of Hepatology*, 67(2), pp.321–327.
- Ostapowicz, G. et al., 2002. Results of a Prospective Study of Acute Liver Failure at 17 Tertiary Care Centers in the United States. *ann intern med*, 137, pp.947–954.

- Regev, A., 2014. Drug-induced liver injury and drug development: industry perspective. *Seminars in Liver Disease*, 34(2), pp.227–239.
- Schacht, A.C. et al., 2016. Radiosynthesis of N-11C-Methyl-Taurine-Conjugated Bile Acids and Biodistribution Studies in Pigs by PET/CT. *Journal of Nuclear Medicine*, 57(4), pp.628–633.
- Shin, D.H. et al., 2014. Hepatic uptake of epirubicin by isolated rat hepatocytes and its biliary excretion after intravenous infusion in rats. *Archives of Pharmacal Research*, 37(12), pp.1599–1606.
- Sjögren, E. et al., 2014. Effects of verapamil on the pharmacokinetics and hepatobiliary disposition of fexofenadine in pigs. *European Journal of Pharmaceutical Sciences*, 57(1), pp.214–223.
- Sorensen, M. et al., 2016. Hepatobiliary Secretion Kinetics of Conjugated Bile Acids Measured in Pigs by 11C-Cholylsarcosine PET. *Journal of Nuclear Medicine*, 57(6), pp.961–966.
- Stevens, J.L. & Baker, T.K., 2009. The future of drug safety testing: expanding the view and narrowing the focus. *Drug Discovery Today*, 14(3–4), pp.162–167.
- Testa, A. et al., 2017. Design, synthesis, in vitro characterization and preliminary imaging studies on fluorinated bile acid derivatives as PET tracers to study hepatic transporters. *Bioorganic and Medicinal Chemistry*, 25, pp.963–976.
- Willmann, J.K. et al., 2008. Molecular imaging in drug development. *Nature Reviews Drug Discovery*, 7, pp.591–607.
- Yang, K. et al., 2013. An Updated Review on Drug-Induced Cholestasis : Mechanisms and Investigation of Physicochemical Properties and Pharmacokinetic Parameters. *Journal of pharmaceutical sciences*, 102(9), pp.3037–3057.

CHAPTER 10:

SUMMARY- SAMENVATTING- CURRICULUM VITAE

SUMMARY

The liver plays a vital role in maintaining homeostasis in the body through essential physiological functions. One of these is the production of bile, a complex fluid containing organic and inorganic solutes. The bulk of the organic constituents is comprised of bile acids, amphiphilic steroid derivatives that are synthesized in the liver and excreted in the small intestine where they help to emulsify fat and solubilize fat-soluble vitamins. Bile acids undergo an efficient enterohepatic cycle, meaning they are reabsorbed in the intestines and are taken back to the liver through the portal circulation. Bile acid transport proteins warrant the efficient hepatobiliary transport of bile acids and their subsequent enterohepatic circulation.

However, disturbances in hepatobiliary transport of bile acids can occur and lead to a toxic accumulation of bile acids in the liver, termed cholestasis. Cholestasis can present itself if drugs interfere with the bile acid transporters, or in certain liver diseases. It is therefore both important to detect this toxicity early on in drug development of new candidate drugs, and to have a representative view on liver function with regards to bile acid transport in liver disease patients.

Therefore, the aim of this dissertation was to develop ^{18}F labeled bile acid analogues for Positron Emission Tomography (PET) imaging that closely resemble endogenous bile acids in molecular structure, *in vitro* and *in vivo* characteristics. It was hypothesized that these radiotracers can be used to detect *in vivo* pharmacological interference with the bile acid transporters in preclinical drug development and can serve as a functional liver imaging tool in liver disease. Consequently, bile acid PET scans can replace the current laborious and invasive *in vivo* experiments during drug development and can also serve as a non-invasive imaging tool to assess and follow-up on liver function in liver disease patients.

The first part of the dissertation provides the reader with the necessary background on the liver and molecular imaging. **Chapter 1** gives a general introduction on liver physiology, bile acid structure and physicochemical properties, biosynthesis and transport. Furthermore, an introduction to molecular imaging is given, with a special focus on PET and ^{18}F radiochemistry. **Chapter 2** covers the topic of molecular imaging in liver disease. First, a

concise background on the different liver diseases that are covered in this dissertation is presented. Then, an overview is given of the recent advances in molecular imaging of the liver. Finally, **Chapter 3** covers the research questions that will be investigated in the following experimental chapters.

In **Chapter 4**, the (radio)synthesis of a set of ^{18}F labeled bile acids was described, based on the backbone of the endogenous cholic acid, glycocholic acid and chenodeoxycholic acid. Non-radioactive fluorinated reference compounds were also synthesized. The radiosynthesis encompassed a $\text{S}_{\text{N}}2$ nucleophilic substitution with ^{18}F fluoride on a mesylated, protected precursor, followed by an alkaline deprotection step and High Performance Liquid Chromatography (HPLC) purification. Four PET tracers were successfully synthesized in moderate radiochemical yields: 3β - ^{18}F fluorocholeic acid (3β - ^{18}F FCA), 3α - ^{18}F fluorocholeic acid (3α - ^{18}F FCA), 3β - ^{18}F fluorocholedeoxycholeic acid (3β - ^{18}F FCDCA), and 3β - ^{18}F fluoroglycocholeic acid (3β - ^{18}F FGCA). The precursors for 12β - ^{18}F fluorocholeic acid (12β - ^{18}F FCA) and 7β - ^{18}F fluorocholeic acid (7β - ^{18}F FCA) could not be labeled with sufficient radiochemical yield and therefore could not be used further for *in vivo* evaluation.

Chapter 5 addressed the *in vitro* evaluation of the developed ^{18}F labeled bile acids. Their stability was assessed in formulation for use, in mouse serum and in presence of primary mouse hepatocytes and was found to be stable for further *in vivo* use. Fluorine substitution possibly hampers metabolization, but does not have a considerable effect on substrate recognition by the relevant bile acid transporters: they are substrates with low micromolar affinity for NTCP, OATP1B1 and BSEP, which is also the case for endogenous bile acids. MRP2 is also used by 3β - ^{18}F FCA. The $\text{LogD}(7.4)$ values of the fluorinated bile acids are also in accordance with endogenous bile acids. The developed compounds were therefore deemed suitable to monitor (disturbed) hepatobiliary transport of bile acids *in vivo* with PET.

Chapter 6 covered the *in vivo* evaluation of the ^{18}F labeled bile acids in healthy, wild-type mice. All tracers showed exclusive hepatic uptake and were excreted in gallbladder and intestines. It was found that three out of four newly developed PET tracers (3α - ^{18}F FCA, 3β - ^{18}F FCA and 3β - ^{18}F FGCA) displayed fast and efficient hepatobiliary transport. The chenodeoxycholeic acid derivate 3β - ^{18}F FCDCA showed both slower and lower hepatic uptake and biliary excretion. Lead compound 3β - ^{18}F FCA showed good inter- and intra-

animal reproducibility and was validated as an *in vivo* bile acid transporter substrate by coadministration of the tracer with rifampicin or bosentan that block the bile acid transporters.

In **Chapter 7**, valorization of 3β -[^{18}F]FCA as a hepatobiliary imaging probe was performed in different mouse models of liver disease. The tracer showed dosage-dependent alterations in its pharmacokinetics after administration of a known cholestatic drug, cyclosporin. In chronic liver disease models of cholangiopathy and non-alcoholic steatohepatitis (NASH), 3β -[^{18}F]FCA was able to detect altered liver functionality and the subsequent recovery from it. In a mouse model for hepatocellular carcinoma (HCC), a lower hepatic uptake of 3β -[^{18}F]FCA was noticed in the tumor lesions. Altered hepatobiliary transport of 3β -[^{18}F]FCA in these chronic liver diseases could be linked to adapted gene expression of the bile acid transport proteins. In models for acute liver injury and liver fibrosis/cirrhosis however, no significant change in 3β -[^{18}F]FCA's hepatobiliary transport was found. The acquired results imply that 3β -[^{18}F]FCA can have a broad application range in preclinical drug development and the (pre)clinical evaluation of liver function through the tracer's (regionally altered) hepatobiliary transport by the bile acid transporters.

The general conclusions of the dissertation's research questions can be found in **Chapter 8**. **Chapter 9** focusses on the broader international context, relevance and future perspectives of this research.

Samenvatting

De lever speelt een belangrijke rol in het onderhouden van homeostase in het lichaam door de verschillende essentiële functies die het orgaan vervult. Eén daarvan is de productie van gal, een complexe vloeistof waarin zowel organische als anorganische stoffen opgelost zijn. Het grootste deel van de organische componenten bestaat uit galzuren, amfifiele steroid-derivaten die aangemaakt worden in de lever en uitgescheiden worden in de dunne darm, waar zij helpen om vetten en vetoplosbare vitamines op te nemen. Galzuren ondergaan een efficiënte enterohepatische cyclus, wat wil zeggen dat zij gereabsorbeerd worden in de darm en opnieuw naar de lever teruggebracht worden via de portale circulatie. Galzuur transporteiwitten staan in voor het efficiënt hepatobiliair transport van galzuren en hun daaropvolgende enterohepatische cyclus.

Verstoringen van het hepatobiliair transport van galzuren kunnen echter voorkomen. Dit kan leiden tot een toxische opstapeling van galzuren in de lever, cholestase. Cholestase kan optreden indien geneesmiddelen interfereren met de galzuurtransporters, of in sommige leverziekten. Het is daarom belangrijk om deze toxiciteit vroeg te kunnen opsporen tijdens de ontwikkeling van een nieuw geneesmiddel, en om een representatief beeld te hebben van de leverfunctie, voor wat betreft het galzuurtransport bij leverpatiënten.

Het doel van dit proefschrift bestond er daarom in om ^{18}F gelabelde galzuuranalogen te ontwikkelen voor Positron Emission Tomography (PET) beeldvorming, die sterk lijken op endogene galzuren qua moleculaire structuur, *in vitro* en *in vivo* eigenschappen. Er werd uitgegaan van de hypothese dat deze radiotracers gebruikt kunnen worden om farmacologische interferentie met de galzuurtransporters *in vivo* op te sporen in preklinische geneesmiddelenontwikkeling, en ook dienst kunnen doen als middel om de leverfunctionaliteit na te gaan bij leverpatiënten. De galzuur PET-scans kunnen bijgevolg de huidige arbeidsintensieve, invasieve *in vivo* experimenten tijdens geneesmiddelenontwikkeling vervangen en kunnen ook dienst doen als contraststof om via niet-invasieve beeldvorming de leverfunctie van leverpatiënten te evalueren en op te volgen.

Het eerste deel van het proefschrift verschaft de lezer de benodigde achtergrondinformatie wat betreft de lever en moleculaire beeldvorming. **Hoofdstuk 1** omvat een algemene inleiding over de fysiologie van de lever, galzuur structuur en fysicochemische eigenschappen, biosynthese en transport. Verder wordt een introductie tot moleculaire beeldvorming gegeven, met focus op PET en ^{18}F radiochemie. In **Hoofdstuk 2** wordt moleculaire beeldvorming van leverziekten behandeld. Eerst wordt een beknopte achtergrond geschetst van de verschillende leverziekten die in dit proefschrift behandeld zullen worden. Daarna wordt een overzicht gegeven van de recente ontwikkelingen in moleculaire beeldvorming van de lever. Tot slot worden in **Hoofdstuk 3** de onderzoeksvragen gepostuleerd die onderzocht zullen worden in de daaropvolgende experimentele hoofdstukken.

In **Hoofdstuk 4** wordt de (radio)synthese van een set ^{18}F gelabelde galzuuranalogen beschreven, gebaseerd op het moleculair skelet van het endogene cholzuur, glycocholzuur en chenodeoxycholzuur. Niet-radioactieve, gefluoreerde referentiestoffen werden ook gesynthetiseerd. De radiosynthese omvatte een $\text{S}_{\text{N}}2$ nucleofiele substitutie met ^{18}F fluoride op een gemesylerde, beschermde precursor, gevolgd door een alkalische deprotectie en opzuivering via High Performance Liquid Chromatography (HPLC). Vier PET-tracers werden succesvol gesynthetiseerd met een gematigd radiochemisch rendement: 3β - ^{18}F fluorocholezuur (3β - ^{18}F FCA), 3α - ^{18}F fluorocholezuur (3α - ^{18}F FCA), 3β - ^{18}F fluorochenodeoxycholezuur (3β - ^{18}F FCDC), en 3β - ^{18}F fluoroglycocholezuur (3β - ^{18}F FGCA). De precursoren voor 12β - ^{18}F fluorocholezuur (12β - ^{18}F FCA) en 7β - ^{18}F fluorocholezuur (7β - ^{18}F FCA) konden niet gelabeld worden met voldoende radiochemisch rendement en konden daarom niet verder gebruikt worden bij de verdere *in vivo* evaluatie.

Hoofdstuk 5 beschrijft de *in vitro* evaluatie van de ontwikkelde ^{18}F gelabelde galzuuranalogen. Hun stabiliteit werd onderzocht in de formulatie voor gebruik, in muis serum en in aanwezigheid van primaire muishepatocyten. De galzuuranalogen werden stabiel genoeg bevonden voor verder *in vivo* gebruik. De introductie van een fluoratoom op de galzuren verstoort mogelijks hun metabolisme, maar heeft geen noemenswaardig effect op substraatherkenning door de relevante galzuurtransporters: de tracers zijn substraten met lage, micromolaire affiniteit voor NTCP, OATP1B1 en BSEP. MRP2 wordt ook gebruikt

door 3β - ^{18}F]FCA. LogD(7.4) waarden van de ^{18}F gelabelde galzuuranalogen werden ook bepaald en zijn in overeenstemming met endogene galzuren. De ontwikkelde stoffen werden daarom geacht in staat te zijn om (verstoord) hepatobiliair transport van galzuren *in vivo* te detecteren met PET.

Hoofdstuk 6 behandelt de *in vivo* evaluatie van de ^{18}F gelabelde galzuuranalogen in gezonde, wild-type muizen. Alle tracers vertoonden enkel opname in de lever, en werden uitgescheiden in galblaas en darmen. Er werd bevonden dat drie van de vier nieuw ontwikkelde PET-tracers (3α - ^{18}F]FCA, 3β - ^{18}F]FCA en 3β - ^{18}F]FGCA) snel en efficiënt hepatobiliair transport vertoonden. Het chenodeoxocholzuur derivaat, 3β - ^{18}F]FCDCA, vertoonde echter zowel een tragere en lagere opname in de lever en biliaire excretie. Tracer 3β - ^{18}F]FCA werd gekenmerkt door een goede reproduceerbaarheid inter- en intra-animal en werd gevalideerd als een *in vivo* galzuurtransporter substraat door coadministratie van de tracer met rifampicine of bosentan, die de galzuurtransporters kunnen blokkeren.

In **Hoofdstuk 7** werden de preliminaire resultaten van 3β - ^{18}F]FCA als hepatobiliaire contraststof gevaloriseerd in meerdere muis modellen voor leverziekte. De tracer vertoonde doseringsafhankelijke veranderingen in zijn farmacokinetiek na toediening van cyclosporine, een geneesmiddel waarvan gekend is dat het aanleiding kan geven tot cholestase. Verder was 3β - ^{18}F]FCA in staat om in chronische leverschademedellen voor cholangiopathie en niet-alcoholische steatohepatitis (NASH) een verstoorde leverfunctie vast te stellen, en het daaropvolgend herstel. In een muismodel voor hepatocellulair carcinoom (HCC) werd een lagere opname van 3β - ^{18}F]FCA vastgesteld in de tumor. Het gewijzigd hepatobiliair transport van de tracer in deze chronische leverziekten kon gelinkt worden aan een gewijzigde genexpressie van de galzuurtransporters. In modellen voor acute leverschade en lever fibrose/cirrose werd er echter geen significante wijziging in 3β - ^{18}F]FCA's hepatobiliair transport waargenomen. De bekomen resultaten geven aan dat 3β - ^{18}F]FCA een breed toepassingsgebied kan hebben in preklinische geneesmiddelontwikkeling en in de (pre)klinische evaluatie van leverfunctie m.b.v. de tracer's (regionaal verschillend) hepatobiliair transport door de galzuurtransporters.

De algemene conclusies van de onderzoeksvragen in dit proefschrift kunnen teruggevonden worden in **Hoofdstuk 8**. **Hoofdstuk 9** behandelt de internationale context, relevantie en toekomstperspectieven van dit onderzoek.

Curriculum Vitae **STEF DE LOMBAERDE**

Personal information

Birth place and date: Deinze, 6 June 1991

Address: Oosteinde 26 bus 0102; 9080 Zaffelare

Phone number: 0477/56.37.42

E-mail: stefdelombaerde@hotmail.com

Education

2014-present: PhD-student (Academic Assistant) at Laboratory for Radiopharmacy, Faculty of Pharmaceutical Sciences, Ghent University:

Development of ^{18}F -labeled bile acid analogues to monitor hepatobiliary transport in liver disease;

Promotors: Filip De Vos & Christian Vanhove

2009-2014: Bachelor in Pharmaceutical Sciences with great distinction (Ghent University)

Master in Drug Development with great distinction (Ghent University)

Master thesis with laboratory for Radiopharmacy:

Optimalisatie radiosynthese van 2-(2-[^{18}F]fluoroethyl)-L-fenylalanine en O-(2-[^{18}F]fluoroethyl)-L-tyrosine; Supervisors: Ken Kersemans, Filip De Vos

Work experience and internships

2014-present: PhD-student (Academic Assistant) at Laboratory for Radiopharmacy, Faculty of Pharmaceutical Sciences, Ghent University

Main occupations during PhD:

-organic (radio)synthesis	-HPLC/TLC
-PET-scans: acquisition and data analysis	-cell culture and uptake assays
-mice liver disease models	-tutor for bachelor and master thesis
-practical exercises analytical chemistry	

2013-2014: Pharmacy Internship Molleman-De Coster, Ruiselede

Courses and certifications

Best poster: new PET/SPECT probes, EMIM conference 2018, San Sebastian, Spain

Leadership Foundation Course (Ghent University; 2016)

Positron Emission Tomography (PET) Methodology (King's College London; 2015)

Translational Biomedical In Vivo Imaging (Ghent University; 2015)

Training in Laboratory Animal Science - FELASA C (2015)

Fluor-18 Chemistry Course (VU Amsterdam; 2014)

Publications

De Lombaerde S, Devisscher L, Verhoeven J, Neyt S, Van Vlierberghe H, Vanhove C, De Vos F; *Validation of hepatobiliary transport PET imaging in liver function assessment: evaluation of $^{36}\text{-}[^{18}\text{F}]\text{FCA}$ in mouse models of liver disease*; submitted to Nuclear Medicine and Biology; 2018

De Lombaerde S, Neyt S, Vanhove C, De Vos F; *In vivo measurement of hepatic drug transporter inhibition with radiolabeled bile acids*; to be published as a chapter of book: Protocols In Experimental Cholestasis Research; Editor: Mathieu Vinken, VUB; 2018

Verhoeven J, Hulpia F, Kersemans K, Bolcaen J, De Lombaerde S, Goeman J, Descamps B, Hallaert G, Van den Broecke C, Deblaere K, Vanhove C, Van der Eycken J, Van Calenbergh S, Goethals I, De Vos F; *Affinity evaluation of phenylalanine derivatives for LAT1 transporter in F98 glioblastoma cells*; submitted to Scientific Reports; 2018

Ciarocchi E, Vanhove C, Descamps B, De Lombaerde S, Vandenberghe S, Belcari N; *Performance evaluation of the LightPath imaging system for intra-operative Cerenkov luminescence imaging*; Physica Medica; 2018; Vol. 52; p 122-128

De Lombaerde S, Kersemans K, Neyt S, Verhoeven J, Vanhove C, De Vos F; *Evaluating Hepatobiliary Transport with ^{18}F -Labeled Bile Acids: The Effect of Radiolabel Position and Bile Acid Structure on Radiosynthesis and In Vitro and In Vivo Performance*; Contrast Media & Molecular Imaging, Volume 2018, Article ID 6345412, 9 pages

De Lombaerde S, Neyt S, Kersemans K, Verhoeven J, Devisscher L, Van Vlierberghe H, Vanhove C, De Vos F; *Synthesis, in vitro and in vivo evaluation of 3 β -[¹⁸F]fluorochoolic acid for the detection of drug-induced cholestasis in mice*; PLoS One. 2017;12: 14 pages

Neyt S, Vliegen M, Verreet B, De Lombaerde S, Braeckman K, Vanhove C, Huisman M, Dumolyn C, Kersemans K, Hulpia F, Van Calenbergh S, Mannens G, De Vos F; *Synthesis, in vitro and in vivo small-animal SPECT evaluation of novel technetium labeled bile acid analogues to study (altered) hepatic transporter function*; Nucl Med Biol.; 2016;43: 642–649.

Oral presentations

Synthesis, in vitro and in vivo evaluation of 3 β -[¹⁸F]fluorochoolic acid, a radiolabeled bile acid to detect drug-induced cholestasis in preclinical drug development; 18th Symposium of the Belgian Society of Nuclear Medicine (BELNUC); 5-7 May 2017; Ghent, Belgium

Synthesis and in vivo PET evaluation of a ¹⁸F bile acid to assess drug-induced liver injury in mice; MedChem 2016: PET & imaging : from chemistry lab to clinical applications; 18th of November 2016; Mont-Saint-Guibert, Belgium

Poster presentations

Evaluating hepatobiliary transport with ¹⁸F labeled bile acids : the effect of radiolabel position and bile acid backbone on radiosynthesis, in vitro and in vivo performance; 13th European Molecular Imaging Meeting (EMIM); 20-23 March 2018; San Sebastian, Spain.

Evaluation of 3 β -[¹⁸F]Fluorochoolic acid in hepatocellular carcinoma bearing mice; 6th OncoPoint research seminar; 28th of February 2018; Ghent, Belgium

Synthesis, in vitro and in vivo evaluation of 3 β -[¹⁸F]fluorochoolic acid, a radiolabeled bile acid to detect drug-induced cholestasis in preclinical drug development; World Molecular Imaging Congress (WMIC) 2016; 7-10 September 2016; New York, USA

Synthesis and in vivo PET evaluation of a ¹⁸F bile acid to assess hepatobiliary transport; Knowledge for Growth 2016; 26th of May 2016; Ghent, Belgium

Languages

Dutch: mother tongue

English: very good

French: good

German: basic

Computer skills

Microsoft Office: Word, Excel, Powerpoint: very good

Pmod Imaging analysis software: good

Graphpad Prism good

SPSS statistics: basic knowledge

Extracurricular activities

Organizing Committee Member of the Belgian Molecular Imaging Community